Measurements and modelling of emissions from biomass burning in Australia

Clare Paton-Walsh
University of Wollongong

Measurements and Modelling of Emissions from Biomass Burning in Australia

A thesis submitted in fulfilment of the requirements for the award of the degree

Doctor of Philosophy

from

UNIVERSITY OF WOLLONGONG

by

Clare Murphy, (née Paton-Walsh), BSc, MSc

Chemistry

(2009)

CERTIFICATION

I, Clare Murphy, (née Clare Paton-Walsh) declare that this thesis, submitted in fulfilment of the requirements for the award of Doctor of Philosophy, in the Department of Chemistry, University of Wollongong, is wholly my own work unless otherwise referenced or acknowledged. The document has not been submitted for qualifications at any other academic institution.

Clare Murphy

Date:

Abstract

This thesis describes work aimed at improving our knowledge of emissions to the atmosphere from Australian vegetation fires. The thesis contains three main parts. First there is a study to characterise the emissions from forest fires in southeast Australia. This uses ground-based Fourier transform infrared solar absorption spectroscopy, coupled with ultra-violet/visible spectroscopy, to explore the properties of smoke plumes from Australian forest fires that passed over the observation site at Wollongong, in New South Wales, Australia (34.4°S, 150.9°E). The particulate loading in the smoke plumes is characterised by the aerosol optical depth, measured at visible wavelengths. Vertically integrated amounts of a several emitted trace gases are also determined, (limited to those detectable by solar absorption spectroscopy in the infrared). Enhanced trace gas amounts of carbon monoxide, hydrogen cyanide, formaldehyde, ammonia, acetylene, ethylene, ethane, formic acid and methanol were measured in the smoke plumes and quantified via the use of emission ratios. The emission ratios determined in this study indicate that emissions from fires in southeastern Australian forests (which are predominantly eucalypts) are broadly similar to those from other geographical regions except for comparatively low emissions of ethane.

The second part of this thesis describes a new method of making estimates of gaseous emissions from fires. Strong correlations between trace gases and aerosol optical depth (AOD) in smoke plumes are used in conjunction with satellite-based measurements of AOD to estimate the total amounts of carbon monoxide and other gases emitted from the Canberra fires of 2003. There are significant difficulties with the new method, in particular the interruption of the satellite record due to clouds or technical problems with the satellite. Nevertheless the estimated emissions of carbon monoxide from the Canberra fires (4.9 – 9.6 Tg), is in agreement with an estimate made by existing techniques. The addition of another tool for making estimates of gaseous emissions from biomass burning is useful for corroborating existing techniques, especially since the sources of

uncertainties inherent in the different techniques are largely independent of one another.

The third part of the thesis is a study to characterise the emissions from savanna fires in the tropical north of Australia. Again ground-based Fourier transform infrared solar absorption spectroscopy is used with automated measurements in the near infrared from a site in Darwin, Northern Territory, Australia, (12.4°S, 130.9°E). Alternatively measurements in the mid infrared can be made by overriding the automated system, and this has been done when there is evidence of significant smoke plumes in the area. Total column amounts of carbon monoxide from Darwin from 2005-2008 show a very clear annual cycle, with evidence of transported pollution from Indonesian fires in 2006. The time series agrees within the expected uncertainties with measurements of carbon monoxide derived from the MOPITT satellite instrument, giving greater confidence to MOPITT retrievals in the tropics. Mid infrared spectra have been recorded through smoke plumes over Darwin on 20 separate days, yielding column amounts of carbon monoxide, formaldehyde, acetylene, ethane and hydrogen cyanide and emission ratios with respect to carbon monoxide for the four latter gases from tropical north Australian savanna fires. Emission ratios for acetylene and ethane from this work are in broad agreement with other literature values, whilst emission ratios for formaldehyde and hydrogen cyanide are significantly higher than the only previous field measurements from Australian savannas (but in agreement with laboratory studies) suggesting storage losses in the earlier study.

Acknowledgements

I would like to acknowledge with deep gratitude the support of my husband Doug and my children Anna, Catherine and Antony, all of whom have coped well with less wifely or motherly input in their lives as this document was being prepared. I also acknowledge the helpful comments, support and guidance provided by all three of my supervisors Nicholas Jones, Steve Wilson and David Griffith and many other colleagues including David Edwards, Di Jolley and Nicholas Deutscher.

I thank Arndt Meier for coming into work over Christmas and New Year in 2001/2002 and running the spectrometer at Wollongong to collect the first of the smoke affected spectra upon which this work is based. I also acknowledge Nicholas Jones and all other colleagues with the Centre of Atmospheric Chemistry who have run the spectrometer in Wollongong and captured smoke plumes as a result.

The spectrometer operating at Darwin is designed to operate automatically for the collection of near-infrared data. The system was designed and installed by the efforts of Paul Wennberg, Jean-Francois Blavier, Geoff Toon, Yael Yavin, Rebecca Washenfelder, Gretchen Keppel-Aleks, Nicholas Deutscher, David Griffith, Glenn Bryant, Brian Connor, Charles Miller and Ross Salawitch. The automated collection of near infrared data at Darwin is kept running, despite frequent glitches, by the efforts of Nicholas Deutscher. Nicholas occasionally has also taken data for me in the mid infrared and has been tirelessly patient in providing advice on how to run the system at Darwin. Technical assistance on site in Darwin (including cooling of the detector with liquid nitrogen) has been provided by John Glowacki, Rex Pearson, Troy Culgan, Mike Alsop, Krzysztof Krzton and Maciej Ryczek, many of whom have also alerted me when there were signs of smoke in Darwin. On other occasions the very useful Geosciences Australia "Sentinel" website (http://sentinel.ga.gov.au/acres/sentinel/) was used in conjunction with wind forecasts for the Darwin region from the Bureaux of Meteorology as a crude fire alert system. Aerosol Optical Depth measurements from Darwin were provided by Bruce Forgan.

The TAPM model was developed at CSIRO and purchased by the University of Wollongong for use in this and other projects. Advice was offered for

its correct use by Martin Cope, Peter Hurley and Bronwyn Dunse. The programs to derive aerosol optical depth from measurements at Wollongong were written by Stephen Wilson. Some aspects of the uncertainty in retrieving total column amounts using the SFIT2 algorithm were estimated using Matlab scripts written by Vanessa Haverd.

Satellite image courtesy of MODIS Rapid Response Project at NASA/GSFC was used in many of the maps showing the location of fires. Some of the maps produced in the software ArcMap used Spatial Analysis Laboratories products OSDM_GMA2001_coastl and OSDM_GMA2001_builtupp that incorporate data which is Copyright Commonwealth of Australia 2001. Back trajectories were generated by the European Centre for Medium-Range Weather Forecasts, (ECMWF) Trajectories, via the website http://badc.nerc.ac.uk/data/ecmwf-trj/ run by the British Atmospheric Data Centre, 2006-2008.

Finally, I would like to acknowledge the financial support of the Australian Research Council in the form of the research grant "Biomass Burning Emissions- An Innovative Technique for Assessing Global Climate Impacts – DP0557407" that made possible a large proportion of the work described in this thesis.

List of Acronyms used in this Thesis

AOD = aerosol optical depth

VMR = volume mixing ratio

InSb = indium antimonide

CO = carbon monoxide

H_2CO = formaldehyde

HCN = hydrogen cyanide

NH_3 = ammonia

HCOOH = formic acid

C_2H_2 = acetylene

C_2H_4 = ethylene

C_2H_6 = ethane

CH_3OH = methanol

Contents

Chapter 1 : Introduction ..... **- 1 -**
1.1 Biomass Burning Emissions ..... - 1 -
1.2 Traditional Methods of Estimating Emissions from Biomass Burning ..... - 2 -
Area Burned ..... - 3 -
Fuel Load & Burning Efficiency ..... - 3 -
Emission Factors & Emission Ratios ..... - 5 -
1.3 Remote Sensing using Fourier Transform Spectrometry and the Network for the Detection of Atmospheric Composition & Change ..... - 8 -
1.4 Background to the Work described in this Thesis ..... - 11 -
1.5 Objectives of the Thesis ..... - 11 -

Chapter 2 : Measurement and Modelling Tools ..... **- 13 -**
2.1 Fourier Transform Spectroscopy ..... - 13 -
2.2 Remote sensing of the Atmosphere by Solar FTIR Spectroscopy ..... - 16 -
Atmospheric Absorption Line Positions ..... - 19 -
Line Broadening and Line Shapes ..... - 21 -
Atmospheric Absorption Line Intensities ..... - 22 -
Calculating Synthetic Atmospheric Spectra ..... - 24 -
2.3 Deriving Trace Gas Amounts from Solar FTIR Spectra ..... - 27 -
Analysis Algorithms ..... - 27 -
Inverse Modelling and Optimal Estimation ..... - 28 -
The averaging kernel and uncertainties ..... - 30 -
Using SFIT2 in practice ..... - 31 -
2.4 Measurements of Aerosol Optical Depth ..... - 33 -
Ground-based Measurements of Aerosol Optical Depth using Ultraviolet and Visible Spectroscopy ..... - 33 -
Satellite-based Measurements of AOD ..... - 37 -
2.5 Atmospheric Modelling using "TAPM" ..... - 37 -

Chapter 3 : FTIR Spectra Recorded through Smoke Plumes from South Eastern Australian Forest Fires & Analysis for Trace Gas Amounts - 40 -

3.1 Spectra Recorded through Smoke Plumes from South Eastern Australian Forest Fires 2001 – 2003 ..... - 40 -

3.2 Analysis of Smoke affected FTIR Spectra for Trace Gas Amounts ..... - 44 -

Analysis for CO using SFIT2 ..... - 44 -

SFIT2 Analysis of Spectra for H_2CO, HCN, NH_3, HCOOH, C_2H_2, C_2H_4 and C_2H_6 ..... - 49 -

Uncertainty Analysis for Derived Column Amounts using SFIT2 ..... - 49 -

CH_3OH Amounts derived using GFIT ..... - 59 -

3.3 Variability of the Sampled Smoke Plumes Illustrated with Time series of CO Vertical Column Amounts ..... - 62 -

3.4 Correlation between AOD and Trace Gases in Smoke Plumes from Southeast Australian Forest Fires ..... - 66 -

3.5 January 1st 2002 ..... - 74 -

3.7 Emission ratios of trace gases using AOD as a proxy for CO ..... - 75 -

3.8 Emission Factors Extrapolated from Emission Ratios to CO ..... - 76 -

3.9 A Potential Method for Estimating Biomass Burning Emissions ..... - 79 -

3.10 Summary and Conclusions ..... - 81 -

Chapter 4 : Modeling Emissions from the Canberra Wildfires of 2003 ..... - 83 -

4.1 The Canberra Wildfires of 2003 ..... - 83 -

4.2 Outline of a Method to Estimate Emissions Using AOD ..... - 85 -

4.3 MODIS Satellite Measurements of AOD during the Canberra Fires ..... - 86 -

4.4 Estimating Gaseous Emissions using MODIS AOD Measurements ..... - 94 -

4.5 Difficulties in Modelling the dispersion of smoke plumes ..... - 97 -

4.6 Emissions Calculations including corrections for double counting using TAPM dispersion modelling - 98 -

4.7 Results and Uncertainties ..... - 113 -

4.8 Total emissions estimates of trace gases from the Canberra fires of 2003. ..... - 118 -

4.9 Summary ..... - 119 -

Chapter 5 : CO and AOD Measurements from Darwin..... - 121 -

5.1 Near-Infrared Spectra Recorded from Darwin 2005-2008..... - 121 -
5.2 Analysis of Near Infrared Spectra for CO..... - 123 -
5.3 Comparison with MOPITT..... 131
5.4 Measurements of AOD from Darwin..... 133
5.5 AOD and Column amounts of CO measured from Darwin 138

Chapter 6 : Emissions from Tropical North Australian Savanna Fires Derived from Ground-based Mid Infrared FTIR Spectra from Darwin..... 141

6.1 Recording of Mid infrared Spectra from Darwin..... 141
6.2 Technical Details of the Analysis of Mid infrared Spectra..... 143
Analysis of Mid infrared Spectra for CO & H_2CO..... 144
Analysis of Mid infrared Spectra for HCN, C_2H_2 and C_2H_6..... 150
6.3 Distinguishing between local and transported smoke..... 155
6.4 Correlations between derived columns of H_2CO and CO..... 164
6.5 Emissions Ratios for H_2CO, HCN, C_2H_2 and C_2H_6 from Tropical North Australian Savanna Fires..... 171
6.6 Correlations between trace gases and AOD..... 178

Chapter 7 : Summary and Conclusions..... 182

7.1 Overview of Main Conclusions..... 182
7.2 Outcomes for Specific Objectives of the Thesis..... 184
7.3 Recommendations for future work..... 189
7.4 Concluding Comments..... 189

List of Tables

Table 3-1: Spectra intervals and interfering gases fitted for each species retrieved using SFIT2 along with uncertainties in the derived column amounts. ..... - 51 -

Table 3-2 : The results of generalised least squares regression analysis on the column amounts of each trace gas and the coincident AOD measurements. - 73 -

Table 3-3: Emission factors calculated in this study alongside emission factors from [Andreae and Merlet, 2001] ..... - 78 -

Table 4-1: Satellite overpasses with a clear image of enhanced AOD from smoke plumes from the Canberra fires during January 2003. ..... - 92 -

Table 4-2: Satellite overpasses with a clear image of enhanced AOD from smoke plumes from the Canberra fires during February 2003. ..... - 93 -

Table 4-3: Estimated total emissions from the Canberra fires for all of the measured trace gases. ..... - 120 -

Table 5-1: Summarises the results of a survey of possible microwindows to use for retrieving atmospheric CO total column amounts. All the major CO lines in the overtone band from approximately 4200cm^{-1} to 4300cm^{-1} are included but only two microwindows were chosen. These are shown in bold. 125

Table 6-1: Spectral intervals and interfering gases fitted for CO and H_2CO retrieved using SFIT2 along with uncertainties in the derived column amounts 147

Table 6-2: Spectral intervals and interfering gases fitted for C_2H_6, C_2H_2 and HCN retrieved using SFIT2 along with uncertainties in the derived column amounts..- 152 -

Table 6-3: Results of regressions analyses on H_2CO and CO retrievals from each of the 20 individual days when significant smoke plumes were sampled with the InSb detector from Darwin. The gradient, intercept and value for the square of the correlation coefficient (r^2) are shown. Days with strong correlations are shown in bold, and mean values for the daily gradients and intercepts are given for spectra recorded between May and September and spectra recorded during October and November. 166

Table 6-4: Emission ratios with respect to CO for this work compared to other measurements in the literature..... 177

List of Figures

Figure 1-1: Photograph of the Bomem DA8 Spectrometer used at the Wollongong NDSC/NDACC complementary site from 1995 until 2008. - 9 -

Figure 1-2: Photograph of solar tracker used at the Wollongong NDSC/NDACC complementary site from 1995 until 2008. - 10 -

Figure 2-1: Time is shown on the x-axis and intensity on the y-axis. Two cosine waves of different frequency are shown at the bottom of the figure, whilst the top of the figure illustrates the sum of the two waves – the "beat frequency". - 13 -

Figure 2-2: The basic components of a Fourier transform spectrometer – in essence a Michelson interferometer. - 15 -

Figure 2-3: An example spectrum recorded by a ground-based solar Fourier transform spectrometer. - 17 -

Figure 2-4: Schematic showing how radiation from the sun passes through different regions of the atmosphere and molecular vibrational/rotational transitions produce characteristic absorption features in the solar spectrum. - 18 -

Figure 2-5: From the spectroscopic atlas by *Meier et al* [2004]: the infrared transmission spectrum of water (top panel), carbon dioxide (middle panel) and methane (bottom panel) in the atmosphere from 500 cm^{-1} to 4400 cm^{-1} as simulated using the HITRAN 2000 database for a solar zenith angle of 70° and concentration profiles taken from US standard atmosphere. - 26 -

Figure 2-6: Photograph showing the Optical fibres used with the Ocean Optics OD2000 grating spectrometer - 33 -

Figure 2-7: Photograph showing the Ocean Optics OD2000 grating spectrometer - 34 -

Figure 2-8: Example of a Langley plot. The x=0 intercept give $V_0(\lambda)$ and the gradient gives τ^t. From http://seawifs.gsfc.nasa.gov/staff/sunphoto/principle.html#Langley_section for illustration purposes only, data not from this thesis. - 36 -

Figure 3-1: Plots showing enhanced amounts of (a) CO (top panel), (b) HCN (middle panel) and (c) H_2CO (bottom panel) in smoke plumes sampled on 1st January 2002. - 42 -

Figure 3-2: Plots showing enhanced amounts of (a) NH_3 (top panel), (b) C_2H_4 (middle panel) and (c) C_2H_6 (bottom panel) in smoke plumes sampled on 1st January 2002. - 43 -

Figure 3-3: *a priori* covariance matrix and VMR used in retrieval of CO. - 46 -

Figure 3-4: Averaging kernel for the retrieval of CO. - 47 -

Figure 3-5: Example fits achieved in the SFIT2 retrieval of CO in all 3 microwindows used: (a) 2057.684 – 2058.000cm^{-1} fitting the P10 line of $^{13}C^{16}O$, (b) 2069.55 – 2069.76cm^{-1} fitting the P7 line of $^{13}C^{16}O$ and (c) 2012.00 – 2012.20cm^{-1} fitting solar CO - 48 -

Figure 3-6: *a priori* covariance matrices and VMR profiles used in the retrieval of (a) H_2CO, (b) HCN, (c) NH_3 and (d) HCOOH. - 52 -

Figure 3-7: *a priori* covariance matrices and VMR profiles used in the retrieval of (a) C_2H_2, (b) C_2H_4 and (c) C_2H_6. Panel (d) shows the initial VMR profile for GFIT analysis of CH_3OH. - 53 -

Figure 3-8: Example fits achieved in the SFIT2 retrieval of H_2CO in both microwindows used: (a) 2778.12 – 2778.80cm^{-1} fitting the H_2CO lines around 2778.48 cm^{-1} and (b) 2780.60 – 2781.17cm^{-1} encompassing the manifold of H_2CO lines around 2780.9 cm^{-1} - 54 -

Figure 3-9: Example fits achieved in the SFIT2 retrieval of HCN in both microwindows used: (a) 3268.00 – 3268.38 cm^{-1} fitting the P14 HCN line and (b) 3287.00 – 3287.48 cm^{-1} fitting the P8 HCN line at 3287.25 cm^{-1}.- 55 -

Figure 3-10: Example fits for the SFIT2 retrievals of (a) NH_3 and (b) HCOOH. - 56 -

Figure 3-11: Example fits for the SFIT2 retrievals of (a) C_2H_2 and (b) C_2H_4.- 57 -

Figure 3-12: Example fits achieved in the SFIT2 retrieval of C_2H_6 in all 3 microwindows used: (a) 2976.60 – 2977.10cm^{-1} (b) 2996.70 – 2997.10cm^{-1} and (c) 3000.10 – 3000.60cm^{-1}. - 58 -

Figure 3-13 Simulated absorptions of methanol, carbon dioxide, water, ammonia and ozone produced by the GFIT algorithm's best fit to an example spectrum for the 1014 cm^{-1} to 1038 cm^{-1} region. The simulations have been offset vertically for clarity. - 60 -

Figure 3-14 Residuals of the best fits that resulted (1) from the analysis described in the text and illustrated in Figure 3-13 and (2) when the methanol was not adjusted in the analysis but left at background levels whilst the NH_3 was fixed at the enhanced amount found from the original GFIT analysis. Also plotted in this figure is a methanol spectrum scaled and offset for comparison. - 61 -

Figure 3-15: Time series of CO column amounts from December 2001 to January 2002. - 63 -

Figure 3-16 Time series of CO column amounts from September 2002 to January 2003. - 63 -

Figure 3-17: Time series of CO column amounts from January 21st 2003. - 64 -

Figure 3-18: Time series of CO column amounts from January 26th 2003. - 65 -

Figure 3-19 Vertical column amounts of CO derived from smoke affected spectra plotted against coincident measurements of AOD. The * symbol indicates the two spectra that were recorded just before the arrival of a distinctive, thick smoke plume on January 1st 2002. Typical smoke-free values are less than 0.1 for AOD and $1.6 \pm 0.5 \times 10^{18}$ for CO column. A generalised least squares linear regression excluding data from January 1st 2002 gave an R^2 value of 0.87. - 67 -

Figure 3-20: Vertical column amounts of HCN (upper panel) and H_2CO (lower panel) derived from smoke affected spectra plotted against coincident measurements of AOD at 500nm. - 69 -

Figure 3-21: Vertical column amounts of NH_3 (upper panel) and C_2H_2 (lower panel) derived from smoke affected spectra plotted against coincident measurements of AOD at 500nm. The * symbol indicates the two spectra that were recorded just before the arrival of a distinctive, thick smoke plume on January 1st 2002. - 70 -

Figure 3-22: Vertical column amounts of C_2H_4 (upper panel) and C_2H_6 (lower panel) derived from smoke affected spectra plotted against coincident measurements of AOD at 500nm. - 71 -

Figure 3-23: Vertical column amounts of HCOOH (upper panel) and CH_3OH (lower panel) derived from smoke affected spectra plotted against coincident measurements of AOD at 500nm. - 72 -

Figure 3-24: MODIS true colour image of South Eastern Australia on January 1st 2002. The red spots show MODIS hotspots – where a thermal anomaly has been detected. Image courtesy of MODIS Rapid Response Project at NASA/GSFC. - 74 -

Figure 3-25: Back trajectories showing projected origin and age of parcels of air arriving over Wollongong at different pressure levels: 950 hPa (pink), 750 hPa (red), 550 hPa (green) and 350 hPa (light blue). The crosses are half hour intervals back in time from noon on the 1st of January 2002. The back trajectories were generated by the European Centre for Medium-Range Weather Forecasts, (ECMWF) Trajectories, via the British Atmospheric Data Centre, 2006-, 2008. Available from http://badc.nerc.ac.uk/data/ecmwf-trj/ . - 75 -

Figure 3-26: Distribution of AOD at 500 nm over the Southeast coast of Australia on January 26th 2003 obtained from the MODIS aerosol product (MOD04), as observed from the Terra (left panel) and Aqua (right panel) platforms. The AOD scale has been converted to column amounts of CO, HCN or H_2CO by applying the relationships derived from the regression equations shown in Table 3-2. (Figure generated by Susan Campbell, CSIRO, Canberra.) - 79 -

Figure 4-1: Images of the Canberra fires, courtesy of the NSW fire service.- 84 -

Figure 4-2: A selection of MODIS AOD images of the Canberra fires of 2003. - 89 -

Figure 4-3: Further MODIS AOD images of the Canberra fires of 2003. - 90 -

Figure 4-4: Smoke plumes from the Canberra fires as seen from MODIS onboard the Aqua satellite on the 18th January 2003. - 91 -

Figure 4-5: Enhanced MODIS AOD from the Canberra fires recorded from the Aqua satellite at 03:35 UT on 9th January 2003. - 95 -

Figure 4-6: Enhanced AOD as seen by the MODIS instrument on Aqua at 04:20UT 10th January 2003. The black area is not covered by the swaths used to make up the image. - 97 -

Figure 4-7: MODIS false-colour image taken on the 7th February 2003 (left hand panel) TAPM grid with area sources shown in grey (right hand panel) - 100 -

Figure 4-8: Typical distribution of emissions chosen for a 24 hour period given in UT. - 101 -

Figure 4-9: Schematic diagram illustrating the method used to estimate the amount of emissions that may be double-counted each day. - 102 -

Figure 4-10: An example where examining the predicted smoke remaining from earlier emissions and the enhancements detected by MODIS AOD shows no overlap and the correction factor C_2 is set to zero- (a) TAPM prediction of location of smoke plume from Canberra fires at 1km from the model run for the 15th January 2003, (b) corresponding MODIS AOD image at this time and (c) TAPM prediction of location of smoke plume at 1km from previous emissions taken from the model run for the 14th January 2003. Comparing (a) and (b) shows whether the location of new emissions predicted by the model coincide with the actual enhancements detected by MODIS, (comparison of the total mass in each yields the correction factor, C_1), whilst (b) and (c) are compared to decide whether the detected enhancements include smoke emitted previously and already counted in the emissions estimate. Here the conclusion is that there is no obvious overlap and C_2=0 and so nothing is subtracted from the emissions calculated from the MODIS AOD image in panel (b). - 105 -

Figure 4-11: An example where the overlap of the predicted smoke remaining from earlier emissions and the enhancements detected by MODIS AOD is not clear. (a) TAPM prediction of location of smoke plume from Canberra fires at 1km taken from the model run for the 22nd January 2003, (b) corresponding MODIS AOD image and (c) TAPM prediction of location of smoke plume at 1km from previous emissions taken from the model run from the 21st January 2003. In this case the correction factor, C_2 is the percentage of non-white pixels in the image shown in (b). - 106 -

Figure 4-12: The proportion of previous emissions that remain in the TAPM modelled area (R%) and the normalisation factors C_1 and C_2 for each day of the fires. - 108 -

Figure 4-13: The estimated emissions of CO for each day alongside the previous emissions still remaining in the area as predicted by TAPM modelling. The sum of these two terms is M_{CO}, the mass of enhanced CO derived from the MODIS AOD data for the day. The accumulated total mass of CO emitted by the fires is also shown on a separate right-hand axis. - 109 -

Figure 4-14: The correction factor C_2 for the larger region calculations. Note that the estimated proportion of previous emissions that remain in the area ($R_{\%}$) and the correction factors C_1 are taken from TAPM results for the smaller area (Figure 4-12). - 111 -

Figure 4-15: The estimated emissions of CO for each day taken from the large region alongside the previous emissions still remaining in the area as predicted by TAPM modelling. (The sum of these two terms is M_{CO}.The accumulated total mass of CO emitted by the fires is also shown on a separate right-hand axis. - 112 -

Figure 4-16: Comparison of ground-based AOD measurements (small grey squares) with MODIS AOD measurements for the single 1° by 1° grid space over Wollongong (small black triangles) and the 9 closest 1° by 1° grid spaces around Wollongong (open triangles). - 115 -

Figure 4-17: Comparison of ground-based FTIR measurements of column CO (grey squares) with MODIS AOD inferred CO columns using the 9 closest 1° by 1° grid spaces around Wollongong (black triangles). The 1σ standard deviations are shown as error bars. The number of spectra used to calculate the average column CO from the FTIR are given above each point. - 115 -

Figure 5-1: Photograph of the TCCON observatory at Darwin showing the container, tracker dome and weather station. - 122 -

Figure 5-2 shows an example InGaAs spectrum extending from 4000cm^{-1} to 12000cm^{-1}. The CO overtone band is around 4200cm^{-1}. - 123 -

Figure 5-3: The *a priori* CO VMR profile used in GFIT analysis of NIR spectra from Darwin. - 124 -

Figure 5-4 : An example fit to the microwindow from 4226.5 cm^{-1} to 4228.3 cm^{-1} fitting CO and CH_4 including the CO line at 4227.36 cm^{-1}. The red line is the measured spectrum, the blue is the simulated spectrum and the green line above shows the difference between the two (the residual). 126

Figure 5-5: An example fit to the microwindow from 4231.5 cm^{-1} to 4232.1 cm^{-1} fitting CO, H_2O, HDO and CH_4 including the CO line at 4231.69 cm^{-1}. 127

Figure 5-6: Shows daily averaged CO column amounts derived from InGaAs spectra recorded at Darwin. Points are the daily average CO column and the error bars are the 1σ standard deviation. 128

Figure 5-7: MODIS true colour image showing an Indonesian smoke plume extending towards Northern Australia on 14th November 2006. 129

Figure 5-8. (Prepared by D.P. Edwards). Monthly averaged CO VMRs (ppbv) at 700 hPa retrieved from MOPITT for November 2005 (upper panel) and November 2006 (lower panel). 130

Figure 5-9. (Produced by D.P. Edwards). MOPITT CO measurements over Darwin (D.P. Edwards) are shown in green and CO from NIR ground-based FTIR measurements (this study) are shown in red. The upper plot shows daily averages as dots and weekly averaged values are plotted as a solid line. The lower plot represents the weekly mean anomaly as differences from the mean value for that week of the year determined from the entire MOPITT time series. 131

Figure 5-10. MOPITT CO columns plotted against FTIR CO columns measured at Lauder, New Zealand and Wollongong and Darwin, Australia. (Produced by D.P. Edwards). 132

Figure 5-11: Photograph of a Middleton Solar SP02 Sunphotometer as used in Darwin. (Photograph reproduced with kind permission of David Mathias of Middleton Solar – see the Middleton Solar website: http://www.middletonsolar.com/products/product11.htm) 134

Figure 5-12. Time series of hourly averaged AOD values from Darwin. The error bars are the 1σ standard deviation of the mean for each hour. 134

Figure 5-13. Time series of daily average CO column amounts plotted alongside time series of daily average AOD at 500nm. The left-hand axis is for CO column amounts and the right hand axis is for AOD at 500 nm. Error-bars

are the 1σ standard deviation of the mean for both CO column amounts and AOD at 500 nm. 135

Figure 5-14: MODIS true colour image from the AQUA satellite with detected thermal anomalies shown as red spots, indicating local fires near Darwin on 31st May 2006. The map was generated in ArcMap using satellite image courtesy of MODIS Rapid Response Project at NASA/GSFC, and coastline and town locations from Spatial Analysis Laboratories (see Acknowledgements.) 137

Figure 5-15: MODIS true colour image from the TERRA satellite with detected thermal anomalies shown as red spots, indicating local fires near Darwin on 27th April 2008. 137

Figure 5-16. Total column amounts of CO derived from near-infrared spectra plotted against coincident sunphotometer measurements of AOD at 500 nm taken from Darwin. 138

Figure 5-17 Total column amounts of CO plotted alongside coincident measurements of AOD at 500nm. The dataset has been cut to remove all AOD values in excess of 0.75. 139

Figure 6-1: Sentinel website showing MODIS thermal anomalies (hotspots) from the afternoon of June 6th 2008 and the MODIS raster (visible image). 142

Figure 6-2: Image from the webcam on top of the container housing the spectrometer at Darwin taken on June 2nd 2008 at 13.50 local time. A large smoke plume is visible to the East behind the hurricane cage and the solar tracker's dome. 143

Figure 6-3: An example InSb spectra recorded from Darwin. 144

Figure 6-4: VMRs and *a priori* covariances plotted against altitude (km) for the 44 modelled layers used in the SFIT2 retrieval of CO (upper panel) and H_2CO (lower panel) 146

Figure 6-5: Example fits to a measured spectrum achieved in the SFIT2 retrieval of CO in all 3 microwindows used: (a) 4226.50 – 4228.30cm^{-1}, (b) 4231.50 – 4232.10cm^{-1} and (c) 4274.00 – 4275.00cm^{-1}. 148

Figure 6-6: Example fits to a measured spectrum achieved in the SFIT2 retrieval of H_2CO in both microwindows used: (a) 2777.88 – 2778.92 cm^{-1} and (b) 2869.435 – 2870.325 cm^{-1}. 149

Figure 6-7: : VMRs and *a priori* covariances plotted against altitude (km) for the 44 modelled layers used in the SFIT2 retrieval of (a) C_2H_6 (b) C_2H_2 and (c) and HCN 151

Figure 6-8: Example fits to a measured spectrum achieved in the SFIT2 retrieval of C_2H_6 in all 3 microwindows used: (a) 2976.60 – 2977.10cm^{-1} (b) 2996.70 – 2997.10cm^{-1} and (c) 3000.10 – 3000.60cm^{-1}. - 153 -

Figure 6-9: Example fits for the SFIT2 retrievals of (a) C_2H_2 from 3304.70 – 3305.40 cm-1, (b)HCN from 3268.00 – 3268.38 cm^{-1} and (c) HCN from 3331.40 – 3331.80 cm^{-1}. - 154 -

Figure 6-10: MODIS true colour image from the Aqua satellite with detected thermal anomalies shown as red spots, indicating widespread fires near Darwin on 4th October 2006. In the image cloud appears as bright white and smoke as white/grey plumes emanating from the fires. 156

Figure 6-11: Back trajectories showing projected origin and age of parcels of air arriving over Darwin at different pressure levels: 950 hPa (pink), 750 hPa (red), 550 hPa (green) and 350 hPa (light blue). The crosses represent hour intervals back in time from 18:00 on the 4th October 2006. The back trajectories were generated by the European Centre for Medium-Range Weather Forecasts, (ECMWF) Trajectories, via the British Atmospheric Data Centre, 2006 - 2008. Available from http://badc.nerc.ac.uk/data/ecmwf-trj/ . 157

Figure 6-12: MODIS true colour image from the Terra satellite on 27th June 2007 with detected thermal anomalies shown as red spots, indicating intense fires approximately 150km southeast of Darwin. (For details of map generation please see Acknowledgements.) 158

Figure 6-13: MODIS true colour image from the Aqua satellite on 27th June 2007 with detected thermal anomalies shown as red spots. One swath is missing but the smoke plumes from the fires detected by the instrument on the Terra satellite approximately 3 hours earlier are clearly seen. (For details of map generation please see Acknowledgements.) 158

Figure 6-14: Back trajectories showing projected origin and age of parcels of air arriving over Darwin at different pressure levels: 950 hPa (pink), 750 hPa (red), 550 hPa (green) and 350 hPa (light blue). The crosses represent hour intervals back in time from 18:00 on 27th June 2007. 159

Figure 6-15: MODIS true colour image from the Aqua satellite on 9th August 2007 with detected thermal anomalies shown as red spots. Smoke plumes are visible from several fires at distances in excess of 200 km from Darwin. 160

Figure 6-16: Back trajectories showing projected origin and age of parcels of air arriving over Darwin at different pressure levels: 950 hPa (pink), 750 hPa (red), 550 hPa (green) and 350 hPa (light blue). The crosses represent hour intervals back in time from 18:00 on 9th August 2007. 160

Figure 6-17: MODIS true colour image from the Terra satellite on 2nd November 2006 with detected thermal anomalies shown as red spots. Scattered fires are detected and clearly visible is a large diffuse smoke plume apparently coming from the north. 161

Figure 6-18: MODIS true colour image from the Aqua satellite on 30th November 2006 with detected thermal anomalies shown as red spots. Scattered fires are detected to the southeast of the region and clearly visible is a large diffuse smoke plume apparently coming from the northwest. 162

Figure 6-19: MODIS true colour image from the Aqua satellite on 20th September 2007 with detected thermal anomalies shown as red spots. Widespread fires are seen in the east and a general build-up of smoke is visible across the region. 163

Figure 6-20: Back trajectories showing projected origin and age of parcels of air arriving over Darwin at different pressure levels: 950 hPa (pink), 750 hPa (red), 550 hPa (green) and 350 hPa (light blue). The crosses represent hour intervals back in time from 18:00 on 20th September 2007. 163

Figure 6-21 Column amounts of H_2CO plotted against column amounts of CO measured simultaneously from Darwin from 2006-2008. The results are shown for each of 20 individual days when smoke was sampled. The plot is colour coded to distinguish measurements made in different times of the

year; orange/red for May/June, green for August, pink for September and blue for October/November. 164
Figure 6-22: MODIS true colour image from the Aqua satellite on 3rd October 2007 with detected thermal anomalies shown as red spots. 167
Figure 6-23: Back trajectories showing projected origin and age of parcels of air arriving over Darwin at different pressure levels: 950 hPa (pink), 750 hPa (red), 550 hPa (green) and 350 hPa (light blue). The crosses represent hour intervals back in time from 18:00 on 3rd October 2007. 168
Figure 6-24. Excess HCN column plotted against excess CO column. 173
Figure 6-25. Excess C_2H_2 column plotted against excess CO column. 174
Figure 6-26. Excess C_2H_6 columns plotted against excess CO columns. 175
Figure 6-27: Plot of Column CO against AOD at 500 nm colour coded by month, for all InSb spectra taken during 2006-2008. 178
Figure 6-28: Plot of Column CO against AOD at 500 nm for subset of InSb spectra taken during May-July 2006-2008. 179
Figure 6-29: Plot of Column H_2CO against AOD at 500 nm for all InSb spectra taken during May-July 2006-2008. 180

Chapter 1 : Introduction

1.1 Biomass Burning Emissions

The burning of forests, woodlands, savanna grasses, agricultural stubble and the burning of wood or peat for fuel are known collectively as "biomass burning". Biomass burning releases large quantities of particulates and trace gases into the atmosphere, impacting upon the chemistry of the troposphere at local to global scales [*Crutzen et al.*, 1990]. Early estimates put the total amount of biomass burned globally at between 6200 - 8700 Tg of dry matter per year, releasing 3,500 Tg (gross) of carbon annually in the form of carbon dioxide (CO_2), equivalent to 40% of the global annual production of CO_2 at the time [*Crutzen et al.*, 1979; *Levine*, 1991].

Fires are also highly variable in their extent and intensity and so biomass burning is a major contributor to the annual variability of tropospheric composition. More recent estimates of global wildfire emissions from 1960 to 2000 have been made using active fire counts from the Along-Track Scanning Radiometer (ATSR) sensor on board the ERS-2 satellite, with values for annual global carbon emissions ranging from 1410 Tg C per annum in 1974, to 3140 Tg C per annum in 1992, with a mean value of 2078 Tg C per annum [*Schultz*, 2002]. The bulk of the biomass burning occurs in the tropics, and an estimated 6-8% of all global carbon emissions due to biomass burning derive from Australian fires [*Kasischke et al.*, 2004; *van der Werf et al.*, 2003]

A large number of different gases are emitted from fires in addition to CO_2. These include:

- the products of incomplete carbon combustion, carbon monoxide (CO), methane (CH_4), formaldehyde (H_2CO), hydrogen (H_2), and other hydrocarbons, including partially oxidised organic compounds such as alcohols, aldehydes, ketones and organic acids and
- products containing other elements in the amino acids and proteins of the biomass such as nitric oxide (NO), nitrogen dioxide (NO_2), nitrous oxide (N_2O),

ammonia (NH_3), hydrogen cyanide (HCN), sulphur dioxide (SO_2) and carbonyl sulphide (OCS) [*Andreae*, 1990].

Dry plant biomass is predominantly carbon (~45% by mass), hydrogen and oxygen, with nutrient elements making up only a minor component: approximately 0.3 – 3.8 % nitrogen, 0.5 – 3.5% potassium, 0.1 – 0.9% sulphur and 0.01 – 0.03 % phosphorous [*Andreae*, 1990]. The emission factors[1] for individual species are controlled mainly by the fuel content but also by the intensity of the fire, with fierce hot fires producing little CO, whilst smouldering fires produce more CO and other incomplete combustion products [*Ward et al.*, 1984]. This means that emission factors for each chemical species vary with both the type of vegetation (eg savanna grasses or woodland trees) [*Beringer et al.*, 1995; *Yokelson et al.*, 1997; *Yoshinori et al.*, 1997] and the characteristics of the fires, such as flaming or smouldering [*Crutzen et al.*, 1979; *Ward and Hardy*, 1984].

Many of the gases released by biomass burning are greenhouse gases or indirect greenhouse gases (gases which react to form greenhouse gases). Many are precursors to formation of tropospheric ozone, a major pollutant, a greenhouse gas and a powerful respiratory irritant with detrimental effects on human health in urban environments [*Gregg et al.*, 2003]. The importance of biomass burning emissions to the variability of tropospheric composition and chemistry [*Lobert et al.*, 1990], coupled with the significance of the emissions in terms of their contribution to greenhouse warming [*Solomon et al.*, 2007], make quantifying the emissions an important scientific problem.

1.2 Traditional Methods of Estimating Emissions from Biomass Burning

The traditional method of estimating the emissions from fires is via Equation 1-1 :

Equation 1-1: $$E_x = A \times FL \times BE \times EF_x$$

[1] The emission factor for a compound is defined as the mass of the compound released per amount of dry matter consumed, usually expressed in units of g kg^{-1}.

where E_x is the emission flux of species *x (kg)*, A is the area burned *(m^2),* FL is the fuel load *(kg m^{-2}),* BE is the burning efficiency and EF_x is the emission factor for the species *x* [*Seiler et al.*, 1980].

Area Burned

In early work, burned area values were based upon estimates provided by the forest services at a regional or national level [*Andreae*, 1990]. In the modern era, assessments of area burned often rely on the use of space and airborne sensors [*Schultz*, 2002]. Remote sensing techniques can be used to determine the number and location of active fires (thermal anomalies or "hot spots"), map the area burned (fire scars) and characterise the ecological effects of the fire once is has been extinguished [*Lentile et al.*, 2006]. For example, false colour images from the MODerate resolution Imaging Spectroradiometer (MODIS) (see http://modis.gsfc.nasa.gov/) instruments on NASA's Earth Observation System satellites (see http://eospso.gsfc.nasa.gov/) provide images of fire scars that may be used to estimate burned areas in regions of the world where persistent cloud-cover is not common [*Kaufman et al.*, 1998b].

Ito and Penner [2004] used a combination of satellite-based estimates by *Gregoire et al,* [2003] and fire counts from the Along Track Scanning Radiometer (ATSR) (see http://www.atsr.rl.ac.uk/) to estimate the area burnt globally during the year 2000 to be 3139 $x10^3$ km^2 yr^{-1}. Grasslands accounted for 72% of this total area, with woodlands and forests making up 14% each. Australia's burnt area (339 $x10^3$ km^2 yr^{-1}) accounted for ~11% of the global total burnt area in this study and within Australia 78% of the burnt area was grasslands, 15% woodlands and 7% forests. Larger estimates for the annual burned area within Australia have been found in other studies for various different years: 870 $x10^3$ km^2 yr^{-1} [*Hurst et al.*, 1994b], 418 $x10^3$ km^2 yr^{-1} [*Russell-Smith et al.*, 2003], 1180 $x10^3$ km^2 yr^{-1} [*van der Werf et al.*, 2003]. More recently *Schultz et al* [2008] compiled a 41 year inventory of fire emissions from 1960 to 2000 and found a mean area burned within Australia of 570 $x10^3$ km^2 yr^{-1}.

Fuel Load & Burning Efficiency

Dry fuel loads can be estimated from samples of material gathered from a known area covered in the vegetation type of interest. For example *Hurst et al*, [1994b]

analysed pre-fire fuel and post-fire ash samples from an area typical of Australian savannas to give the dry mass[2] (DM) load and the carbon content. The difference in mass load between the pre-fire fuel and post fire ash was used to give the total dry mass load burned (kg DM ha^{-1}) and combined with the pre-fire fuel and ash carbon content values to give both the mass of fuel carbon burned (kg C ha^{-1}) and the mass of carbon released to the atmosphere (kg C ha^{-1}). More recently satellite imagery from the AVHRR and MODIS satellites instruments has been used to estimate vegetation cover [*Defries et al.*, 2000; *Hansen et al.*, 2002]. This has been combined with measurements made at the ground of typical biomass density for different vegetation types and areas including litter fuel [*Matthews*, 1997] and/or remote sensing of leaf area index [*Myneni et al.*, 1997] to yield improved estimates of fuel loads.

The burning efficiency (also know as the combustion factor) is the fraction of biomass exposed to fire that actually burns and is dependent upon the fuel type and moisture content [*Ito and Penner*, 2004]. These are compiled from detailed field studies [*Carvalho et al.*, 1998; *Carvalho et al.*, 2001; *Fearnside et al.*, 1993; *Fearnside et al.*, 1999; *Fearnside et al.*, 2001; *Graca et al.*, 1999] similar to that described above by *Hurst et al*, [1994b]. The burning efficiency in grasslands may be determined using satellite imagery of the percentage of green grass to total grass estimated from the leaf area index [*Myneni et al.*, 1997].

Ito and Penner [2004] give combustion factors and fuel loads (in kg DM m^{-2}) for grasslands, woodlands and forests in different regions of the world. For Australia the fuel loads are 0.45 kg DM m^{-2} for grasslands, ~3.1 kg DM m^{-2} for woodlands and 14.2 kg DM m^{-2} for forests. Australian values for the combustion factors are 0.67 for grasslands, 0.40 for woodlands and 0.33 for forests. Multiplying up the area burned, fuel loads and combustion factors gives the biomass burned within Australia as 80 Tg DM $yr^{-1}$from grasslands, 63 Tg DM $yr^{-1}$from woodlands and 107 Tg DM yr^{-1} from forests, giving a total of 250 Tg DM yr^{-1}. It is worthwhile noting that although grasslands account for 72 % of the total area burned annually in Australia, due to lower fuel loads they provide only 32% of the dry matter burned. In contrast, forests represent only 14%

[2] The dry mass (DM) load is the mass of fuel excluding the water content in a given area, typically quoted in units of kg DMm^{-2} or kg DM ha^{-1}.

of the area burned but, with 30 times the fuel loads of grasslands and only half the burning efficiency, they provide 43% of the dry matter burned in Australia.

To understand the emissions from the Australian continent it is therefore necessary to characterise the emissions from the eucalyptus forests in the south and east of the country and the savanna grasslands and woodlands in the tropical north.

Emission Factors & Emission Ratios

The emission factor for a compound "x" is defined as the mass of the compound released (M_X) per amount of dry matter consumed ($M_{biomass}$), typically expressed in units of g kg^{-1}. The total amount of dry matter consumed ($M_{biomass}$) may be determined from knowledge of the total mass of carbon emitted (M_C) and the fractional carbon content of the biomass burned (X_C), such that the emission factor may be derived from Equation 1-2.

Equation 1-2: $$EF_X = \frac{M_X}{M_{biomass}} = \frac{M_X}{M_C}.X_C$$

Only detailed field studies that include determination of the carbon content of the fuel can determine emission factors directly. One example is the study described above by *Hurst, et al*, [1994] where pre-fire fuel and post-fire ash samples were analysed from an area typical of Australian savannas to give both the carbon content (X_C) and the dry mass load (kg DM ha^{-1}). Gas phase Fourier transform infrared (FTIR) spectroscopy, matrix isolation FTIR spectroscopy and chemiluminescence techniques were used to derive excess concentrations of a large number of different trace gases in smoke samples taken from the ground and from a light aircraft [*Hurst et al.*, 1994a; *Hurst et al.*, 1994b]. Since most possible carbon containing species emitted from the fires were measured, the sum of all these species could be used to estimate the total mass of carbon emitted (M_C). The fraction of the total mass of carbon emitted to the atmosphere as each species could then be used to derive emission factors for these gases by the carbon mass-balance method [*Radke et al.*, 1988]. Laboratory studies are better suited to direct measurements of emission factors because the carbon content of the biomass and the

carbon budget of the fire are readily determined [*Andreae et al.*, 2001; *Holzinger et al.*, 1999; *Yokelson et al.*, 1996].

An alternative approach to characterising the emissions from biomass burning is to determine an emission ratio. An emission ratio is obtained by dividing the enhanced concentration ($\Delta[x]$) of a trace gas *"x"* measured in a smoke plume by the enhanced concentration of a reference gas ($\Delta[x_{ref}]$), usually CO_2 or CO. Ambient background concentrations of the gases must be subtracted from the concentrations measured in the smoke to determine the "enhanced" concentrations [*Andreae and Merlet*, 2001]. For example the emission ratio of HCN relative to CO is given by Equation 1-3:

Equation 1-3: $$ER_{HCN/CO} = \frac{\Delta[HCN]}{\Delta[CO]} = \frac{[HCN]_{smoke} - [HCN]_{ambient}}{[CO]_{smoke} - [CO]_{ambient}}$$

Emission ratios to CO or CO_2 may be converted to emission factors via Equation 1-4 by using a suitable emission factor for the reference gas (EF_{REF}) derived from laboratory measurements or from field studies such as described in *Hurst et al*, [1994b].

Equation 1-4: $$EF_X = ER_{(X/\ REF)} \frac{MW_X}{MW_{REF}} EF_{REF}$$

where EF_X is the emission factor of the gas x (by mass),

$ER_{(X/REF)}$ is the emission ratio of gas x relative to the reference gas (by mole),

MW_X and MW_{REF} are the molecular weights of gas x and the reference gas respectively and

EF_{REF} is the emission factor of the reference gas (by mass), taken from the literature.

As noted above, emission factors depend upon both the fuel content and the characteristics of the fire. Emissions from forest fires during the intense flaming stages will be different from emissions during the latter smouldering stages, as incomplete combustion becomes more dominant [*Crutzen et al.*, 1979]. Ideal emission factors for

use in Equation 1-1 will represent the overall mean emission factor for all stages of a fire, in proportion to their contribution to the total emissions. Grassland fires tend to burn principally in intense flames as little fuel remains after the flaming stage [*Ward and Hardy*, 1984]. The amount of different nutrient elements varies significantly between different fuel types, so that emission factors vary with the type of vegetation [*Beringer et al.*, 1995; *Yokelson et al.*, 1997; *Yoshinori and Kanno*, 1997]. For example emission factors from Australian eucalypts could be different to emission factors from American boreal forests. Several large-scale field campaigns have been undertaken in different parts of the world in order to characterise the biomass burning emissions from the regional ecosystems. Examples include:

- The South Africa Fire-Atmosphere Research Initiative (SAFARI) project [*Andreae et al.*, 1996; *Lindesay et al.*, 1996];
- The Southern Tropical Atlantic Region Experiment (STARE) [*Andreae et al.*, 1996],
- The Transport and Atmospheric Chemistry near the Equator – Atlantic (TRACE-A) over southern Africa, the South Atlantic and Brazil [*Fishman et al.*, 1996],
- The Experiment for Regional Sources and Sinks of Oxidants in central Africa (EXPRESSO) [*Delmas et al.*, 1999], and
- Smoke Clouds and Radiation – Brazil (SCAR-B) [*Kaufman et al.*, 1998a]

Despite the global significance of Australian biomass burning, measurements of emissions from vegetation fires in Australia have been relatively sparse. In addition to the work by *Hurst et al*, [1994a] [1994b] described above, two further detailed studies of emission ratios of trace gases were made as part of the Biomass Burning and Lightning Experiment (BIBLE)-A and B in August-October 1998 and 1999 [*Kondo et al.*, 2003; *Shirai et al.*, 2003a]. There are some other measurements from Australian savanna fires in the literature that cover a more limited range of species [*Folkins et al.*, 1997; *Sawa et al.*, 1999] as well as controlled laboratory-based fire experiments and many measurements from savannas fires elsewhere in the world e.g. [*Andreae and Merlet*, 2001; *Christian et al.*, 2003; *Yokelson et al.*, 1996].

Where there are multiple estimates of the emission factor of a given trace gas from a particular ecosystem in the literature, the spread of values is often large. This is due to the naturally variability of the emissions, sampling the biases one stage of burning over another, as well potential biases in the measurement techniques. Consequently, further measurements are useful additions to our knowledge of biomass burning emissions especially where new techniques are employed or new ecosystems sampled.

1.3 Remote Sensing using Fourier Transform Spectrometry and the Network for the Detection of Atmospheric Composition & Change

The principal measurement technique used in this thesis is remote sensing of the atmosphere using Fourier transform spectrometry. Many gases were first discovered in the atmosphere during the 1940's from their absorption features in the infrared solar spectrum. These early optical absorption measurements of the atmosphere using the Sun as a source were made with grating spectrometers and examples of atmospheric gases first detected this way include methane and CO [*Migeotte*, 1948; 1949]. Continuous or semi-continuous records of infrared solar atmospheric absorption spectra have been made from ground-based Fourier transform spectrometers (FTS) since the late 1970s and early 1980s, when the first ground-based solar-tracking FTS systems were installed at Kitt Peak National observatory in the USA and at the Jungfraujoch Observatory in Switzerland. Initially interest was focused on the detection and quantification of stratospheric trace gases [*Rinsland et al.*, 1986; *Zander et al.*, 1986]. The discovery of the Antarctic ozone hole [*Farman et al.*, 1985] intensified interest in stratospheric chemistry and helped support the establishment of the Network for Detection of Stratospheric Change (NDSC). This global network of instrument sites became operational in 1991 (http://www.ndsc.ncep.noaa.gov/), with ground-based FTS amongst the suite of primary techniques being used. Other NDSC instruments are lidars for ozone, temperature, water and aerosols; microwave instruments for ozone, water and chlorine monoxide; UV/Visible spectrograph for ozone and nitrogen dioxide; Dobson/Brewer spectrophotometers for total column ozone and regular ozone sondes. This resulted in a huge increase in the number of infrared solar absorption measurements being made around the globe during the next few years, e.g. [*Bell et al.*,

1994; *Bell et al.*, 1996; *Bell et al.*, 1998; *Blumenstock et al.*, 1997; *David et al.*, 1993; *Griffith et al.*, 1998b; *Jones et al.*, 1994; *Liu et al.*, 1992; *Mahieu et al.*, 1995; *Notholt*, 1994; *Notholt et al.*, 1997; *Toon et al.*, 1999; *Toon et al.*, 1995; *Zander et al.*, 1994].

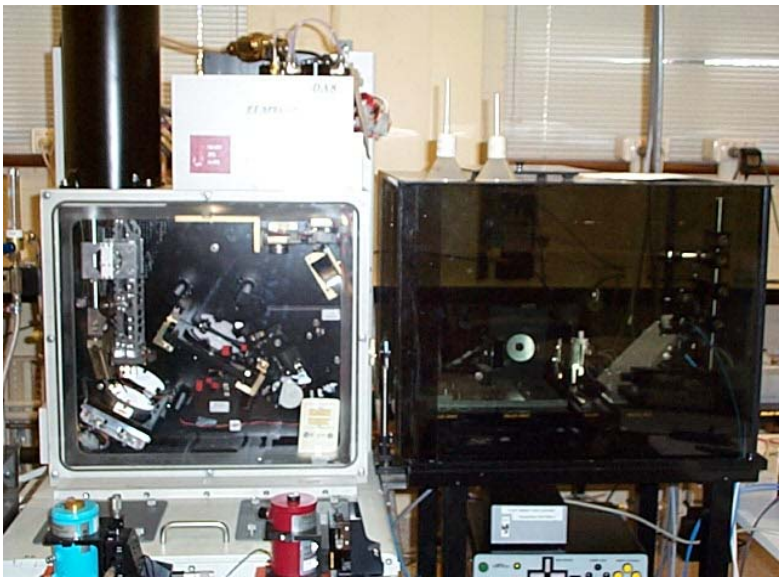

Figure 1-1: Photograph of the Bomem DA8 Spectrometer used at the Wollongong NDSC/NDACC complementary site from 1995 until 2008.

The NDSC complementary site at Wollongong began measurements in 1995 [*Griffith et al.*, 1998a]. A commercial Fourier transform spectrometer - Model DA8, ABB-Bomem, Quebec, Canada, (see Figure 1-1), was coupled to a solar tracker that was constructed in-house (see Figure 1-2). The spectrometer has been operating whenever the weather condition permits from 1995 until the present day, and underwent a major refurbishment in 2001. The spectrometer is equipped with an indium-antimonide (InSb) detector and a mercury cadmium telluride (MCT) detector and uses a potassium bromide (KBr) beamsplitter.

More recently interest in atmospheric chemistry has been focused on tropospheric pollution and anthropogenic emissions of greenhouse gases [*Barret et al.*, 2003; *Mahieu et al.*, 1995; *Rinsland et al.*, 2000; *Rinsland et al.*, 2001; *Rinsland et al.*, 2002; *Zhao et al.*, 2000; *Zhao et al.*, 2002]. As a result, the NDSC has changed its emphasis and name to the Network for Detection of Atmospheric Composition and Change (NDACC). The complementary station at Wollongong has recently been upgraded with a new Fourier transform spectrometer (model IFS 125HR, Bruker Optics, Ettlingen, Germany) and an accompanying solar tracker built by the same

company, however the measurements described in this thesis were all recorded on the older Bomem DA8 instrument.

Figure 1-2: Photograph of solar tracker used at the Wollongong NDSC/NDACC complementary site from 1995 until 2008.

Remote sensing of the atmosphere using ground-based Fourier transform infrared spectrometry with the sun as a source has the potential to be a useful tool for making measurements of biomass burning emissions. Many trace gases that are emitted by fires are detectable by this technique and the resulting measurements are vertically integrated improving the chances of obtaining a good representative sample. CO from biomass burning measured using solar FTIR from the ground has been reported in the literature [*Koike et al.*, 2006; *Petersen et al.*, 2008; *Senten et al.*, 2008] and also from ship borne measurements [*Velazco et al.*, 2005]. There are a few other published studies using ground-based solar FTIR to measure other biomass burning indicators such as HCN, C_2H_2 and C_2H_6 [*Rinsland et al.*, 1999; *Zhao et al.*, 2000; *Zhao et al.*, 2002] and one recent paper that estimates emission ratios with respect to CO [*Nagahama et al.*, 2007]. Also in the literature are publications resulting from some of the work described in this thesis [*Paton-Walsh et al.*, 2004; *Paton-Walsh et al.*, 2005; *Paton-Walsh et al.*, 2008; *Rinsland et al.*, 2005], see **Appendix 1**.

1.4 Background to the Work described in this Thesis

Before the work outlined in this thesis began, smoke plumes from the 2001-2002 New South Wales fires had been measured at Wollongong on 9 days between December 24th 2001 and January 4th 2002. There were also smoke events sampled on 7 days during September and October 2002. It was clear that some of these spectra contained very large enhancements of certain gases associated with biomass burning. A preliminary analysis of the infrared spectra from December 2001 and January 2002 had yielded greatly enhanced total column amounts of CO, but with high uncertainties and some obvious problems with the analysis technique. Aerosol optical depth (AOD) values at 500nm and other wavelengths had been calculated from UV-visible spectra (that had been collected coincidentally with the FTIR spectra) and plotted against the CO columns to show a correlation that was generally strong but with anomalous behaviour on January 1st 2002.

As part of the work described in this thesis, further smoke plumes were sampled from Wollongong on 13 days between November 2002 and January 2003 including plumes from the Canberra fires of January 2003.

1.5 Objectives of the Thesis

1 The first objective of the work described in this thesis was to analyse and interpret the existing spectroscopic measurements of smoke plumes sampled from Wollongong. The analysis was aimed at extracting information that would be useful in quantifying emissions from Australian forest fires. This work is described in Chapter 3.

2 The second objective derived from the strong correlations between AOD and trace gas amounts established whilst fulfilling the first objective. This second aim was to use these correlations along with satellite measurements of AOD to make a total emissions estimate from an individual fire episode within Australia. The chosen fires were the Canberra fires of 2003 and this work is described in Chapter 4.

3 The third objective was to collect a similar dataset of spectroscopic measurements of smoke plumes from the fires in the savanna grasslands and woodlands in the tropical north of Australia. The resulting dataset would be analysed in a similar manner to the measurements of smoke plumes from forest fires in the southeast of the country to characterise the emissions from biomass burning throughout Australia. This work is described in Chapter 5 and Chapter 6.

The overriding aim of the work described in this thesis is to contribute to our knowledge of emissions from biomass burning to the atmosphere in Australia. In particular this work aims to improve our ability to make quantitative estimates of emissions from both forest and savanna fires within Australia. A new technique for estimating the total emissions from an individual fire episode is presented and applied to the Canberra fires of 2003. The extent to which the specific aims listed above were successful is discussed in Chapter 7 - the summary and conclusions.

Chapter 2 : Measurement and Modelling Tools

2.1 Fourier Transform Spectroscopy

Fourier transform spectroscopy is a technique whereby all frequencies of a spectrum are recorded simultaneously by a detector and resolved into individual frequencies with appropriate intensities by a mathematical process known as a Fourier transform, (after the French mathematician Jean Baptiste Fourier, who developed the mathematics in the early 19th Century).

To understand the basic principles of Fourier transform spectroscopy first consider a coherent source emitting radiation of a precise frequency, ν. The amplitude of the wave plotted against time will be a cosine wave. Now consider a source emitting two different but precise frequencies (i.e two cosine waves). The amplitude of the radiation with time will be the sum of the two waves – a "beat frequency" that has variable amplitude as the two component frequencies move in and out of phase with one another (see Figure 2-1).

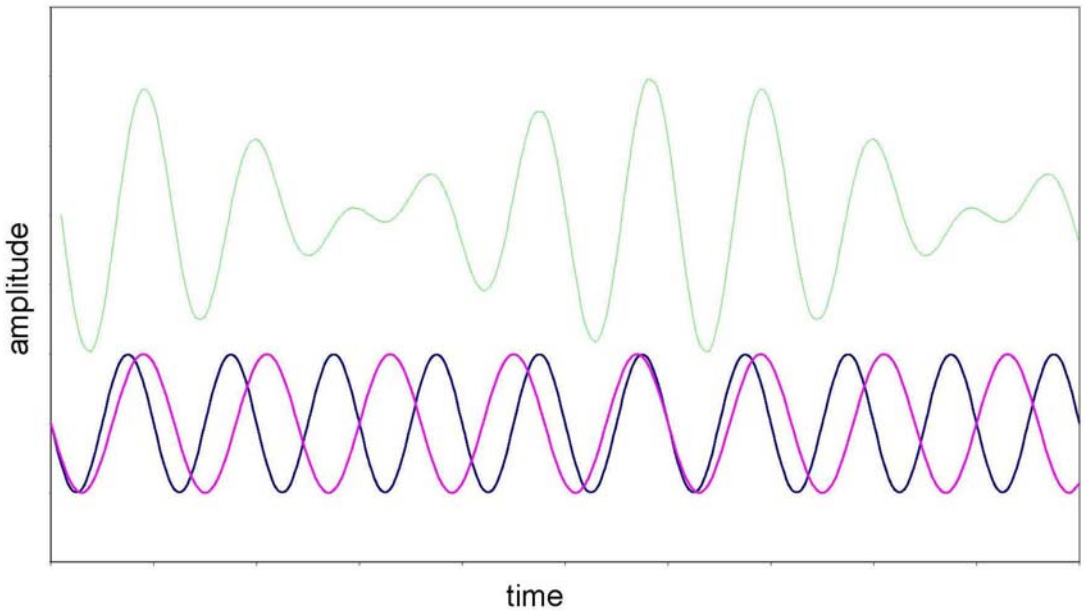

Figure 2-1: Time is shown on the x-axis and intensity on the y-axis. Two cosine waves of different frequency are shown at the bottom of the figure, whilst the top of the figure illustrates the sum of the two waves – the "beat frequency".

The combined wave may be resolved into its components mathematically (by the Fourier transform) given sufficient sampling. Since each component wave has a frequency, amplitude and a phase then two components have six unknowns that must be evaluated from the composite wave. Thus observations of the composite wave at six points in time will yield sufficient information to solve for the six unknowns and determine the component waves. As more and more waves are added, each with a different frequency, maximum amplitude and phase, the combined wave becomes more and more complex and the number of points that must be sampled increases but the principle remains the same. A complex wave may be resolved into its component frequencies using a Fourier transformation that is carried out by computer [*Brault et al.*, 1971; *Forman*, 1966].

The frequencies of radiation in the infrared are too high for detectors to respond fast enough for time domain amplitudes to be collected directly. Instead an interferometer may be used to modulate the radiation at audio frequencies proportional to the infrared frequencies and the combined wave sampled as a function of the optical path difference between the two interferometer mirrors. In practice this sampling is usually achieved by sending a visible helium-neon laser along the optical axis of the interferometer to provide a reference for sampling the infrared detector signal as a function of optical path difference. The use of a helium-neon laser also provides an accurate frequency calibration for the x-axis of the resultant interferograms.

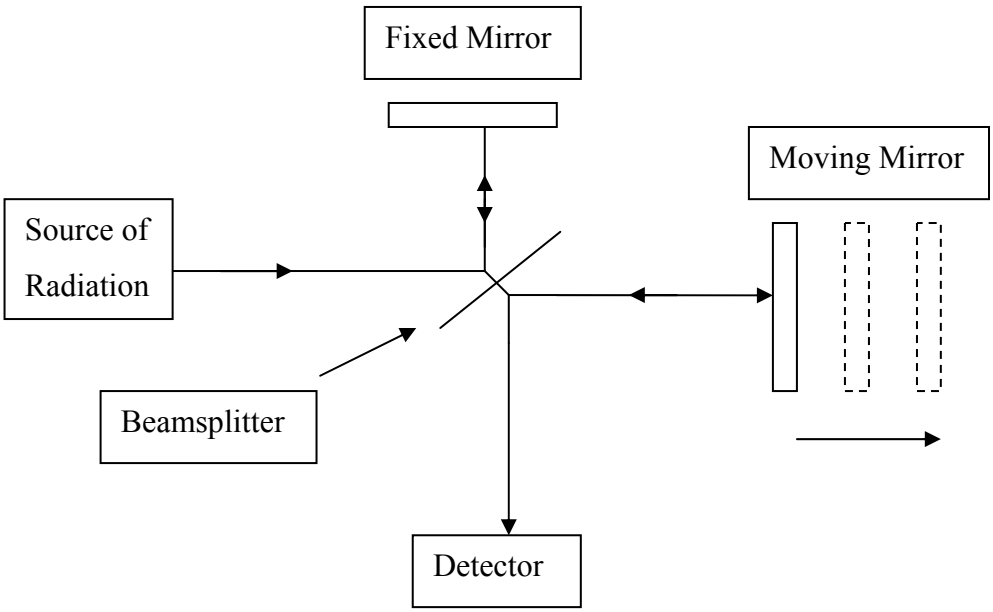

Figure 2-2: The basic components of a Fourier transform spectrometer – in essence a Michelson interferometer.

Figure 2-2 shows the basic components of a Fourier transform spectrometer, which is in essence a Michelson interferometer. It is easiest to visualise how it works by first considering a single frequency of light travelling through the spectrometer (for instance the helium-neon laser light). At the beamsplitter approximately half the radiation is reflected towards the fixed mirror, whilst the other half is transmitted towards the moving mirror. The moving mirror travels at a constant velocity and the two halves of radiation recombine and interfere back at the beamsplitter. Approximately half this modulated radiation is reflected/transmitted back towards the source, whilst the other half is reflected/transmitted towards the detector. Ideally (ignoring phase shifts), the amplitude of the interference pattern recorded by the detector will be at a maximum when both mirrors are exactly the same distance from the beamsplitter – known as zero path difference (ZPD). For a single frequency the same maximum will be achieved whenever the path difference is an exact number of wavelengths because the two halves of radiation will constructively interfere. Similarly the amplitude of the interference pattern will go to zero whenever the path difference is a half wavelength (or some odd multiple of this) because the two halves of radiation will destructively interfere. The result is that a cosine wave will be produced with a frequency dependent upon velocity of the moving mirror and the optical frequency [*Griffiths et al.*, 1986].

Two frequencies will produce a beat frequency as shown in Figure 2-1, and very complex combinations can be resolved into component frequencies using a Fourier transformation. The principle is the same as for a pure time domain spectra but now the sampling takes place at a speed that can be achieved by available detectors.

In laboratory based Fourier transform spectroscopy a background spectrum is taken with the spectrometer set-up as shown in Figure 2-2. The sample is then placed either between the source and the beamsplitter or between the beamsplitter and the detector and another spectrum recorded. The ratio of the background and sample spectra yields the transmittance spectrum of the sample. Further details of Fourier transform spectroscopy may be found in the literature [*Abrams et al.*, 1994; *Brault and White*, 1971; *Brault*, 1996; *Davis et al.*, 1980; *Griffiths and de_Haseth*, 1986; *Sumner et al.*, 2001].

2.2 Remote sensing of the Atmosphere by Solar FTIR Spectroscopy

In ground-based solar Fourier transform spectroscopy of the atmosphere the Sun is the source and the sample is the atmosphere, which lies between the source and the beamsplitter. The resulting spectra record the radiation reaching the ground as a function of frequency (modified by the spectrometer's optical components). An example spectrum is shown in Figure 2-3 and a schematic of the measurement set-up is shown in Figure 2-4. The shape of the resulting spectrum depends upon the solar radiation reaching the top of the earth's atmosphere, absorption by the atmosphere and the optical properties of the instrument recording the radiation. The solar radiation reaching the top of the earth's atmosphere is in essence a blackbody curve at 5800K with emission and absorption lines of gases in the solar atmosphere imposed. Terrestrial atmospheric absorption lines (positions, strengths and shapes) will be discussed in detail in this section, along with instrumental effects. These lines contain information about the species of trace gases present in the atmosphere (line positions), the amounts of each gas present (line depths/areas) and some information about the altitude distribution of each gas (line shapes). In reality there is also a component of radiation as a result of atmospheric emission, but this is so small in comparison to the radiation from the sun that its effects are negligible.

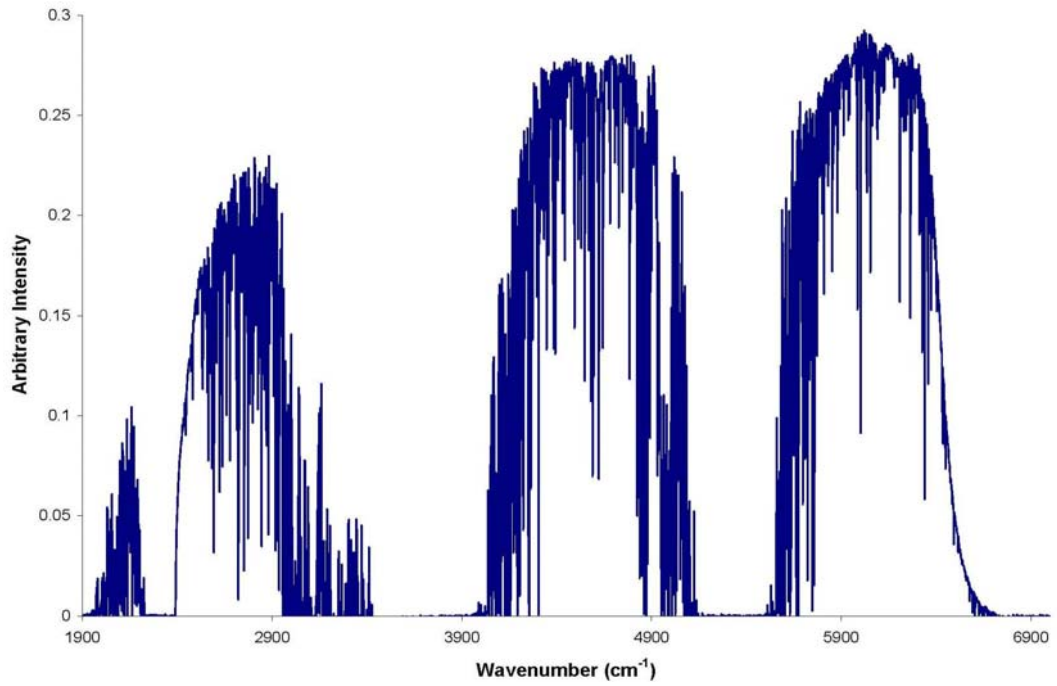

Figure 2-3: An example spectrum recorded by a ground-based solar Fourier transform spectrometer.

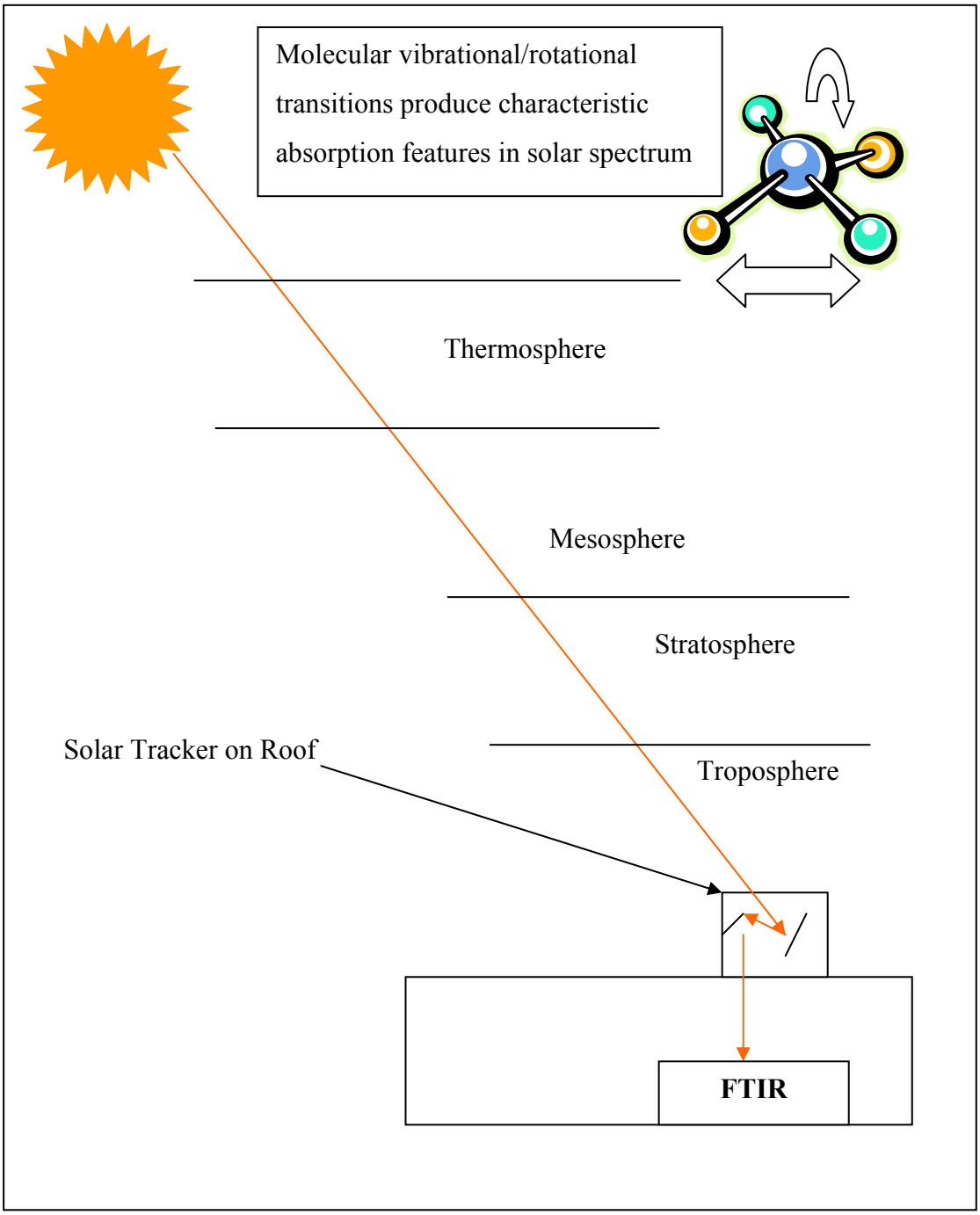

Figure 2-4: Schematic showing how radiation from the sun passes through different regions of the atmosphere and molecular vibrational/rotational transitions produce characteristic absorption features in the solar spectrum.

Clearly it is not possible to measure a background spectrum or a set of calibration spectra when the atmosphere is the sample. For this reason the analysis of these spectra requires the calculation of a synthetic spectrum using a database of absorption line parameters such as the HITRAN database [*Rothman et al.*, 1998;

Rothman et al., 2003; *Rothman et al.*, 2005] and a model of the atmospheric conditions such as pressure, temperature and gas concentrations that all vary with altitude. The calculation must also take into account instrumental effects such as line shape and resolution.

The HITRAN (HIgh resolution TRANsmission) database contains calculated quantum mechanical parameters that describe the vibrational-rotational transitions of the most common atmospheric molecules. Parameters include the line positions (frequencies of absorption lines), line strengths at a reference temperature and pressure, lower state energy and pressure broadening and shift parameters. The HITRAN 2004 database contains line parameters for 39 atmospheric gases including the wavenumber of each absorption line, the integrated line strengths at 296K, the lower state energy $\boldsymbol{E_0}$, the air-broadened Lorentzian half-width at atmospheric pressure and its temperature dependence.

Atmospheric Absorption Line Positions

The characteristic absorption features seen in Figure 2-3 are caused by molecules absorbing radiation at frequencies that correspond to the allowed transitions between different vibrational and rotational states. The frequencies at which molecules absorb are determined by the allowed transitions between energy levels of the molecule and provide a unique identifier of trace gases in the atmosphere. Vibrational energy states are much more widely spaced than rotational energy states and so the line position is determined mainly by the change in vibrational state with small frequency differences depending on the accompanying change in rotational energy.

The energy of allowed states of a simple diatomic molecule can be approximated by Equation 2-1:

Equation 2-1

$$E = \hbar\sqrt{\frac{k_f}{\mu}}(v + 1/2) + BJ(J+1)$$

(if it is assumed that molecule behaves like a simple harmonic oscillator and a rigid rotor) and where:

- $\hbar$ is Planck's constant divided by 2π,
- k_f and μ are the force constant and the reduced mass of the molecule respectively,
- B is the rotational constant ($B=\hbar/2I$, where I is the moment of inertia, the product of the reduced mass and the square of the radius of rotation)
- and v and J are the vibrational quantum number and rotational quantum number of the state respectively.

For diatomics the allowed transitions between states are $\Delta v = \pm1,\pm2,\pm3, \ldots$ and $\Delta J = \pm1$.

A vibration-rotation transition with $\Delta v= -1$ results in an *emission* spectrum and a transition with $\Delta v= +1$ an *absorption* spectrum, and both types of spectra may be accompanied by either a gain in rotational energy $\Delta J=+1$ or a loss in rotational energy $\Delta J= -1$. This produces a spectrum with two branches, one either side of the pure vibrational frequency, v_0. The R branch corresponds to a vibrational transition accompanied by a gain in rotational energy $\Delta J= +1$ and consists of a set of lines spaced approximately 2B apart to the high frequency side of the pure vibrational frequency, v_0, becoming more closely packed as the rotational energy increases further from the band centre, (assuming $B_1 < B_0$). The P branch corresponds to a vibrational transition accompanied by a loss in rotational energy $\Delta J= -1$ and consists of a set lines spaced approximately 2B apart to the low frequency side of the pure vibrational frequency, v_0, becoming more widely spaced as the rotational energy increases away from the band centre. Linear polyatomic molecules can also vibrate in a manner such that the dipole moment is changed perpendicular to the principal axis of rotational symmetry and in this case the selection rules also allow $\Delta J = 0$, i.e. the vibrational energy change can occur without an accompanying change in rotational energy. In such spectra the Q-branch appears at the band centre between the P and R branches (at the pure vibrational frequency, $\boldsymbol{v_0}$). The Q-branch is a relatively intense feature because the vibrational transitions occur from all existing rotational states with approximately the same energy change and hence the same frequency.

Line Broadening and Line Shapes

As a consequence of Heisenberg's uncertainty principle, absorption lines are never infinitely narrow. The uncertainty in the energy of a state multiplied by the uncertainty in time (the lifetime of a state) must be greater or equal to ħ, ($\Delta E \Delta t > \hbar$). So the shorter the lifetime, the larger the uncertainty in a state's energy and the broader the absorption or emission line (as the energy uncertainty manifests itself as an uncertainty in the frequency of the line). Uncertainty broadening due to the radiative or intra-molecular lifetime of the state in isolation is always present but for vibrational-rotational states is usually very small ($< 10^{-6}$ cm^{-1}). Another form of uncertainty broadening, which dominates at atmospheric pressures, is collisional broadening (also called pressure broadening) and occurs when the collisions of atoms, ions or gas molecules shorten the lifetime of states. In gases it is proportional to pressure and this means that absorption lines from spectra taken through the whole atmosphere will have different shapes depending upon the distribution of the absorbing gas in the atmosphere. A gas that is mainly located in the troposphere (such as methanol) will display broad absorption lines because of the high pressure whilst predominantly stratospheric gases (like ozone) will produce much narrower lines since the pressure is low. Uncertainty broadening leads to a Lorentzian line shape contribution at a given wavenumber υ:

Equation 2-2:
$$f_L(v) = \frac{\alpha_L / \pi}{(v - v_0)^2 + {\alpha_L}^2}$$

where v_0 is the absorption line frequency in wavenumbers, and α_L is the Lorentzian half-width at half height, which is proportional to the total pressure.

Absorption lines due to atmospheric gases are also subject to Doppler broadening. Doppler broadening occurs because molecules that travel with different velocities with respect to the light source, absorb at different wavelengths just as light from stars accelerating away from the earth is red-shifted. Doppler broadening produces a Gaussian line shape due to the Gaussian distribution of molecular velocities:

Equation 2-3:
$$f_G(v) = \frac{1}{\alpha_G \sqrt{\pi}} \exp\left(- \frac{(v - v_0)^2}{{\alpha_G}^2} \right)$$

where α_G is the Gaussian half-width at half height and is given by:

Equation 2-4

$$\alpha_G = \frac{\nu_l}{c}\sqrt{\frac{2kT}{m}}$$

where **k** is the Boltzman constant, **T** is the Kelvin temperature and **m** is the molecular mass.

Pressure broadening (with Lorentzian lineshape) dominates in the troposphere[3], but its effects drop off rapidly with altitude as the pressure drops. Doppler broadening (with Gausssian line shape) is temperature dependent but its variation through the atmosphere is much smaller than pressure broadening. Stratospheric gas lines are primarily Doppler broadened and the two types of broadening become equally significant at around 25 km. The convolution of Lorentzian and Gaussian line shapes produces a Voigt line shape. This variation of the shape and width of absorption lines with the pressure of the absorbing gas means that spectra of atmospheric gases contain information about the altitude of the absorbing gas as well as the total number of absorbing molecules in the path.

Atmospheric Absorption Line Intensities

The integrated line strength of each absorption line of each molecule is determined by the transition probability, the population and degeneracy of the initial state and the number of absorbing molecules in the path. In local thermodynamic equilibrium the population of states is determined by the Boltzmann distribution, which is dependent upon the temperature of the absorbing molecules and for this reason line strengths are temperature dependent.

At a given wavenumber (***ν***), the intensity of radiation (the radiative power) that reaches the ground ***I***(***ν***), is related to the radiative power at the top of the atmosphere $\boldsymbol{I_0}(\nu)$ by Equation 2-5:

[3] Typical values for a mid-size molecule are $\alpha_L \sim 0.15$ cm^{-1} atm^{-1} and $\alpha_G \sim 0.004$ cm^{-1}.

Equation 2-5:
$$I(\nu) = I_0(\nu)e^{-m\tau(\nu)}$$

where $\boldsymbol{\tau(\nu)}$ is the *optical depth* of the atmosphere and ***m*** is the *airmass factor* - a geometrical factor accounting for the slant path through the atmosphere.

In order to calculate a synthetic spectrum all molecules that absorb in the spectral region being simulated must be considered together. At any given wavenumber ($\boldsymbol{\nu}$), the contribution to the optical depth (τ) for every absorption line ***l*** of each molecule **x**, is given by

Equation 2-6:
$$\tau_x^l(\nu) = \sigma_x^l(\nu).a_x$$

where σ_x^l**(υ)** is the absorption coefficient or cross section at **υ**, for the each absorption line *l* of each molecule x, (typically in units of cm^2 $molecule^{-1}$) and a_x is the amount of molecules x, in units of molecules cm^{-2}. The absorption coefficient σ_x^l**(υ)** is the convolution **(⊗)** of the integrated line strength, S_x^l and the pressure broadening and Doppler broadening line-shapes:

Equation 2-7:
$$\sigma_x^l(\nu) = S_x^l \otimes \left[f_L(\nu)\right]_x^l \otimes \left[f_G(\nu)\right]_x^l$$

The integrated line strength is temperature dependent because of the temperature dependence of the population of the lower-state energy and a small contribution from the spontaneous emission. The integrated line strength at any given temperature **S(T)** may be calculated using the integrated line strengths at 296K and other parameters given in HITRAN with Equation 2-8:

Equation 2-8
$$S(T) = S(296)\frac{Q(296)}{Q(T)}.\frac{\exp(-\frac{c_2E_0}{T})}{\exp(-\frac{c_2E_0}{296})}.\frac{(1-\exp(-\frac{c_2\nu_0}{T}))}{(1-\exp(-\frac{c_2\nu_0}{296}))}$$

where Q(296) and Q(T) are the partition functions at these temperatures and c_2 is the second radiation constant, ($c_2=hc/k$ = 1.439 cm K) [*Griffith*, 1996].

Calculating Synthetic Atmospheric Spectra

The dry atmosphere is composed of mainly nitrogen (78%) and oxygen (21%) with minor and trace gases making up the other 1%. The normal modes of vibration of nitrogen and oxygen are infrared inactive because the symmetry of the molecules is such that vibrations do not cause a change in the dipole moment, so there is nothing for incoming infrared radiation to interact with. Thus the main constituents of the atmosphere transmit infrared radiation and the infrared spectrum of the atmosphere as shown in Figure 2-3 is dominated by minor constituents and trace gases such as water, carbon dioxide and methane. This is the reason that these species are important greenhouse gases.

The temperature, pressure and concentrations of trace gases in the atmosphere change continuously with altitude. In order to calculate a synthetic spectrum the atmosphere is modelled as a series of homogeneous layers each with a defined temperature, pressure and gas composition[4]. To model the radiative transfer through the atmosphere the path length of radiation from the sun through each layer of the modelled atmosphere must be calculated using a ray-tracing algorithm that takes into account the solar zenith angle at the time of the measurement and the effects of atmospheric curvature and refraction. At least thirty different atmospheric layers are required in order to do the radiative transfer calculation without errors in this calculation becoming a dominant uncertainty [*Meier et al.*, 2003].

Following on from Equation 2-6, when all the absorption lines of all molecules are considered, the total optical depth at any given frequency, $\tau(\nu)$, is the sum of the contribution of all the absorption lines of all molecules, for all homogeneous layers:

[4] The amounts of atmospheric trace gases are often measured in mole ratios, defined as the number of moles of the substance of interest per mole of air. For trace gases the usual units are micro moles per mole ($\mu mol.mol^{-1}$) – sometimes expressed as parts per million (ppm), e.g. 5 ppm CO means 5

Equation 2-9:
$$\tau(\nu) = \sum_{layers} \sum_{i} \sum_{k} \tau_i^k(\nu)$$

The true atmospheric transmittance spectrum, $\boldsymbol{T(\nu)}$ is the ratio of the intensity at the ground, $\boldsymbol{I(\nu)}$, and the intensity at the top of the atmosphere, $\boldsymbol{I_0(\nu)}$:

Equation 2-10:
$$T(\nu) = \frac{I(\nu)}{I_0(\nu)} = \exp(-\tau(\nu))$$

The calculation of the synthetic spectrum must also include the effects of instrumental parameters such as the resolution and instrumental line-shape including phase error and wavelength shift. The spectrum that will actually be measured is a convolution of the intensity at the ground, $\boldsymbol{I(\nu)}$ and the instrumental line-shape. The instrumental line-shape (ILS) may be derived using measurements of low-pressure gas cells [*Hase et al.*, 1999], or a theoretical ideal ILS can be calculated from the instrument's field of view, resolution and the apodisation function[5].

Example simulations calculated in this manner are shown in Figure 2-5 [*Meier et al.*, 2004]. In these cases the infrared transmission spectra that result from just one component atmospheric gas at a time are given, namely water, carbon dioxide and methane. The spectra are simulated from 500 cm^{-1} to 4400 cm^{-1} using the HITRAN 2000 database for a solar zenith angle of 70° and concentration profiles taken from US standard atmosphere. Details of forward model simulations for specific analyses are provided later in the thesis.

---

molecules of carbon monoxide per million molecules of air). For ultra-trace gases the units often used are nano moles per mole ($nmol.mol^{-1}$) or picomoles per mole ($pmol.mol^{-1}$).

[5] An apodisation function is a mathematical function that is applied to the interferogram that may give greater weight to the information around ZPD compared to information at greater optical path differences. In the analyses presented in this thesis a boxcar apodisation function was used that gives equal weight to the information throughout the interferogram.

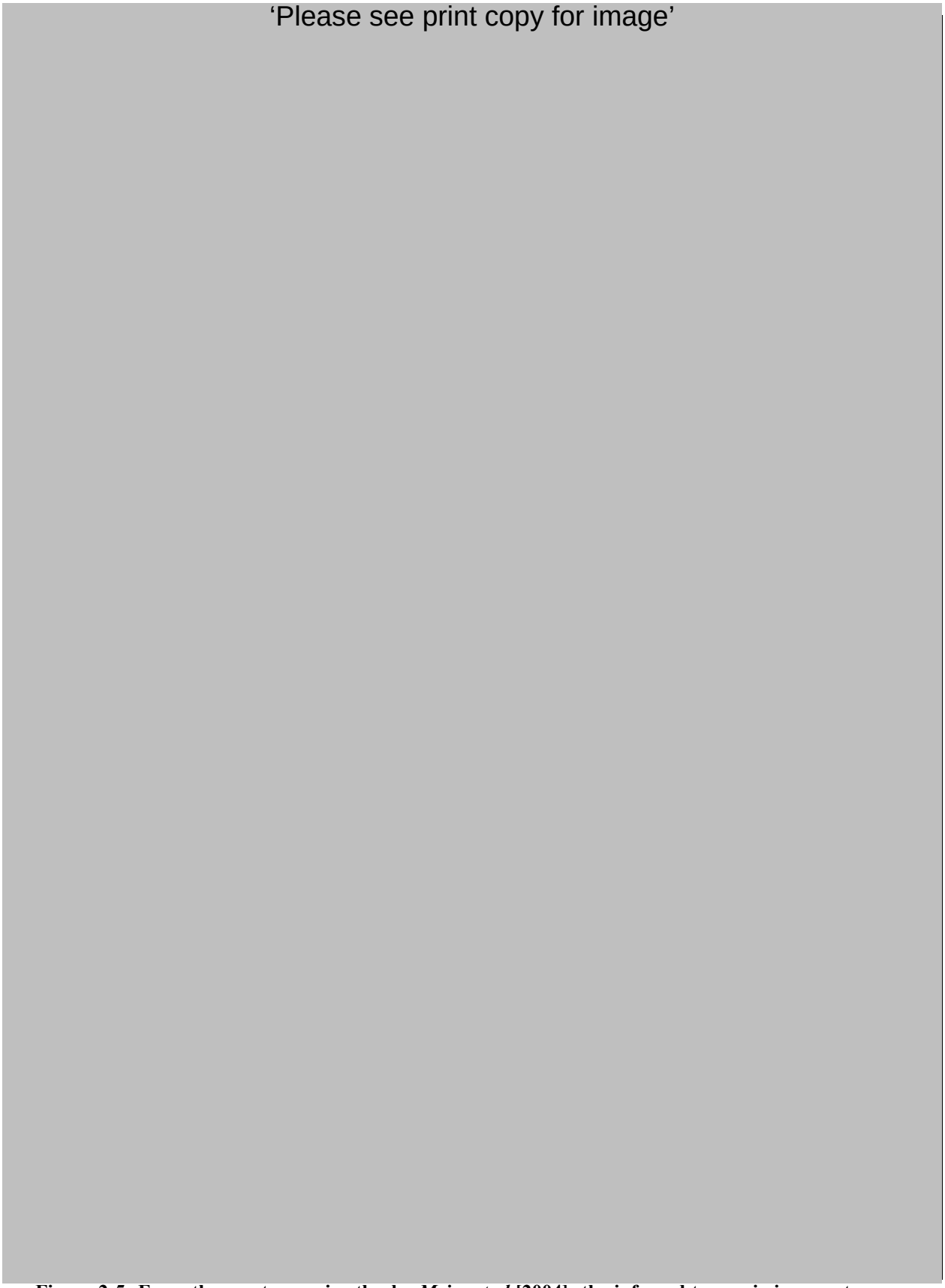

Figure 2-5: From the spectroscopic atlas by *Meier et al* [2004]: the infrared transmission spectrum of water (top panel), carbon dioxide (middle panel) and methane (bottom panel) in the atmosphere from 500 cm^{-1} to 4400 cm^{-1} as simulated using the HITRAN 2000 database for a solar zenith angle of 70° and concentration profiles taken from US standard atmosphere.

2.3 Deriving Trace Gas Amounts from Solar FTIR Spectra

Analysis Algorithms

Over the years several different analysis algorithms have been developed to perform the retrieval of trace gas amounts from solar FTIR spectra. All the techniques calculate a synthetic spectrum using a "forward model" as described above, that includes a model of the instrumental effects and a layered model of the atmosphere with assumptions about environmental parameters such as the pressure, temperature and composition of each layer. The synthetic spectrum is compared to the measured spectrum and adjustments made to the forward model until a best fit with the measured spectrum is obtained.

Different analysis algorithms allow different adjustments to the forward model in order to achieve the best fit to the measurement.

- "SFIT1" [*Rinsland et al.*, 1982; *Rinsland et al.*, 1984] and "GFIT" [*Washenfelder et al.*, 2006a] allow only a scaling of the *a priori* concentration profile of the absorbing gases to achieve best fit. This means that the distribution of the absorbing gas is defined entirely by the *a priori* assumptions – the fitting process for example cannot put more gas in the troposphere and less in the stratosphere but must multiply the concentration in each of the modelled layers by the same multiplicative factor.
- Later development "SFIT2" [*Pougatchev et al.*, 1995] using optimal estimation techniques [*Rodgers*, 1990] aimed to extract the limited spectral information on the vertical distribution of the target gas, which is contained in the shape of the absorption features as a result of pressure broadening by the surrounding atmospheric gases [*Hase et al.*, 2004; *Rinsland et al.*, 1998].
- More recently another analysis code ("PROFITT") has been developed using optimal estimation techniques that allows the temperature profile and concentration profiles to be adjusted [*Hase et al.*, 2004].

There are other analysis codes in use but all of the retrievals described in this thesis use either GFIT or SFIT2. GFIT uses an iterative nonlinear least square fit of the

calculated spectrum to the measured spectrum varying the total column amount of the absorber whilst keeping the shape of the volume mixing ratio (VMR) profile constant until a best fit is obtained. Thus a total column amount is obtained but the result may be influenced by the VMR profile assumed in the forward model and the information about the vertical distribution of the absorber that is contained in the shape of the absorption line in the measured spectrum is not used.

Inverse Modelling and Optimal Estimation

In contrast to GFIT, SFIT2 allows the VMR profile of the absorbing gas in the simulated spectrum to be adjusted so that the shape of the absorption line can best fit the measured spectrum. The principle difficulty in this technique is that the radiative transfer model requires at least thirty atmospheric layers to achieve a reasonable model of the transmission of solar radiation through the atmosphere, but the shape of an absorption feature typically contains between one and five independent pieces of information. Thus the problem is mathematically underdetermined and much of the information must still be provided by the *a priori* concentration profile in the forward model.

SFIT2 uses an inverse modeling technique [*Rodgers*, 1990; *Rodgers*, 2000] to extract the VMR profile of the gases of interest from the measured spectrum. The VMRs of the gas of interest at each of the modeled layers are the variables of interest (called state variables or together the state vector **x,** with n elements). The measured spectrum (a series of observed radiances at different frequencies) is represented by the observation vector **y** (with m elements), and the forward model, **F**, describes the relationship between the observation vector **y** (the spectrum) and the state vector **x**, (the VMRs of the gases of interest).

Equation 2-11: $$y = F(x, b) + \varepsilon$$

where **b** is a *parameter vector* including all model variables that are not to be optimized (also called the *model parameters*), and **ε** is the error vector including errors in the observations, in the forward model, and in the model parameters.

Inverting Equation 2-11, **x** may be obtained given **y**, but due to the error term **ε** the best that can be achieved is a statistical estimate. As stated before the problem is mathematically underdetermined and in optimal estimation **x** is weighted by our prior (*a priori*) knowledge of the state vector $\mathbf{x_a}$ (the *a priori* VMR profile). The optimal solution of **x** including this *a priori* knowledge is called the "*optimal estimate"* or the '*retrieval*' (also sometimes called the "*a posteriori* solution").

The *a priori* estimate has its own error: $x_a = x + \varepsilon_a$ and the key to solving the optimal estimation problem is weighting the error statistics of ε and ε_a [*Rodgers*, 2000].

The inverse problem lends itself to the use of matrix algebra, and the *Jacobian matrix*, ***K***, is a linearization of the forward model that represents the sensitivity of the observation variables **y** to the state variables **x**, assembled in matrix form [*Jacob*, 2007]:

Equation 2-12:
$$K = \nabla_x F = \frac{\partial y}{\partial x}$$

K changes with **x** and so it is calculated initially for the *a priori* value $\mathbf{x_a}$ and then re-calculated iteratively until the solution converges. The algorithm iterates until the cost function ***J(x)*** is minimised by solving for $\nabla_x J(x) = 0$ as shown in Equation 2-13 :

Equation 2-13:
$$\nabla_x J(x) = 2S_a^{-1}(x - x_a) + 2K^T S_\varepsilon^{-1}(Kx - y) = 0$$

where S_a and S_ε are the *a priori* error and observational error covariance matrices respectively (the matrix equivalents of ε_a and ε). Note that observational error includes errors in the forward model as well as spectral noise and that in many instances it is the forward model error that dominates the S_ε matrix.

The solution to Equation 2-13 yields the *optimal estimate* or *retrieval* $\hat{x}$ and is given by Equation 2-14:

Equation 2-14:
$$\hat{x} = x_a + G(y - Kx_a)$$

where G is known as the *gain matrix* and describes the sensitivity of the retrieval to the observations, i.e. $G = \frac{\partial \hat{x}}{\partial y}$, and is given by Equation 2-15:

Equation 2-15:
$$G = (K^T S_\varepsilon^{-1} K + S_a^{-1})^{-1} K^T S_\varepsilon^{-1}$$

The averaging kernel and uncertainties

The ability of the measured spectrum to constrain the VMR profile of the gas of interest, (the state vector, x) is given by the *averaging kernel matrix* $A = \frac{\partial \hat{x}}{\partial x}$, which represents the sensitivity of the retrieval $\hat{x}$ to the true state vector x. The *averaging kernel matrix,* **A=GK**, i.e. it is the product of the gain matrix $G = \frac{\partial \hat{x}}{\partial y}$ and the Jacobian matrix $K = \frac{\partial y}{\partial x}$.

The information content may be defined in terms of the degrees of freedom for signal which is the trace of the averaging kernel. Mathematically this is the sum of the diagonal elements of the averaging kernel matrix [*Rodgers*, 2000].
Using the averaging kernel matrix leads to an alternative expression for the *optimal estimate* or *retrieval* $\hat{x}$**:**

Equation 2-16:
$$\hat{x} = Ax + (I_n - A)x_a + G\varepsilon$$

where I_n is the identity matrix of dimension n. There are three terms on the right hand side of Equation 2-16. The first term, Ax represents the contribution of the true state x to the solution. The second term $(I_n - A)x_a$ represents the contribution of the *a priori* assumptions. The third term Gε is the contribution from random observational error. An ideal measurement would have an averaging kernel matrix that was an n dimensional identity matrix, $A = I_n$ in which case the second term is zero [*Jacob*, 2007; *Rodgers*, 2000].

The second term in Equation 2-16, [(In – A)xa] is called the *smoothing uncertainty* (since it results in a smoothing of the retrieval towards the *a priori* values). The third term, Gε, is known as the *retrieval uncertainty* (or *signal-to-noise uncertainty*) but again it should be noted that this includes not only measurement noise but also errors in the forward model such as errors in the HITRAN database and that

these factors often dominate the spectral noise. There may also be errors in the forward model that are correlated with one another and are therefore not random, potentially leading to uncharacterised biases in the retrievals. One other error that can be estimated is the *temperature uncertainty*, due to errors in the assumed temperature profile in the forward model. These lead to errors in the line strengths and resulting retrieved trace gas amounts that may be calculate using Equation 2-8.

Using SFIT2 in practice

The use of optimal estimation techniques in SFIT2 for extracting slant column amounts is a delicate balancing act to ensure that as much information as possible is extracted from the actual measurement without adding spectral noise (or noise from errors in the forward model) which will result in unrealistic or non-physical output. The inverse model uses matrix algebra as described above to minimize the cost function that is dependent upon both the measured spectrum and the *a priori* information. The weight given to the spectrum depends upon the signal-to-noise ratio that is input into the retrieval code whilst the weight given to the *a priori* concentration profile is determined by a covariance matrix input into the code. The retrieval may be further constrained by an interlayer correlation number that determines how rapidly the concentration is expected to change from one atmospheric layer to the next. For example a Gaussian inter layer correlation number of 4 means that the retrieved values for the VMRs in nearby layers are constrained to lie within a Gaussian distribution with a half width at half maximum of 4km.

In practice the technique used for all the retrievals described in this thesis involved the following general steps:

1. Choose a suitable region (microwindow) of the spectrum (one or more).
2. Decide upon a reasonable first *a priori* concentration profile for the target gas.
3. Choose an initial signal-to-noise ratio for the dataset. This is a guess based on the smallest signal-to-noise values of the real spectra, this may still be too high as the fits are often limited by inaccuracies in the simulated spectrum rather than spectral noise of the measured spectrum.
4. Decide upon a reasonable covariance matrix (and interlayer correlation factor) given the likely range of tropospheric concentrations.

5. Examine the quality of fit achieved and check the concentration profiles retrieved for unrealistic or non-physical properties (negative concentrations, or excessive oscillations in the concentration profile derived).
6. Vary the signal-to-noise used to optimise the retrieval.
7. Change the covariance matrix, *a priori* concentration profile and/or microwindows used as necessary, and repeat.

The process can be laborious and contains a certain amount of trial and error especially when trying to retrieve gases that have small absorption features that are more susceptible to spectral noise or that have significant interference from absorption by other gases. In these cases the choice of microwindow(s) is especially critical. The actual information content within a particular microwindow varies depending upon the number of different lines being used in the retrieval, their temperature dependence and how sensitive they are to the effects of pressure broadening. The larger the region of the spectrum used (the microwindow) the more information available to determine the "background" level around the absorption lines of interest. The theoretical information content can be calculated and if the HITRAN database were perfect then large microwindows would always produce better results. Recently a program for calculating the optimum microwindow to use has been written [*Notholt et al.*, 2006], but in reality imperfections in the HITRAN database produce differences in the simulated spectrum and measured spectrum that can limit the ability to achieve a good fit to the measured data and bias the retrieval. For this reason the choice of microwindow is also subject to some trial and error and subjective judgement.

The inverse modeling described above retrieves the slant column. A more useful term is the vertical column amount (also called the total column amount) that normalizes the slant column amount to the equivalent column directly overhead by dividing by the ratio of air-masses. The airmass is calculated using the ray tracing model "fscatm" that models the path of solar radiation through the earth's atmosphere [*Meier et al.*, 2003]. In an unchanging atmosphere the vertical column (unlike the slant column) will not change with solar zenith angle but will be constant throughout the day. Specific details for retrieval schemes used in this thesis are provided later.

2.4 Measurements of Aerosol Optical Depth

Ground-based Measurements of Aerosol Optical Depth using Ultraviolet and Visible Spectroscopy

Aerosol optical depth (AOD) is a measure of the light extinguished by scattering by aerosols in the atmosphere and is derived from measurements of solar spectral irradiance. Spectral irradiance measurements can be made using ground-based sun-photometers [*Tomasi et al.*, 1983; *Volz*, 1974]. In this study the sun-photometer at Wollongong used the sun-tracker shown in Figure 1-2. A small part of the edge of the solar beam from the tracker is picked off, reflected onto white specular surfaces and sent by two separate optical fibres (see Figure 2-6) to two Ocean Optics OD2000 grating spectrometers with a 2048 pixel CCD detector arrays spanning the visible and some ultraviolet wavelengths (see Figure 2-7). Details of the sun-photometer in Darwin are given in section 5.4.

Figure 2-6: Photograph showing the Optical fibres used with the Ocean Optics OD2000 grating spectrometer

The amount of solar radiation of a particular wavelength that reaches the earth's surface depends upon the distance between the Sun and the earth, the optical depth of the atmosphere at that wavelength for normally incidenct radiation (see Equation 2-5) and the relative airmass.

Figure 2-7: Photograph showing the Ocean Optics OD2000 grating spectrometer

At any given wavelength, λ, the total optical depth of the atmosphere ($\tau^t(\lambda)$) is composed of components of optical depth due to Rayleigh scattering ($\tau^R(\lambda)$), aerosol scattering ($\tau^a(\lambda)$) and molecular absorption of gases ($\tau^g(\lambda)$), as expressed in Equation 2-17.

Equation 2-17: $$\tau^t(\lambda) = \tau^R(\lambda) + \tau^a(\lambda) + \tau^g(\lambda)$$

The optical depth of the atmosphere in the infrared region of the spectrum was discussed earlier, but in the infrared the contributions due to Rayleigh scattering and aerosols are insignificant and only optical depth due to molecular absorption is considered (see Equation 2-6).

The Rayleigh optical depth component can be calculated [*Bodhaine et al.*, 1999] and molecular absorption can be minimised by choosing wavelengths that are largely unaffected by molecular absorption. Thus the AOD of the atmosphere can be determined at suitable wavelengths with minimal molecular absorption by subtraction of the Rayleigh scattering component from the total AOD of the atmosphere.

The total column optical depth of the atmosphere is defined as the difference between the solar irradiance at the ground if the Sun were directly overhead and the solar irradiance at the top of the atmosphere. Measurements of solar irradiance at the ground vary with airmass and this leads to a method for calibration (called the Langley

technique) that estimates both the solar irradiance that would be measured at the top of the atmosphere and the total column atmospheric optical depth, τ^t.

The Langley technique is an extrapolation based on repeated sunphotometer measurements as the Sun moves across the sky during a cloudless morning or afternoon. An expression for the response of the UV-visible spectrometer at the ground at a given wavelength (λ) is given in Equation 2-18:

Equation 2-18: $$V(\lambda) = V_0(\lambda)\exp[-m\tau^t(\lambda)]$$

Where

- ***V(λ)*** is the UV-visible spectrometer's response at the ground at wavelength (λ)
- ***$V_0(\lambda)$*** is the response of UV-visible spectrometer to the mean solar irradiance at the top of the atmosphere at wavelength (λ)
- ***m*** is the airmass, which depends upon the solar zenith angle at the time of the measurement

Note that Equation 2-18 is similar to Equation 2-5 except that instead of the true radiative power at the ground, ***I***, and at the top of the atmosphere, $\boldsymbol{I_0}$, used in Equation 2-5, it is the response of the instrument to this radiative power at the top of the atmosphere, ***$V_0(\lambda)$*** that is being determined.

As the Sun moves across the sky, the solar zenith angle, θ varies and a series of measurements of the instrument's response at the ground ***$V(\lambda)$*** are made. For a plane-parallel atmosphere, (ignoring the secondary effects of pressure changes & changes in the vertical distribution of atmospheric gases), the airmass factor may be calculated approximately from the solar zenith angle θ, where $m = \sec(\theta)$.

Taking the logarithm of the Equation 2-18, gives Equation 2-19:

Equation 2-19: $$\ln[V(\lambda)] = \ln[V_0(\lambda)] - m\tau^t(\lambda)$$

The Langley method requires a reasonable span of solar zenith angles – from ~60° - 75° or more. As long as there are no clouds and the aerosol loading does not change significantly during the measurement period, then the atmospheric optical depth τ^t should not change significantly during the observations. If these conditions hold then

a plot of $V(\lambda)$ versus m will yield a reasonable straight line. By extrapolating back to $m = 0$, the radiance that would be measured by the instrument if it were placed at the top of the atmosphere may be obtained. The gradient of the straight line is the total atmospheric optical depth τ^t [*Soufflet et al.*, 1992; *Wilson et al.*, 2002].

Spectral irradiance measurements described in this thesis were calibrated using the Langley technique as described above from data collected on clear days before and after the smoke measurements. Individual estimates of AOD at 500 nm were derived from each measurement of irradiance through subtraction of the calculated Rayleigh scattering component, and the mean value calculated for the period of time taken to record each of the infrared spectra. Although our measurements span the visible spectrum, maximum signal intensity and minimum interference by molecular absorbance is obtained at 500nm. For Wollongong AOD values were calculated (& calibrated via the Langley technique) using a suite of pre-written programs (Stephen Wilson, University of Wollongong), whilst for Darwin the data were provided pre-calibrated at one minute intervals (Bruce Forgan, Bureau of Meteorology) and the value closest to the time of measurement was used with an uncertainty determined by the variance in AOD taken from the closest six measurements. An example Langley plot is shown in Figure 2-8.

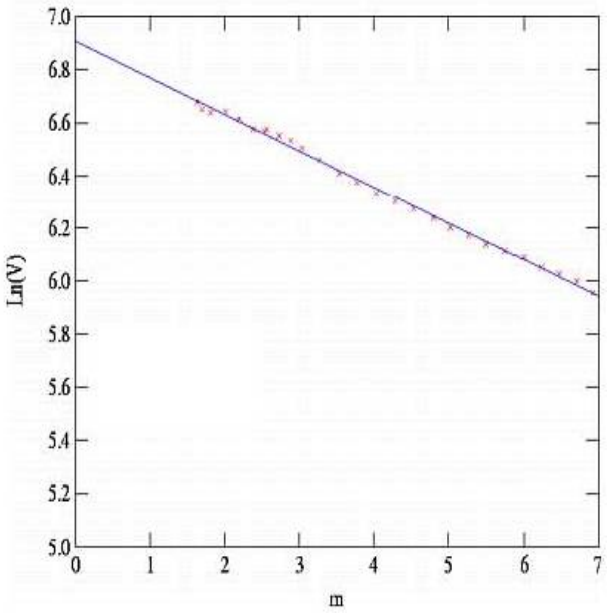

Figure 2-8: Example of a Langley plot. The x=0 intercept give $V_0(\lambda)$ and the gradient gives τ^t. From http://seawifs.gsfc.nasa.gov/staff/sunphoto/principle.html#Langley_section for illustration purposes only, data not from this thesis.

Satellite-based Measurements of AOD

Interest in aerosol measurements has grown dramatically with concern over global warming and the realization of the complex and uncertain role that aerosols play in climate change [*Rasool et al.*, 1971] . In fact aerosol radiative forcing is the most uncertain component of global climate models. The huge horizontal and vertical variability of aerosol loading makes remote sensing measurements especially useful for monitoring atmospheric aerosols.

In recent years satellite remote sensing measurements of AOD have been made from the AVHHR (Advanced Very High Resolution Radiometer) sensor; SeaWiFS, [http://seawifs.gsfc.nasa.gov/SEAWIFS.html] (Sea-viewing Wide Field-of-view Sensor) and two MODIS (Moderate Resolution Imaging Spectrometer) instruments [http://modis.gsfc.nasa.gov/], on board the NASA Earth Observing System satellites Terra and Aqua [*Kaufman et al.*, 1990; *Kaufman*, 1993; *Kaufman et al.*, 2003; *King et al.*, 1999; *Remer et al.*, 2002; *Zhao et al.*, 2003].

The principles of determining AOD from spectral irradiance measurements from space are similar to those outlined above for ground-based measurements except that the solar radiation measured is backscattered from aerosols and molecules in the atmosphere or reflected from the earth's surface and back into space. The algorithms used to derive AOD are much more complex as they need to account for the variable reflectivity of the earth's surface. Separate algorithms are used to derive AOD over land and sea and work is ongoing to optimise these algorithms [*Kleidman et al.*, 2005; *Levy et al.*, 2007].

2.5 Atmospheric Modelling using "TAPM"

TAPM (**T**he **A**tmospheric **P**ollution **M**odel) was developed by Peter Hurley & others from Australia's Commonwealth Scientific and Industrial Research Organisation (CSIRO) and runs on a standard personal computer [*Hurley et al.*, 2005]. TAPM was designed to allow companies to meet their obligations to Environmental Protection Agencies by enabling them to predict the concentrations of pollutants emitted by their

industries in the local and regional environment. Although it has been designed primarily as a model for studying local pollution it is capable of modeling pollution flows on a regional scale. It has performed well in a number of verification studies [*Edwards et al.*, 2004; *Hurley*, 2000; *Hurley et al.*, 2003; *Hurley et al.*, 2001; *Luhar et al.*, 2003; 2004].

TAPM uses synoptic analyses to set-up large-scale meteorological fields and then predicts the airflows important to the smaller scale, (such as sea breezes or terrain induced flows), by solving approximations to the fundamental fluid dynamics and scalar transport equations. The model solutions for winds, specific humidity and potential virtual temperature are periodically normalized to mean synoptic analyses values.

TAPM is designed to allow up to 5 different grid levels, with the finer grids nested in the larger grids. A separate grid can be used to examine the pollution levels predicted by the model. This allows the large-scale meteorological input to be used as well as very fine detail around the source of emissions and around the area in which the pollution levels are of interest.

TAPM includes databases of synoptic analyses of meteorological data, terrain, vegetation and soil type and sea-surface temperature. The databases used in the configuration of TAPM described in this project are:

- six-hourly synoptic scale analyses from the Australian Bureau of Meteorology on a longitude/latitude grid at 0.75- or 1.0-degree grid spacing (approximately 75 km or 100 km);
- Australian terrain height data from Geoscience Australia on a longitude/latitude grid at 9-second grid spacing (approximately 0.3 km);
- Australian vegetation and soil type data from CSIRO Wildlife and Ecology on a longitude/latitude grid at 3-minute grid spacing (approximately 5 km) and
- Rand's global long-term monthly mean sea surface temperatures from the US National Center for Atmospheric Research on a longitude/latitude grid at 1-degree grid spacing (approximately 100 km) [*Alexander et al.*, 1976].

The air pollution component in TAPM has both a Lagrangian particle module and a Eulerian grid module. It is this latter module that is of interest for the regional scale modeling described in this thesis. It calculates concentration fields for a particular pollution grid given the relevant emissions and background concentrations of key chemical species. The model includes representations of advection, diffusion, chemical reactions and wet and dry deposition processes. TAPM can be run in tracer mode or in chemistry mode. In the tracer mode the model uses emission rates of the given tracer(s) and calculates the dispersion that results from advection and diffusion but there is no representation of chemical processes. All model runs described in this thesis use the tracer mode.

Chapter 3 : FTIR Spectra Recorded through Smoke Plumes from South Eastern Australian Forest Fires & Analysis for Trace Gas Amounts

3.1 Spectra Recorded through Smoke Plumes from South Eastern Australian Forest Fires 2001 – 2003

Spectra were recorded through smoke plumes from the 2001-2002 New South Wales forest fires passing over Wollongong (34.5°S, 150.9°E) on 9 days between December 24th 2001 and January 4th 2002[6]. There were also smoke events sampled on 7 days during September and October 2002 and 13 days between November 2002 and January 2003 including plumes from the Canberra fires of January 2003. In total more than seventeen hundred infrared solar atmospheric absorption spectra were recorded through smoke plumes originating from many different bushfires. Simultaneous and co-located direct solar spectral irradiance measurements spanning the visible wavelengths were also made, so that the AOD of the atmosphere during the time of the infrared measurements could be determined.

The infrared spectra were sorted according to the AOD measured simultaneously at 500nm. Only spectra with AOD at 500nm above 0.1 were included in the dataset, thereby reducing the number of smoke affected spectra to be analysed in all filter regions to a little over one thousand. Spectra were originally recorded at resolutions varying from 0.02 cm^{-1} to 0.004 cm^{-1}, but all spectra were analysed at a resolution of 0.02 cm^{-1} with higher resolution spectra being retransformed to increase the signal-to-noise and yield a consistent set of spectra.

The optical filters that were used transmit in the following wavenumber regions:

Filter 1:	3950cm^{-1} to 4400 cm^{-1}
Filter 2:	2900cm^{-1} to 3400 cm^{-1}
Filter 3:	2400cm^{-1} to 3200 cm^{-1}
Filter 4:	2000cm^{-1} to 2600 cm^{-1}
Filter 5:	1900cm^{-1} to 2200 cm^{-1}
Filter 7:	950 cm^{-1} to 1300 cm^{-1}
Filter 8:	700 cm^{-1} to 1050 cm^{-1}

Filters 1 through 5 were used with the InSb detector, whilst filters 7 and 8 were used with the MCT detector. Note that no spectra used filter 6 which spans the regions covered by filters 7 and 8.

Some of the gases commonly associated with biomass burning can be clearly seen to be enhanced in some of the smoke affected spectra by simple examination of the region of absorption. These enhancements were particularly large on the 1st January 2002 and Figure 3-1 and Figure 3-2 show examples for CO, HCN, H_2CO, NH_3, ethylene (C_2H_4) and acetylene (C_2H_2).

[6] Spectra recorded before October 2002, were taken by Arndt Meier and other members of the centre for atmospheric chemistry. Most smoke affected spectra recorded after this date were taken by the candidate or by Nicholas Jones.

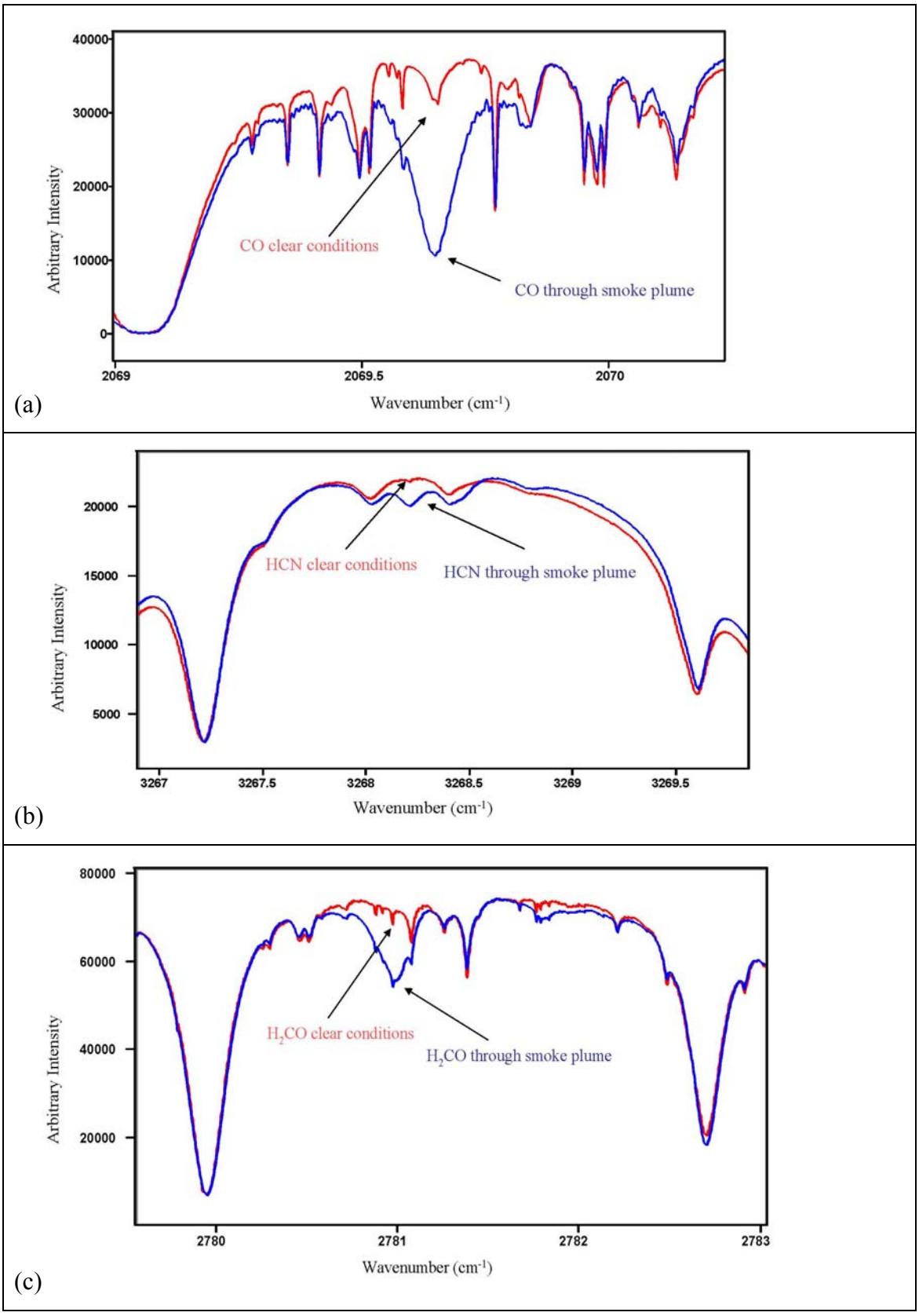

Figure 3-1: Plots showing enhanced amounts of (a) CO (top panel), (b) HCN (middle panel) and (c) H_2CO (bottom panel) in smoke plumes sampled on 1st January 2002.

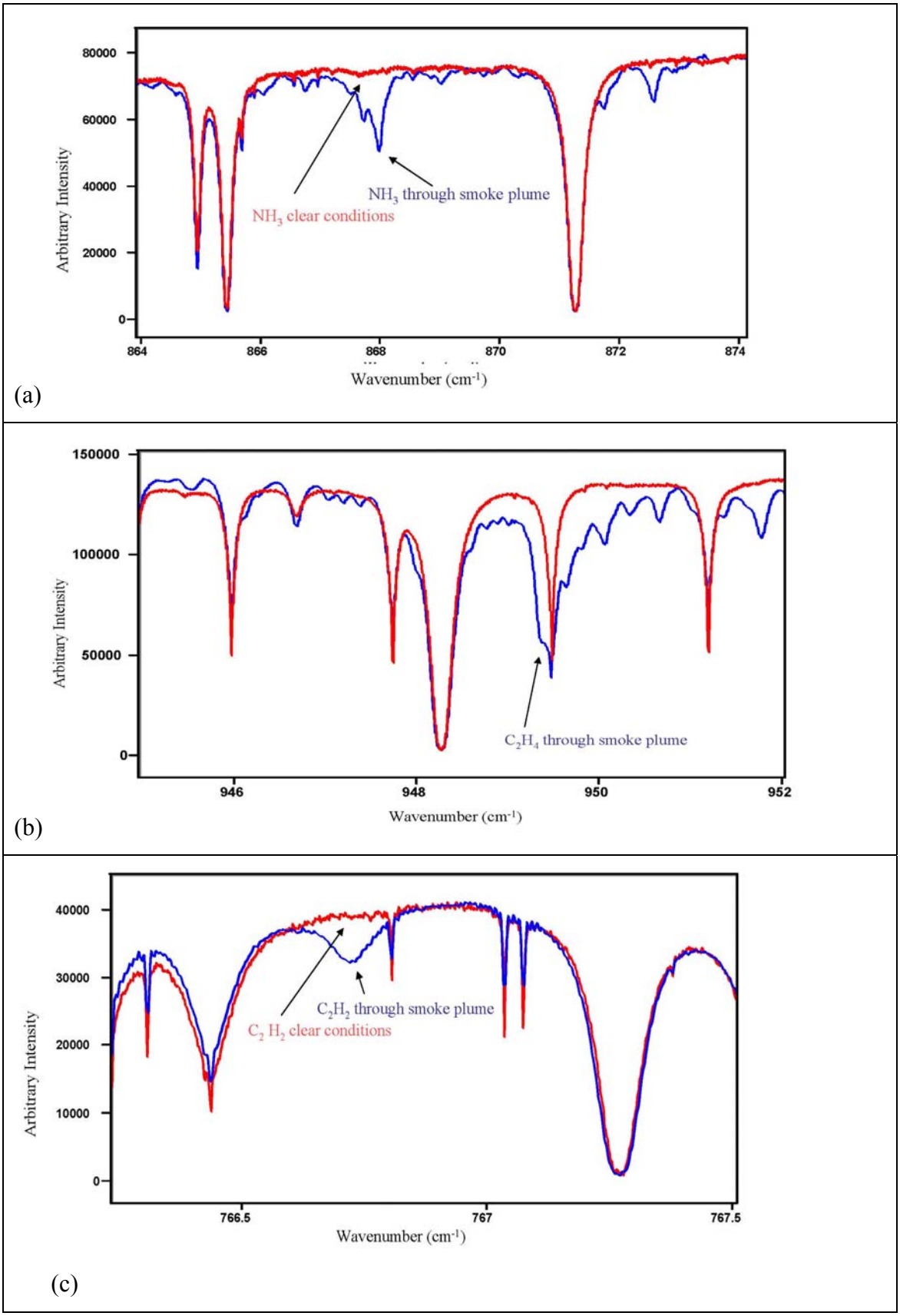

Figure 3-2: Plots showing enhanced amounts of (a) NH_3 (top panel), (b) C_2H_4 (middle panel) and (c) C_2H_6 (bottom panel) in smoke plumes sampled on 1st January 2002.

3.2 Analysis of Smoke affected FTIR Spectra for Trace Gas Amounts

Daily temperature and pressure data from balloon sondes launched from Sydney airport were splined with National Meteorological Centre data to produce temperature and pressure profiles from 0-100km for use in the forward model. When more than one sonde was available and the infrared spectra were recorded during a short time period, the sonde closest to the time of the infrared measurements was used. Otherwise daily mean measured temperature and pressure values were used when spectra were taken throughout the day.

Methanol (CH_3OH) retrievals were performed using GFIT[7] [*Washenfelder et al.*, 2006b] which allows a single scaling of the concentration of the target gas at all altitude layers. For all other gases retrievals were performed using SFIT2 [*Rinsland et al.*, 1998], returning the concentration profile of the target gas which best fits a suitably weighted combination of the measured and simulated spectra, (further details of these retrieval algorithms are given in section 2.4).

A significant difficulty with analysing the smoke affected spectra was determining a good choice of *a priori* VMR profile for each of the relevant atmospheric gases. The true VMR profiles of spectra taken through thick smoke plumes will have anomalously large amounts of gases associated with biomass burning, in the troposphere when compared to clean air. There was already some evidence of a correlation with AOD and one of the aims of the analysis was to determine how strong this correlation was. For this reason a single retrieval method for all of the smoke affected spectra was required regardless of whether the spectra were taken through thick smoke plumes (and had very large enhancements of gases and particulates from biomass burning), or through thinner plumes with much smaller enhancements.

Analysis for CO using SFIT2

[7] At the time that the analysis was undertaken SFIT2 did not have the required auxiliary line parameters (vibrational modes and their temperature dependencies). For this reason GFIT was used to analyse for this additional molecule.

The first gas to be retrieved was CO. The lines commonly used to fit the main carbon monoxide isotope ($^{12}C^{16}O$) are the R2 and R3 lines of the fundamental vibration, but these are strongly saturated under normal atmospheric conditions making them less sensitive to enhanced CO in the smoky atmosphere than weaker lines. For this reason absorption lines of the fundamental vibration of the isotope $^{13}C^{16}O$ are used in the analysis because they are weaker due to the lower abundance (1.1%) of this isotope in the atmosphere. It is assumed that the isotopic fractionation in the smoke plumes is the same as in normal background atmospheric CO. This assumption may increase the uncertainty in the CO retrieved column amounts by 2%, since biomass carbon can be up to 2% lighter in ^{13}C.

Spectra that used either optical filter 4 or optical filter 5 were analysed for CO total column amounts using the P10 and P7 lines of the fundamental vibration for the isotope $^{13}C^{16}O$ at 2057.8575 cm^{-1} and 2069.6559 cm^{-1} respectively and a third microwindow was used to fit an interfering feature of CO in the sun's atmosphere (see Table 3-1 for details). This "solar CO" feature was calculated separately in SFIT2 using a solar model "COG450" similar to that described by *Hase et al* [2006].

Defining an appropriate *a priori* concentration profile for CO and an accompanying covariance matrix was difficult because of the tendency for SFIT2 to return non-physical negative concentrations in some altitude layers if the measured column amount is substantially lower than the *a priori* column amount. This is mathematically valid (if non-physical) and is not necessarily a problem if the information content is low at the altitudes where negative concentrations are retrieved. However often this be behaviour is the result of instability in the retrieval and the total column amounts returned may be invalid. Instability also results if the signal-to-noise assumed by the optimal estimation algorithm is either greater than the signal-to-noise of the spectrum itself or greater than the apparent signal-to-noise that results from imperfections in the simulated spectrum as a result of errors in the forward model. This means that the most practical approach is often to use an *a priori* profile with a significantly lower total column than the average expected from the dataset and to compensate by using larger values in the covariance matrix, (S_a). The approach taken for CO was to do a two stage analysis.

A first retrieval was run for CO using all the spectra recorded with optical filter 4, using a VMR profile for CO typical of clean air and a covariance matrix with

diagonal elements set to 1.00 throughout. The set of retrieved profiles from this initial run was then used to define the second stage of analysis. First an *a priori* profile was defined by averaging the retrieved profiles that corresponded to the lower two-thirds of retrieved column amounts, but this new profile proved to be unstable for retrieving lower amounts of CO. A new *a priori* profile was created by reducing the concentration in each layer by 50% and the diagonal elements of the covariance matrix were defined by rounding up the actual variance in the retrieved profiles for each altitude layer. The final *a priori* VMR profile and diagonal elements of the covariance matrix used are shown in Figure 3-3 . The retrieval was further constrained by a Gaussian inter layer correlation factor of 4km[8].

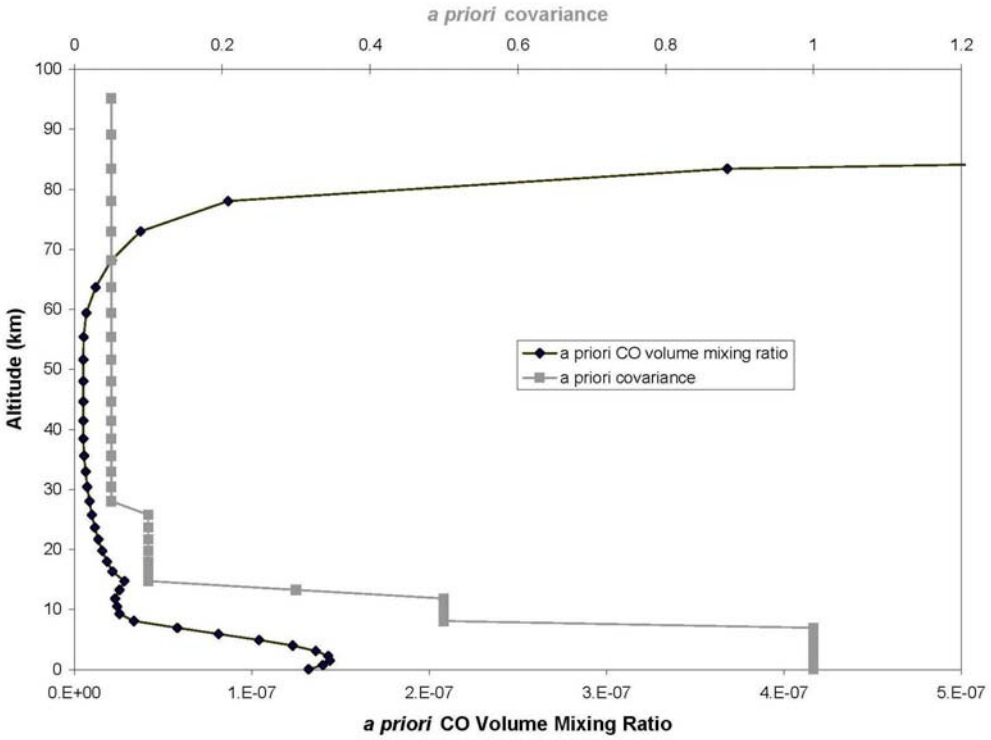

Figure 3-3: ***a priori*** **covariance matrix and VMR used in retrieval of CO.**

This gave stable results with good fits of simulated and measured spectra for both large and small enhancements of CO. Finally the signal-to-noise ratio (S:N) was increased from a low value until the retrieved amount stopped increasing and the residuals from the fit of simulated and measured spectra stopped reducing at a S:N

[8] A Gaussian inter layer correlation factor of 4km is an empirical way of defining the off-axes elements of the covariance matrix by making the points fit a Gaussian shape peaking at the diagonal elements and with a width of 4km.

value of 225. The averaging kernel for this retrieval (using the *a priori* VMR profile) is shown in Figure 3-4. This analysis was then repeated for all the spectra recorded with optical filter 5 with similar results illustrated by the fits shown in Figure 3-5. Note that the S:N value of 225 was used for both filters 4 and 5 and that the spectra from these two filter regions yielded similar fits.

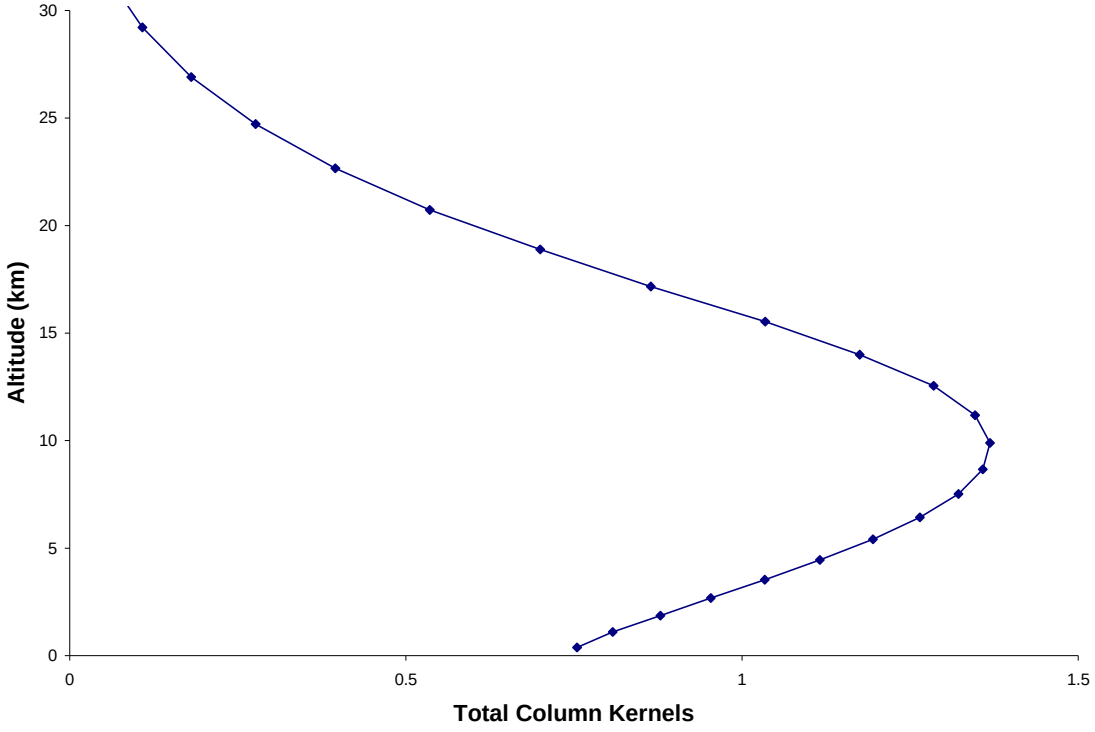

Figure 3-4: Averaging kernel for the retrieval of CO.

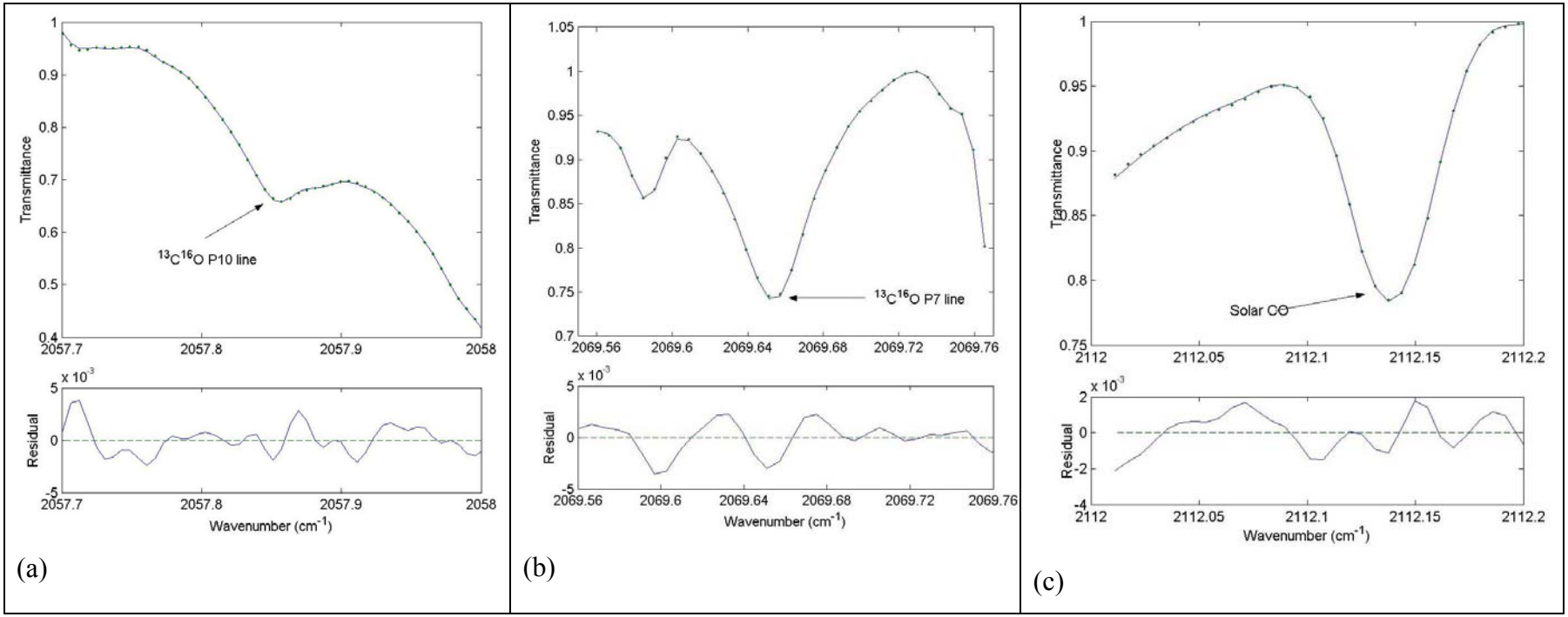

Figure 3-5: Example fits achieved in the SFIT2 retrieval of CO in all 3 microwindows used: (a) 2057.684 – 2058.000cm^{-1} fitting the P10 line of $^{13}C^{16}O$, (b) 2069.55 – 2069.76cm^{-1} fitting the P7 line of $^{13}C^{16}O$ and (c) 2012.00 – 2012.20cm^{-1} fitting solar CO

SFIT2 Analysis of Spectra for H_2CO, HCN, NH_3, HCOOH, C_2H_2, C_2H_4 and C_2H_6

The other gases analysed using SFIT2 were H_2CO, HCN, NH_3, formic acid (HCOOH), C_2H_2, C_2H_4 and ethane (C_2H_6). A two-stage approach similar to that taken for CO was used in the analyses of these gases. First *a priori* concentration profiles typical of Northern Hemisphere clean air were used (taken from the "refmod 95" set of standard profiles [*Mahieu et al.*, 1997; *Pougatchev et al.*, 1998]), followed by a second stage of analysis that used the average of the retrieved profiles from the initial analysis as the new *a priori* concentration profile and the variance of the concentration at each altitude layer as the basis on which to construct a new *a priori* covariance matrix. For several gases (C_2H_4, HCOOH, HCN and H_2CO), the variance of the first stage retrievals was very similar to that of CO and so the same covariance matrix defined by the CO analysis was used in all these cases. The final analysis of HCOOH and C_2H_4 used the original *a priori* VMR profile typical of clean air because using the average retrieved profile produced instabilities in the retrievals. The final *a priori* VMR profiles and diagonal elements of the covariance matrices used for each gas are plotted in Figure 3-6 to Figure 3-12. For each of the gases retrieved using SFIT2 the details of the retrieval are given in Table 3-1. Listed are the filter region(s) used for each retrieval, the signal-to-noise value used, the spectral interval or intervals used and the interfering gases that were also fitted in the retrieval. It should be noted that the use of a first stage of retrievals to define the covariance matrices is an unconventional approach. Under normal circumstances the use of data from a satellite instrument to define the covariance would be preferred, however in this case the level of enhancements of gases associated with biomass burning in some of the spectra are extremely unusual and would not be captured by use of standard satellite-derived climatology.

Uncertainty Analysis for Derived Column Amounts using SFIT2

The effects of pressure broadening on the shape of absorption features allow for limited vertical resolution in the measurements: - the smoothing uncertainty is the uncertainty in the total column amount that results from the inability of the retrieval to distinguish perfectly between absorption at different altitudes. The signal-to-noise

uncertainty is the column amount of each trace gas that is undetermined due to the noise in each spectrum, given the chosen value for signal-to-noise in the analysis. This signal-to-noise value may be significantly lower than the signal-to-noise of the spectrum in the region of interest. This is because it is a measure of how well the spectrum can be fitted and so depends also upon the quality of the simulated spectrum and is often dominated by errors in the forward model, rather than true spectral noise.

This uncertainty is the dominant uncertainty for many of our target gases because of the small absorption features being fitted. These first two uncertainties were calculated separately for each individual spectrum using Matlab scripts (see Equation 2-16) and the values given in the uncertainty tables are the mean of all the analysed spectra. Also included are the temperature sensitivities of the absorption features used, calculated from the HITRAN line parameters using Equation 2-8 and assuming a temperature uncertainty of 5°C. This estimate is quite large because of the large temperature variations in the boundary layer and lower troposphere where the majority of the target gases are concentrated. Finally these three components of uncertainty are added in quadrature to give a total uncertainty for each spectrum. The mean values of these main uncertainties affecting the precision of the trace gas retrievals are given in Table 3-1.

Table 3-1: Spectra intervals and interfering gases fitted for each species retrieved using SFIT2 along with uncertainties in the derived column amounts.

Trace Gas	Filter Region	S:N in retrieval	Spectral Interval(s) fitted (cm^{-1})	Interfering Gases Fitted in retrieval	Smoothing Uncertainty	Signal-to-noise Uncertainty	Temperature Uncertainty	Total Uncertainty
C_2H_4	Filter 8	225	945.00 – 952.00	H_2O, CO_2, NH_3	3.5%	3.8%	3%	6.4%
NH_3	Filter 8	200	1046 – 1046.75	H_2O, O_3, CH_4	14.5%	16.5%	2.7%	22.4%
HCOOH	Filter 7	800	1104.40 – 1106.00	H_2O, HDO, O_3	5.8%	26.6%	2.0%	27.5%
CO	Filter 4 Filter 5	225	2057.68 – 2058.00 2069.55 – 2069.76	CO_2, O_3	5.8%	2.5%	1.3%	6.5%
H_2CO	Filter 3	400	2778.12 – 2778.80 2780.60 – 2781.17	CO_2, O_3, CH_4	3.1%	10.8%	1.6%	11.4%
C_2H_6	Filter 3	150	2976.60 – 2977.10 2996.70 – 2997.10 3000.10- 3000.60	H_2O, H_2CO, CH_4, O_3	4.4%	3.0%	2.3%	5.8%
C_2H_2	Filter 2	500	3304.80 – 3305.30	H_2O, HDO	4.7%	8.5%	1.9%	10%
HCN	Filter 2	500	3268.00 – 3268.38 3287.00 – 3287.48	H_2O	9.8%	3.3%	2.1%	10.6%

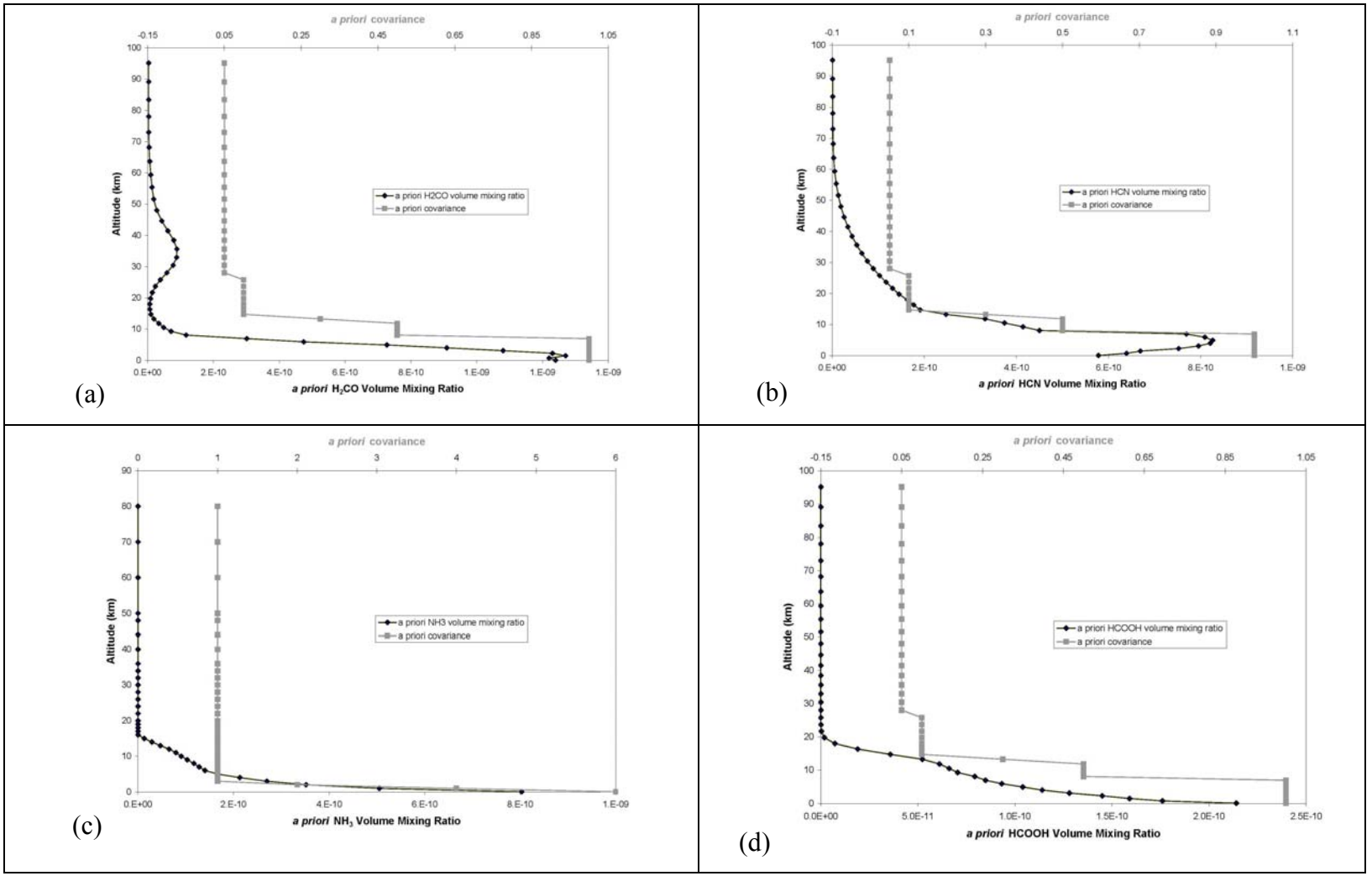

Figure 3-6: *a priori* covariance matrices and VMR profiles used in the retrieval of (a) H_2CO, (b) HCN, (c) NH_3 and (d) HCOOH.

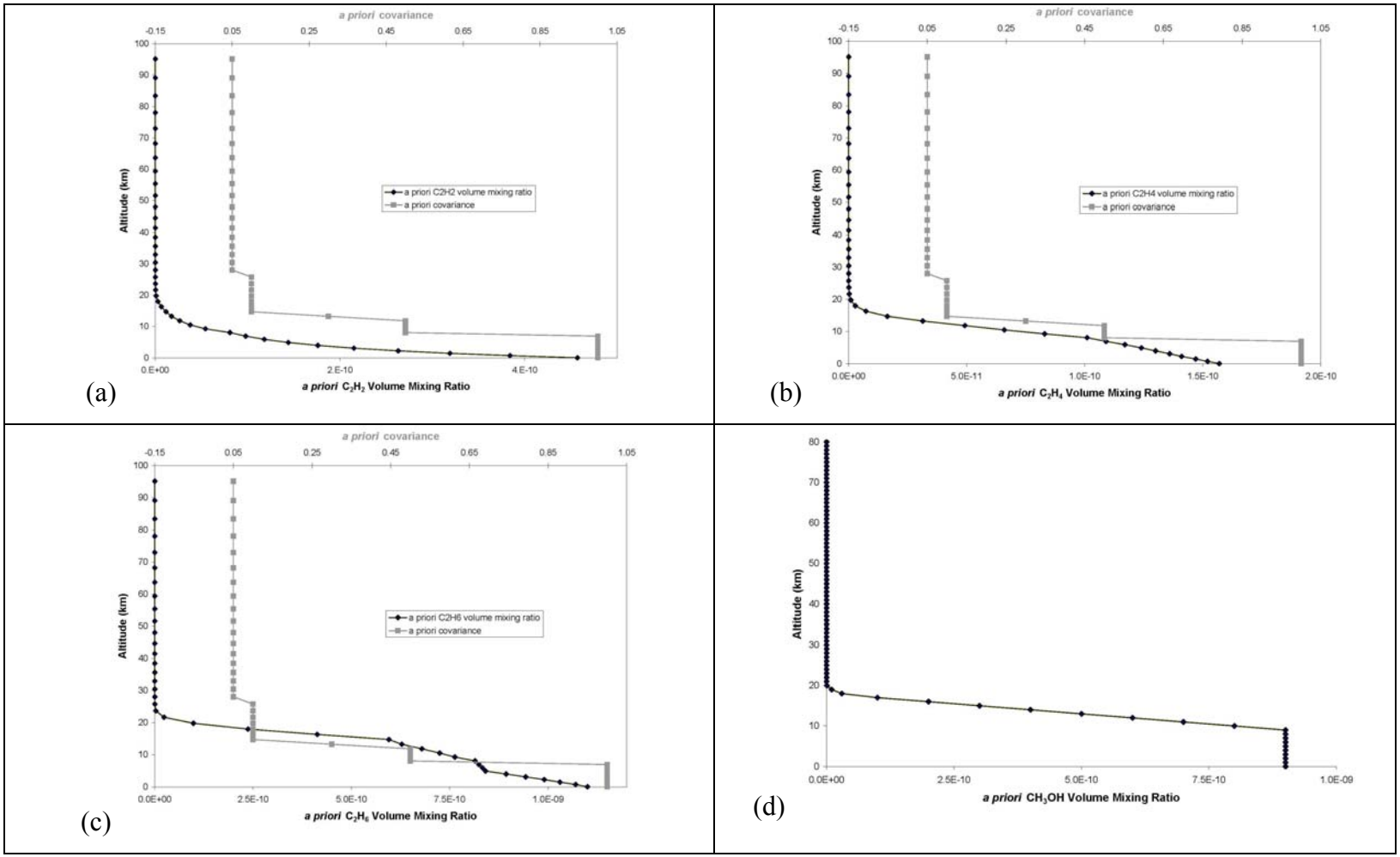

Figure 3-7: *a priori* covariance matrices and VMR profiles used in the retrieval of (a) C_2H_2, (b) C_2H_4 and (c) C_2H_6. Panel (d) shows the initial VMR profile for GFIT analysis of CH_3OH.

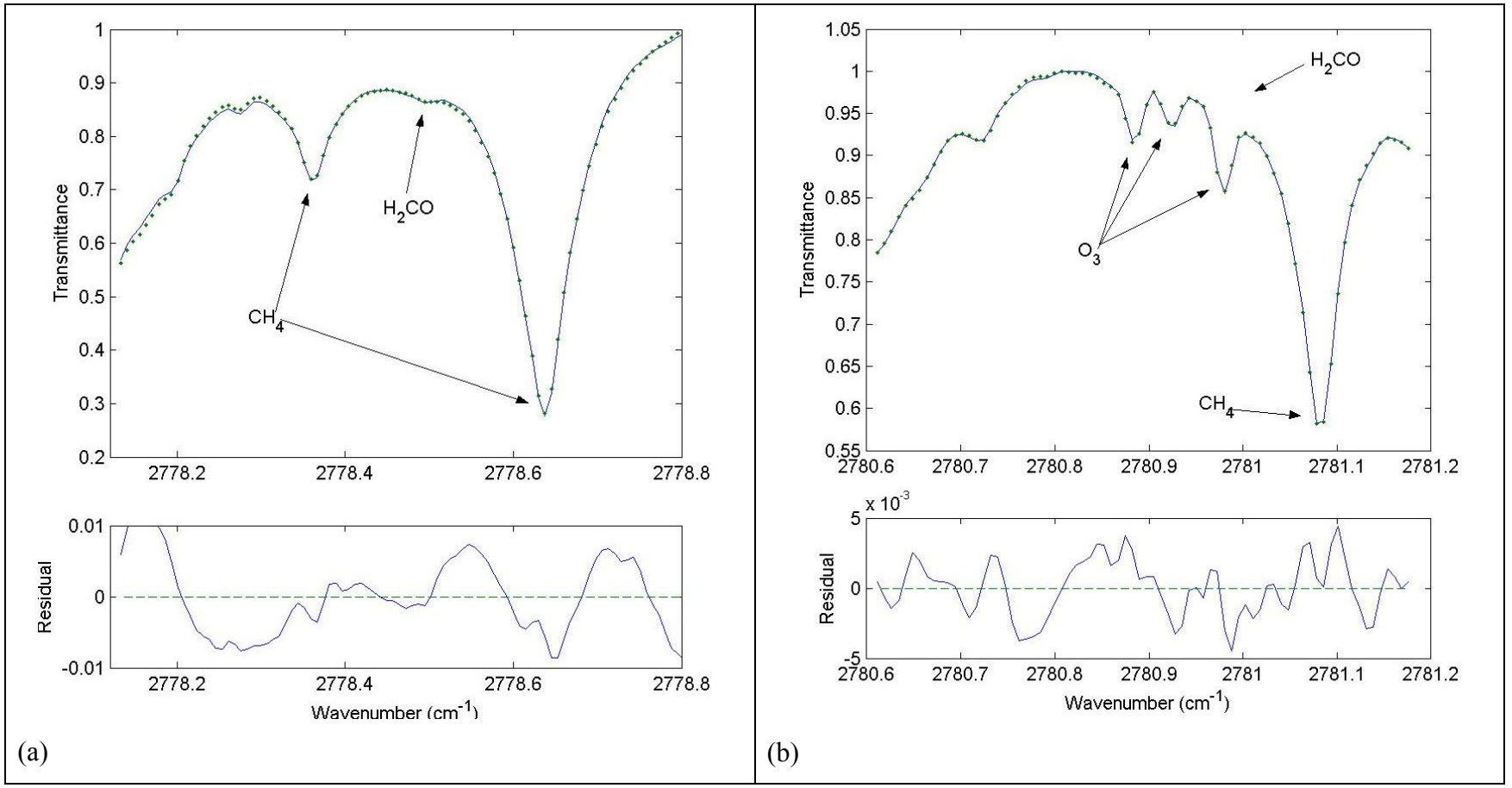

Figure 3-8: Example fits achieved in the SFIT2 retrieval of H_2CO in both microwindows used: (a) 2778.12 – 2778.80cm^{-1} fitting the H_2CO lines around 2778.48 cm^{-1} and (b) 2780.60 – 2781.17cm^{-1} encompassing the manifold of H_2CO lines around 2780.9 cm^{-1}

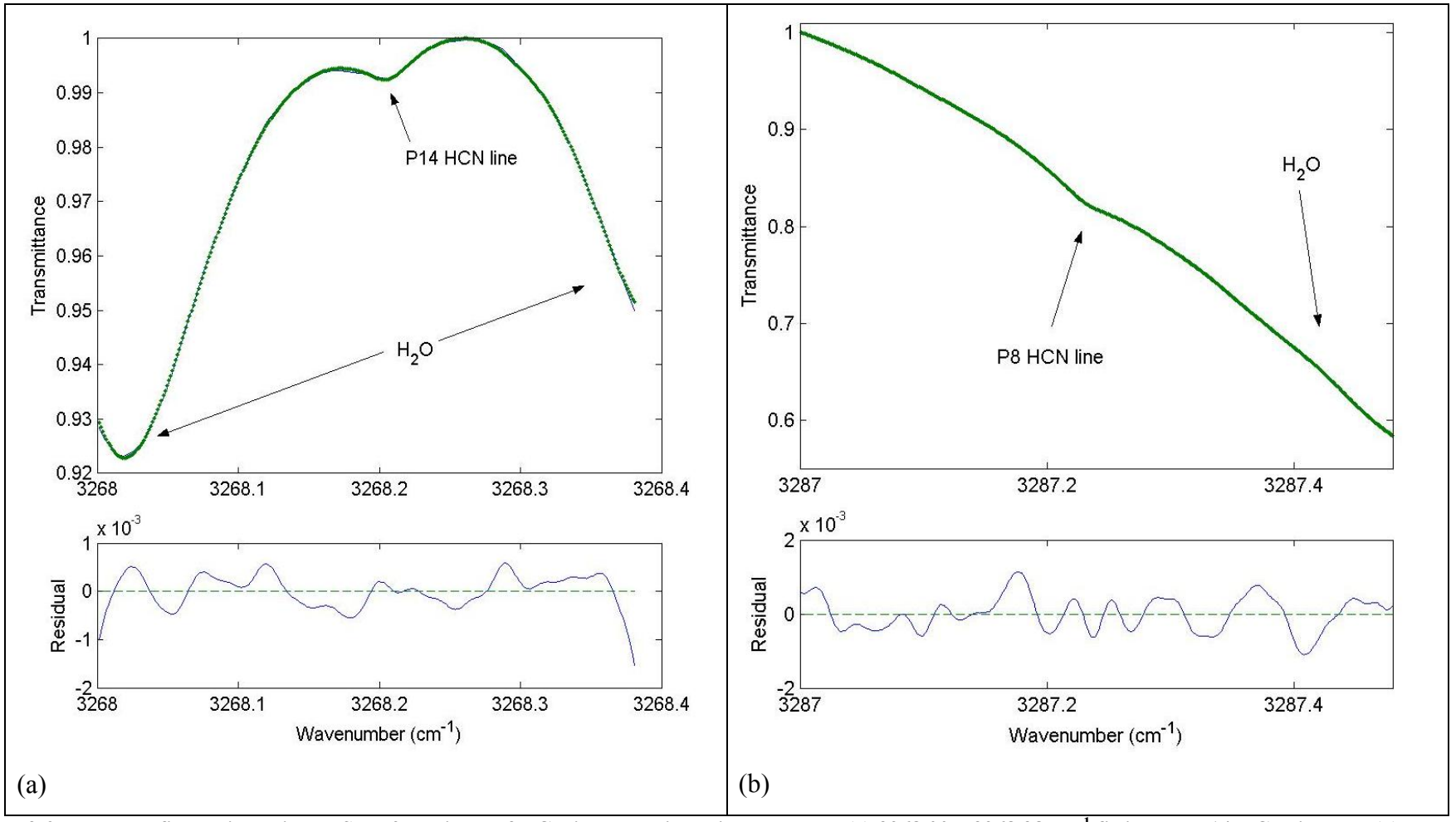

Figure 3-9: Example fits achieved in the SFIT2 retrieval of HCN in both microwindows used: (a) 3268.00 – 3268.38 cm^{-1} fitting the P14 HCN line and (b) 3287.00 – 3287.48 cm^{-1} fitting the P8 HCN line at 3287.25 cm^{-1}.

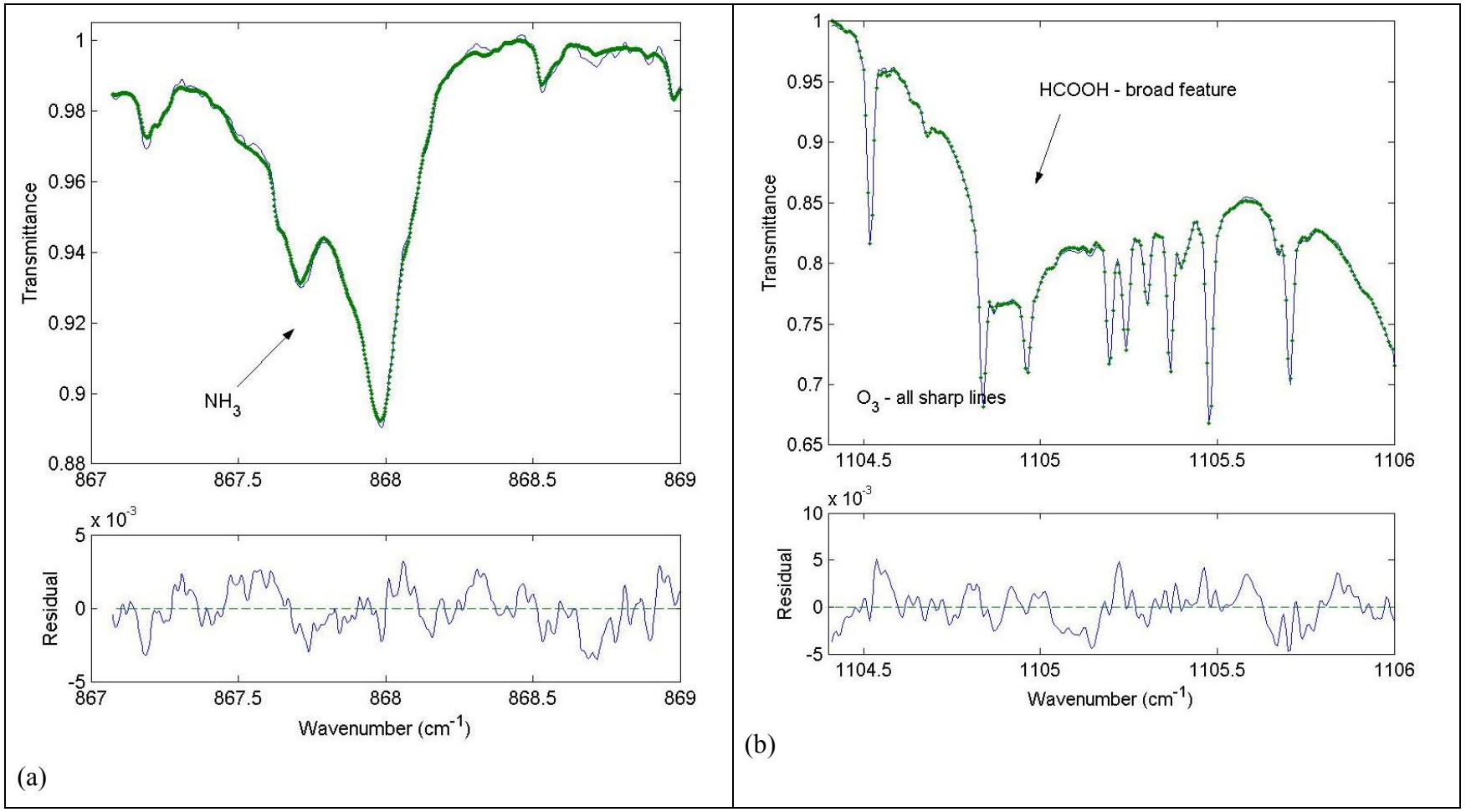

Figure 3-10: Example fits for the SFIT2 retrievals of (a) NH_3 and (b) HCOOH.

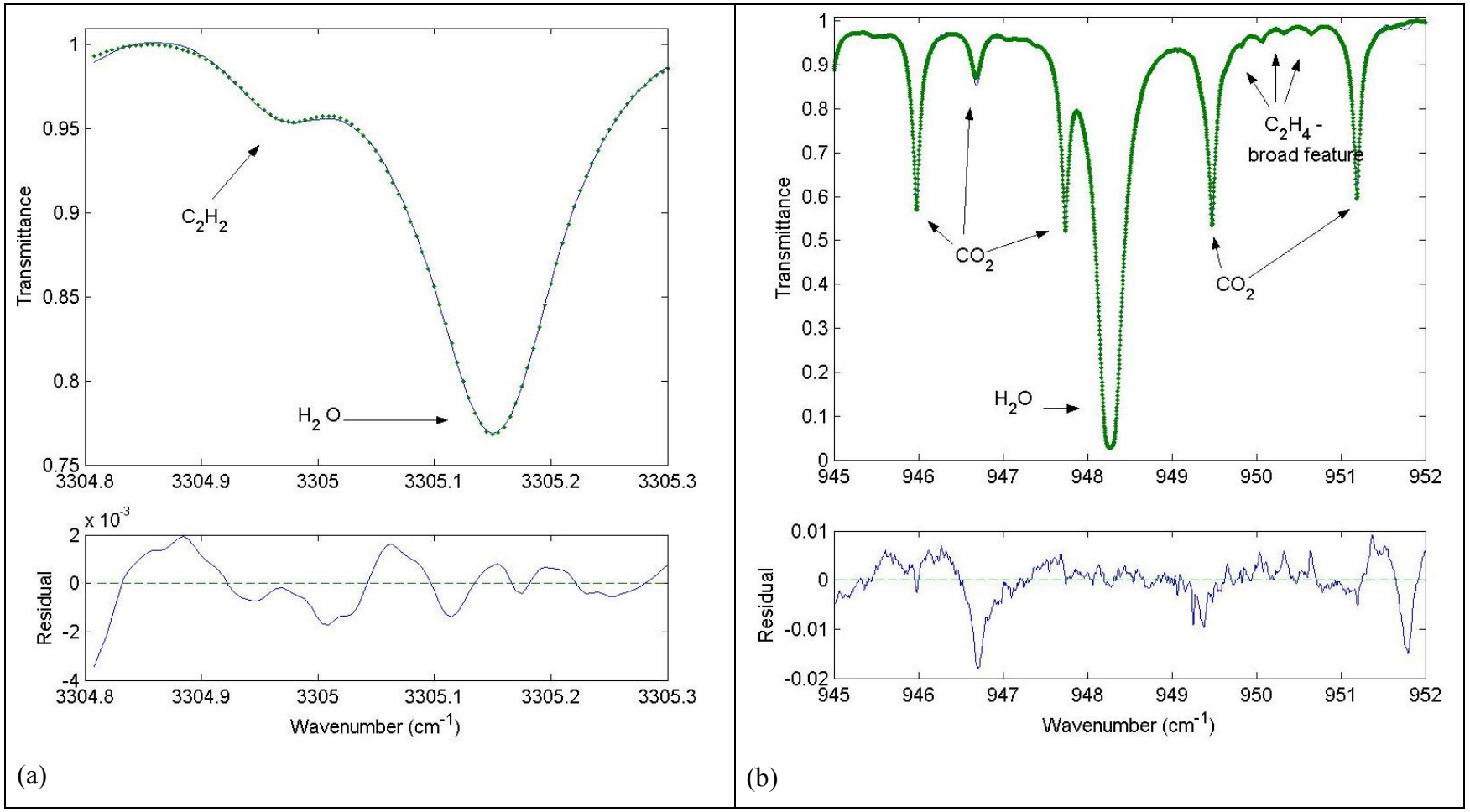

Figure 3-11: Example fits for the SFIT2 retrievals of (a) C_2H_2 and (b) C_2H_4.

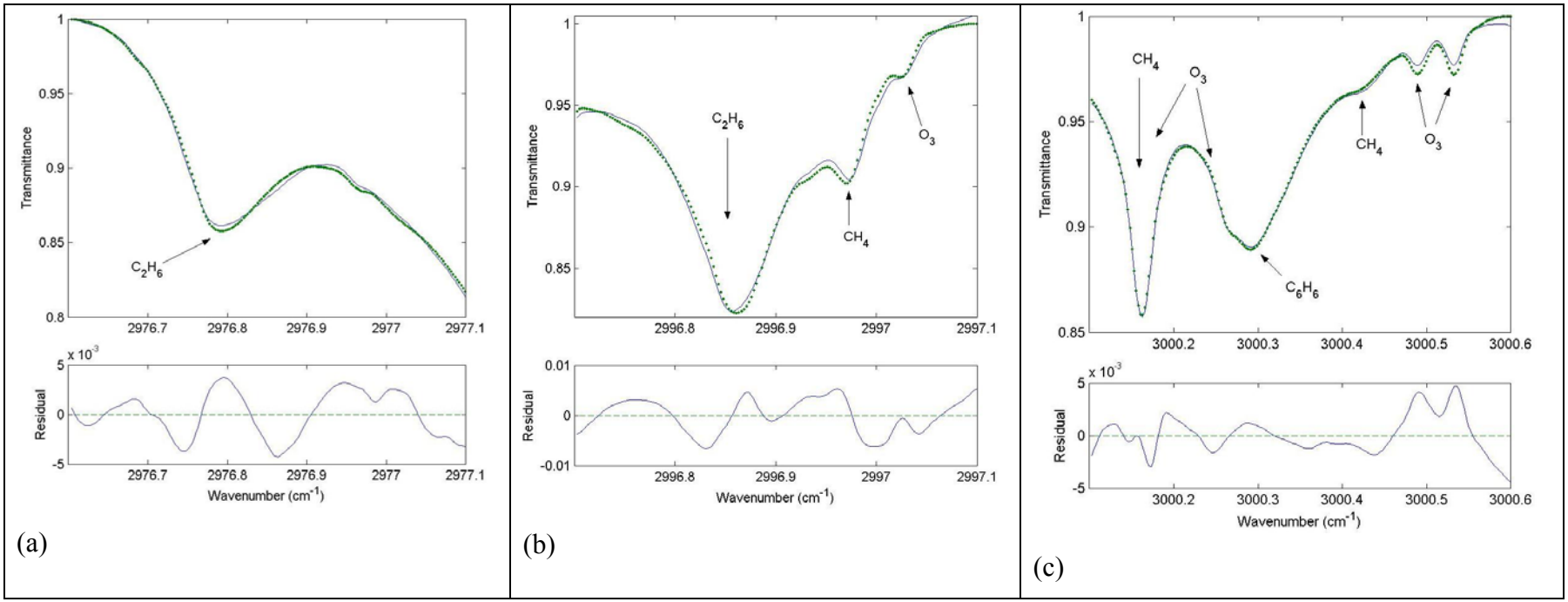

Figure 3-12: Example fits achieved in the SFIT2 retrieval of C_2H_6 in all 3 microwindows used: (a) 2976.60 – 2977.10cm^{-1} (b) 2996.70 – 2997.10cm^{-1} and (c) 3000.10 – 3000.60cm^{-1}.

CH_3OH Amounts derived using GFIT

CH_3OH was not included in the original analyses but column amounts were derived from the same set of spectra at a later date when the HITRAN line parameters became available [*Rothman et al.*, 2005]. At the time that the analysis was undertaken SFIT2 did not have the required auxiliary line parameters (vibrational modes and their temperature dependencies). For this reason GFIT [G. Toon, Jet Propulsion Laboratories - see [*Washenfelder et al.*, 2006b]] was used to determine the vertical column amount of CH_3OH from each spectrum recorded using optical filter 7. The absorption features for CH_3OH are very broad and they coincide with several ozone lines. The stark differences between the clear and smoke affected spectra seen for the other trace gases retrieved are not so obvious to the naked eye for CH_3OH.

Daily NCEP (National Centre for Environmental Prediction) temperature and pressure data were used for a 70 layer model of the atmosphere. Pressure and temperature dependent atmospheric absorption coefficients for each gas in each layer were then calculated line-by-line in the chosen spectral window using the HITRAN04 database [*Rothman et al.*, 2005]. In this study the spectra were analysed for CH_3OH within smoke plumes of unknown altitudes and vertical extent, so the initial mixing ratio profile for CH_3OH was chosen to be 900 parts per trillion (ppt) from the ground to 9 km with the mixing ratio decreasing linearly with altitude to 100 ppt at 17 km and then decreasing rapidly to 0.001 ppt at 23 km and remaining at this value to the top of the atmosphere.

Figure 3-13 shows the simulated absorptions of CH_3OH, carbon dioxide, water, NH_3 and ozone produced by the GFIT algorithm's best fit to an example spectrum for the 1014 cm^{-1} to 1038 cm^{-1} region. The simulations have been offset vertically for clarity.

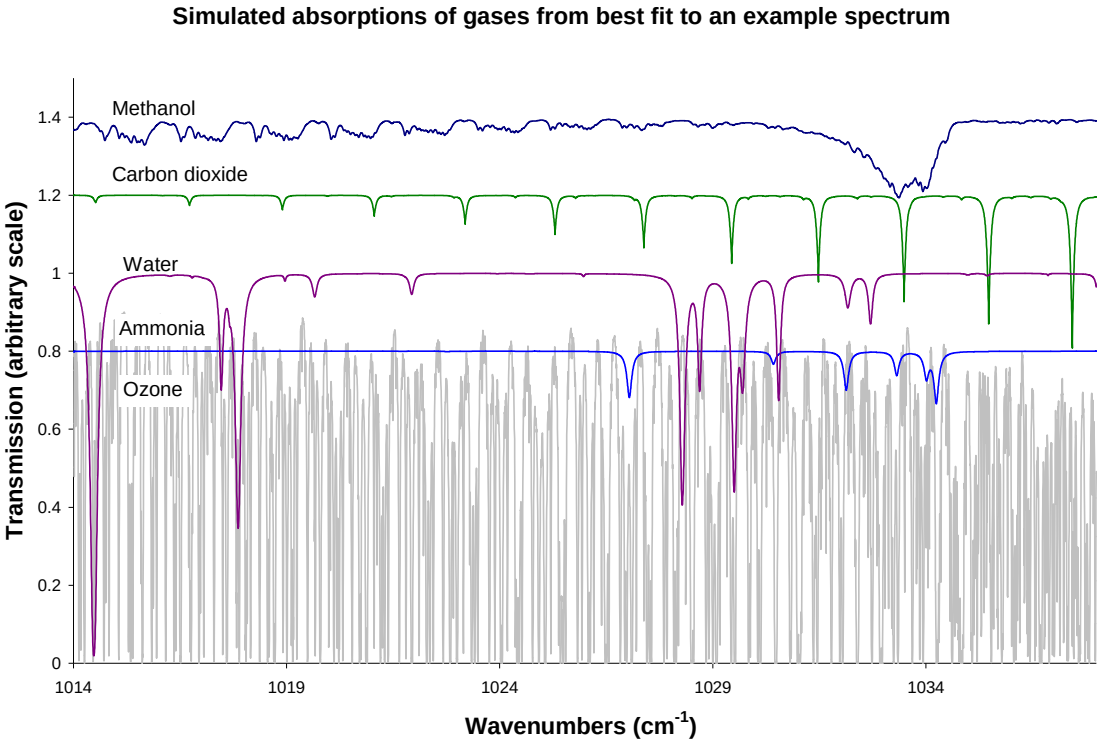

Figure 3-13 Simulated absorptions of methanol, carbon dioxide, water, ammonia and ozone produced by the GFIT algorithm's best fit to an example spectrum for the 1014 cm^{-1} to 1038 cm^{-1} region. The simulations have been offset vertically for clarity.

Figure 3-14 shows two sets of residuals: firstly the residuals from the analysis shown in Figure 3-13, and secondly the residuals from the best fit that resulted when CH_3OH was fixed at assumed background levels in the analysis (and NH_3 was fixed at the enhanced amount found from the original GFIT analysis). Also plotted in Figure 3-14 is a CH_3OH spectrum that has been scaled and offset for comparison. The second set of residuals shown in Figure 3-14 clearly shows the shape of the missing enhanced CH_3OH amounts in the simulation.

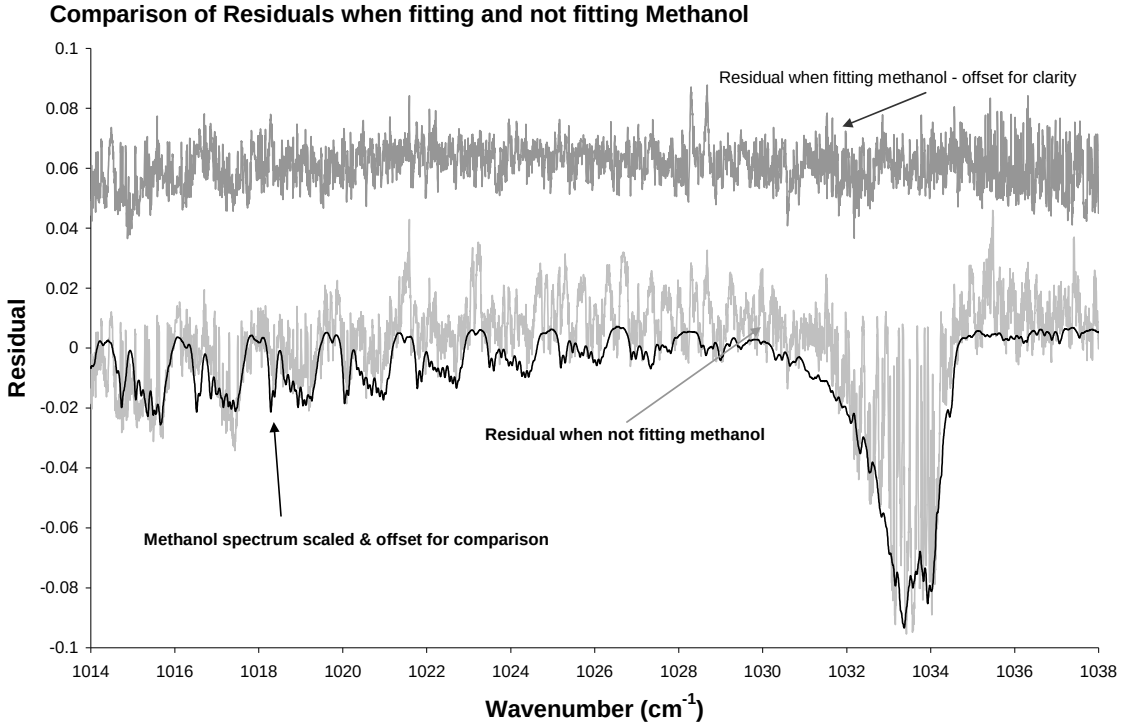

Figure 3-14 Residuals of the best fits that resulted (1) from the analysis described in the text and illustrated in Figure 3-13 and (2) when the methanol was not adjusted in the analysis but left at background levels whilst the NH_3 was fixed at the enhanced amount found from the original GFIT analysis. Also plotted in this figure is a methanol spectrum scaled and offset for comparison.

In GFIT, for each absorbing gas the whole mixing ratio profile is scaled by a single factor and thus no information about the altitude of the absorber is obtained from the spectra. This lack of altitude information results in a large uncertainty in the temperature of the CH_3OH because the smoke plume could be dispersed or it could be located in a narrow altitude region anywhere within the troposphere or in extreme cases even penetrate into the lower stratosphere [*Fromm et al.*, 2006]. Evidence from the retrieval of other gases from these smoke plumes (eg CO) suggests that plumes from the January 2003 fires typically peaked at an altitude of around 4km, whilst many other smoke plumes extended to the ground. The actual vertical distribution differs from day to day and so this uncertainty adds to the imprecision of the dataset as a whole.

Temperature differences of around 80 – 90 K are typical between the ground and the tropopause, and our analysis assumes that CH_3OH mixing ratio is constant across the lowest 9km of the troposphere. This assumption results in an estimated temperature uncertainty of 20 K at one sigma leading to uncertainty in the CH_3OH absorption line

strengths (due to unknown temperatures) and derived column amounts of 4.4%. This is a significant contribution to the uncertainty of the measurements and can manifest itself as a reduction in the precision of the measurements, a systematic bias or a combination of the two. This temperature uncertainty is the dominant uncertainty when the sampled smoke plumes are thick and the concentration of CH_3OH is large. The other main contribution to the precision of the measurements is the signal-to-noise uncertainty. This is the column amount of each trace gas that would produce the equivalent area of absorption feature as the noise in each spectrum. This uncertainty dominates when the smoke is thin and the absorption feature being fitted is weak. The mean value for the analysis was 4.9%. These two components are added in quadrature to give an estimate of the total uncertainty (precision) for each spectrum, with a mean value of 6.7% for all spectra included in the analysis.

3.3 Variability of the Sampled Smoke Plumes Illustrated with Time series of CO Vertical Column Amounts

The data set of smoke affected spectra taken from Wollongong contains some spectra that were recorded through thick smoke plumes that have very large enhancements of all the trace gases associated with biomass burning, (for example spectra taken on 1st January 2002 and 21st and 26th January 2003). There are also many spectra taken through more dissipated smoke plumes with much lower enhancements of trace gases. This can be illustrated by looking at the time series of CO column amounts. This shows great variability with more than an order of magnitude between the largest and smallest total column amounts of CO. Significant variability is also shown within days as well as from day to day as the thickness of smoke plumes overhead varies. The complete time series of derived total column amounts of CO from the smoke affected spectra are plotted in two separate time series in Figure 3-15 and Figure 3-16. Figure 3-15 shows the vertical column amounts of CO derived from spectra recorded on 9 days between December 24th 2001 and January 4th 2002 that sampled the large fires around Sydney and other parts of New South Wales that were burning at this time. The largest enhancements are seen on 1st January 2002 when there were fires burning within a few

kilometres of the observation site at the University of Wollongong and eye-witnesses reported thick smoke at ground level.

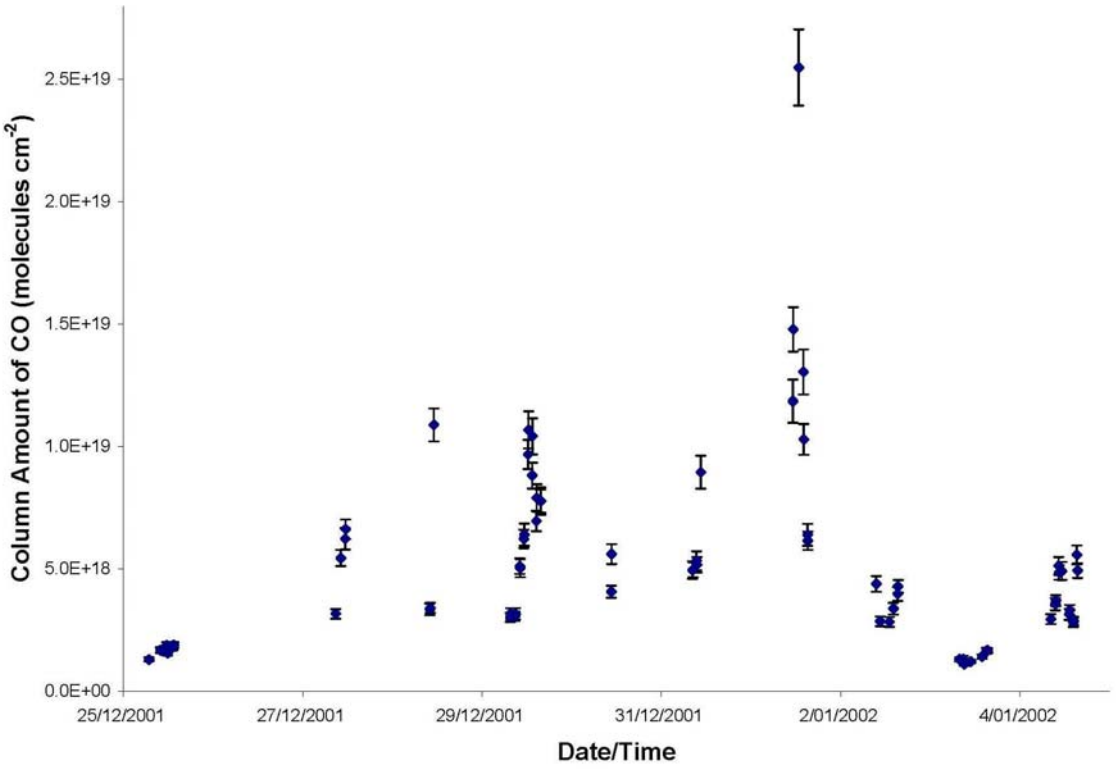

Figure 3-15: Time series of CO column amounts from December 2001 to January 2002.

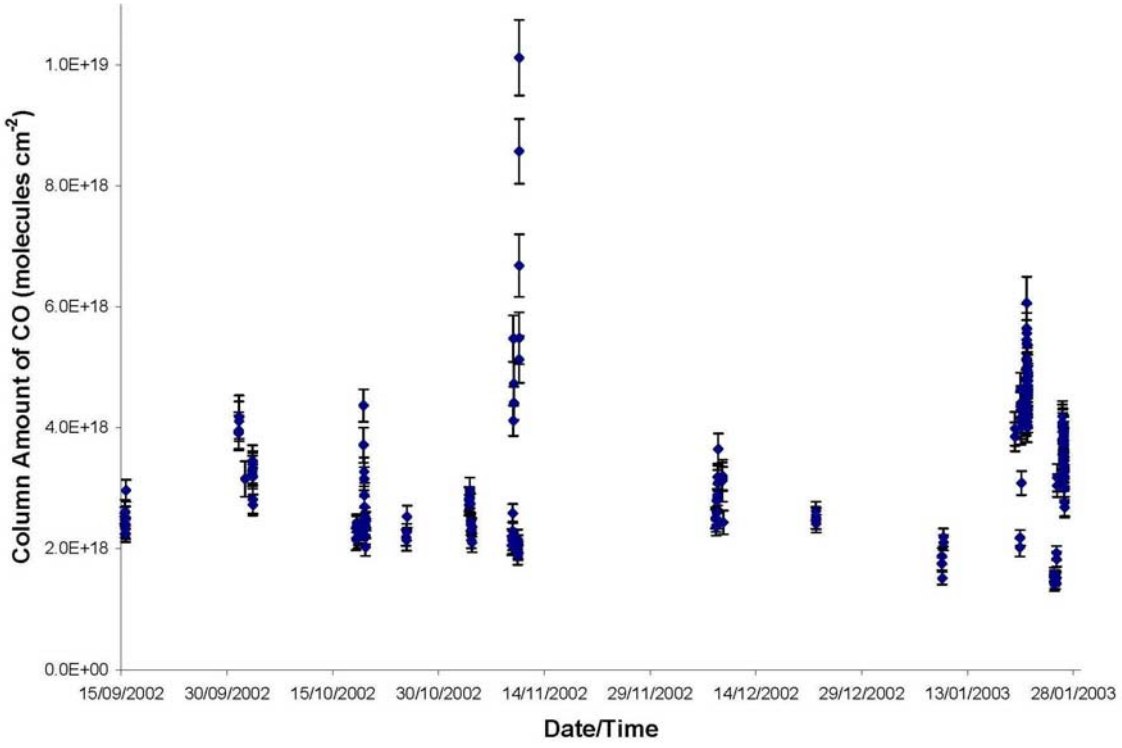

Figure 3-16 Time series of CO column amounts from September 2002 to January 2003.

Figure 3-16 shows CO total column amounts derived from spectra taken through smoke plumes sampled on 20 days between September 2002 and January 2003 including plumes from the Canberra fires of January 2003. The largest enhancements are seen on the 9th and 10th of November but the CO columns are very variable on these days. In contrast smoke plumes sampled late in January 2003 from the Canberra fires are relatively consistent as illustrated for January 21st 2003 in Figure 3-17 and for January 26th 2003 in Figure 3-18. Note that the measurements are made using seven filters in rotation and CO is derived from both filters 4 and 5 and so the data appears in pairs of data points separated by slightly larger gaps as filters 1,2,3, 7 and 8 are sampled.

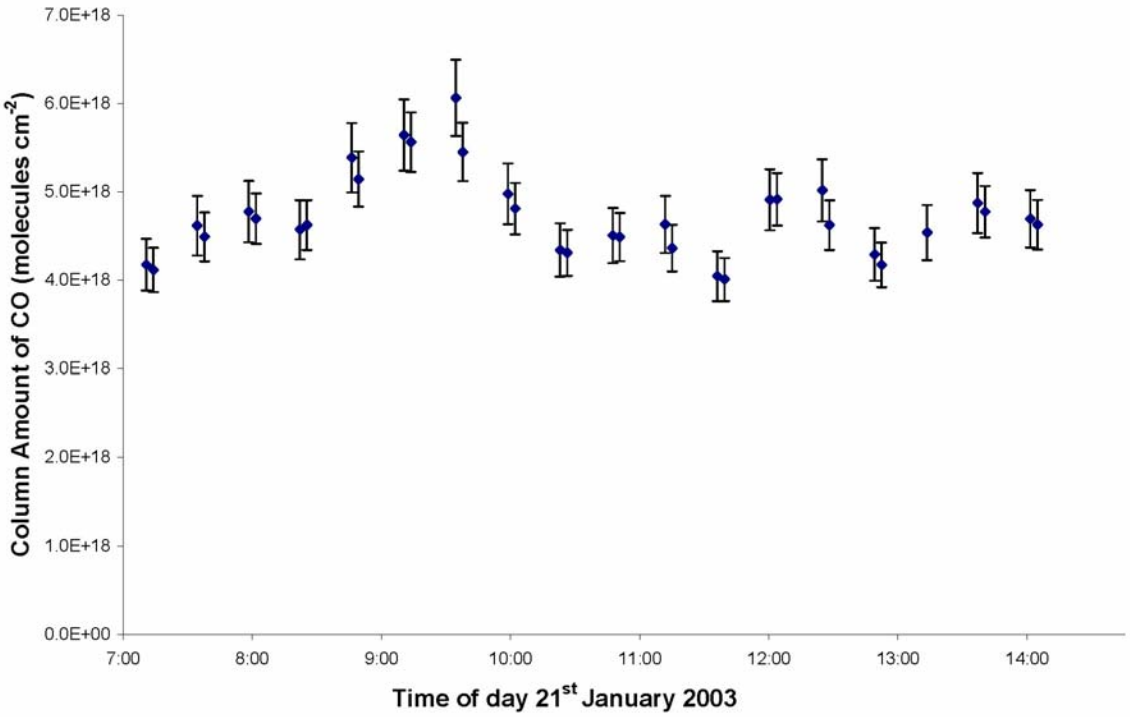

Figure 3-17: Time series of CO column amounts from January 21st 2003.

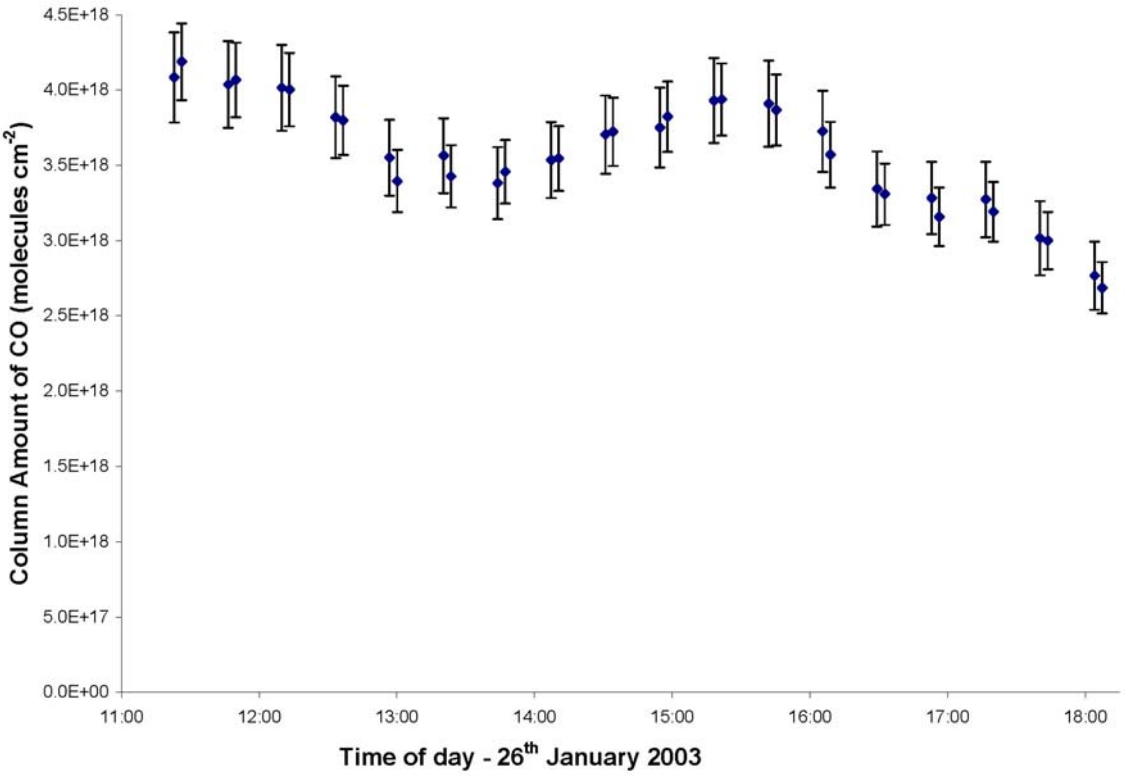

Figure 3-18: Time series of CO column amounts from January 26th 2003.

3.4 Correlation between AOD and Trace Gases in Smoke Plumes from Southeast Australian Forest Fires

Whilst the infrared spectra described above were being recorded, simultaneous and co-located spectral irradiance measurements were made using the Ocean Optics OD2000 grating spectrometers (see section 2.4, Figure 2-7). These measurements determine the AOD of the atmosphere at 500 nm at 30 second intervals. The relevant measurements are averaged to give the AOD of the atmosphere during the time that each infrared spectrum was recorded. The duration of the infrared spectra varied from approximately 2 minutes to approximately 10 minutes depending upon the resolution and number of scans used.

Figure 3-19 shows vertical column amounts of CO that were derived from the spectra taken through smoke plumes plotted against the simultaneous, co-located measurements of AOD. The error-bars shown in column amounts of CO represent the one-sigma precision of the measurements, which includes all of the uncertainties listed in Table 3-1 and illustrates the scatter expected from the measurement repeatability. The error-bars shown in the AOD measurements combine an uncertainty from the calibration with the one-sigma standard deviation of the measurements of AOD throughout the time of collection of each infrared spectrum. The latter includes both the real variation in AOD (due to varying amounts of smoke) and measurement noise. The data have been colour coded to distinguish different time periods. A star symbol indicates the two spectra that were recorded just before the arrival of a distinctive, thick smoke plume on January 1st 2002. Figure 3-19 shows a strong correlation between column CO and AOD that is quite consistent for 269 independent spectra from many varied forest fire episodes over all the different time periods, with the exception of some of the spectra recorded on January 1st 2002.

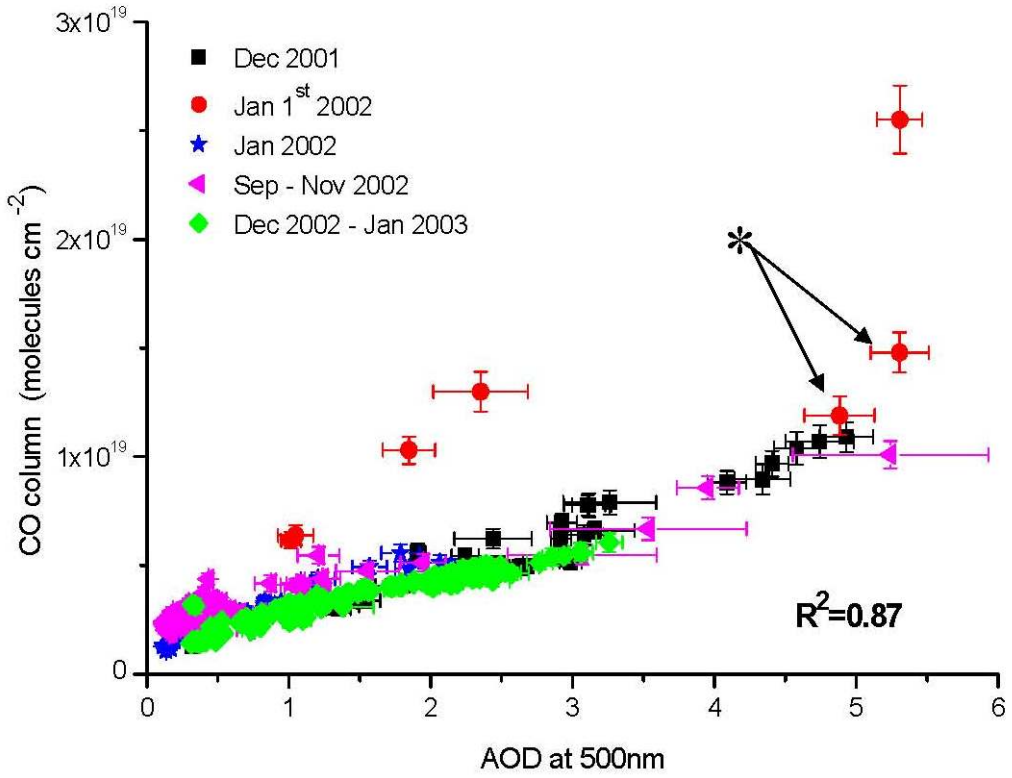

Figure 3-19 Vertical column amounts of CO derived from smoke affected spectra plotted against coincident measurements of AOD. The * symbol indicates the two spectra that were recorded just before the arrival of a distinctive, thick smoke plume on January 1st 2002. Typical smoke-free values are less than 0.1 for AOD and 1.6 ± 0.5 x10^{18} for CO column. A generalised least squares linear regression excluding data from January 1st 2002 gave an R^2 value of 0.87.

It is clear that the spectra recorded after the arrival of the thick smoke plume on January 1st 2002 are outliers in this dataset and this is discussed in more detail below. A generalised least squares linear regression that takes into consideration uncertainties in both the x-axis and the y-axis was performed on the dataset excluding all spectra from January 1st 2002. This gave a value of 0.87 for the square of the correlation coefficient ($R^2 = 0.87$) and the following equation relating CO and AOD:

Equation 3-1 : $$CO = \left((1.5 \pm 0.1)AOD + (1.5 \pm 0.1)\right)x10^{18} \text{ molecules.cm}^{-2}$$

There is some indication that the linear relation between CO column and AOD may not hold at very large values of AOD. This might reflect a true breakdown of the correlation or it could be an artefact of the measurements. There is some uncertainty in the estimated "dark current" – i.e. the signal produced when no light falls on the

detector. In most instances this uncertainty is insignificant but at very high values of AOD the grating spectrometer is detecting very low levels of light and the extra uncertainty may be significant. This additional uncertainty in the AOD measurements is difficult to quantify and has not been included in the error bars shown in Figure 3-19.

The correlation between the other trace gases derived from the smoke affected spectra and coincident measurements of AOD are shown in Figure 3-20 through Figure 3-23. Again the data from the 1st January 2002 appear erroneous and were excluded before the regression analysis was undertaken and the correlation coefficients found. The strongest correlations are seen for CH_3OH, CO, C_2H_6 and H_2CO followed by HCN, C_2H_2, C_2H_4, NH_3 and HCOOH. The weaker correlations for NH_3 and HCOOH result from a combination of shorter atmospheric lifetimes and larger measurement uncertainties.

The correlations of all the trace gases with AOD were determined using generalised least squares orthogonal distance regression analysis using the software tool from the website (http://www.eurometros.org/ Distributions: "xgenline"). These correlations are summarised in Table 3-2 which gives the number of spectra that yielded successful retrievals, the square of the correlation coefficient (R^2) and the gradient and the intercept derived from the regression analysis along with the 1σ uncertainties in both gradient and intercept. It is important to note that the uncertainty in the regression analysis is an under-estimate of the true uncertainty because it (wrongly) assumes that the uncertainties are uncorrelated. Also there are significant other systematic uncertainties in the forward model that will contribute to the accuracy of these equations such as the uncertainties in the HITRAN line parameters used.

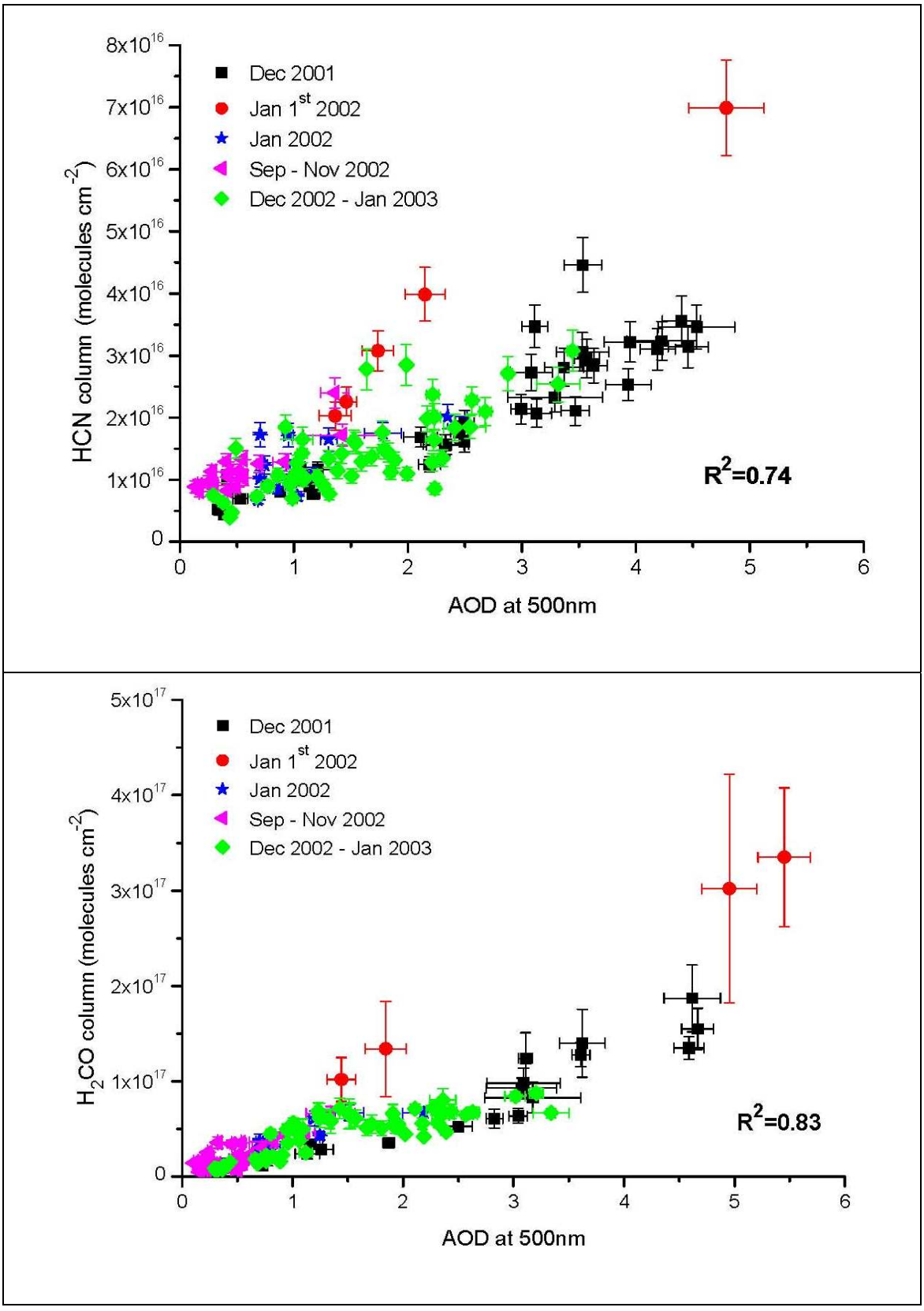

Figure 3-20: Vertical column amounts of HCN (upper panel) and H_2CO (lower panel) derived from smoke affected spectra plotted against coincident measurements of AOD at 500nm.

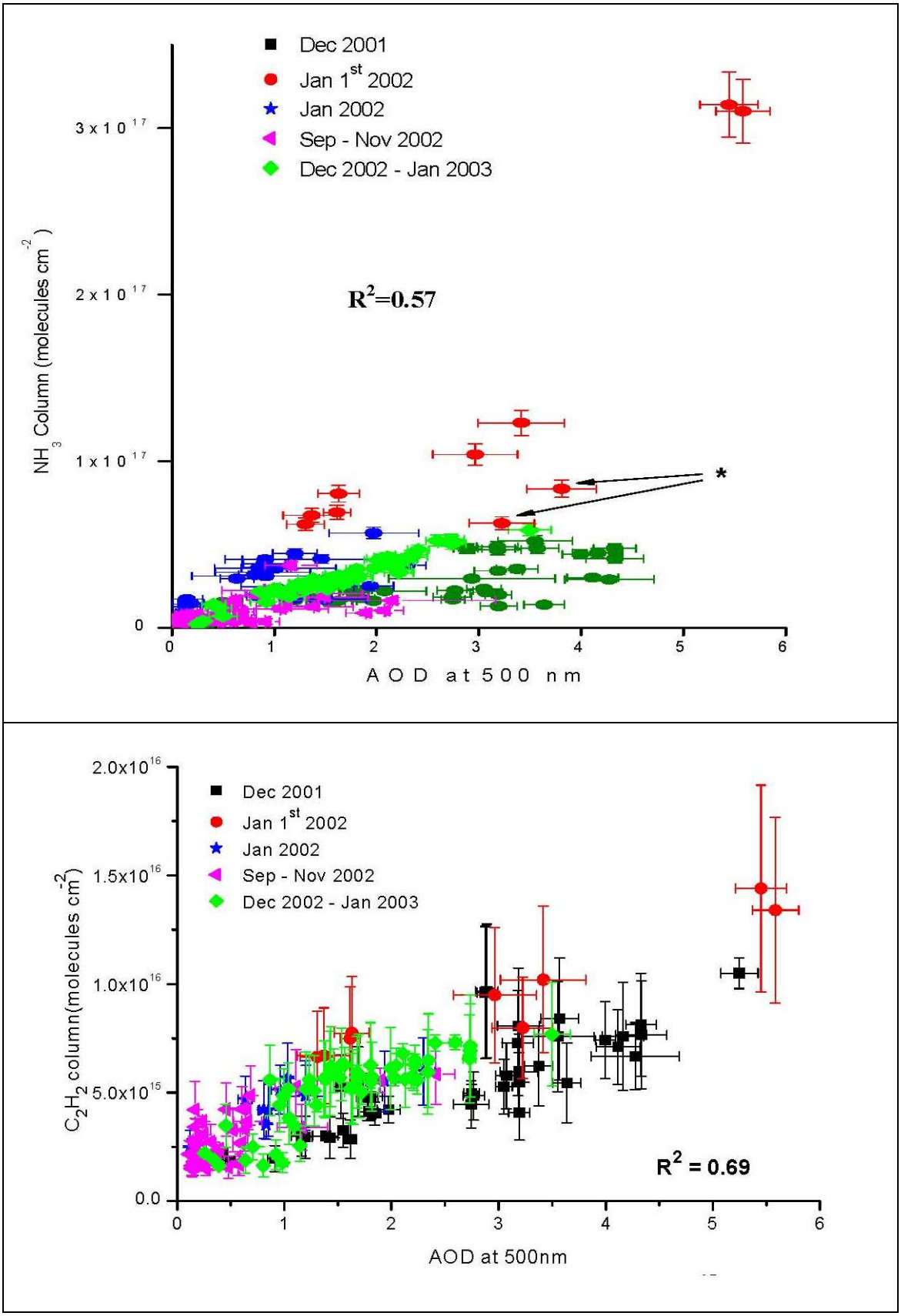

Figure 3-21: Vertical column amounts of NH_3 (upper panel) and C_2H_2 (lower panel) derived from smoke affected spectra plotted against coincident measurements of AOD at 500nm. The * symbol indicates the two spectra that were recorded just before the arrival of a distinctive, thick smoke plume on January 1st 2002.

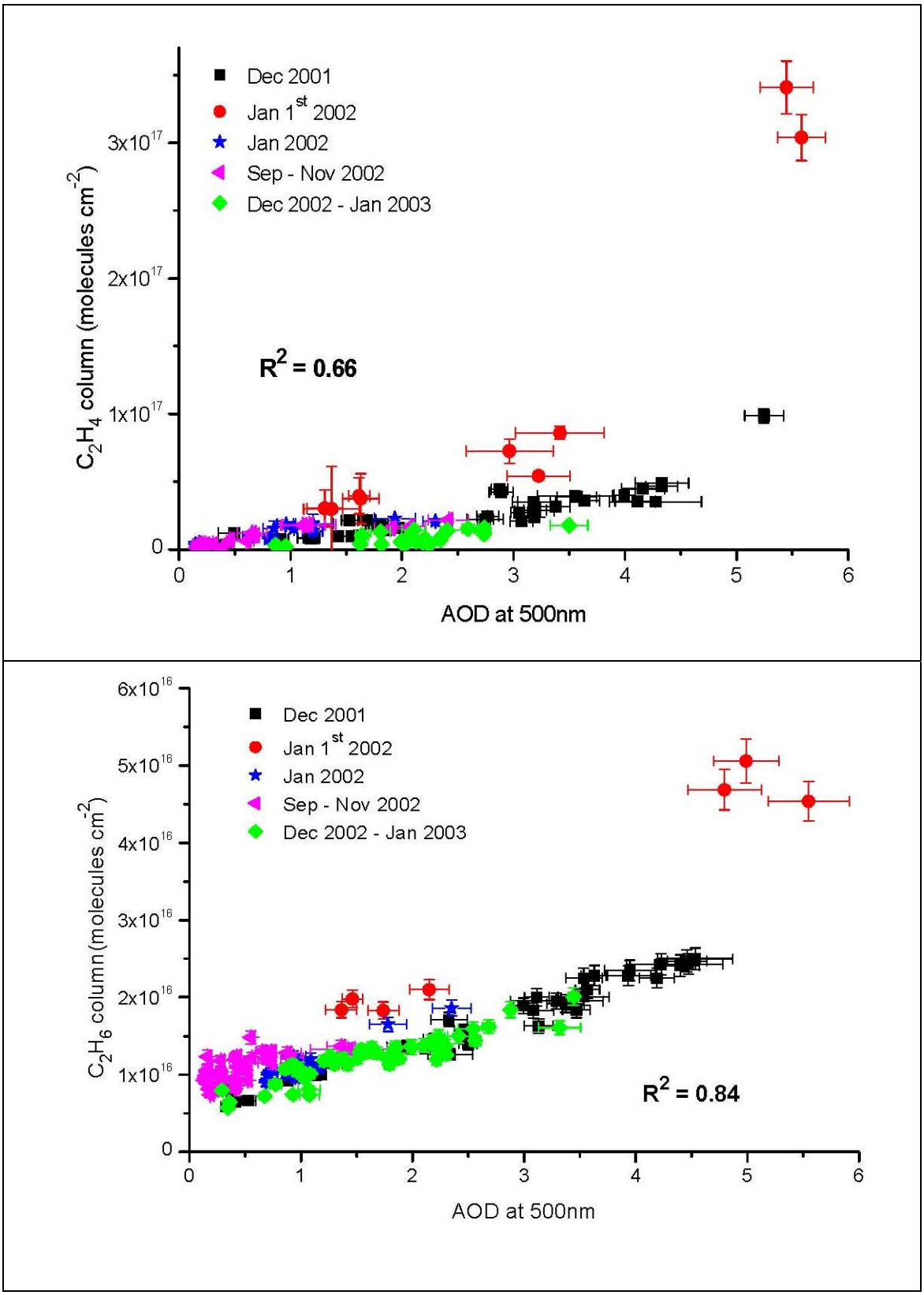

Figure 3-22: Vertical column amounts of C_2H_4 (upper panel) and C_2H_6 (lower panel) derived from smoke affected spectra plotted against coincident measurements of AOD at 500nm.

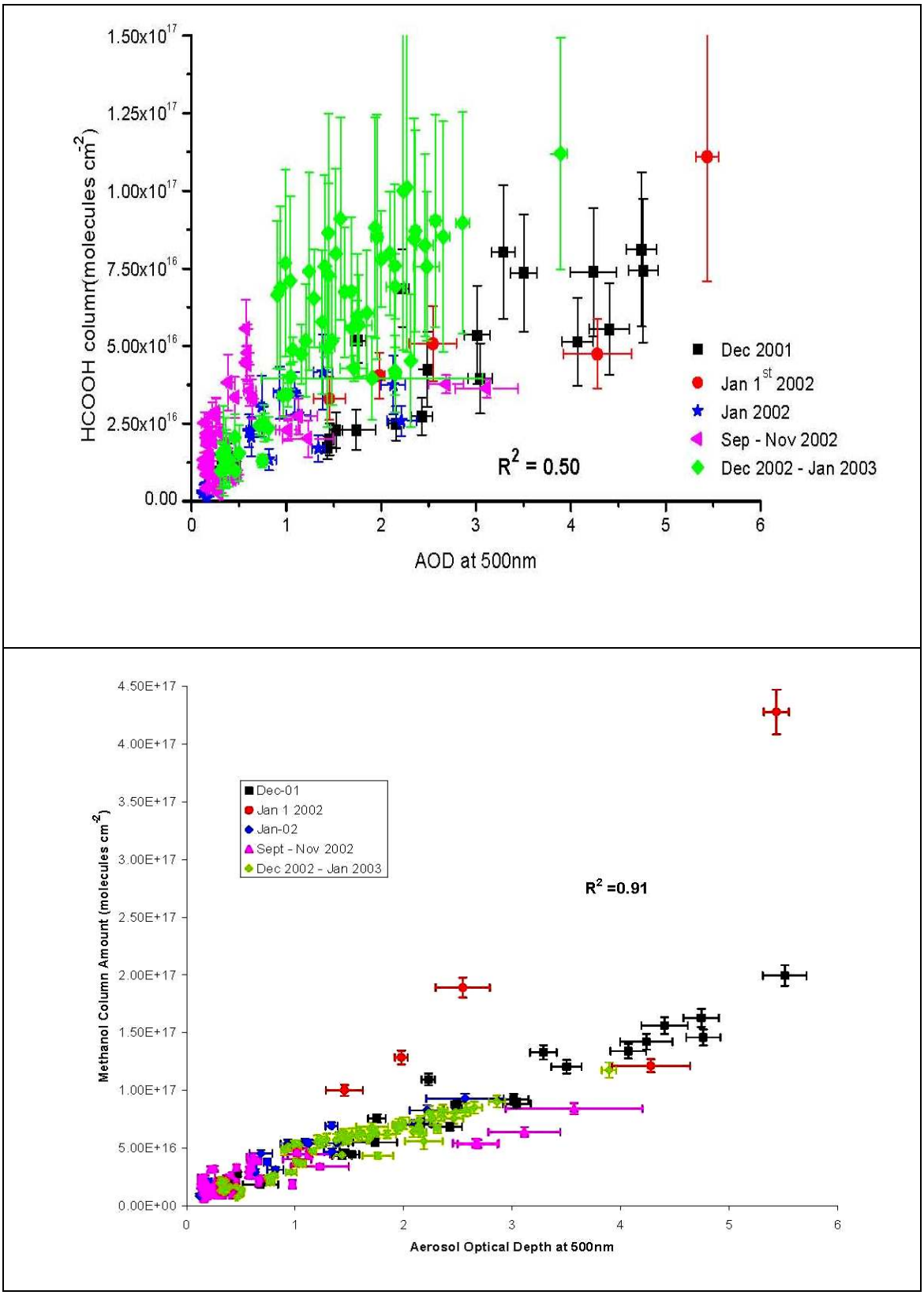

Figure 3-23: Vertical column amounts of HCOOH (upper panel) and CH_3OH (lower panel) derived from smoke affected spectra plotted against coincident measurements of AOD at 500nm.

Table 3-2 : The results of generalised least squares regression analysis on the column amounts of each trace gas and the coincident AOD measurements. The number of spectra and R^2 values are given, along with the gradient and intercept of the best fit linear relationship between trace gas amounts and AOD for each gas along with their 1σ uncertainties.

Trace Gas	No. of Spectra	R^2	Gradient (molecules cm^{-2})	Intercept (molecules cm^{-2})
CO	269	0.87	$(1.5 \pm 0.1) \times 10^{18}$	$(1.5 \pm 0.1) \times 10^{18}$
HCN	122	0.74	$(5.3 \pm 0.2) \times 10^{15}$	$(4.8 \pm 0.2) \times 10^{15}$
NH_3	183	0.57	$(1.1 \pm 0.1) \times 10^{16}$	$(0.8 \pm 0.2) \times 10^{16}$
H_2CO	122	0.83	$(2.5 \pm 0.1) \times 10^{16}$	$(0.1 \pm 0.1)] \times 10^{16}$
C_2H_2	129	0.69	$(3.5 \pm 0.1) \times 10^{15}$	$(3.9 \pm 0.1) \times 10^{15}$
C_2H_4	102	0.66	$(9.8 \pm 0.8) \times 10^{15}$	$-(1.9 \pm 1.7) \times 10^{15}$
C_2H_6	145	0.84	$(3.4 \pm 0.1) \times 10^{15}$	$(7.2 \pm 0.1) \times 10^{15}$
HCOOH	150	0.50	$(2.1 \pm 0.1) \times 10^{16}$	$(0.1 \pm 0.1) \times 10^{16}$
CH_3OH	198	0.91	$(2.9 \pm 0.1) \times 10^{16}$	$(0.7 \pm 0.1) \times 10^{16}$

3.5 January 1st 2002

The correlations between the trace gases and AOD, evident from Figure 3-19 through Figure 3-23 are consistent for hundreds of independent spectra from many different fire episodes over all the different time-periods sampled with the exception of some of the spectra recorded on January 1, 2002. On the morning of January 1, 2002 there was thick ground level smoke and one spectrum was recorded using the optical filters which transmitted in the regions used to derive C_2H_4, NH_3, HCOOH and both of the regions used to derive CO, before the arrival of an exceptionally thick smoke plume was noted. An eye-witness (Arndt Meier) reported that the sun looked a dull red viewed through this plume and that there was a strong smell of smoke at ground-level. After the arrival of this plume most of the trace gas-to-AOD plots show exceptional behaviour, with much higher trace gas to AOD ratios.

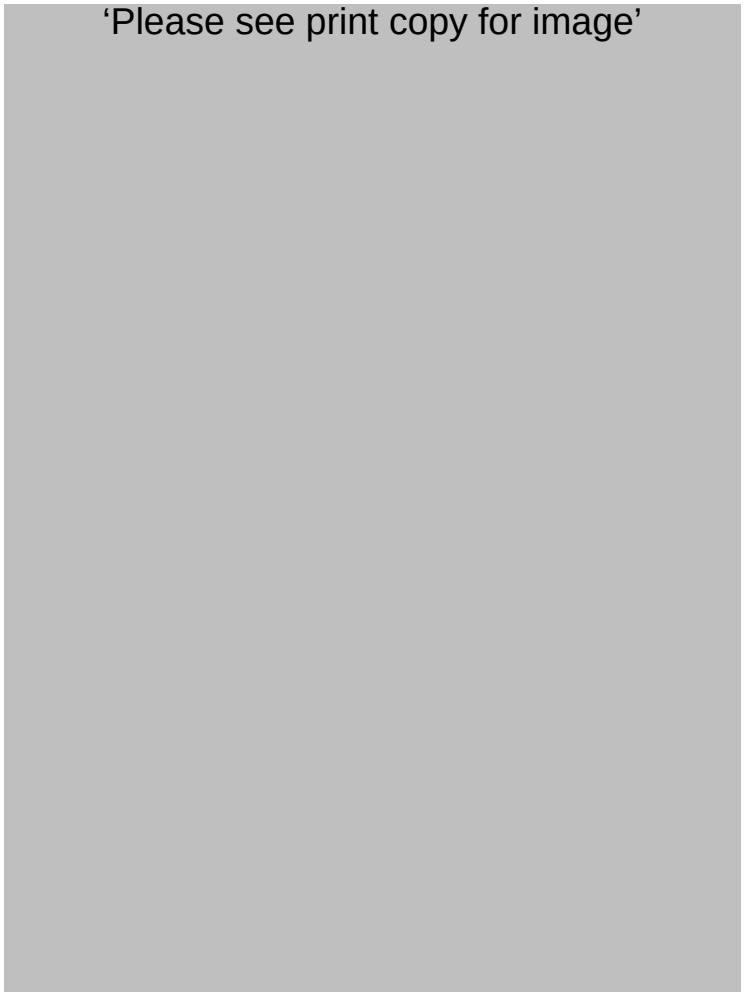

Figure 3-24: MODIS true colour image of South Eastern Australia on January 1st 2002. The red spots show MODIS hotspots – where a thermal anomaly has been detected. Image courtesy of MODIS Rapid Response Project at NASA/GSFC.

A possible explanation for this anomalous data is that the smoke plume sampled on January 1, 2002 was from one of the fires burning very near (< 5km) the measurement site (see Figure 3-24) and the aerosols had not yet coalesced into a comparably stable form, resulting in a lower AOD value than older smoke. This theory is supported by back trajectory analysis (see Figure 3-25) that indicates that air parcels passed over the region where the fires were located within half an hour or less of reaching Wollongong.

Figure 3-25: Back trajectories showing projected origin and age of parcels of air arriving over Wollongong at different pressure levels: 950 hPa (pink), 750 hPa (red), 550 hPa (green) and 350 hPa (light blue). The crosses are half hour intervals back in time from noon on the 1st of January 2002. The back trajectories were generated by the European Centre for Medium-Range Weather Forecasts, (ECMWF) Trajectories, via the British Atmospheric Data Centre, 2006-, 2008. Available from http://badc.nerc.ac.uk/data/ecmwf-trj/ .

3.7 Emission ratios of trace gases using AOD as a proxy for CO

Trace gas concentrations within smoke plumes can vary rapidly with time, so the concentration levels are usually converted to relative emission ratios by dividing by coincident measurements of CO or CO_2 [*Hurst et al.*, 1994a]. CO is used as a reference gas in this case, because the excess levels of CO_2 present in smoke are difficult to measure with sufficient accuracy against its large and variable background total column

amount. In this study we have no coincident measurements of CO with the other trace gases because the column amounts are derived from spectra recorded at different times using different optical filters. Depending on filter combinations, the difference in times between various tracers and CO could be between 10 and 30 minutes. Instead we have calculated molar emission ratios with respect to CO using AOD as a *de-facto* measurement of the CO column via the regression analyses results given in Table 3-2.

First, all data with AOD less than 1.0 were excluded because of the large uncertainties introduced when taking the ratio of two small numbers. For the remaining spectra, we calculated emission ratios by dividing the excess amount of the trace gas over background levels by the excess amount of CO over background levels, (taken from measurement of CO column amounts). The choice of background AOD is not critical for this analysis as it is very low. We have chosen a background optical depth of 0.03[9], based on analysis of earlier measurements at Wollongong [*Phillips*, 2001] and the long-term AOD record observed at Cape Grim [*Wilson and Forgan*, 2002]. The background values for CO and the other tracers were obtained from the regression plots with respect to AOD (see Table 3-2) using a background value for AOD over Wollongong of 0.03 [*Phillips*, 2001]. The resulting emission ratios are given in Table 3-3.

3.8 Emission Factors Extrapolated from Emission Ratios to CO

A parameter frequently used to characterise emissions from fires is the emission factor, which is defined as the amount of a compound released per amount of dry matter consumed, expressed in units of grams per kilogram (g kg^{-1}). To convert our data from emission ratios with respect to CO to emission factors, we use Equation 1-4.

The emission ratios from this study have been converted to emission factors using the mean emission factor for CO, (EF_{CO}) for extra-tropical forests of 107 ± 37 g kg^{-1} (personal communication, M.O. Andreae, 2005, being an update of previous estimates [*Andreae and Merlet*, 2001]). These emission factors are given in Table 3-3

[9] There are two threshold values for AOD as well as a background AOD value. Only spectra that were taken when AOD values were significantly enhanced over usual values (> 0.1) were analysed for total column amounts. Only spectra that were taken when AOD values exceeded 1.0 were used to determine emission ratios. Background AOD at Wollongong is estimated to be 0.03.

alongside the mean emission factor of each trace gas from extra-tropical forest measurements taken from *Andreae and Merlet* [2001].

The emission factors calculated for Australian temperate forest fires in this study for C_2H_2, HCOOH and H_2CO agree well with the average for all extra-tropical forests, while those for C_2H_4 and NH_3 are comparatively low, but lie within one-sigma uncertainty levels. Most of the measurements in this study occur many kilometres downwind of the fires and so shorter-lived species such as NH_3 may yield lower than the expected emission ratios with respect to CO. The age of smoke sampled in this dataset varies between different time periods and this contributes to the variability of the shorter-lived species. Only the results for the emission factors of HCN and C_2H_6 show significant departure from the values quoted by *Andreae and Merlet* [2001]. In the case of HCN the *Andreae and Merlet* [2001] value is questionable because it is a "best guess", (based on an extrapolation from measurements made from savanna and grassland fires), whilst our value for HCN of (0.43 ± 0.22) g kg^{-1} is in better agreement with airborne FTIR measurements through smoke plumes from Alaskan forest fires of 0.61 g kg^{-1} [*Goode et al.*, 2000]. For C_2H_6, the measurement uncertainties in this study are low; the expected atmospheric lifetimes of CO and C_2H_6 are similar [*Trentmann et al.*, 2003] and hence the emission ratio with respect to CO is very consistent throughout the measurements from many different fire episodes. Previously reported emission ratios for C_2H_6 from Northern Australian savanna fires by *Shirai et al* [2003b] are consistent with those reported here but lower than those reported by *Hurst et al* [1994b]. The high range data of *Hurst et al* [1994b] used a limited number of grab samples that may not have been well mixed enough to provide a truly representative sample. It can be concluded that relatively low emission of C_2H_6 is a characteristic of Australian temperate forest fires where the fuel source is predominantly varieties of eucalyptus trees.

Table 3-3: Emission factors calculated in this study alongside emission factors from [Andreae and Merlet, 2001]

Trace Gas	No.of Spectra	Emission Ratio to CO (mol/mol) ± 1σ standard deviation	Emission Factor (this study) g kg^{-1} DM	Emission Factor (Andreae & Merlet) g kg^{-1} DM
C_2H_4	77	0.0057 ± 0.0027	0.61 ± 0.36	1.2 ± 0.5
NH_3	68	0.0095 ± 0.0035	0.62 ± 0.31	1.7 ± 1.3
HCOOH	75	0.021 ± 0.010	3.7 ± 2.1	2.4 ± 2.3
H_2CO	60	0.023 ± 0.007	2.6 ± 1.2	1.9 ± 0.7
C_2H_6	79	0.0023 ± 0.0005	0.26 ± 0.11	0.73 ± 0.41
C_2H_2	77	0.0034 ± 0.0014	0.34 ± 0.18	0.26 ± 0.11
HCN	77	0.0042 ± 0.0016	0.43 ± 0.22	(0.81)
CH_3OH	166	0.019 ± 0.001	2.3 ± 0.8	2.0 ± 1.4

Note that the uncertainties quoted for this study are derived from the large uncertainty in the emission factor for CO, (35%), combined in quadrature with the one-sigma standard deviation in the emission ratio to CO for each trace gas. The uncertainties shown for the mean emission factors from extra-tropical forest measurements are the one-sigma standard deviations of all the measurements used. The literature based emission factor for HCN, given in parenthesis, is an estimate extrapolated from measurements from savanna fires.

3.9 A Potential Method for Estimating Biomass Burning Emissions

The difficulty of estimating the total mass of fuel burned is a major limitation to traditional methods of estimating total emissions to the atmosphere from biomass burning, especially on a global scale. The trace gas-to-AOD correlations presented here suggest an alternative approach based on satellite-derived AOD data. In previous studies, good agreement has been found between ground-based sun photometer measurements of AOD (as used in this study) and AOD measurements from four satellite-based sensors (TOMS, MODIS, MISR and ATSR-2) [*Schmid et al.*, 2003]. Thus the gas-to-AOD correlations shown in Table 3-2 can be used to translate directly from the satellite-measured AOD into an estimated column amount of each trace gas present in a fire-affected region.

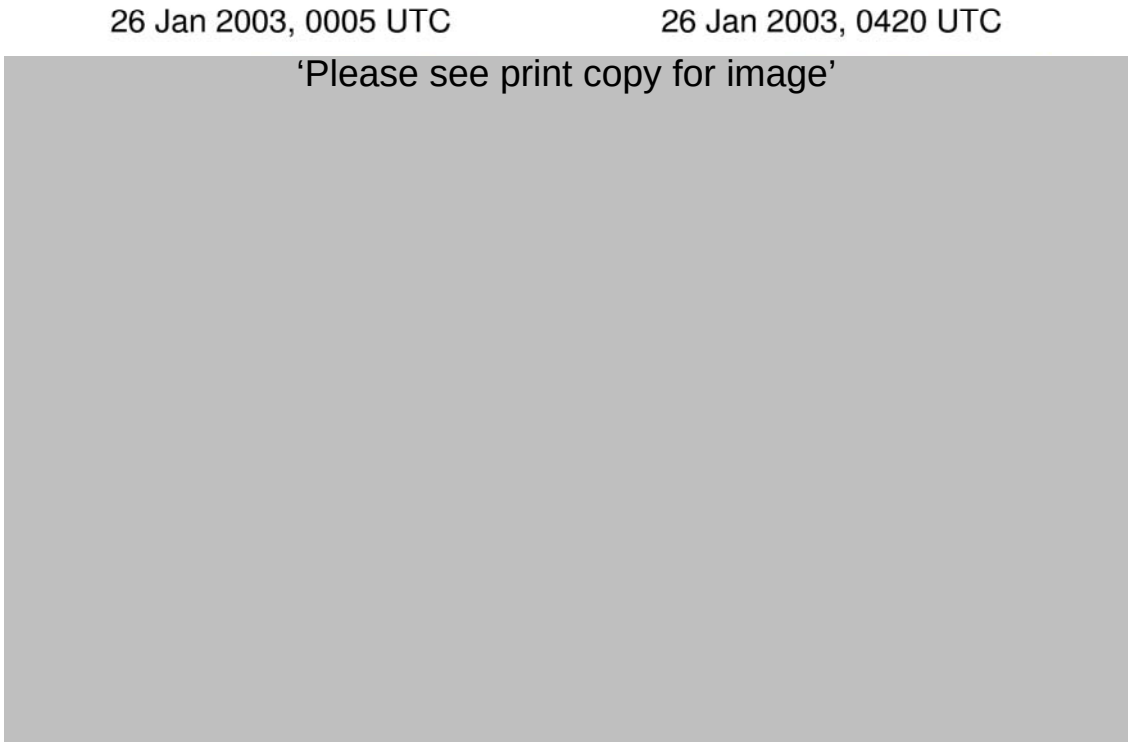

Figure 3-26: Distribution of AOD at 500 nm over the Southeast coast of Australia on January 26th 2003 obtained from the MODIS aerosol product (MOD04), as observed from the Terra (left panel) and Aqua (right panel) platforms. The AOD scale has been converted to column amounts of CO, HCN or H_2CO by applying the relationships derived from the regression equations shown in Table 3-2. (Figure generated by Susan Campbell, CSIRO, Canberra.)

Figure 3-26 shows enhanced values of AOD on January 26th 2003 generated by the bushfires that burned for several weeks beginning January 12th 2003 in the alpine areas of Southeastern Australia. The data were obtained from the Moderate Resolution Imaging Spectroradiometer (MODIS) instruments on board the NASA Earth Observing System satellites Terra (daily pass, approximately 10:30 local time) and Aqua (daily pass, 13:30 local time) [*Chu et al.*, 2002; *Remer et al.*, 2002]. The white pixels indicate areas where the retrieved AOD was below the detection threshold of 0.05 or has been rejected by the retrieval algorithm, for example through contamination by cloud or sun-glint.

The AOD values at 500 nm measured by the MODIS instruments above Wollongong on January 26th 2003 were 1.1 ± 0.1 and 1.0 ± 0.1 respectively, compared to the ground-based sun-photometer measurements of AOD of 1.3 ± 0.3. The satellite measurements are integrated over a 10 km square area at two distinct times, whereas the sun-photometer readings sample less than 1 m^2 but are averaged over the day. Therefore the values are only expected to be broadly comparable. There are a limited number of other occasions when there are reasonably coincident measurements available of significantly enhanced AOD from fires available from both MODIS and the ground-based sun-photometer. Comparison of these data show that MODIS AOD is on average 27% ± 23% lower than the equivalent ground-based data (see Figure 4-16).

Included in Figure 3-26 are the column amounts of CO, HCN or H_2CO derived by applying the relationships given in Table 3-2. If the vertical distribution of the smoke was also known, this mapping of column amounts of biomass burning products could be used to infer ground level concentrations of trace gases. Although column measurements alone are not good indicators for the ground-level concentration, when coupled with meteorological transport models these images might provide useful estimates of average exposure levels where no ground based measurements exist [*Chu et al.*, 2003].

Moreover the mapping of column amounts illustrated in Figure 3-26 provides the basis of a method for estimating total emissions of trace gases from biomass burning episodes. The total amount of each trace gas present at any one time can be found by integrating over the total area of the plume, but integration over time is also needed to get a total emissions estimate. Satellite radiance measurements can confirm the presence of fires [*Dozier*, 1980] and so the duration of a fire episode may be estimated with a

time resolution defined by the time between each satellite pass over the area of interest. Each time the satellite passes overhead it can make a new measurement of the AOD, and hence the total amount of trace gases present in a defined "active" region. The amount of AOD that remains in the active region from earlier emissions may be estimated with the aid of a dispersion model, thereby ensuring that "double counting" of the smoke plumes is avoided.

The trace-gas-to-AOD ratios have only been measured for Australian forest fires and since emission factors may vary with fuel type, further measurements are required to extend this method to other geographical regions or fires types. Another limitation is that cloud cover inhibits the satellite AOD measurements and so emissions may be under-estimated. Also the smoke must dissipate out of the defined active region (where the fires are burning) before the trace-gas-to-AOD ratios change significantly as a result of the different atmospheric lifetimes of the various components: (hours for NH_3 and H_2CO; days for the particulate matter that causes elevated AOD; 1-2 months for CO and approximately 3 months for HCN) [*Li et al.*, 2000; *Mauzerall et al.*, 1998].

Despite these limitations, the measurements described here provide a potential new method for estimating emissions from biomass burning. The dominant uncertainties in the proposed methodology are different from those in traditional on-the-ground estimates, making this an ideal complementary technique.

3.10 Summary and Conclusions

A thorough analysis of ground-based solar absorption spectra taken through smoke plumes from Australian forest fires has yielded vertically integrated measurements of emitted trace gases C_2H_2, C_2H_4, C_2H_6, HCOOH, CO, H_2CO, HCN, NH_3 and CH_3OH. The measured trace gas amounts are well correlated with simultaneous, co-located measurements of AOD, suggesting a potential use of satellite-based AOD measurements in making estimates of the total gaseous emissions from biomass burning. This possibility is made especially interesting because satellite-based AOD measurements are sensitive right down to ground-level [*Gonzalez et al.*, 2003], unlike most satellite-based measurements of trace gases. Emission ratios with respect to CO have been calculated for C_2H_2, C_2H_4, C_2H_6, HCOOH, H_2CO, HCN, NH_3 and CH_3OH using AOD as a proxy for CO. Converting to emission factors using an average

value for the emission factor of CO from previous studies indicates that Australian forest fire emissions are broadly similar to those from other geographical regions except for comparatively low emissions of C_2H_6.

Chapter 4 : Modeling Emissions from the Canberra Wildfires of 2003

4.1 The Canberra Wildfires of 2003

Abnormally high temperatures and low rainfall were experienced in southeastern Australia in the second half of 2002 due to a severe El Niño-related drought that created conditions of extreme fire danger, with an abundance of dry fuel ready to burn. On the 8th January 2003, fires were started by lightning strikes in the region around Canberra and the Snowy Mountains [*Webb et al.*, 2004]. The fires burned for several weeks, reaching their maximum intensity on the 18th January 2003 when a firestorm engulfed several outer suburbs of Canberra (see photographs in Figure 4-1). Four lives were lost and there was widespread damage to property including 491 houses lost. The fires also caused extensive damage to rural grazing property, forests and bushland in the area with substantial losses of farming stock and wildlife [*Webb et al.*, 2004]. At the peak of the firestorm on the 18th January 2003 there were pyro-cumulonimbus eruptions that injected smoke plumes into the stratosphere [*Fromm et al.*, 2006].

The fires continued throughout January and well into February until they were eventually extinguished with the help of heavy rainfall towards the end of February 2003. It has been estimated that the carbon emissions from these fires alone may have exceeded 40 Mt [*Mitchell et al.*, 2006], which is more than a third of the total biomass burning carbon emissions estimated for Australia for the year 2000 by Ito and Penner, [2004].

Smoke plumes from these fires passed overhead and were measured by the remote sensing Fourier transform spectrometer at Wollongong as described in Chapter 3. This fire episode provides an excellent opportunity to trial the potential method for estimating emissions from biomass burning proposed in section 3.9.

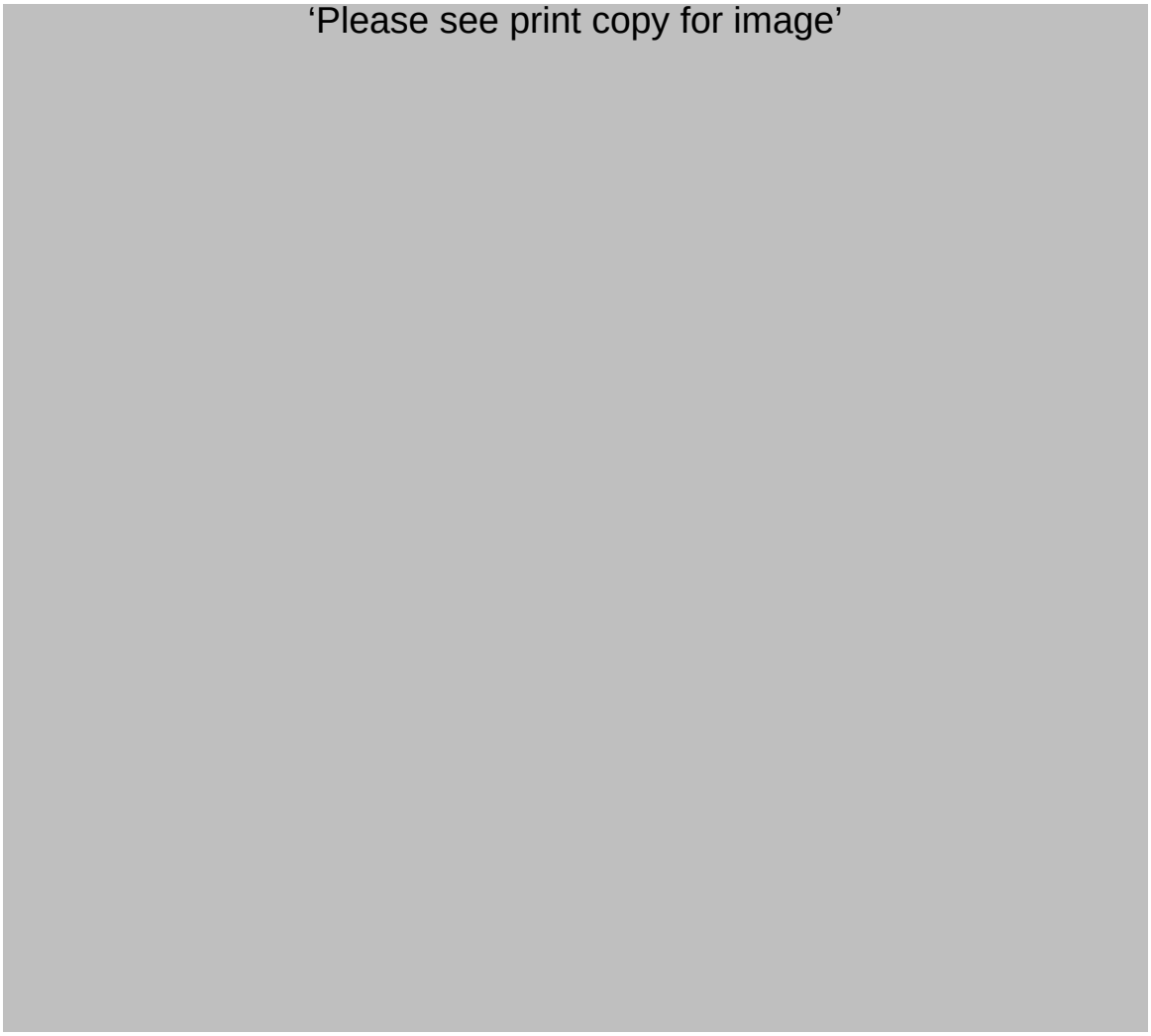

Figure 4-1: Images of the Canberra fires, courtesy of the NSW fire service.

4.2 Outline of a Method to Estimate Emissions Using AOD

In this chapter, the total mass of CO[10] that was emitted from the Canberra fires is estimated using aerosol AOD measurements from the Moderate Resolution Imaging Spectroradiometer, (MODIS) satellite instruments. These instruments are carried onboard two different satellites that orbit the arth approximately every 12 hours, with each instrument providing AOD measurements once per day (no measurement is possible during the night-time overpass).

In Chapter 3 total column amounts of CO and AOD were shown to be strongly correlated in smoke affected spectra, such that satellite images of AOD in a fire-affected region could be translated into images of total column CO (see Figure 3-26). Thus the enhanced atmospheric CO loading from the fires may be measured by the satellite at each overpass. Smoke detected by one satellite overpass may remain in the fire-affected region long enough to be detected by the satellite overpass on the following day. Thus simple summing of all the observed enhancements in atmospheric CO loading would result in double counting of some of the emissions. For this reason the method employs a dispersion model so that the amount of double counting may be estimated and corrected for.

The basic steps in making the emissions estimate are:

1. Extract all the clear satellite AOD images of the fire-affected area for the days of interest and average the AOD data over a 1° by 1° grid spacing.
2. Establish the background AOD in the fire-affected area using averaged MODIS AOD on a pre-fire day.
3. Calculate the enhanced AOD that is likely to be associated with smoke using the averaged MODIS AOD measurements on the days after the fires started.
4. Convert the enhanced MODIS AOD to enhanced column amounts of CO from the relationships CO to AOD data determined from ground-based measurements in Chapter 3, (see Table 3-2 and Figure 3-26). This gives the total enhanced atmospheric mass of CO in the area on each of the days of interest.

[10] Emissions of gases other than CO are also estimated in this chapter, but CO is used as the example gas in the description of the method.

5. Run a regional dispersion model for each day of interest so that the amount of CO emissions that remain in the area for long enough (~ 1 day) to contribute to more than one satellite image of enhanced AOD can be estimated.
6. Subtract the modelled amounts remaining from the previous day's emissions, from the total enhanced atmospheric mass of CO in the area (determined from the MODIS AOD images on each day), thereby avoiding any double counting of smoke plumes. This gives the total CO emitted by the fires for each day.
7. Finally sum the calculated CO emitted by the fires each day to give the total CO emissions for the entire fire episode.

4.3 MODIS Satellite Measurements of AOD during the Canberra Fires

The Moderate Resolution Imaging Spectroradiometer, (MODIS) instruments provide high radiometric sensitivity in 36 spectral bands ranging in wavelength from 0.4 μm to 14.4 μm [*Kaufman et al.*, 1990; *Kaufman*, 1993; *Kaufman et al.*, 2003; *King et al.*, 1999; *Remer et al.*, 2002; *Zhao et al.*, 2003]. They are carried on both the Terra and Aqua satellites (orbiting at an altitude of 705km), providing global coverage every 1 to 2 days with a swath that is 2,330-km cross track by 10km along the track at nadir. For most parts of the globe, including southeast Australia, twice daily coverage at local times of about 10:30 (Terra) and 13:30 (Aqua) is achieved. Each instrument contains a two-mirror off-axis collimating telescope, which collects radiant energy and directs it into four refractive objective assemblies, covering the visible, near infrared, short-wave to medium-wave infrared and long-wave infrared regions of the spectrum.

The MODIS instruments' products include visible images, AOD (also called aerosol optical thickness) and thermal anomalies (pinpointing the locations of fires) [*Kaufman et al.*, 1998b]. MODIS AOD (product MOD 04) data are retrieved over the oceans globally and over the large portions of the continents at the spatial resolution of 10 x 10 km [*Chu et al.*, 1998; *Kaufman et al.*, 1997; *Tanre et al.*, 1997]. Separate algorithms are used to derive AOD over sea and land, with recent work to optimise these algorithms including the deep-blue algorithm developed to derive aerosol optical thickness over bright land areas [*Kleidman et al.*, 2005; *Levy et al.*, 2007].

MODIS "hdf" format images over southeastern Australia covering the time period from 7th January to 28th February 2003 were downloaded from http://modis.gsfc.nasa.gov/data/dataprod/index.php and the AOD and latitude and longitude data extracted. These data were re-projected and plotted as a series of maps; one for each satellite overpass. Many of the images have large numbers of white pixels where the algorithms have rejected the data either as a result of cloud interference, sea-glint or other technical difficulties, resulting in interruptions in the twice daily time series of images. Some of the images also contain black pixels where the image is composed of swaths with no measurements in the black area. For most days from the 8th January 2003 until 26th of February 2003 (the duration of the fires) there was only one satellite image where enhanced AOD was clearly visible, and for many days the best available image itself contained significant numbers of white pixels. For a few days there were clear views of the smoke plumes from two separate images and in these instances both images were used. In contrast there were no usable MODIS images of the fires from the 27th January 2003, the 14th February 2003 or the 21st February 2003.

The satellite overpasses with the clearest images of enhanced AOD from the Canberra fires were chosen for use in making an estimate of the total emissions of specific trace gases from these fires and are listed in Table 4-1 and Table 4-2. Some of these images are shown in Figure 4-2 and Figure 4-3 and the complete set of images is provided in Appendix 2. The extracted data from all of these images were averaged over 1° x 1° grid spaces, ready for use in estimating gaseous emissions from the fires. Two regions were used – a large area aimed at capturing the full extent of fresh smoke plumes emanating from Canberra fires, and a smaller region that could be modelled by the available dispersion model (TAPM). The exact regions used were:

1. Large Area: 1° x 1° grid spaces extending from -25° to -46° latitude and 135° to 160° longitude, (400 1° x 1° grid spaces in total)
2. Smaller Area: 1° by 1° grid spaces extending from -30° to -40° latitude and 143° to 155° longitude, (120 1° x 1° grid spaces in total)

An example of a MODIS AOD image from the large area is shown in the left hand panel in

Figure 4-4 alongside the corresponding visible image in the middle panel and the MODIS AOD image from the smaller area in the right hand panel. The images are

from the Aqua satellite overpass on the 18th January 2003. Also clearly visible in the middle panel are tightly clustered red pixels in a line to the south west of Canberra. These indicate thermal anomalies detected in the MODIS infrared spectral bands as a result of the extensive fires burning in the region on this day. A large area of white pixels is present in both AOD images. Comparison of the large area AOD image and the visible image shows that whilst a large smoke plume extending over the ocean is captured fairly well in the AOD image, the plume of smoke emanating from the active fires is lost within the white pixel areas. It is known that there was a large firestorm on this day that produced pyro-cumulus clouds that penetrated into the stratosphere [*Fromm et al.*, 2006] and so it is not surprising that the MODIS algorithm returns white pixels in the region of the active fires. However, the emissions will be underestimated as a result of the white pixels unless the plume remains in the area at the time of the next satellite overpass. Significantly, the large smoke plume extending over the ocean that is captured in both the visible image and the large area AOD image, is missed by the smaller area AOD image, resulting in further underestimation of the emissions.

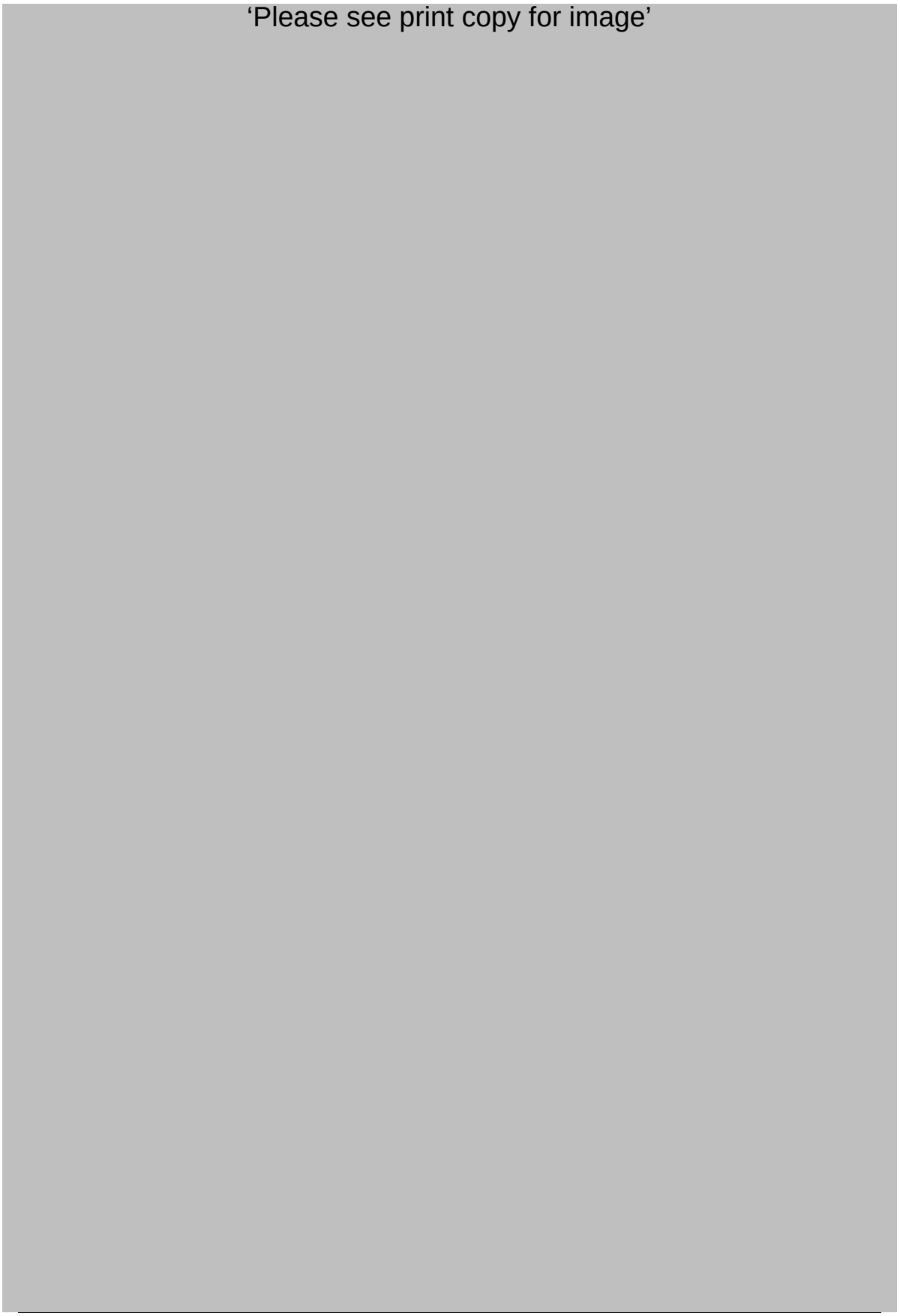

Figure 4-2: A selection of MODIS AOD images of the Canberra fires of 2003.

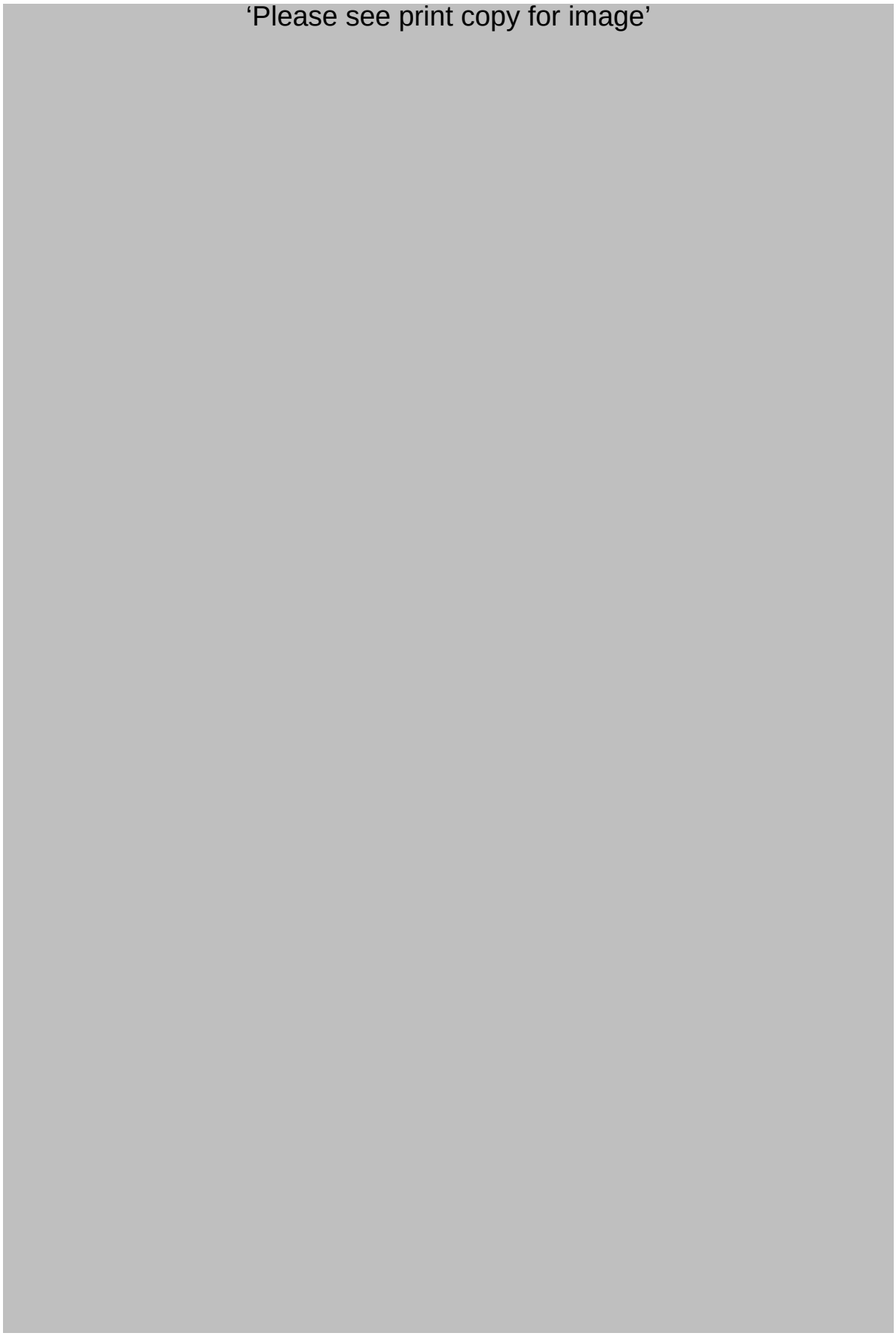

Figure 4-3: Further MODIS AOD images of the Canberra fires of 2003.

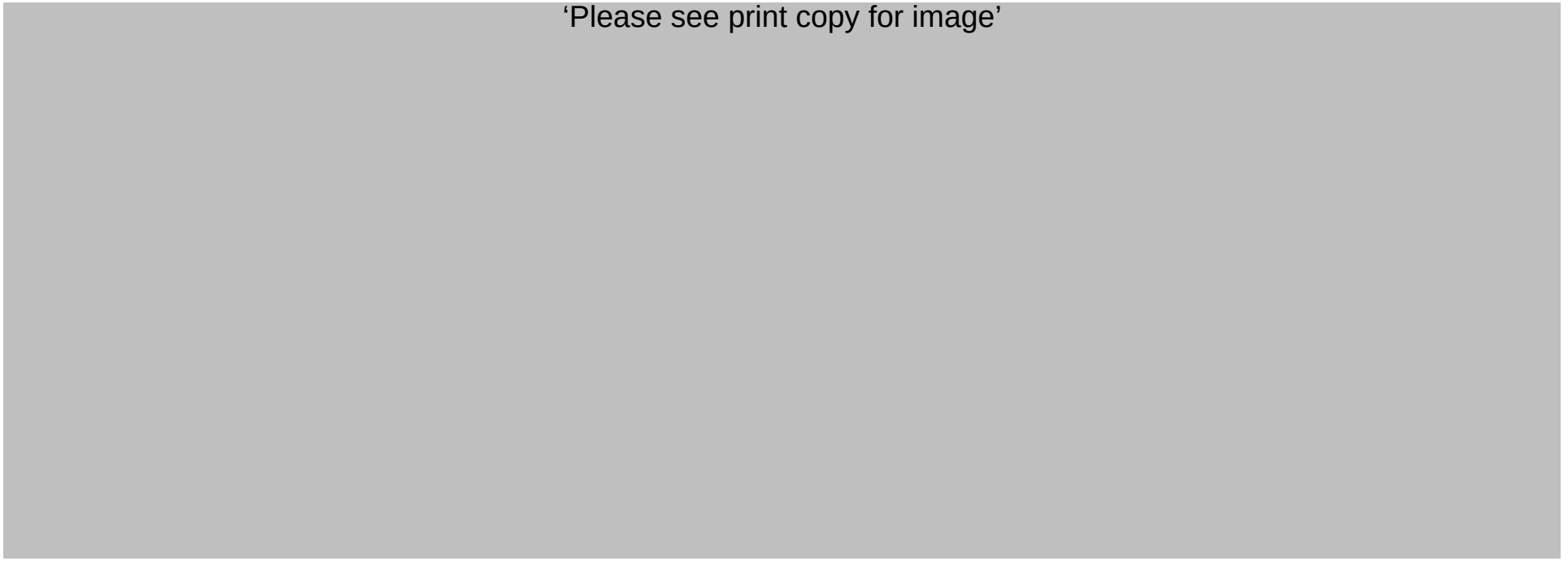

Figure 4-4: Smoke plumes from the Canberra fires as seen from MODIS onboard the Aqua satellite on the 18th January 2003.

Left panel: MODIS AOD over "large area"

Middle panel: MODIS visible image with thermal anomalies shown as red pixels.

Right panel: MODIS AOD over "smaller area".

Note that significant amounts of smoke visible to the eye in the middle panel are missed by the MODIS AOD algorithm as shown in both the left-hand and right-hand panels.

Table 4-1: Satellite overpasses with a clear image of enhanced AOD from smoke plumes from the Canberra fires during January 2003.

Date (dd/mm/yyyy)	Time (UT)	Satellite	Comment
7/01/2003	03:45	Aqua	Used for background AOD
8/01/2003			Fires start
9/01/2003	03:55	Aqua	1st image of enhanced AOD from fires
10/01/2003	04:20	Aqua	
11/01/2003	00:50	Terra	
12/01/2003	04:05	Aqua	
13/01/2003	00:35	Terra	
	00:40	Terra	
	23:40	Terra	Averaged with Aqua image from 14th Jan
14/01/2003	03:55	Aqua	
15/01/2003	00:25	Terra	
16/01/2003	03:40	Aqua	
17/01/2003	04:25	Aqua	
18/01/2003	03:30	Aqua	
19/01/2003	00:00	Terra	
20/01/2003	03:15	Aqua	
21/01/2003	04:00	Aqua	
22/01/2003	00:30	Terra	
23/01/2003	03:45	Aqua	
	03:50	Aqua	
24/01/2003	00:20	Terra	
	23:25	Terra	Averaged with Aqua image from 25th Jan
25/01/2003	03:35	Aqua	
26/01/2003	00:05	Terra	
	04:15	Aqua	
27/01/2003	23:55	Terra	Averaged with Aqua image from 28th Jan
28/01/2003	04:05	Aqua	
29/01/2003	04:45	Aqua	
30/01/2003	03:50	Aqua	
	03:55	Aqua	
31/01/2003	04:35	Aqua	
	23:30	Terra	Averaged with Aqua image from 1st Feb

Table 4-2: Satellite overpasses with a clear image of enhanced AOD from smoke plumes from the Canberra fires during February 2003.

Date (dd/mm/yyyy)	Time (UT)	Satellite
1/02/2003	03:40	Aqua
2/02/2003	04:25	Aqua
3/02/2003	03:30	Aqua
4/02/2003	04:10	Aqua
5/02/2003	03:15	Aqua
6/02/2003	04:00	Aqua
7/02/2003	04:40	Aqua
8/02/2003	03:45	Aqua
	03:50	Aqua
9/02/2003	04:30	Aqua
10/02/2003	03:35	Aqua
11/02/2003	04:15	Aqua
	04:20	Aqua
12/02/2003	03:20	Aqua
	03:25	Aqua
13/02/2003	04:05	Aqua
15/02/2003	03:50	Aqua
	03:55	Aqua
16/02/2003	04:35	Aqua
17/02/2003	03:40	Aqua
	03:45	Aqua
18/02/2003	04:25	Aqua
19/02/2003	03:30	Aqua
20/02/2003	04:10	Aqua
22/02/2003	04:00	Aqua
23/02/2003	04:40	Aqua
24/02/2003	03:45	Aqua
	03:50	Aqua
25/02/2003	04:30	Aqua
26/02/2003	03:35	Aqua

4.4 Estimating Gaseous Emissions using MODIS AOD Measurements

The first step in making an estimate of the emissions of trace gases from the Canberra fires using the AOD measurements from the MODIS instruments is to establish a reasonable background value for AOD in the region. There are sources of enhanced AOD other than smoke and so the background must be chosen carefully so as not to overestimate the emissions by including AOD that results from dust or sea salt aerosols.

MODIS data from January 7th 2003 over the smaller region (from -30° to -40° latitude and 143° to 155° longitude) were analysed to find the background AOD over southeastern Australia before the fires started. The AOD was averaged over 1° by 1° grid spaces for all MODIS data points available from the 03:45 UT Aqua overpass. Only 1° by 1° grid spaces with more that 10 points were considered because of the possibility of getting a few spuriously high pixels near to points that are rejected by the MODIS algorithm. The maximum AOD value for a 1° by 1° grid space on the 7th January before the fires started was 0.2, and so this was taken as a threshold value to identify smoke.

The average AOD value for a 1° by 1° grid space on the 7th January before the fires started was 0.11 and this was used as a "background" value. In the subsequent days, whilst the fires burned, AOD values above 0.2 are assumed to result from particulates in the smoke emitted from the fires. Each grid space with an averaged AOD value above 0.2 was included in the calculation and the background value of 0.11 subtracted before converting to enhanced CO via Equation 4-1 below.

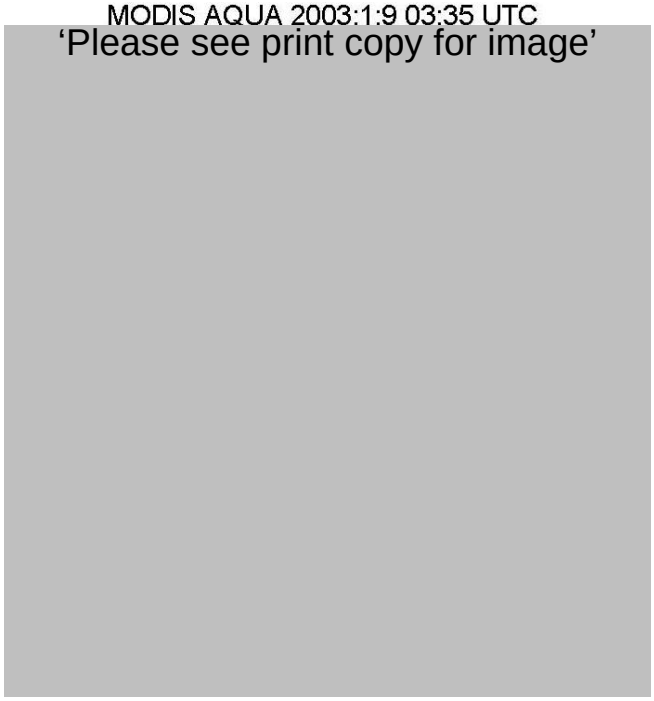

Figure 4-5: Enhanced MODIS AOD from the Canberra fires recorded from the Aqua satellite at 03:35 UT on 9th January 2003.

The first clear image of enhanced AOD, (see Figure 4-5). is the Aqua overpass on the 9th January 2003 at 03:35 Universal Time (UT), which corresponds to 13:35 Australian Eastern Standard Time (AEST) on the day after the fires started by lightning strikes [*Fromm et al.*, 2006]. The 1° by 1° averaged MODIS AOD data from this swath were sorted to extract all values of AOD in excess of 0.2. The enhancement in AOD for each extracted 1° by 1° grid space was calculated by subtracting the background value of 0.11 and converted to an enhanced atmospheric loading of CO, ($M_{CO\text{-}day\text{-}n}$) in the area on day *n:*

Equation 4-1:
$$M_{CO-day_n} = \frac{(AOD_{grid} - 0.11).G_{CO:AOD}A_{grid}}{N_A}.MW_{CO}$$

Where

- AOD_{grid} is the 1° by 1° grid averaged AOD as measured by MODIS
- **0.11** is the background AOD subtracted from enhanced AOD measurements
- $G_{CO:AOD}$ is 1.5 x10^{18} molecules cm^{-2} (the gradient of CO to AOD given in Table 3-2, determined by regression analysis of the data shown in Figure 3-19)

- A_{grid} is 1.02 x10^{14}- the area of the grid spaces in cm^2 using conversion factors of 111.12 km for 1° latitude and 92.12 km for 1° longitude
- N_A *is* Avagadro's Number = 6.02 x10^{23} mol^{-1} and
- MW_{CO} is the molecular weight of CO (28 g mol^{-1})

Summing the enhanced CO calculated using Equation 4-1 for all the 1° x 1° grid spaces with AOD over the threshold value of 0.2 gives a total enhanced atmospheric CO loading of 5.17 x10^{10} g in the region from -30° to -40° latitude and 143° to 155° longitude) at the time of the satellite overpass on the 9th January 2003. It is assumed that all of the enhancement in atmospheric CO load calculated this way results from emission from the fires from when they started on the 8th January to the time the satellite recorded the image.

The next clear image of enhanced AOD from the Canberra fires came from the Aqua overpass the following day, on the 10th January 2003, (see Figure 4-6). The total enhanced atmospheric CO loading can be calculated as described above, but this time there is a possibility that some of the enhancement is due to emissions from the fires that were also captured in the MODIS image from the 9th January and so have already been included in the total emissions calculation. To avoid the possibility of double counting areas of enhanced AOD in the emissions calculations, it is necessary to model the dispersion of the smoke plumes from the fires. The modelling of the dispersion of emissions from the fires is described in the following sections.

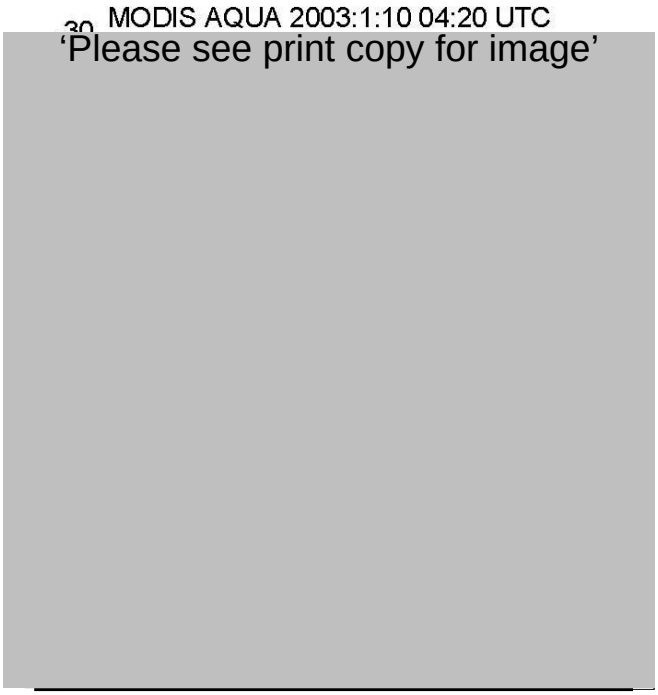

Figure 4-6: Enhanced AOD as seen by the MODIS instrument on Aqua at 04:20UT 10th January 2003. The black area is not covered by the swaths used to make up the image.

4.5 Difficulties in Modelling the dispersion of smoke plumes

The task of matching modelled data to satellite measurements is an inherently difficult one, and this case is no exception. Several difficulties arise when attempting to estimate the proportion of emissions that remain in the area long enough to be double counted by being captured by more than one satellite image of enhanced AOD.

1. Fires burn semi-continuously but typically only a single image per day of the distribution of smoke is available. Also, the satellite images give the horizontal distribution of smoke plumes but provide no information about the vertical distribution of the smoke. As a result, the model must make some assumptions about location and time profile of emissions of smoke over the previous 24 hours in order to try to replicate the observed distribution. Since these assumptions may not be correct, the horizontal distribution of emissions in the model may not be a good match to the distribution of the smoke actually measured from the satellite. In some cases a proportion of the emissions from the previous 24 hours in the model may have already been dispersed out of the

modelled area before the time of the satellite overpass and a correction factor ($\mathbf{C_{1A}}$) will be required to account for this.

2. The transportation of emissions within dispersion models is not necessarily mass-conserving[11], so a correction factor ($\mathbf{C_{1B}}$) may be required to adjust for this [*Hu et al.*, 2008].

3. The horizontal distribution of the emissions remaining in the model may overlap with white pixels (or black pixels) in the satellite image for the relevant day and thus not actually be double counted at all. In many cases yet another correction factor ($\mathbf{C_2}$) is required to account for the proportion of remaining emissions that are likely to be missed within the white pixels of the satellite image. In other instances visual inspection of the model output alongside the satellite image is sufficient to establish that the emissions remaining in the model are located in areas where the satellite image has white or black pixels, and in these cases any emissions remaining in the model will not be detected by the satellite image of the day and so may be ignored, ($\mathbf{C_2} = 0$).

4.6 Emissions Calculations including corrections for double counting using TAPM dispersion modelling

The model used to estimate the dispersion of smoke plumes was the "The Air Pollution Model" (TAPM) described in section 2.6. The model was configured with a 10 x 10 km grid spacing (~0.1° by 0.1°) centred on Canberra and covering a total area of 1000 km by 1000 km equivalent to the smaller of the two regions discussed above (approximately -30° to -40° latitude and 143° to 155° longitude). The larger region (from -25° to -46° latitude and 135° to 160° longitude) is beyond the scope of TAPM,

[11] Mass inconsistency is common in air quality models and various methods have been developed to overcome this problem *[Hu and Odman, 2008],* but none are implemented within TAPM's Eulerian mode.

which is designed to model local to regional scale areas, so here we consider only the smaller region.

Two area sources to the southwest of Canberra were chosen to represent the source of all emissions throughout the duration of the fires. The approximate location of the area sources were taken with reference to a MODIS false-colour image taken on the 7th February 2003 showing the location of fire scars from the Canberra fires.

Figure 4-7 shows the TAPM modelled area (with the area sources marked in grey) alongside the MODIS false-colour image from the 7th February 2003. The large area sources were used in preference to point sources (e.g. from thermal hotspots detected by MODIS) because test runs of the model suggested that the problems of lack of mass-conservation were less severe in TAPM when using area sources as opposed to point sources. This simplification could lead to differences in the predicted location of the smoke plumes, however the synoptic scale meteorology used is on a 0.75° longitudinal by 1° latititudinal grid (approximately 75km by 100km) so it is unlikely that the resulting uncertainty will be significant compared to the effects of missed smoke plumes caused by the incomplete time series and white pixels in the available images.

Having established the area of release for the emissions, the rate of release must also be calculated. The simplest option is to assume that the total mass of CO is emitted at a constant rate throughout the time between satellite overpasses (or from the start of the fires to the first image showing enhanced AOD). Another possibility is to attempt to reflect the fact that the intensity of the fires and the resulting emissions are likely to peak during the heat of the day and die down substantially overnight.

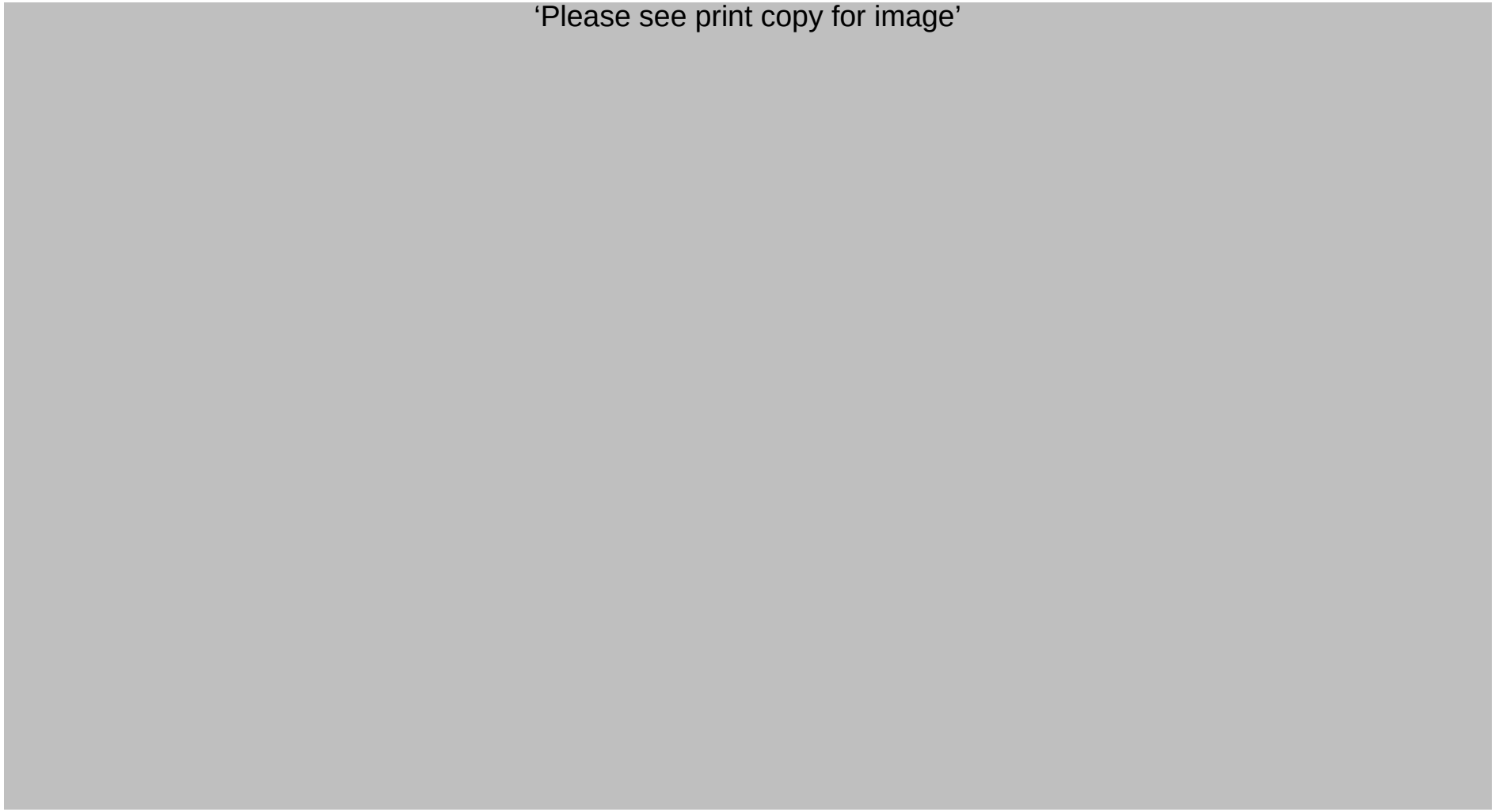

Figure 4-7: MODIS false-colour image taken on the 7th February 2003 (left hand panel) TAPM grid with area sources shown in grey (right hand panel)

The distribution of emissions chosen for a 24 hour period is shown in Figure 4-8, with the percentage of total emission for each hour shown as a histogram. Peak emissions are assumed/defined to occur from 01:00 – 07:00 UT which is 11:00 - 17:00 AEST, and are assumed/defined to decrease to a constant low level of half peak rate at night-time with a three quarters rate for evening and morning time.

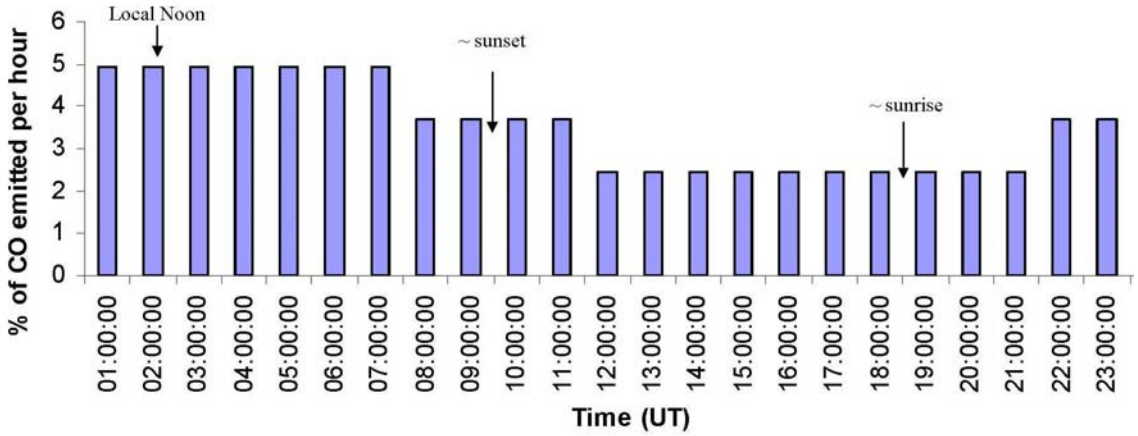

Figure 4-8: Typical distribution of emissions chosen for a 24 hour period given in UT.

The emissions were mixed over the first 5 altitude layers of the model (from ground level to 300m), with an exit velocity of 5 ms^{-1} and a temperature of 200°C. After emission the CO was treated as a chemically inert tracer.

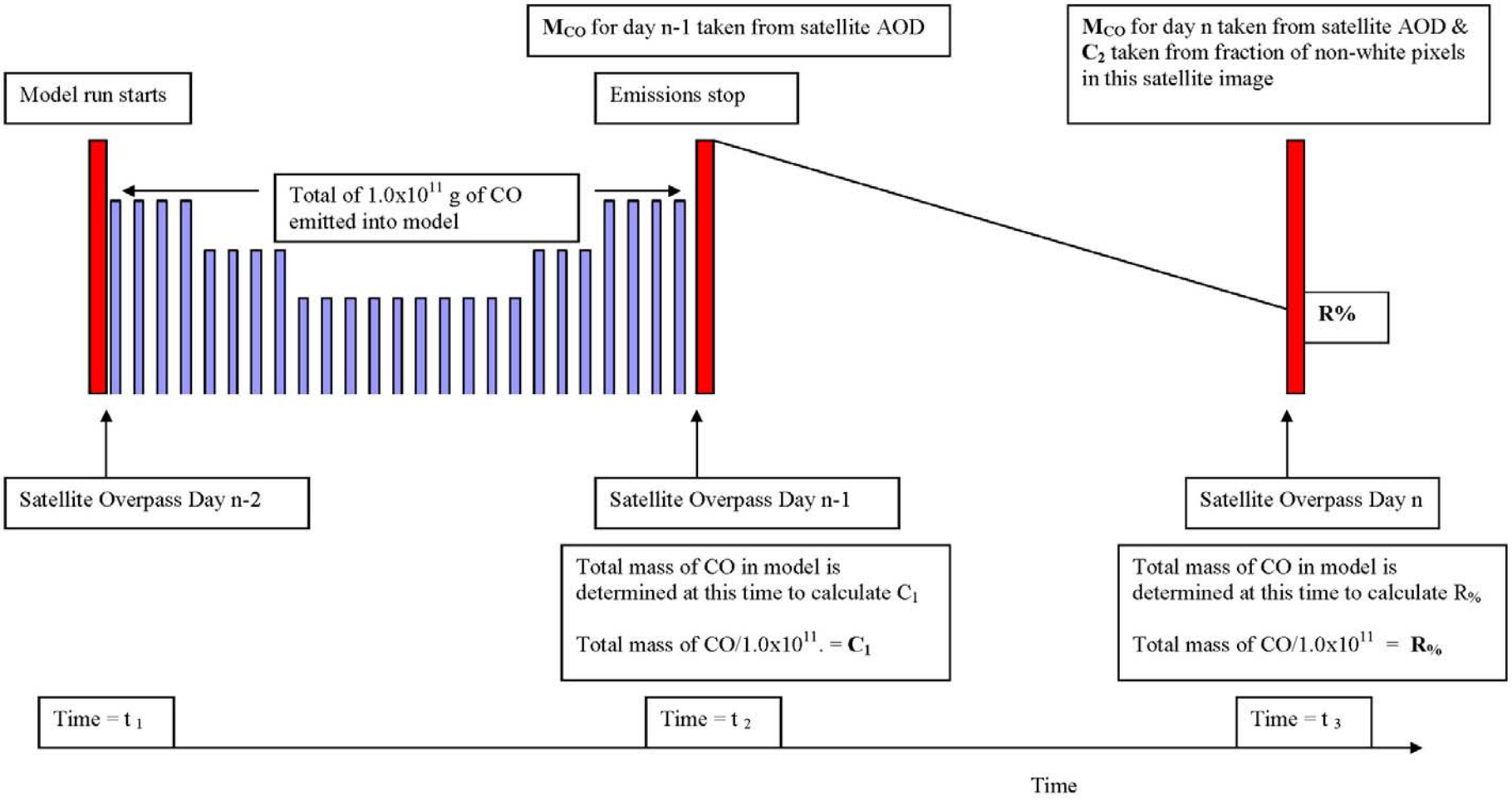

Figure 4-9: Schematic diagram illustrating the method used to estimate the amount of emissions that may be double-counted each day.

The method of estimating the amount of double counting is illustrated by the schematic diagram shown in Figure 4-9. For each day "**n**" that there was a clear MODIS AOD image of the Canberra fires, a separate model run is used to estimate double counting of emissions, starting two days earlier and releasing the emissions into the model during the first day[12] (between times $\mathbf{t_1}$ and $\mathbf{t_2}$). For simplicity, the same nominal total mass of CO (1.0×10^{11} g) is released into the model for each run and then scaled appropriately later in the calculations. The emissions in the model stop at the time of the satellite overpass on the second day (time = $\mathbf{t_2}$) and the model continues forward in time with no further emissions. On the third day at the time of the satellite overpass of interest (time = $\mathbf{t_3}$), the fraction of enhanced atmospheric CO loading that still remains in the model ($\mathbf{R_{\%}}$) is determined:

$\mathbf{R_{\%}}$ = (the total mass of CO in the model at time $\mathbf{t_3}$)/(1.0×10^{11} g).

The average value for $\mathbf{R_{\%}}$ from all the model runs is 46%, indicating the scale of the double-counting effect.

As discussed in section 4.5 the modelling has imperfections such that other correction factors are needed. Ideally, if the assumed rate and location of all the emissions detected at the time of the satellite overpass on day "**n-1**" were correct, none of the modelled emissions had yet dissipated out of the region and the model was perfectly mass-conserving, then the total mass of CO in the model at time t_2 would be 1.0×10^{11} g. In reality the modelling is not perfect and a correction factor $\mathbf{C_1}$ is applied:

$\mathbf{C_1}$ = (the total mass of CO in the model at time $\mathbf{t_2}$)/(1.0×10^{11} g).

Note that the correction factor $\mathbf{C_1}$ is the sum of the correction factors $\mathbf{C_{1A}}$ and $\mathbf{C_{1B}}$ discussed previously. These factors cannot be estimated separately but their combined effects given by $\mathbf{C_1}$ may easily be extracted from the TAPM concentration fields. The average value for $\mathbf{C_1}$ from all the model runs is 105% ± 27%. This correction factor encompasses a number of imperfections in the model but the fact that the average value is greater than 100% indicates that lack of mass-conservation is a real issue, with the mass of emitted CO increasing as it is transported within the model. The average correction factor is relatively small but with a large degree of scatter.

[12] The emissions are released in the hours between one satellite overpass and the next, so the exact times of emissions vary from one day to the next depending upon the times of the clear MODIS AOD

Dividing $\mathbf{R_{\%}}$ by $\mathbf{C_1}$ produces the fraction of emissions that remain in the area from one satellite overpass to the next and hence may be double-counted:

$$\frac{\mathbf{R_{\%}}}{\mathbf{C_1}} = \frac{\text{(the total mass of CO in the model at time } \mathbf{t_3})}{\text{(the total mass of CO in the model at time } \mathbf{t_2})}$$

The presence of white pixels (and black pixels) in the MODIS AOD images means that not all of the CO emissions that remain in the area from one satellite overpass to the next are actually double-counted. The likelihood of actual double counting is estimated by use of the second correction factor, $\mathbf{C_2}$. This is the fraction of grid spaces that contain real MODIS AOD values in the day's satellite image (are neither white nor black pixels). Hence if only 60% of the grid spaces actually have a value for AOD, then only 60% of the CO remaining from earlier emissions is likely to be detected by the satellite measurements. In some cases it may be clear (from visual inspection of the model output alongside the satellite image) that there is no overlap between where enhanced AOD is seen by the satellite and where the model predicts that smoke remains from earlier emissions, and in these cases any mass remaining in the model may be ignored, (by setting $\mathbf{C_2} = 0$). Ideally the comparison between model output and satellite image would be done grid space by grid space, but in reality the accuracy of the dispersion of emissions in the model make averaging over the entire region a more practical approach.

The average value for $\mathbf{C_2}$ for the smaller region from all fire days is 51%.

Figure 4-10 shows an example where $\mathbf{C_2}$ is set to zero, whilst Figure 4-11 shows an example where there is overlap and $\mathbf{C_2}$ is the fraction of pixels in the satellite AOD image that have real MODIS AOD values. (All the MODIS AOD images are shown in Appendix 2 along with the relevant TAPM model predictions for this time.)

---

images used in the calculation.

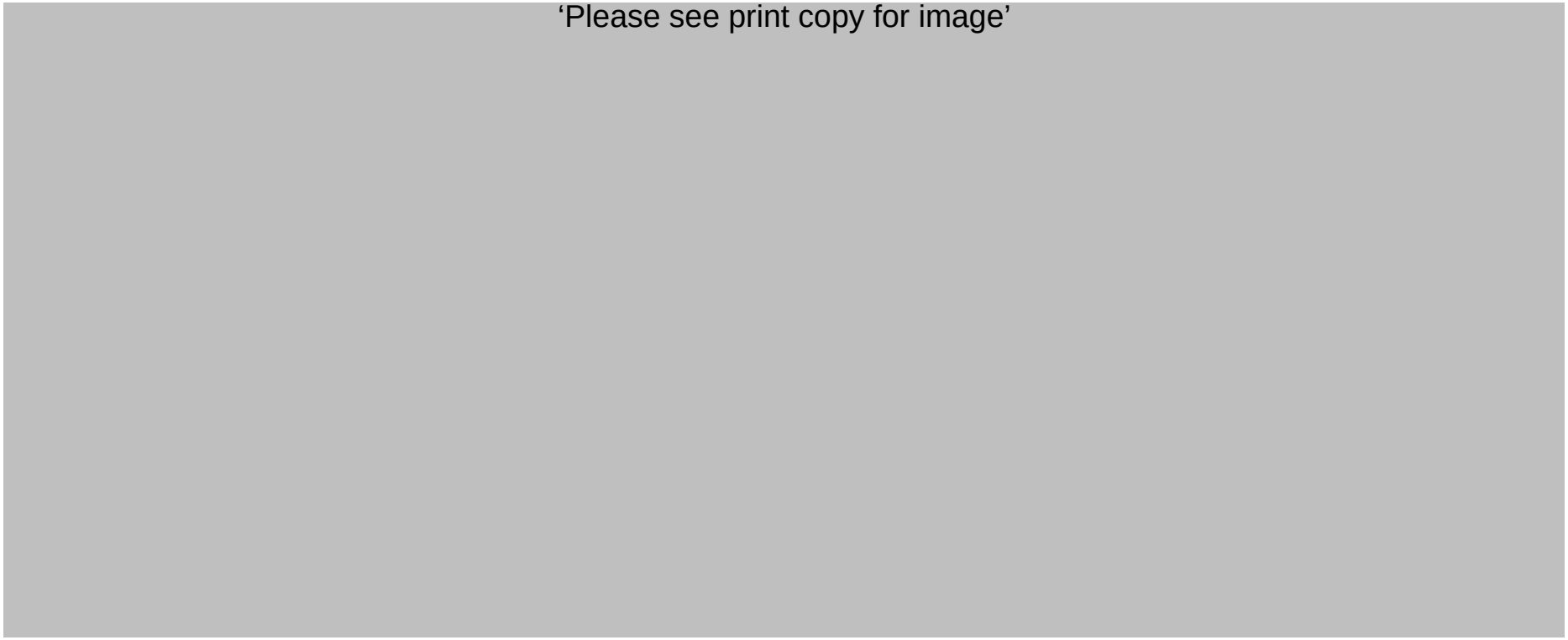

Figure 4-10: An example where examining the predicted smoke remaining from earlier emissions and the enhancements detected by MODIS AOD shows no overlap and the correction factor C_2 is set to zero- (a) TAPM prediction of location of smoke plume from Canberra fires at 1km from the model run for the 15th January 2003, (b) corresponding MODIS AOD image at this time and (c) TAPM prediction of location of smoke plume at 1km from previous emissions taken from the model run for the 14th January 2003. Comparing (a) and (b) shows whether the location of new emissions predicted by the model coincide with the actual enhancements detected by MODIS, (comparison of the total mass in each yields the correction factor, C_1), whilst (b) and (c) are compared to decide whether the detected enhancements include smoke emitted previously and already counted in the emissions estimate. Here the conclusion is that there is no obvious overlap and C_2=0 and so nothing is subtracted from the emissions calculated from the MODIS AOD image in panel (b).

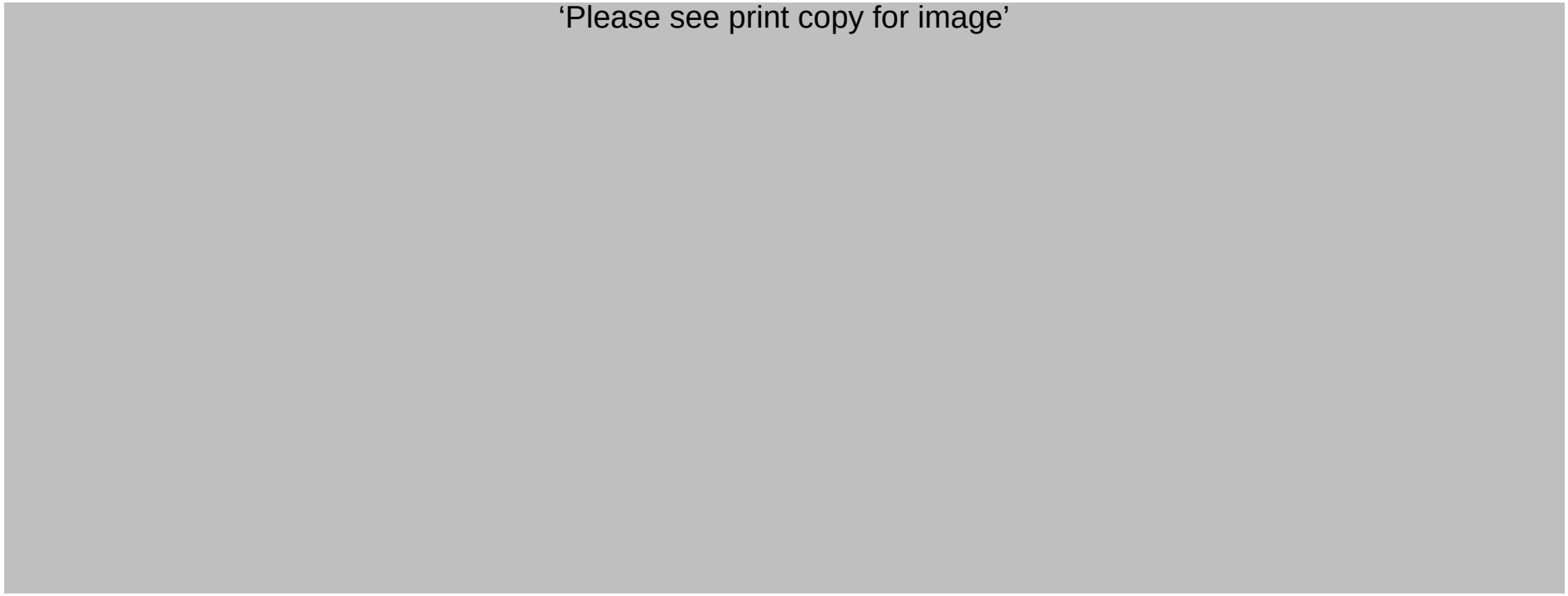

Figure 4-11: An example where the overlap of the predicted smoke remaining from earlier emissions and the enhancements detected by MODIS AOD is not clear. (a) TAPM prediction of location of smoke plume from Canberra fires at 1km taken from the model run for the 22nd January 2003, (b) corresponding MODIS AOD image and (c) TAPM prediction of location of smoke plume at 1km from previous emissions taken from the model run from the 21st January 2003. In this case the correction factor, C_2 is the percentage of non-white pixels in the image shown in (b).

Now that the factors that contribute to the amount of emissions subject to double-counted have been established, the estimated CO emitted on any day **n**, $E_{CO\text{-}day\text{-}n}$, may be calculated using Equation 4-2.

Equation 4-2:
$$E_{CO-day_n} = M_{CO-day_n} - \left(\frac{R_{\%}}{C_1} \times C_2 \times M_{CO-day_{n-1}} \right)$$

where

- $M_{CO\text{-}day\text{-}n}$ is the mass of enhanced atmospheric CO in the area derived from the MODIS AOD image for day **n**,
- $R_{\%}$, is the fraction of the total mass of CO emitted into the model (1.0×10^{11}g) that still remains in the model at the time of the satellite overpass on day **n**, (at time = $\mathbf{t_3}$)
- C_1 is the fraction of the total mass of CO emitted into the model (1.0×10^{11}g) that is present in the model at the time of the satellite overpass on day **n-1**, (at time = $\mathbf{t_2}$).
- C_2 is the fraction of grid spaces in the MODIS AOD data on day n that contain real AOD values (not white pixels or black pixels), unless there is clearly no overlap between modelled plumes and satellite detected AOD enhancements, in which case C_2 is set to zero.
- $M_{CO\text{-}day\text{-}n\text{-}1}$ is the mass of enhanced atmospheric CO in the area derived from the MODIS AOD image for day **n-1**

The procedure described above was used for all fire days to give the proportion of previous emissions that remain in the TAPM modelled area ($\mathbf{R_{\%}}$) and the normalisation factors $\mathbf{C_1}$ and $\mathbf{C_2}$ for each day of the fires, (see Figure 4-12). These correction factors are then used to proportion $\mathbf{M_{CO}}$ (the enhanced atmospheric CO loading deduced from the day's MODIS AOD image), between the estimated mass of CO emitted that day and the mass of CO remaining in the area from previous emissions, (see Figure 4-13), i.e. the sum of these two terms is $\mathbf{M_{CO}}$. Also shown in Figure 4-13 is the accumulated emission of CO as the fires progress.

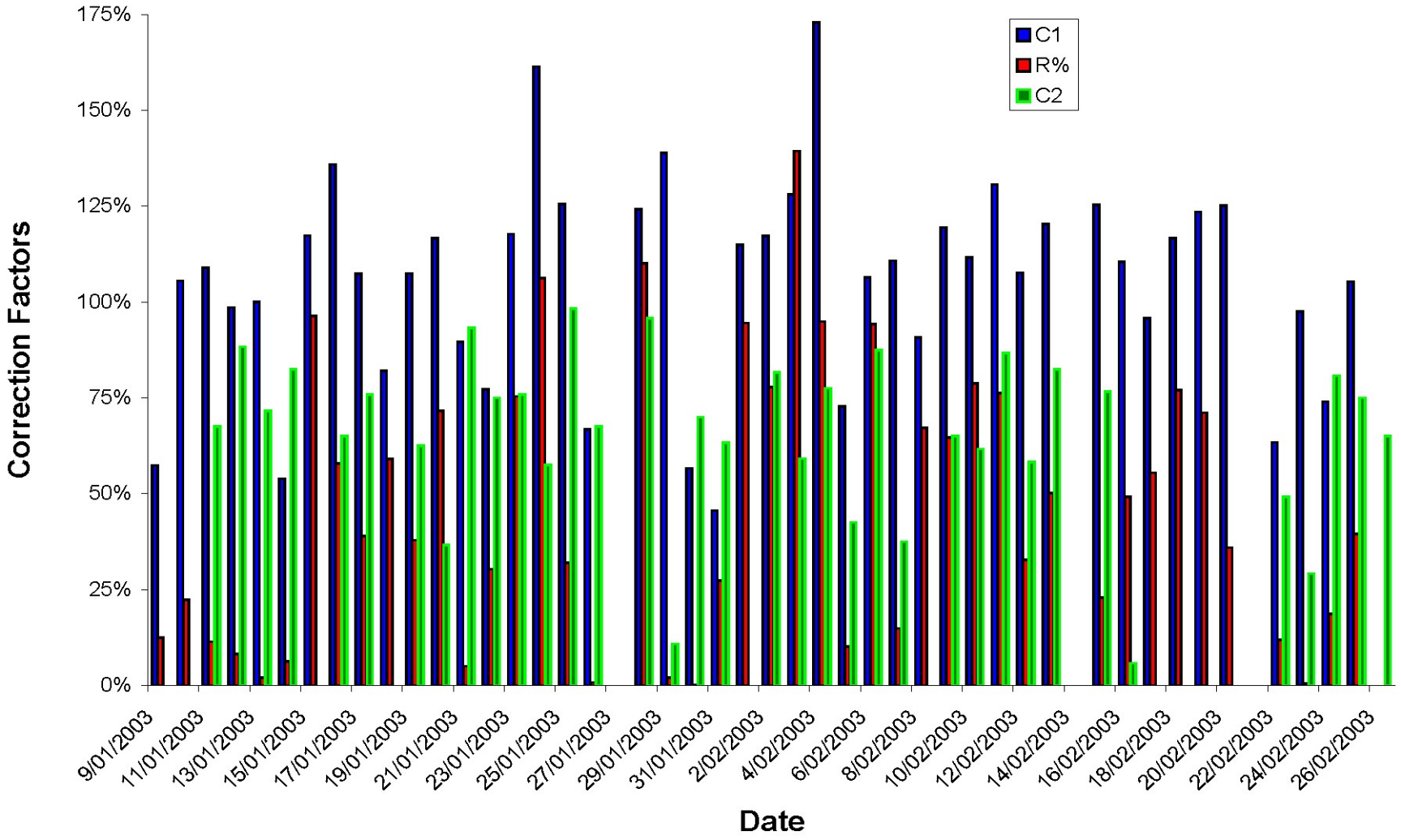

Figure 4-12: The proportion of previous emissions that remain in the TAPM modelled area (R%) and the normalisation factors C_1 and C_2 for each day of the fires.

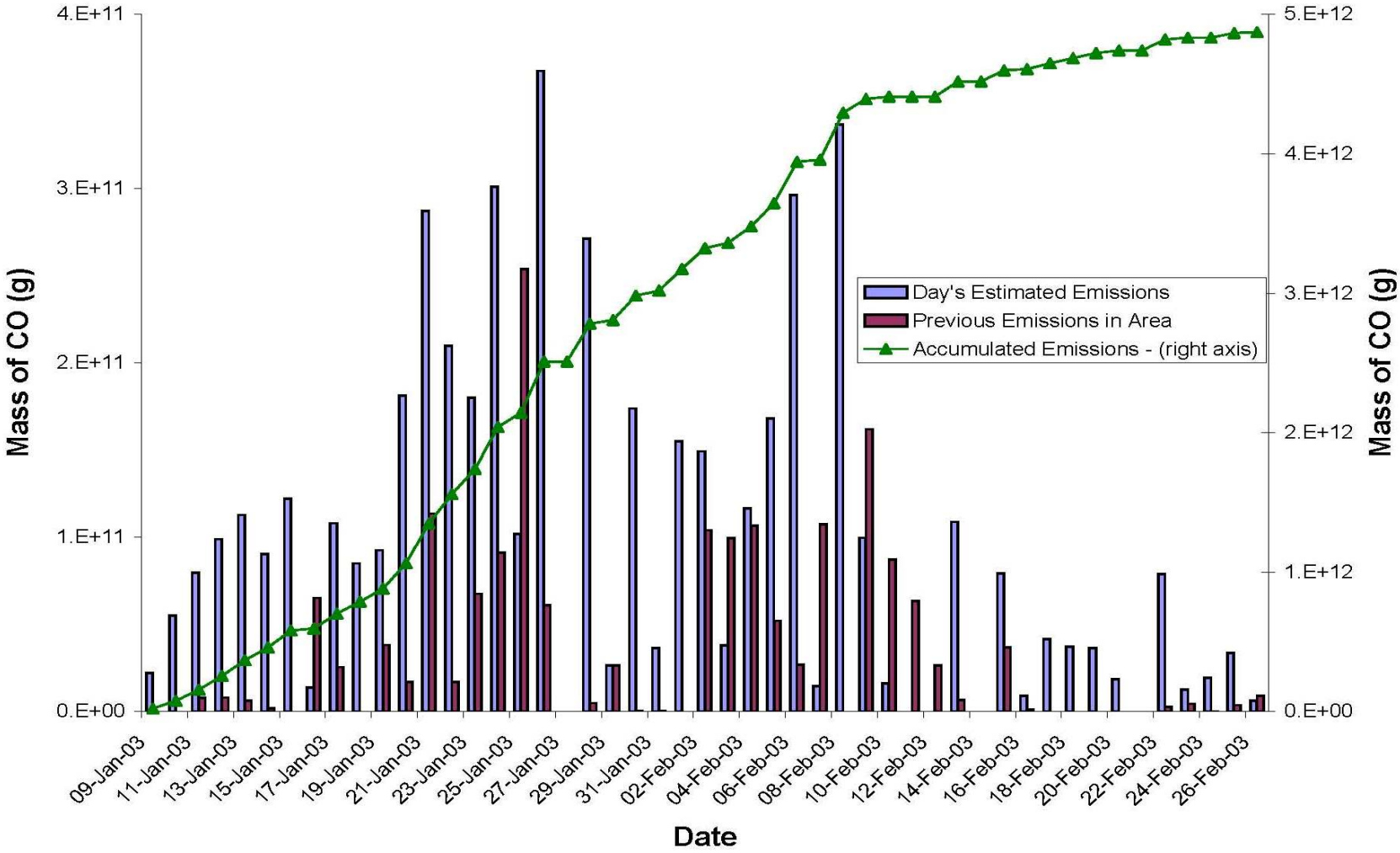

Figure 4-13: The estimated emissions of CO for each day alongside the previous emissions still remaining in the area as predicted by TAPM modelling. The sum of these two terms is M_{CO}, the mass of enhanced CO derived from the MODIS AOD data for the day. The accumulated total mass of CO emitted by the fires is also shown on a separate right-hand axis.

Using the method described above, the total mass of CO emitted by the Canberra fires from 8th January 2003 to 26th February 2003 is estimated to be 4.9×10^{12} g (4.9 Tg). The major uncertainty in this estimate is likely to arise from smoke plumes that are missed either as a result of white pixels in the MODIS data or because the emissions have dispersed out of the region before the satellite passes overhead. One extreme example of this occurred on the 18th January 2003 when the fires were at their most intense [*Fromm et al.*, 2006]. On this day the smaller region from -30° to -40° latitude and 143° to 155° longitude is dominated by white pixels and so the enhanced CO loading in the atmosphere at the time of the satellite overpass estimated by the method described above is low (8.5×10^{10} g). Extending the region sampled to the larger region from -25° to -46° latitude and 135° to 160° longitude captures a large smoke plume to the northeast of the fires over the ocean (see Figure 4-4). Using this larger area the total enhanced atmospheric CO estimated from the Aqua overpass on the 18th January 2003 is an order of magnitude greater at 8.5×10^{11} g. The estimated emissions for days up to the 17th January 2003 are all below 2.5×10^{11} g so clearly these emissions are mainly fresh emissions from the 18th January that are missed when using the smaller region.

The use of the small region is thus likely to lead to an underestimate of the total emissions. For this reason calculations using MODIS AOD data were also undertaken for a larger region (from -25° to -46° latitude and 135° to 160° longitude). As mentioned before this region is too large for the TAPM model. Instead TAPM results from the smaller region were applied to the larger region to estimate the proportion of smoke remaining from earlier emissions, ($\mathbf{R_{\%}/C_1}$). Since the modelling does not encompass the entire region it is not possible to use visual clues to decide the degree of overlap between real AOD data (not white or black pixels) and the modelled remaining smoke plumes. Thus for the larger region the second correction factor $\mathbf{C_2}$ is simply the fraction of pixels with real MODIS AOD in the image for the day, (see Figure 4-14). The average value for $\mathbf{C_2}$ for the larger region from all fire days is 53%. The results of the calculations for the larger region are given in Figure 4-15.

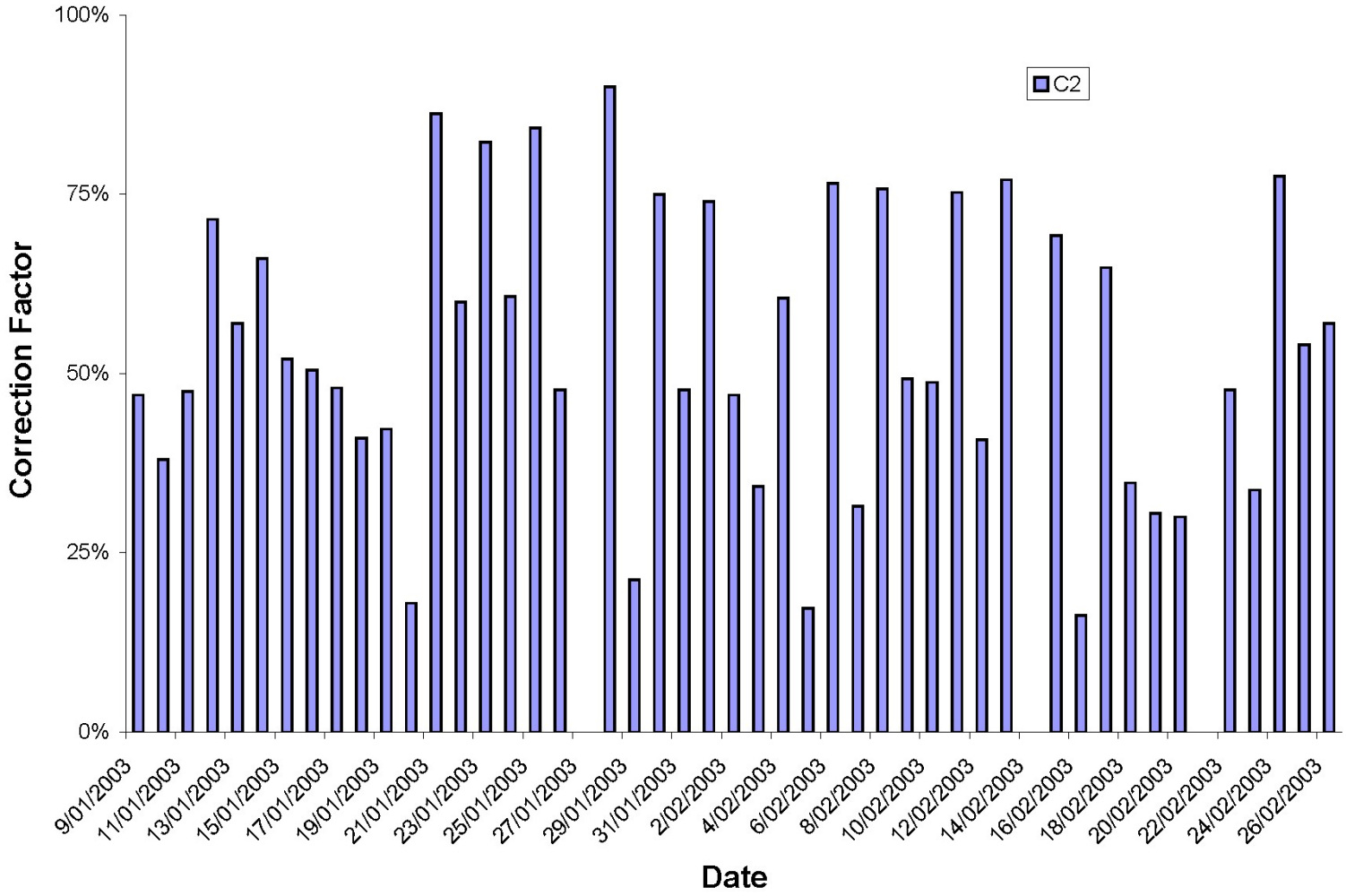

Figure 4-14: The correction factor C_2 for the larger region calculations. Note that the estimated proportion of previous emissions that remain in the area ($R_{\%}$) and the correction factors C_1 are taken from TAPM results for the smaller area (Figure 4-12).

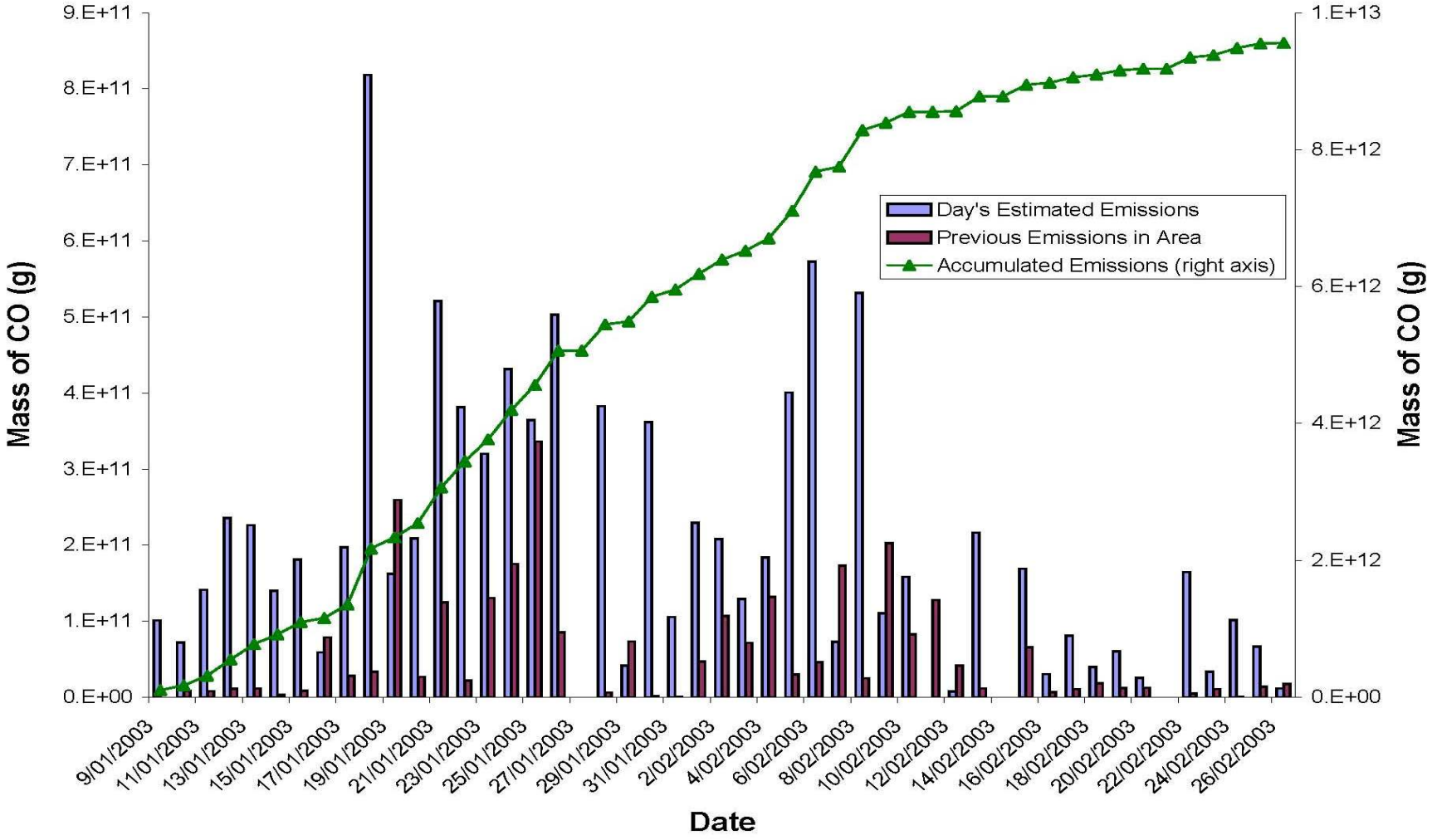

Figure 4-15: The estimated emissions of CO for each day taken from the large region alongside the previous emissions still remaining in the area as predicted by TAPM modelling. (The sum of these two terms is M_{CO}.The accumulated total mass of CO emitted by the fires is also shown on a separate right-hand axis.

The results from the smaller and larger regions may be combined to give a range for the total emissions. The lower value can be given with some confidence as the smallest mass of CO that could have been emitted from the fires, whilst the upper limit could still be an underestimate if smoke plumes missed in the white pixels of the MODIS AOD outweigh any possible double counting that results from using the dispersion model results from the smaller region.

4.7 Results and Uncertainties

Using MODIS AOD data the estimated total amount of CO emitted from the Canberra fires is 4.9 – 9.6 Tg. The lower figure in this range comes from calculations using the smaller region (that probably underestimates the emissions as explained above). The higher figure in the range comes from calculations using the larger region and may be overestimated or underestimated depending upon the relative magnitude of the effects of

1. double counting smoke not dispersed from the region between satellite overpasses (leading to overestimation of the emissions) and
2. undetected enhancements in AOD that result from smoke missed between clear satellite images or lost in the white pixels, (leading to underestimation of the emissions).

There are five obvious sources of uncertainty in this method:

1. Uncertainties in the relationships between AOD and trace gas amounts range from approximately 3% - approximately 10% (see Table 3-2).

2. Uncertainties resulting from the choice of the threshold value of AOD used to identify enhanced AOD that results from smoke and the choice of background AOD that is subtracted from the MODIS measured AOD to give enhanced AOD. The sensitivity of the estimated emissions to the choice of background value may be determined by using an AOD value of 0.2 for both the threshold value and the background value, yielding lower total emissions estimates,

(18% lower for the TAPM region and 21% lower for the larger region). A value of 10% being approximately half this difference is used as an estimated uncertainty that derives from the choice of background AOD value.

3. Potential biases between (a) the ground-based AOD measurements used to define the relationships between AOD and trace gas amounts and (b) the 1° by 1° averaged MODIS AOD values used to make the total emissions calculations. The viewing geometry of the two instruments differs and the satellite measurements are integrated over a large area at a single time whereas the ground-based measurements sample less than 1 m square but are averaged over several hours, therefore the values are only expected to be broadly comparable. Figure 4-16 shows the comparison between MODIS AOD measurements and ground-based AOD measurements indicating that the MODIS data are on average 27% ± 23% lower than the equivalent ground-based data. This could be caused by instrumental, analysis or orographic differences, leading to a potential underestimate of the emissions. Figure 4-17 shows the comparison of column CO amounts inferred from the MODIS AOD measurements using the nine closest 1° by 1° grid spaces to Wollongong compared to CO column amounts directly measured by ground-based FTIR. The difference here is reduced to 17% ±18% because of the effect of adding in the background column of 1.5×10^{18} molecules cm^{-2} of CO.

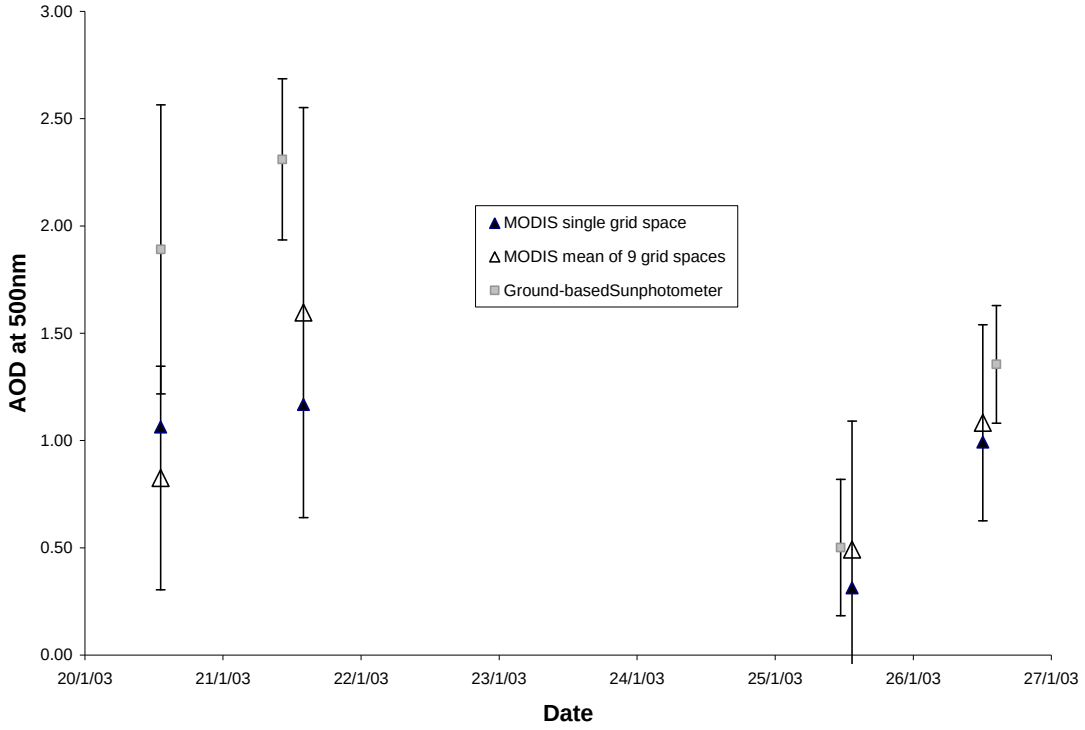

Figure 4-16: Comparison of ground-based AOD measurements (small grey squares) with MODIS AOD measurements for the single 1° by 1° grid space over Wollongong (small black triangles) and the 9 closest 1° by 1° grid spaces around Wollongong (open triangles).

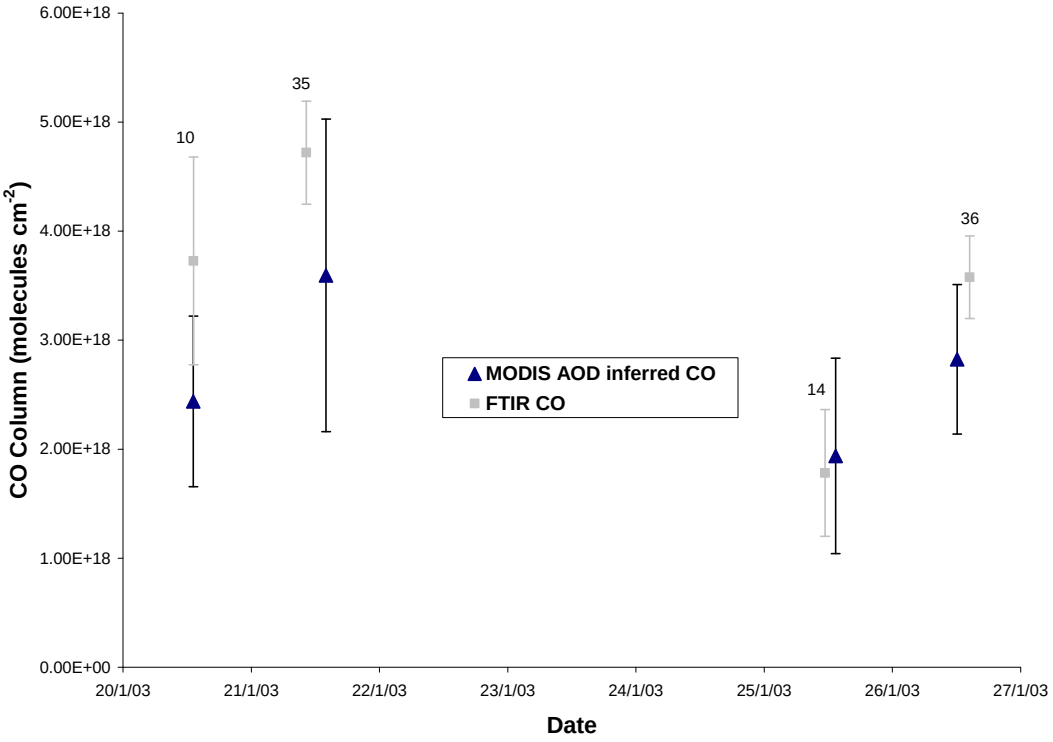

Figure 4-17: Comparison of ground-based FTIR measurements of column CO (grey squares) with MODIS AOD inferred CO columns using the 9 closest 1° by 1° grid spaces around Wollongong (black triangles). The 1σ standard deviations are shown as error bars. The number of spectra used to calculate the average column CO from the FTIR are given above each point.

4. Undetected enhancements in AOD that result from smoke missed between clear satellite images or lost in the white pixels may lead to an underestimate of the emissions. The average percentage of white pixels is 34% in the larger region and 47% in the smaller region. Some of the undetected smoke may be detected the following day so the white pixel count must be adjusted by the amount that is modeled as being lost from the region each day. This modeling was only done for the smaller region so the value of 59% is used for both regions (see below for estimate of 41% average amount of emissions remaining the following day). This gives an uncertainty (in the form of a negative bias) of 20% for the larger region and 28% for the smaller region.

5. Errors in the TAPM modeling of the dispersion of smoke from the region may lead either to double counting smoke not dispersed from the region, or to wrongly identifying fresh smoke as being from earlier emissions. Hence uncertainties in the dispersion modeling can lead to both underestimates and overestimates of emissions. The average % of the emissions still remaining in the model at the time of the next satellite overpass is 41% (smaller region only).

Clearly there are some significant assumptions & potential errors in the TAPM dispersion modeling:

(a) The satellite images give the horizontal distribution of the smoke plumes but not the vertical distribution. Thus it is necessary to model the dispersion of the smoke from the assumed source areas. The detected enhancements in AOD are all assumed to result from emissions in the previous 24 hours, and are released from the two area sources in the centre of the modeled region. The resulting model output shows an average of 41% of emissions still remaining in the model the following day. No correction is made for emissions still remaining 2 days later, because of the difficulty in trying to determine the dispersion of smoke when at least the vertical location is unknown. It is estimated that this will introduce an error of less than 10% and be partially offset by the overestimate of

the amount of emissions remaining from one day to the next that derives from the assumption that all detected enhancements were emitted in the centre of the model.

(b) The use of area sources reduces the problems of the lack of mass conservation in the model, but does not truly represent the locations of the active fires on each day. The synoptic scale meteorology used is on a 0.75° longitudinal by 1° latititudinal grid so this rough analysis of the location of the fires is unlikely to introduce major additional uncertainties.

(c) The fact that TAPM is not mass conserving means that the use of a normalizing factor is required and adds uncertainty to the estimate of the proportion of the smoke plume that is dispersed out of the region by the time the next satellite overpass occurs. The average and 1σ standard deviation for the normalization factor used is 105% ± 27%.

(d) An assumption about the rate of emission from the fires is made. A constant rate could be assumed – instead it was assumed that the fires would burn more fiercely during the day than at night.

It is not a simple task to quantify the uncertainties introduced into the emissions estimate by errors in the dispersion modeling. The average adjustment made to try to avoid double counting of smoke is the percentage of emissions remaining in the model multiplied by the percentage of non-white pixels. The average adjustment to the predicted emissions is to reduce the measured enhancement by 26% in the smaller region and by 25% in the larger region. Calculation of 1σ standard deviations of the adjusted amounts yields values of 32% and 26% respectively. These numbers must be interpreted with caution since clearly the adjustments do not follow a normal distribution as they are constrained to fall between 0 and 100%. In order to construct a budget for the total uncertainties in the estimated emissions using MODIS AOD, a value must be assigned to the uncertainty in the modeling of remaining smoke and the resulting adjustment to the emissions calculated for the day. For this purpose an arbitrary guess is made that the uncertainties amount to half of the average adjustment made and a value of 13% is therefore assigned.

The uncertainties analysis described above is limited by sections of the budget that are hard to quantify. The resulting total uncertainties are very similar for the different gases

and different regions and may therefore be simplified by rounding up and assigning an uncertainty of ± 32 % to all emissions estimates. A table listing all the uncertainties is given in Appendix 4.

4.8 Total emissions estimates of trace gases from the Canberra fires of 2003

The estimate from this study, of 4.9 – 9.6 Tg CO released from the Canberra fires, compares with a total carbon emissions estimate of in excess of 40 Tg C from the Canberra fires made using the product of burned area, above-ground biomass, fraction consumed and emission factor [*Mitchell et al.*, 2006] & [private communication *M. Raupach and R. Mitchell*]. Two independent estimates of both the total annual global carbon emissions and the total annual global emissions of CO from vegetation fires give the % of total carbon emitted as CO as 16% [*Ito and Penner*, 2004] and 22% [*Schultz et al.*, 2008]. Using a mean value of 19% gives a value for the emissions of CO from the *Raupach/Mitchell* estimate of 7.6 Tg CO. This is within the estimated range from this study.

This is a very significant emission from a single fire episode given that the mean global annual emission of CO from all vegetation fires is estimated as 330 Tg CO yr^{-1} for the 41 years from 1960 – 2000 [*Schultz et al.*, 2008] and in a separate study as 496 Tg CO yr^{-1} for the year 2000 [*Ito and Penner*, 2004]. Estimates for the total annual CO emissions from Australian vegetation fires in the literature include:

1. between 11 - 40 Tg CO yr^{-1} for the years 1960-2000, averaging 23 Tg CO yr^{-1} [*Schultz et al.*, 2008]
2. 17 Tg CO yr^{-1} for 1991 [*Hurst et al.*, 1994b]
3. 7 Tg CO yr^{-1} for 2000 [*Hoelzemann et al.*, 2004]

Thus the *Raupach/Mitchell* estimate of CO emitted from the Canberra fires actually exceeds the lowest of the estimates for the total annual CO emissions from all Australian fires for the year 2000. A better comparison is the study by Shultz *et al* [2008], that covers 41 years from 1960 – 2000. The estimate in this study for the

Canberra fires is 17% – 33% of the average estimated annual CO emission by Shultz *et al* [2008] from all Australian vegetation fires, which also includes burning of savanna grasslands and woodlands in the tropical north of Australia.

Table 4-3 shows estimated total emissions from the Canberra fires for all of the trace gases measured at Wollongong by FTIR remote sensing through the smoke plumes. Lower and upper estimates are defined by using the values for the mass of each trace calculated from the enhanced AOD detected by MODIS in both the smaller and the larger regions defined above. Where available, the estimated average global annual emissions of the trace gases from all vegetation fires from Shultz *et al* [2008] are also given, along with the percentage of the average global annual emissions that were emitted by the Canberra fires. By this calculation the total H_2CO released by the Canberra fires represents 3.1% of the average annual global emission of H_2CO by vegetation fires. In contrast the C_2H_6 released represents only 0.7% of the average annual global emissions from vegetation fires.

4.9 Summary

In this chapter a new technique for estimating emissions from large vegetation fires has been applied to the Canberra fires of 2003. Future improvements in the algorithms for determining the AOD of the atmosphere from satellite-based instruments like MODIS will reduce the fraction of white pixels and improve the accuracy of this method. Additional improvements would result from the use of an atmospheric dispersion model with better mass-conservation properties, that could cover a larger area whilst retaining the resolution of the meteorological inputs.

In summary, there are significant uncertainties inherent in the use of this method, but conventional methods of estimating emissions from biomass burning also suffer from large uncertainties. The uncertainties in the study described in this thesis are mainly independent of the uncertainties in conventional methods of estimating emissions and so this new technique is a valuable additional tool for characterising emissions from vegetation fires.

Table 4-3: Estimated total emissions from the Canberra fires for all of the measured trace gases.

Gas	Lower Estimate of Mass emitted from Canberra Fires[1] (Tg)	Higher Estimate of Mass emitted from Canberra fires[2] (Tg)	Average Global Annual Emissions (Tg)	% of average global annual emissions from Canberra Fires[3]
CO	4.9	9.6	330	2.2%
HCN	0.017	0.034	Not available	
NH_3	0.036	0.070	4.90	1.1%
H_2CO	0.081	0.16	3.90	3.1%
C_2H_2	0.011	0.022	Not available	
C_2H_4	0.032	0.062	4.80	1.0%
C_2H_6	0.011	0.022	2.30	0.7%
HCOOH	0.068	0.13	Not available	
CH_3OH	0.094	0.18	7.70	1.8%

Notes:

1. Lower estimate comes from calculations using the smaller of the two regions.
2. Higher estimate comes from calculations using the larger of the two regions.
3. The average of the lower and higher emissions estimate for the Canberra fires expressed as a percentage of the average global emissions from vegetation fires as given in Schultz *et al* [2008] for years 1960 – 2000.

Chapter 5 : CO and AOD Measurements from Darwin

The measurements and modeling described in the previous chapters characterize the emissions from southeast Australian forest fires. Tree species on the Australian continent are predominantly types of eucalypts, and so the measurements are likely to be representative of forest fires elsewhere in Australia. Forest fires represent 14% of the annual burnt area and 43% of the dry matter burned in Australia, with the rest coming from burning of savanna grasslands and woodlands [*Ito and Penner*, 2004]. In order to fully characterize the emissions from biomass burning in Australia measurements of emissions from savanna regions must also be made.

5.1 Near-Infrared Spectra Recorded from Darwin 2005-2008

Solar remote sensing measurements have been made from Darwin since August 2005 as part of the Total Column Carbon Observing Network (TCCON) [*Deutscher et al.*, 2009]. This network was established with the aim of making measurements of total column amounts of carbon dioxide to a precision of 0.1% or better. The network of high resolution Fourier transform spectrometers is designed to be able to establish the differences in carbon dioxide amounts between Northern and Southern hemispheres and to act as a validation network for the Orbiting Carbon Observatory (OCO). The instrument at Darwin (see Figure 5-1) is one in the network that is run with an automated system which includes the dome, weather station, solar tracker and Fourier transform spectrometer.

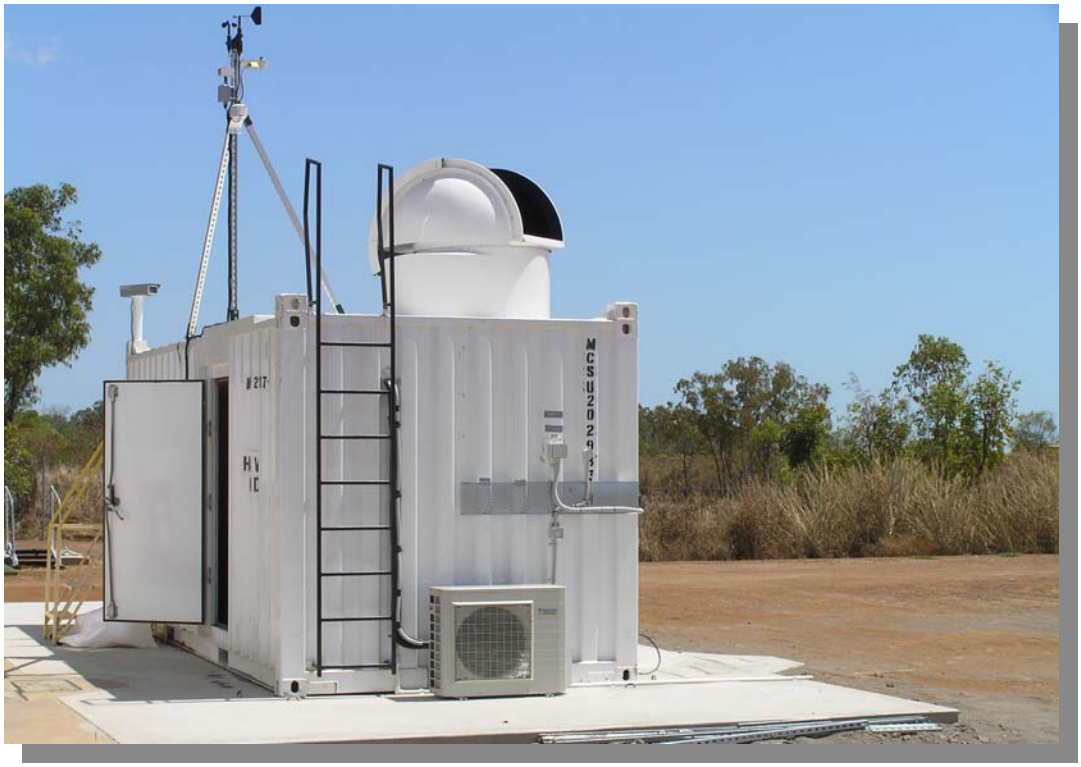

Figure 5-1: Photograph of the TCCON observatory at Darwin showing the container, tracker dome and weather station.

All of the spectrometers in the network are equipped with two near infrared detectors, a silicon (Si) detector that is sensitive from approximately 9000cm^{-1} to 15500cm^{-1} and an indium gallium arsenide (InGaAs) detector that is sensitive from approximately 4000cm^{-1} to 12000cm^{-1}. These collect two simultaneous spectra by use of a dichroic filter to split the solar beam between the two detectors. Spectra are recorded with a resolution of 0.02 cm^{-1} at a sample rate of 20 kHz (equivalent to a scanner speed of 0.633 cm s^{-1}), resulting in a collection time of 76 s for a single scan. The spectra from the InGaAs detector are used to retrieve carbon dioxide (CO_2) from bands near 6200cm^{-1} and the spectra from the Si detector are used to retrieve simultaneous oxygen (O_2) columns from the A-band near 13000cm^{-1}. By ratioing the CO_2 columns to simultaneous O_2 columns the many uncertainties that come from errors in the radiative transfer calculations and instrumental effects will be removed. The regions of the spectrum include those used by the OCO satellite instrument and include the CO overtone band at 4260 cm^{-1}. The automated system ensures that spectra are recorded whenever the weather conditions permit so CO data are available with very good temporal coverage since August 2005 when the system began operation. The

spectrometer in Darwin is also equipped with an InSb detector that is sensitive from approximately 2000cm^{-1} to 6500cm^{-1}. InSb spectra are also recorded with a resolution of 0.02 cm^{-1} and an integration time of 76 seconds by manual intervention to override the automation system and are discussed in more detail in the chapter 6.

5.2 Analysis of Near Infrared Spectra for CO

More than one hundred and seventy thousand InGaAs spectra were recorded between August 2005 and May 2008. Some of the spectra have lower signal-to-noise ratios than others due to rapid corrosion of the solar tracker mirrors which were replaced in November 2005 and again in October 2006. To date it has not been possible to analyse these spectra with profile retrieval using SFIT2 (because of data storage issues), but they have been analysed with GFIT for CO total column amounts using the overtone band at 4260cm^{-1}. Figure 5-2 shows an example InGaAs spectrum from August 2005.

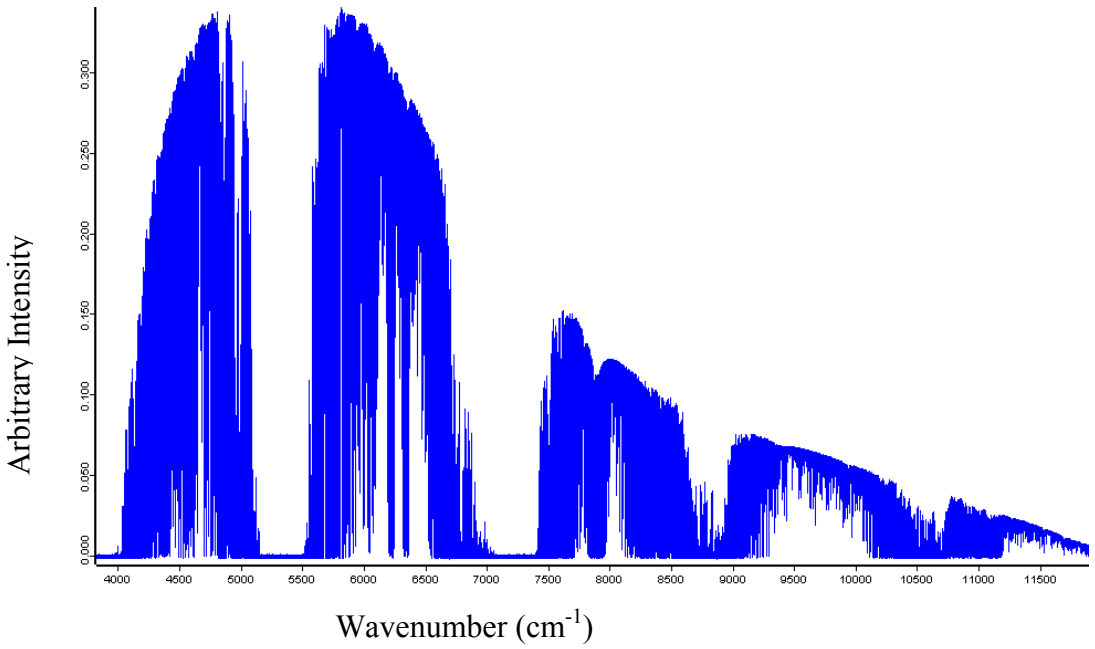

Figure 5-2 shows an example InGaAs spectrum extending from 4000cm^{-1} to 12000cm^{-1}. The CO overtone band is around 4200cm^{-1}.

As described earlier, the GFIT fitting algorithm scales the initial (*a priori*) VMR profile by a single multiplicative factor and for this reason the resulting columns can be

quite sensitive to the choice of initial VMR profile. For this analysis an initial profile was created by adapting a measured profile from the northern hemisphere [*Pougatchev et al.*, 1998] by reducing the tropospheric CO to give 73 ppb of CO at the ground decreasing slowly with altitude and converging with the measured values at 14 km. The resulting profile is shown in Figure 5-3 and was chosen to be representative of clean air conditions in Darwin.

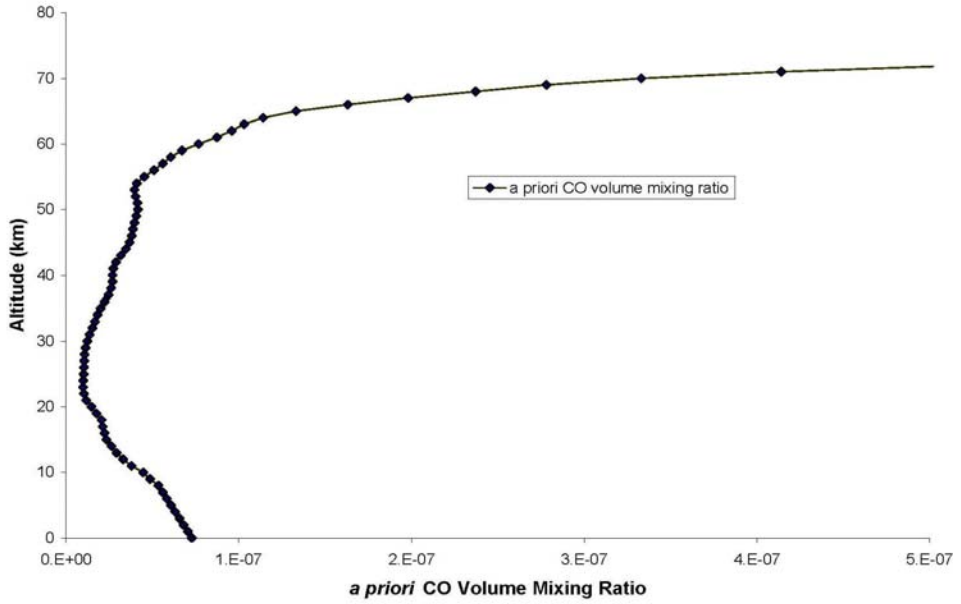

Figure 5-3: The *a priori* CO VMR profile used in GFIT analysis of NIR spectra from Darwin.

A survey of CO lines in the 1st overtone band from 4200cm^{-1} to 4300cm^{-1} was conducted in order to locate suitable microwindows for retrieving atmospheric CO total column amounts. Fits to microwindows in this region can be poor due to interference from poorly characterised solar CO lines making many of the possible options unsuitable. Table 5-1 summarises the results of this survey – two microwindows were chosen from 4226.5 cm^{-1} to 4228.3cm^{-1} fitting CO and CH_4 and from 4231.5 cm^{-1} to 4232.1 cm^{-1} fitting CO, H_2O, HDO and CH_4.

Table 5-1: Summarises the results of a survey of possible microwindows to use for retrieving atmospheric CO total column amounts. All the major CO lines in the overtone band from approximately 4200cm^{-1} to 4300cm^{-1} are included but only two microwindows were chosen. These are shown in bold.

line position (cm^{-1})	start window (cm^{-1})	end window (cm^{-1})	gases to fit	fit	comment
4199.92	4198.30	4201.10	CO, CH4, H2O	poor	overlapping water and solar features
4209.34	4209.05	4210.15	CO, CH4, H2O, HDO	poor	overlapping solar feature - poor fit
4213.95	4213.35	4215.25	CO, CH4, H2O, HDO	poor	overlapping water and solar features
4222.95	4222.45	4225.00	CO, CH4, H2O, HDO	poor	overlapping water and solar features
4227.36	**4226.50**	**4228.30**	**CO, CH4**	**good**	**small underlying solar feature**
4231.69	**4231.50**	**4232.10**	**CO, CH4, H2O, HDO**	**good**	**small underlying solar feature**
4235.95	4235.21	4236.41	CO, CH4, H2O, HDO	poor	overlapping solar feature - poor fit
4244.26	4243.40	4245.60	CO, CH4	poor	overlapping solar feature - poor fit
4248.32	4248.26	4248.38	CO, CH4	poor	interfering solar feature
4274.74	4274.00	4275.00	CO, CH4, H2O, HDO	ok	small underlying solar feature
4278.24	4277.12	4278.92	CO, CH4	poor	overlapping ch4 and solar features
4281.66	4281.35	4281.95	CO, CH4	poor	overlapping solar feature - poor fit
4285.00	4284.09	4285.35	CO, CH4	not bad	interfering solar feature - not very good fit
4288.29	4287.45	4292.15	CO, CH4, H2O, HDO	not bad	interfering solar feature - not very good fit
4291.50	4290.40	4292.15	CO, CH4, H2O, HDO	not bad	interfering solar feature - not very good fit
4297.70	4297.00	4299.20	CO, CH4	poor	overlying solar feature - poor fit
4300.70	4299.00	4301.70	CO, CH4	poor	overlying solar feature - poor fit
4303.62 & 4306.48	4302.72	4307.22	CO, CH4, H2O	poor	overlying solar feature - poor fit
4309.26	4308.50	4310.20	CO, CH4, H2O, HDO	poor	overlying solar feature - poor fit

When the atmosphere is very smoky the VMR profile has too little CO in the troposphere and the shape of the absorption line in the calculated spectrum is too narrow. The resulting total column amount retrieved from GFIT profile scaling is too low. The magnitude of this effect was estimated by analysing the spectra recorded with the InSb detector (see Chapter 6) with both the GFIT analysis described above and with SFIT2 optimal estimation profile retrieval. The overall bias between the two retrieval methods for the InSb spectra was 10%, with the GFIT results lower than SFIT2 results. It should be noted that the InSb spectra are mainly from the dry season and hence on average smokier than the InGaAs spectra, which accentuates this bias. The bias is roughly zero for days when the total column is low (~ 1.2 x10^{18} molecules cm^{-2}) and increases to 15% - 20% for higher total columns in smoky conditions (~2.5 x10^{18} molecules cm^{-2}). Example fits to the two microwindows are given in Figure 5-4 and Figure 5-5.

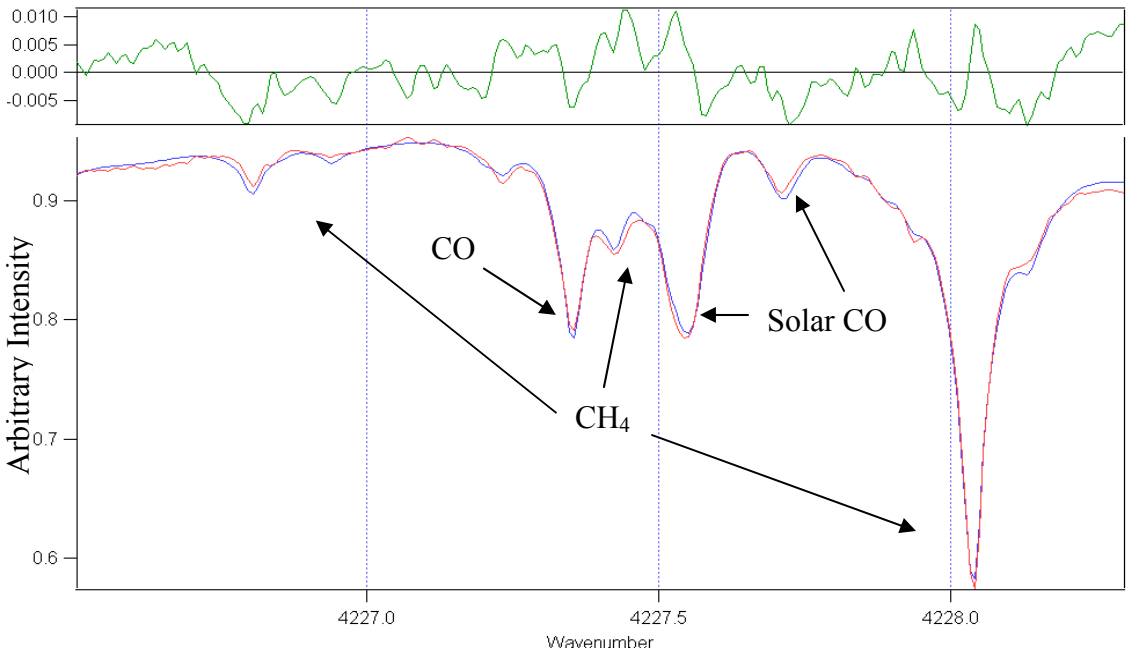

Figure 5-4 : An example fit to the microwindow from 4226.5 cm^{-1} to 4228.3 cm^{-1} fitting CO and CH_4 including the CO line at 4227.36 cm^{-1}. The red line is the measured spectrum, the blue is the simulated spectrum and the green line above shows the difference between the two (the residual).

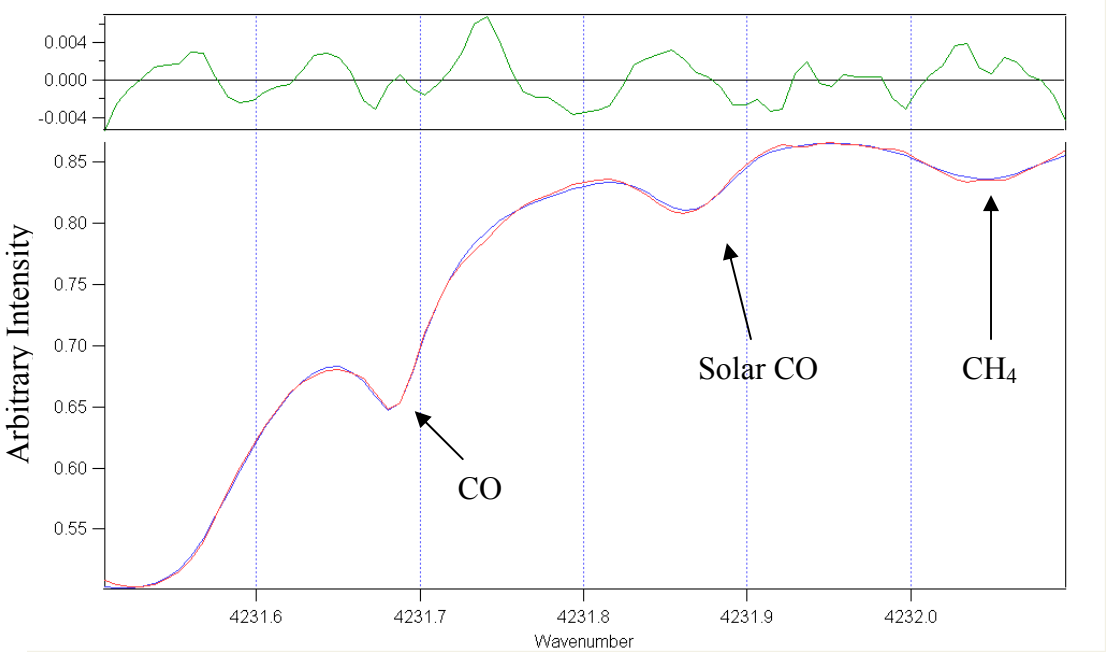

Figure 5-5: An example fit to the microwindow from 4231.5 cm^{-1} to 4232.1 cm^{-1} fitting CO, H_2O, HDO and CH_4 including the CO line at 4231.69 cm^{-1}.

The derived column amounts for over 170,000 spectra were loaded into the software package "Igor-pro" for post-processing. Spectra with signal-to-noise uncertainties in the derived column amount greater or equal to 1.0 $x10^{18}$ molecules cm^{-2} were excluded as were spectra for which the fitting had run to the maximum 10 iterations and therefore not converged fully. Daily averages were then calculated using a script modified from that used for post-processing of the CO_2 columns. Days with fewer than 10 spectra remaining after the post-processing were excluded, whilst all other days are plotted in Figure 5-6.

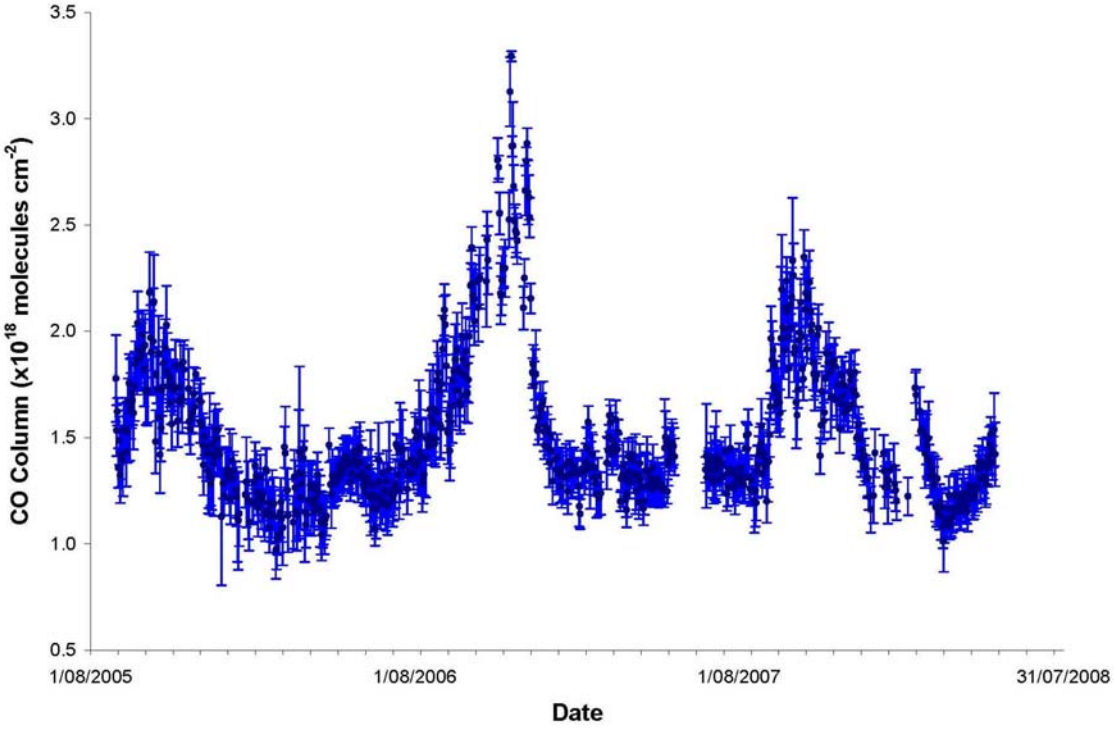

Figure 5-6: Shows daily averaged CO column amounts derived from InGaAs spectra recorded at Darwin. Points are the daily average CO column and the error bars are the 1σ standard deviation.

The time series of daily average CO total column amounts shown in Figure 5-6 has some interesting features, including an annual cycle with values typically peaking around 2 – 2.5 x10^{18} molecules cm^{-2} towards the end of the local dry season in September or October. This equates to an in situ amount of ~130 nmol.mol^{-1} in the lowest 1km of the atmosphere. Low values (~ 1.1 x10^{18} molecules cm^{-2}) are usual from January to March in the wet season, (equivalent to the *a priori* profile with a concentration in the lowest 1km of 72 nmol.mol^{-1}). Peak values in 2006 are noticeably larger and later, peaking at around 2.8 x10^{18} – 3.0 x10^{18} molecules cm^{-2} in November 2006, (~ 200 nmol.mol^{-1} in lowest 1km). During 2006 there were exceptionally severe fires in Indonesia [*Rinsland et al.*, 2008] where the fire season is later than in northern Australia. Transported pollution from these fire events provides a possible explanation for the unusual CO column amounts observed in this El Nino year. One example occurred on 14th November 2006, when an Indonesian smoke plume extended towards Northern Australia and is captured well by the MODIS true colour image shown in Figure 5-7.

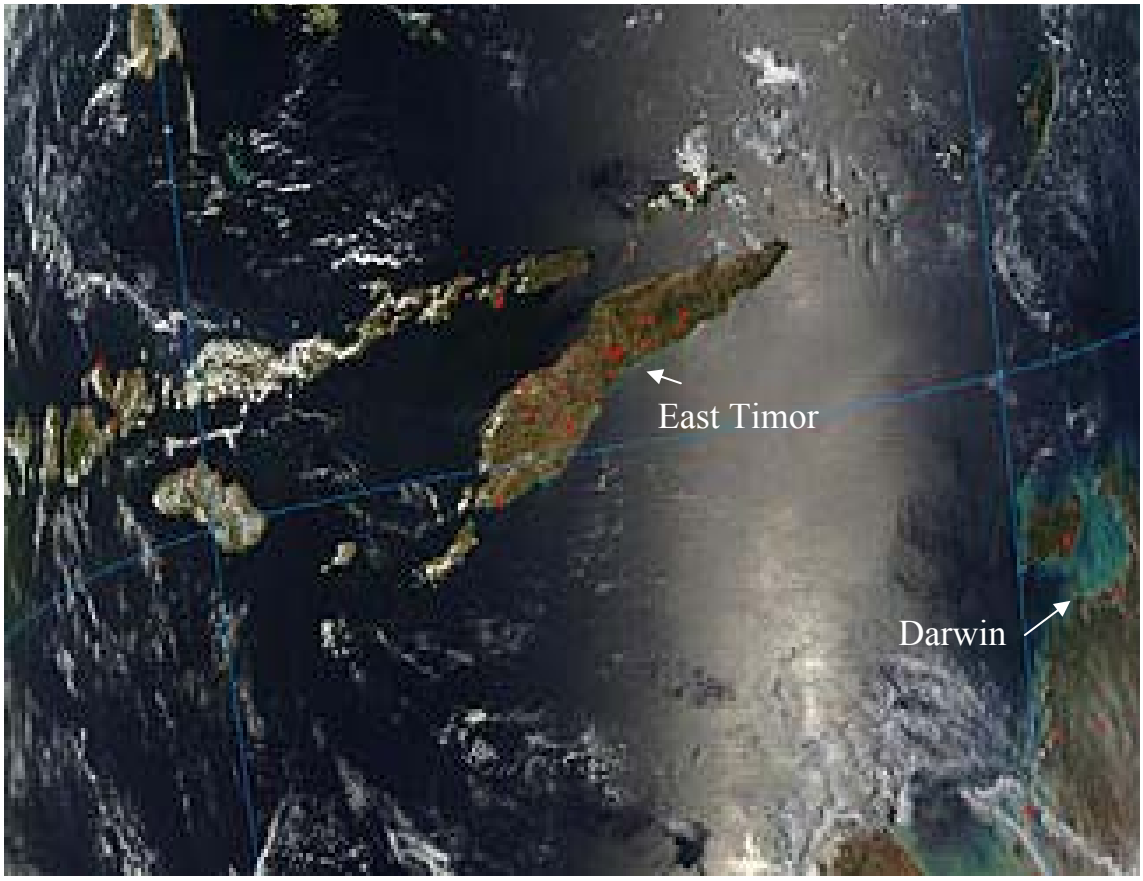

Figure 5-7: MODIS true colour image showing an Indonesian smoke plume extending towards Northern Australia on 14th November 2006.

The transported pollution from the unusually intense Indonesian fires of 2006 is also clearly visible in CO measurements made from space by the MOPITT instrument on board the NASA EOS Terra satellite in November 2006 (see Figure 5-8 lower panel). Large enhancements in the average monthly CO amounts are visible all across Indonesia and extending west far into the Indian Ocean, east into the North Pacific Ocean, north into China and south into the north & west of Australia. The monthly averaged amounts of CO during November 2005 (not an El Nino year) are shown for comparison in the upper panel of Figure 5-8.

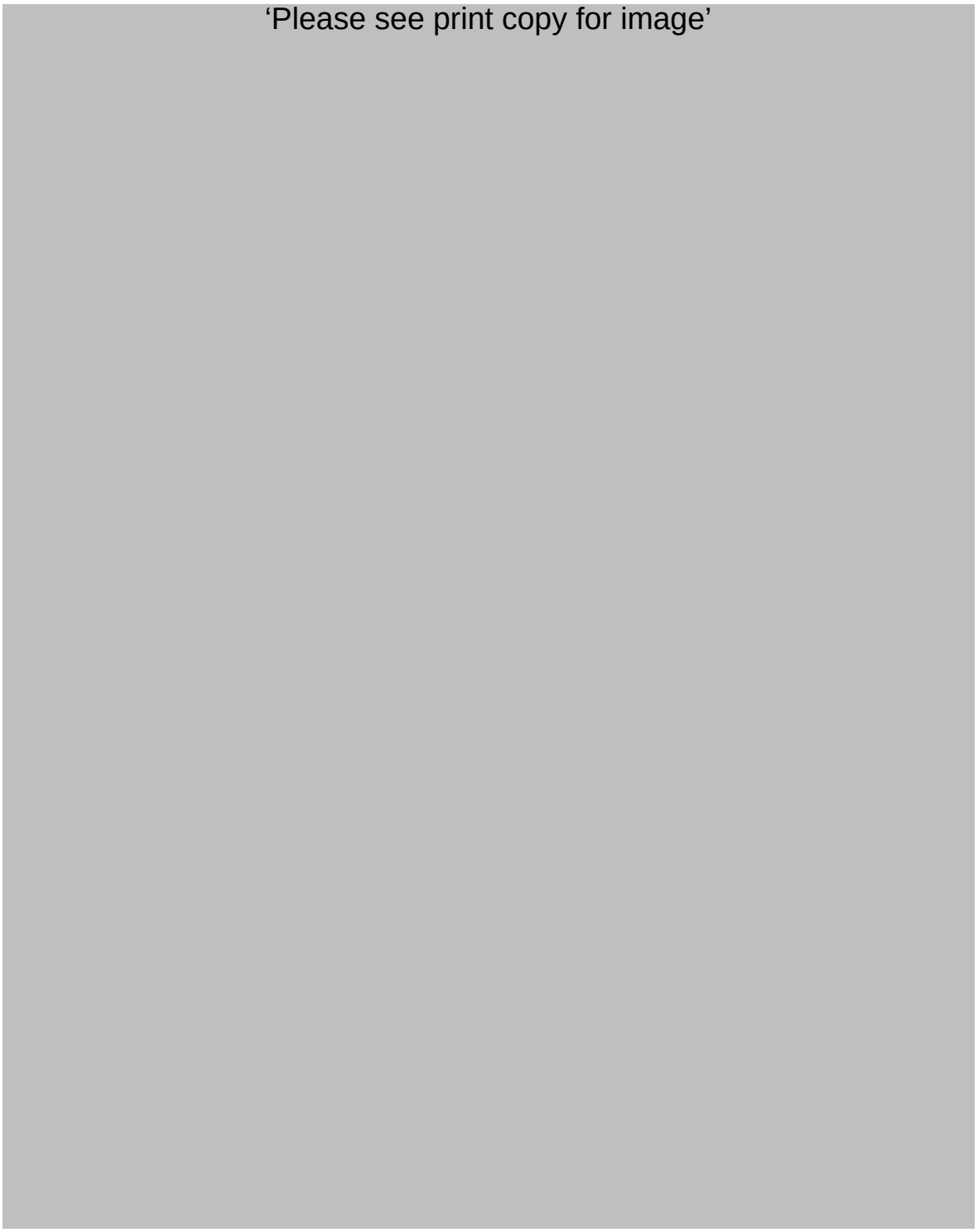

Figure 5-8. (Prepared by D.P. Edwards). Monthly averaged CO VMRs (ppbv) at 700 hPa retrieved from MOPITT for November 2005 (upper panel) and November 2006 (lower panel).

5.3 Comparison with MOPITT

MOPITT is a nadir sounding instrument (downward pointing) on the NASA EOS Terra satellite launched in 1999. MOPITT measures the upwelling infrared radiance at 4.7 μm [*Drummond et al.*, 1996]. Optimal estimation techniques analogous to those used in ground-based FTIR retrievals are used to obtain concentration profiles of CO on a global basis at a reasonably high horizontal (~22km) and vertical resolution (~5km) [*Pan et al.*, 1998]. The time series of CO columns derived from the NIR spectra from Darwin have been compared with CO columns over Darwin from the MOPITT instrument (see Figure 5-9), provided by David Edwards of the National Center for Atmospheric Research (NCAR).

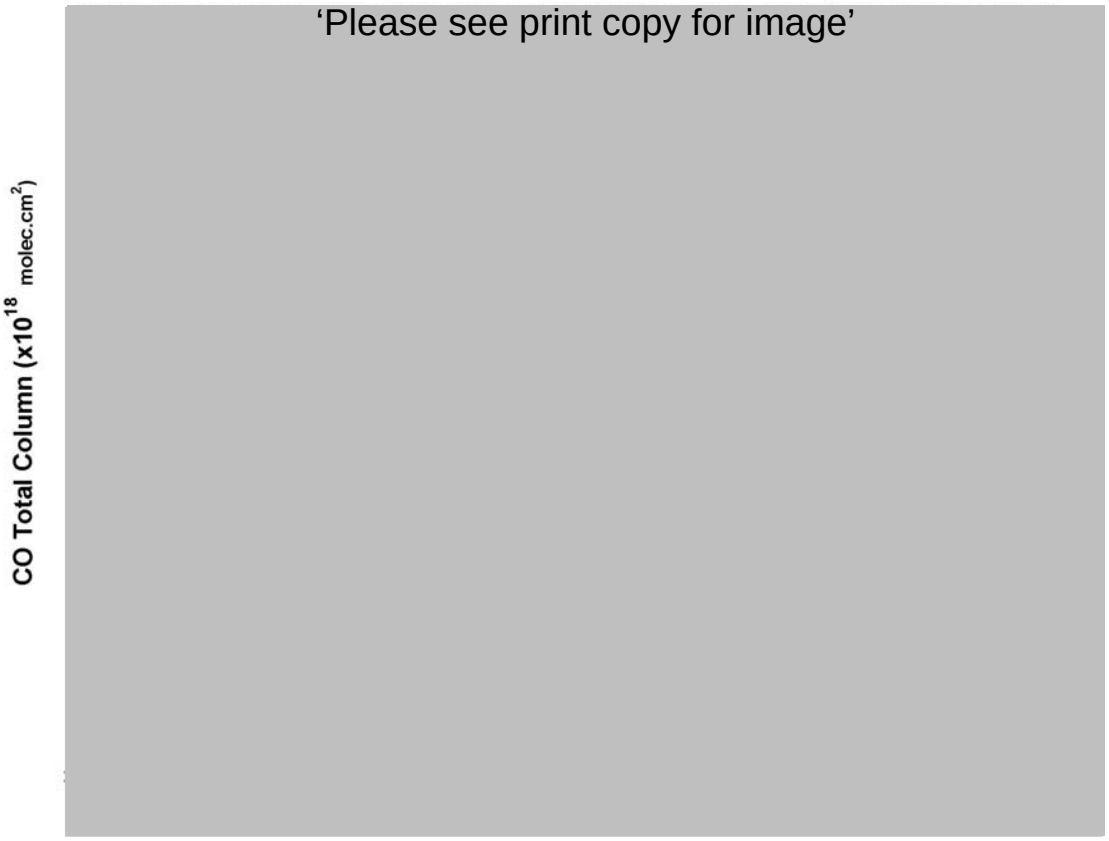

Figure 5-9. (Produced by D.P. Edwards). MOPITT CO measurements over Darwin (D.P. Edwards) are shown in green and CO from NIR ground-based FTIR measurements (this study) are shown in red. The upper plot shows daily averages as dots and weekly averaged values are plotted as a solid line. The lower plot represents the weekly mean anomaly as differences from the mean value for that week of the year determined from the entire MOPITT time series.

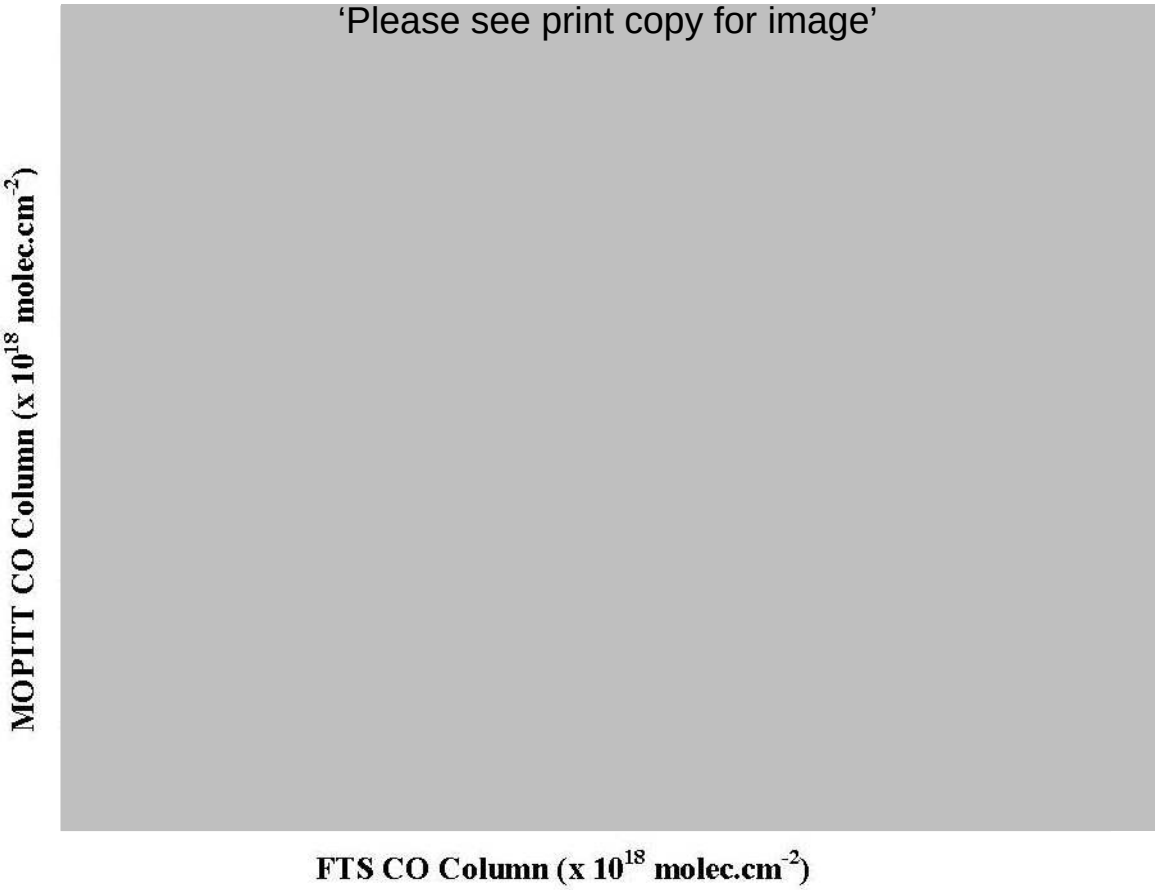

Figure 5-10. MOPITT CO columns plotted against FTIR CO columns measured at Lauder, New Zealand and Wollongong and Darwin, Australia. (Produced by D.P. Edwards).

The comparison between CO total columns derived from MOPITT and ground-based NIR spectra from Darwin shows a small bias between the two instruments (~10%) with the ground-based FTS values being lower. This difference is explicable by the different *a priori* profiles used in the two analysis procedures. As discussed above, a comparison of total column amounts derived using GFIT profile scaling and SFIT2 optimal estimation showed a negative bias of about 10% for GFIT, although this bias will be exaggerated because dry season InSb spectra were used that were specifically aimed at capturing smoke plumes (see Chapter 6). The MOPITT algorithm uses optimal estimation techniques with an *a priori* CO profile chosen from northern hemisphere climatology which will tend to produce a small positive bias (high CO columns) in clean air conditions in the southern hemisphere [*Pan et al.*, 1998]. Note that the comparison is done without smoothing the data with the averaging kernals of the data from the two instruments [*Rodgers et al.*, 2003]. Previous intercomparisons between

MOPITT CO and CO from ground-based FTIR spectrometers have shown inclusion of the averaging kernals has little impact on the resulting comparison *[Edwards, D. P. pers. communication]*.

The level of agreement between the two data sets is within that expected by the known biases. In particular, there do not seem to be significant events that are captured by the ground-based instrument and not by the satellite instrument. This is illustrated by the high correlation coefficient ($r^2 = 0.92$) determined from regression analysis of the weekly data shown in the plot of MOPITT CO columns versus NIR FTIR CO columns in Figure 5-10. Also shown are comparisons between MOPITT CO columns and CO columns derived from MIR FTS measurements at Wollongong and Lauder, New Zealand. The correlation coefficients are smaller for Lauder and Wollongong indicating that these sites are more likely to be influenced by smaller scale local sources that are not captured by the satellite instrument. This provides evidence that the CO time series from Darwin is dominated by regional scale processes such as large savanna fires in the northern tropical regions of Australia and smoke plumes transported from Indonesia, Africa and South America.

5.4 Measurements of AOD from Darwin

AOD data from sunphotometer measurements at Darwin were provided by Bruce Forgan of the Australian Bureau of Meteorology. The instrument used was a Middleton Solar SP02 Sunphotometer (see Figure 5-11) coupled to a Middleton solar tracker.

The instrument receives direct sun with a field of view of 5° and the radiation is detected through a set of 10 nm bandpass filters centred at 410 nm, 500 nm, 610 nm and 778 nm onto a silicon photodiode detector. Spectral transmission data are taken in parallel at each of the above wavelengths at 45 seconds past each minute with an integration time of 0.08 seconds. AOD values are calculated as described in section 2.4 and in addition an *Alexandrov* cloud filter is applied. This is an algorithm designed to separate out the effects of clouds from other aerosols [*Alexandrov et al.*, 2005].

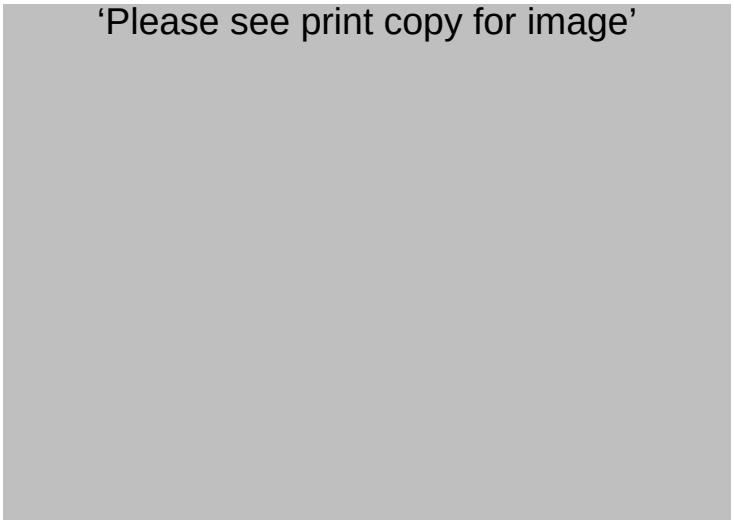

Figure 5-11: Photograph of a Middleton Solar SP02 Sunphotometer as used in Darwin. (Photograph reproduced with kind permission of David Mathias of Middleton Solar – see the Middleton Solar website: http://www.middletonsolar.com/products/product11.htm)

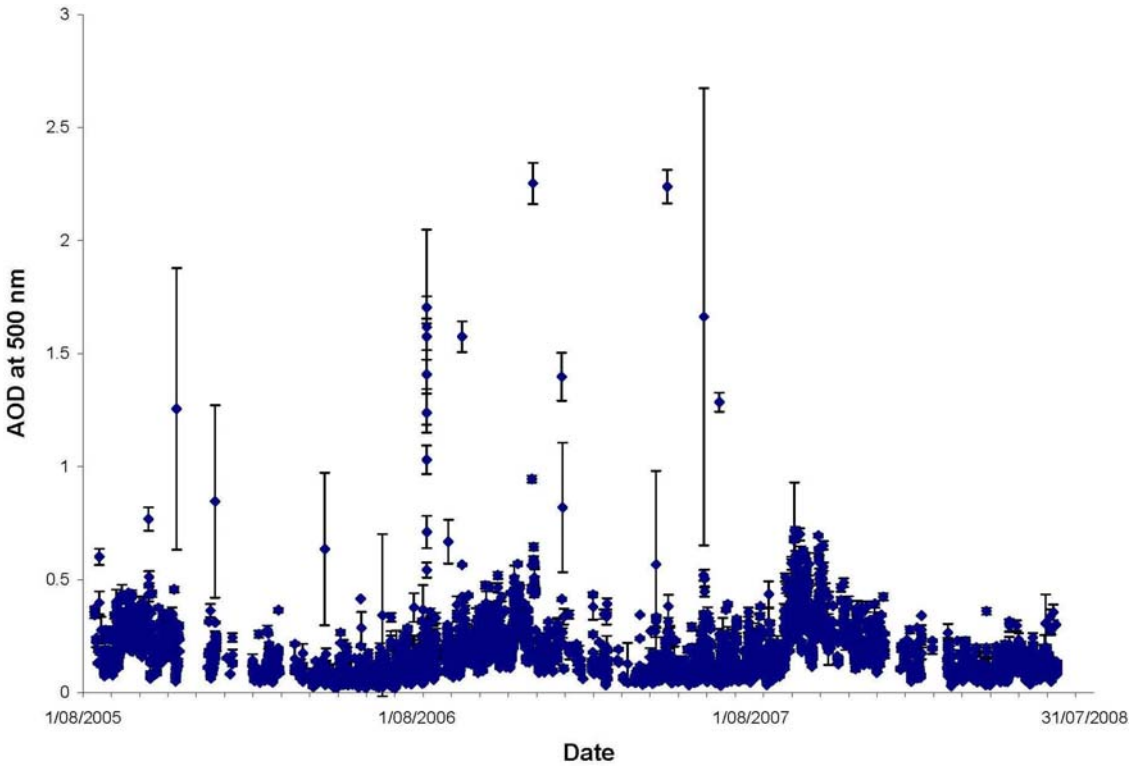

Figure 5-12. Time series of hourly averaged AOD values from Darwin. The error bars are the 1σ standard deviation of the mean for each hour.

Time series of hourly averaged AOD values at 500 nm are shown in Figure 5-12 with the 1σ standard deviation of the mean for each hour shown as error bars. The

figure is dominated by a few anomalously high values, many also with large error bars due to rapidly varying AOD values. Most of these high AOD values are not matched by increases in the CO column and so are not associated with smoke events, one exception being the 27th June 2007 when a thick smoke plume passed over the site at Darwin just before dusk. Presumably the other anomalously high AOD values are the result of clouds that the filter failed to pick up. The time series also shows an annual cycle with AOD at a minimum towards the end of the wet season in early April and peaking at around 0.35 in late September or early October at the end of the local dry season. These more general features are seen more clearly in the daily averaged values of AOD at 500 nm which are plotted in red in Figure 5-13 along with the daily averaged CO column amounts (shown in blue) derived from the NIR ground-based FTIR spectra as described above.

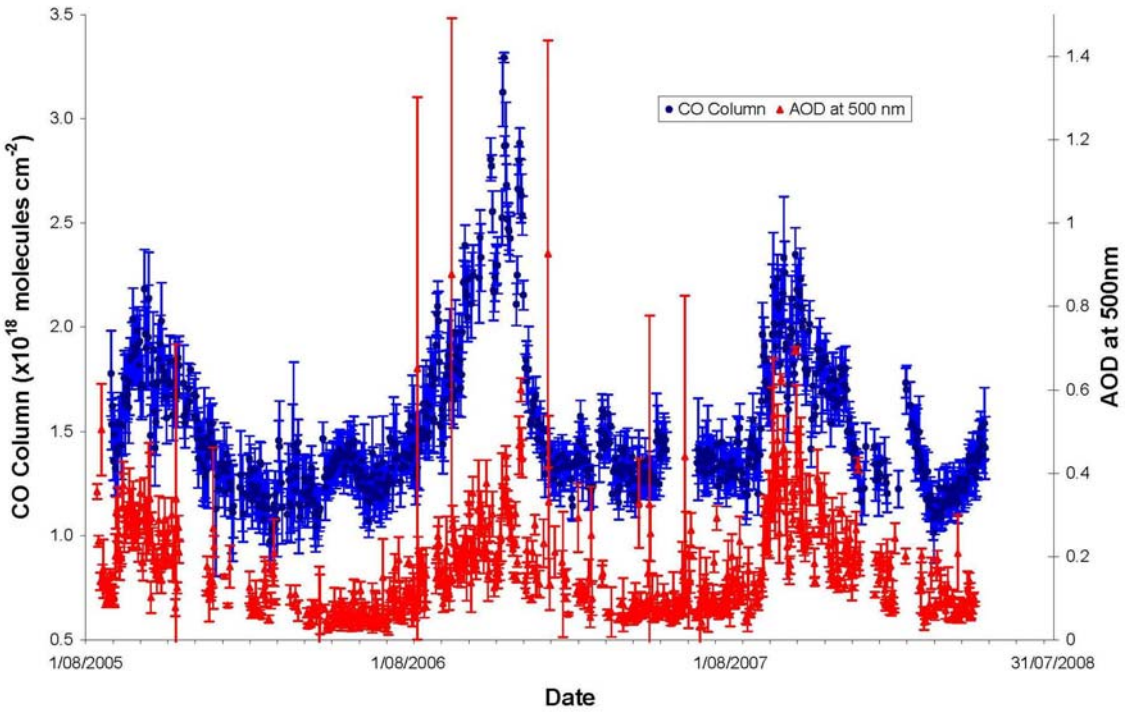

Figure 5-13. Time series of daily average CO column amounts plotted alongside time series of daily average AOD at 500nm. The left-hand axis is for CO column amounts and the right hand axis is for AOD at 500 nm. Error-bars are the 1σ standard deviation of the mean for both CO column amounts and AOD at 500 nm.

The time series of daily average AOD at 500nm and CO column amounts (Figure 5-13) both show a steep rise in early September 2005 peaking at around 0.35

and $2.1x10^{18}$ molecules cm^{-2} respectively in late September and early October, before dropping off more gradually to background values of approximately 0.05 and 1.1 $x10^{18}$ molecules cm^{-2} respectively at the end March or early April 2006. A similar pattern is seen in 2007 with a very sharp rise in AOD and CO columns in early September 2007 peaking somewhat higher at around 0.6 and $2.3x10^{18}$ molecules cm^{-2} respectively in late September and early October, before again dropping off slowly to background values. The picture in the El Nino year of 2006 is substantially different from the other two years, with a more gradual rise in both AOD and column CO amounts starting in August and with peak values significantly later in late November or early December 2006. The peak in CO column amounts is substantially higher than in the other two years at around 2.8 $x10^{18}$ – 3.0 $x10^{18}$ molecules cm^{-2}, whilst the peak values of AOD at around 0.4 – 0.5 are not unusually high. The cause of the later and higher peak values of CO column amounts in 2006 has already been identified as transported smoke from the unusually intense biomass burning in Indonesia during the El Nino year of 2006 (see Figure 5-8). The effect of these fires on the time series of AOD can be seen by unusually high values of AOD for late November and early December 2006 elongating the peak in time. It is possible that the more gradual rise in both AOD and CO columns is also the result of transported smoke from Indonesian fires earlier in the year. The lifetime of smoke aerosols in the atmosphere is significantly shorter than that of CO and so the peak values in AOD from the transported smoke are not higher than the usual peak value associated with more local burning earlier in the year.

Another interesting feature in Figure 5-13 is a small peak in the CO column amounts in late May and early June 2006 – the early dry season and a time period usually associated with local biomass burning in the tropical north of Australia. Images from the MODIS instruments aboard the Aqua and Terra satellites confirm the presence of local fires during this time (see example from 31st May 2006 in Figure 5-14). The peak is not well echoed in the AOD record suggesting that the *Alexandrov* cloud filter may have removed some of the enhanced AOD values actually caused by smoke aerosols.

Figure 5-14: MODIS true colour image from the AQUA satellite with detected thermal anomalies shown as red spots, indicating local fires near Darwin on 31st May 2006. The map was generated in ArcMap using satellite image courtesy of MODIS Rapid Response Project at NASA/GSFC, and coastline and town locations from Spatial Analysis Laboratories (see Acknowledgements.)

High CO column amounts are also notable during February and March 2008, which could be the result of local controlled burning. MODIS visible images during this time are dominated by cloud cover thereby obscuring the view of any possible fires. The CO column amounts drop back slowly to a minimum in late March before climbing steadily in late April and early May when there was significant local burning (see example in Figure 5-15).

'Please see print copy for image'

Figure 5-15: MODIS true colour image from the TERRA satellite with detected thermal anomalies shown as red spots, indicating local fires near Darwin on 27th April 2008.

5.5 Correlations between AOD and Column amounts of CO measured from Darwin

Looking at Figure 5-13 showing AOD at 500nm plotted alongside column amounts of CO the two time series seem to be reasonably well correlated with each other. Unlike at Wollongong, the FTIR spectrometer and sun-photometer at Darwin do not share the same solar tracker but are separated by a distance of about 20m. Thus the viewing geometries are not identical and this could affect the correlation between AOD and CO especially if there is a large amount of smoke at very low altitudes.

In order to establish the correlation factor between AOD at 500 nm and column CO it is necessary to find the sunphotometer measurements that are most coincident in time with the spectra used to determine CO column amounts. All spectra that did not have corresponding measurements of AOD taken within one minute of each other either side of the time associated with the spectrum's zero path difference were excluded. Only about half of the original 170,000 spectra met this requirement giving a dataset of 85,022 spectra with coincident AOD measurements.

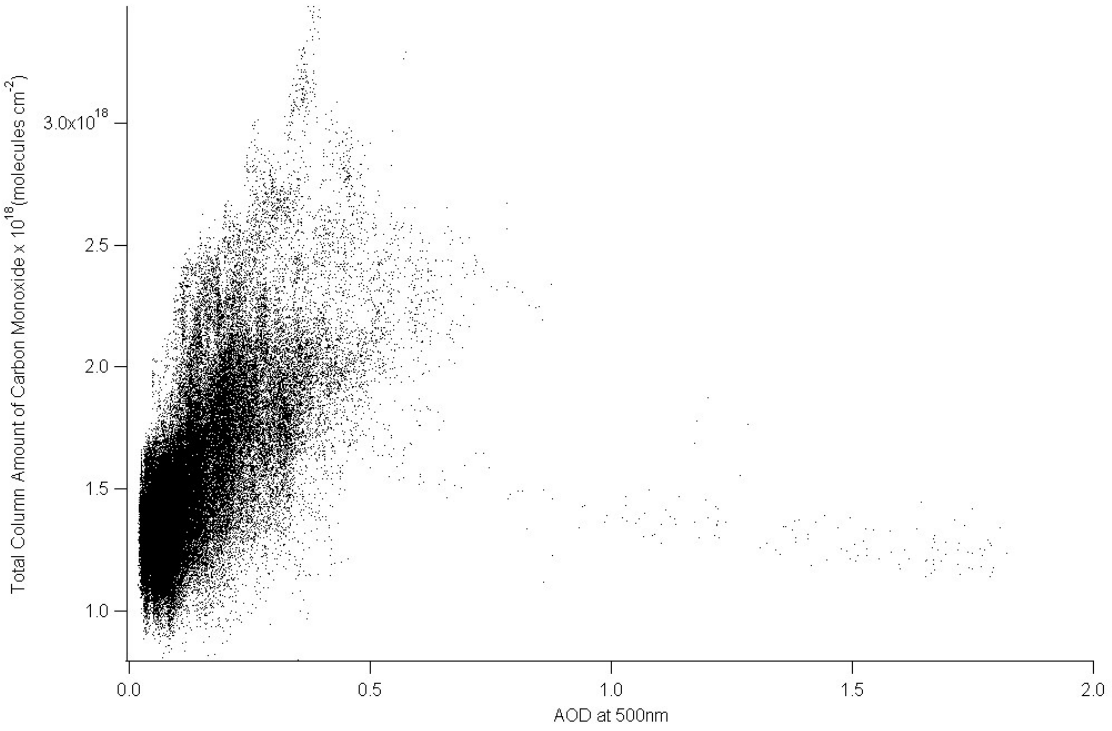

Figure 5-16. Total column amounts of CO derived from near-infrared spectra plotted against coincident sunphotometer measurements of AOD at 500 nm taken from Darwin.

The plot of total column CO against coincident measurements of AOD at 500 nm taken from Darwin shown in Figure 5-16 exhibits high values of AOD (in excess of 0.75) that have no obvious correlation with CO columns. Such high values were also seen in Figure 5-12 and Figure 5-13 with no enhancement in the CO column amounts. Many of these were suspected to result from the failure of the *Alexandrov* filter to fully remove the effects of clouds.

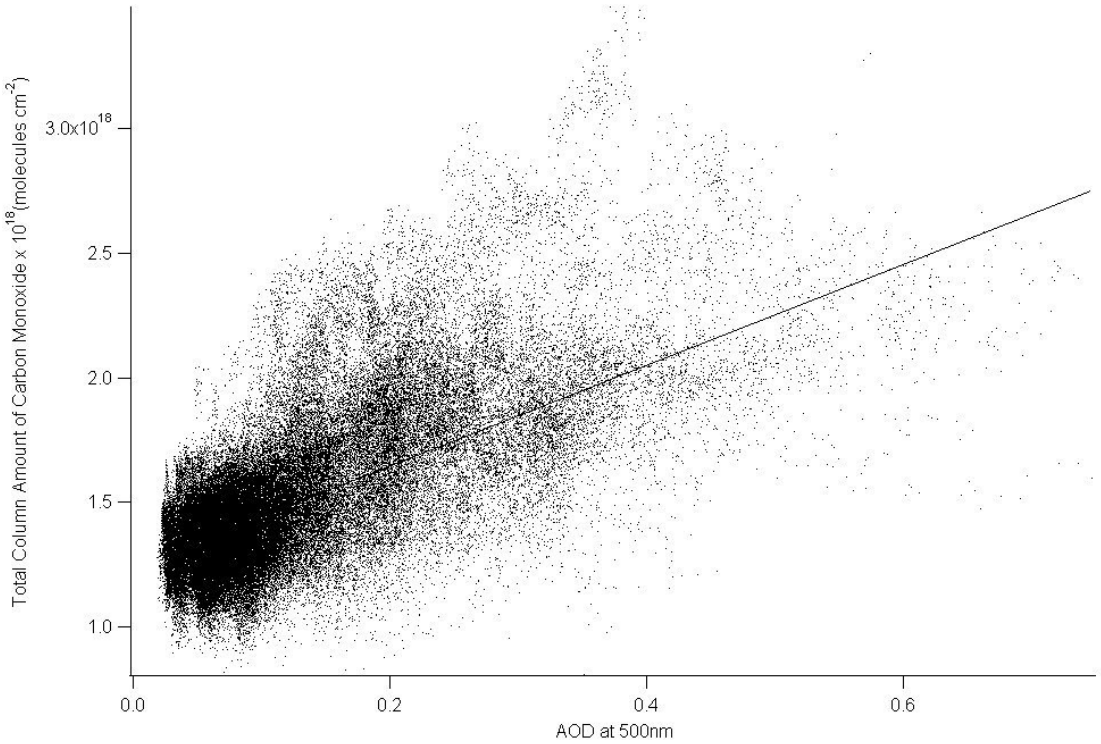

Figure 5-17 Total column amounts of CO plotted alongside coincident measurements of AOD at 500nm. The dataset has been cut to remove all AOD values in excess of 0.75.

In an attempt to minimise the effects of cloud interference all spectra with a coincident measurement of AOD at 500 nm that exceeded 0.75 were removed from the dataset leaving 84,874 spectra. The CO column amounts retrieved from these spectra are plotted against their coincident values for AOD at 500 nm in Figure 5-17. Linear regression gives a relationship CO = $[(1.7 \pm 0.1)\ \text{AOD} + (1.4 \pm 0.1)]\text{x}10^{18}$ molecules cm^{-2} (uncertainties are at 1σ) Assuming that the effect of transported pollution from distant fires is small when taken over the length of the whole time series, then this regression equation is representative of the relationship between CO column amounts

and AOD at 500 nm for tropical north Australian savanna fires. The CO to AOD ratio is slightly higher than that found for forest fires CO = [(1.5 ± 0.1)AOD + (1.5 ± 0.1)] x 10^{18} molecules cm^{-2}, (see Chapter 3).

Previous measurements suggest that CO emissions are lower from savanna fires than from forest fires [*Andreae and Merlet*, 2001], so this suggests that the aerosol loading is also lower, either as a result of lower emissions of aerosols from savanna fires or because the aerosol has been lost through aging of the smoke before it is sampled.

The correlation between AOD and column amounts of CO shown in Figure 5-17 (r^2=0.20) is significantly less strong than that found for forest fires (see Figure 3-19). However, the data in Figure 3-19 and Figure 5-17 are not really comparable because the former is from a subset of data already identified as being affected by smoke plumes whilst the latter includes all data. Nevertheless the lack of a very strong correlation between AOD and CO column amounts suggests that satellite measurements of AOD should not be used in isolation as a means of estimating biomass burning emissions from the savanna areas of tropical north Australia. The method will require use of accompanying data of thermal hotspots to confirm the existence of fires in the region.

Chapter 6 : Emissions from Tropical North Australian Savanna Fires Derived from Ground-based Mid Infrared FTIR Spectra from Darwin

6.1 Recording of Mid infrared Spectra from Darwin

In order to study the atmospheric pollution caused by nearby savanna fires, the solar remote sensing spectrometer in Darwin has been adapted to allow the occasional use of an additional InSb detector that is sensitive from approximately 1800cm^{-1} to 6500cm^{-1}. This region of the mid infrared (MIR) includes absorption features of some of the gases of interest that are emitted during biomass burning such as CO, HCN, H_2CO, C_2H_2 and C_2H_6. Ideally spectra would also be recorded using a MCT detector allowing measurements of NH_3, C_2H_4, HCOOH and CH_3OH but this cannot be done with the calcium fluoride beamsplitter used in the spectrometer. Regular changing of the beamsplitter has the potential to alter the optical path slightly with the possibility of compromising the precision of the retrieved CO_2 columns. Since optimal precision CO_2 columns are the primary target for all TCCON instruments, additional measurements on the spectrometer at Darwin are limited to the InSb detector and calcium fluoride beamsplitter combination.

The instrument may be switched from its normal dual operation mode recording simultaneous spectra on the near infrared InGaAs and Si detectors to recording just InSb spectra. This is achieved by logging into the computer by remote access and recompiling the automatic acquisition program with an alternative set of parameters for the operation of the spectrometer. Filling the detector dewar with liquid nitrogen required to cool the InSb detector is not automated and so the help of the local technicians in Darwin is required to manually fill the detector's dewar each time it is run. On site personnel also provide occasional fire alerts when smoke is affecting the local area. Additionally local fire activity can be monitored using the Geosciences Australia Sentinel website (http://sentinel.ga.gov.au/acres/sentinel/) that shows the

locations of thermal anomalies detected by MODIS instruments onboard the NASA Terra and Aqua satellites (see Figure 6-1). The Bureau of Meteorology provides predictions of wind speed and direction (http://www.bom.gov.au/weather/nt/), but in practice the visible MODIS raster image on the Sentinel website provides a more practical guide as illustrated by the visible smoke plumes in Figure 6-1.

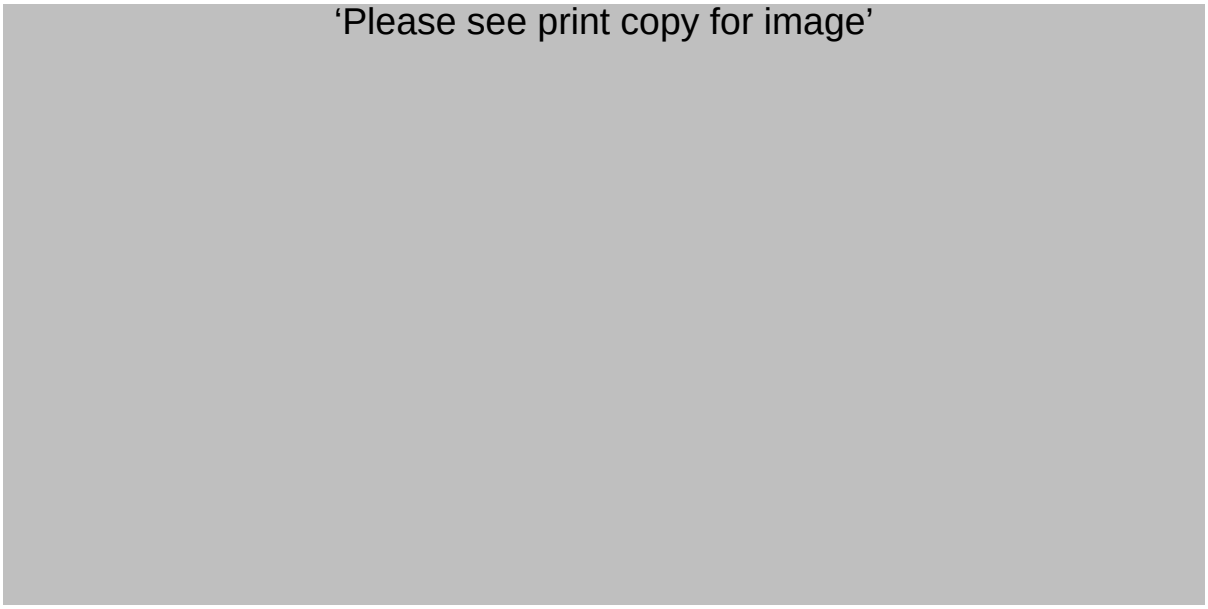

Figure 6-1: Sentinel website showing MODIS thermal anomalies (hotspots) from the afternoon of June 6th 2008 and the MODIS raster (visible image).

There is also a north-looking webcam located on top of the container but smoky conditions are frequently not visible from this image. An exception to this is shown in Figure 6-2 where the presence of a large smoke plume to the East is easily seen behind the cage used to protect the solar tracker in the event of excessively high wind conditions. The collection of data using the InSb detector is much more sporadic than the automated collection of spectra in the near infrared and so the time series of the extra gases that it provides (HCN, H_2CO, C_2H_2 and C_2H_6) have a much poorer temporal coverage than CO.

Figure 6-2: Image from the webcam on top of the container housing the spectrometer at Darwin taken on June 2nd 2008 at 13.50 local time. A large smoke plume is visible to the East behind the hurricane cage and the solar tracker's dome.

6.2 Technical Details of the Analysis of Mid infrared Spectra

Over eleven thousand InSb spectra have been recorded from Darwin since April 2006 on 45 separate days, of which 20 days have been identified as affected by significant amounts of smoke pollution. Spectra were initially recorded using a germanium filter (August – December 2005) and afterwards a long pass filter (LP6500, Spectrogon, Sweden) to cut out frequencies above 6500cm^{-1}. No other optical filters were used so the whole region from 2000 cm^{-1} to 6500cm^{-1} is recorded in a single spectrum. This has the advantage that all the gases of interest that can be retrieved from these spectra are recorded simultaneously but the disadvantage that the signal-to-noise is significantly lower than that achieved when a narrow band optical filter is used. As noted earlier (see section 6.2) there were also some problems with rapid degradation of

the solar tracker mirrors resulting in their replacement in October 2006[13]. For this reason the signal-to-noise values are not consistent throughout the dataset. In all spectra the signal-to-noise values are substantially lower in the regions used to analyse HCN, C_2H_2 and C_2H_6 than in the regions used to analyse CO and H_2CO because of absorption by water vapour, as illustrated by an example spectrum in Figure 6-3. For this reason spectra were coadded (typically 9 at a time) to improve the signal-to-noise before analysing for HCN, C_2H_2 and C_2H_6.

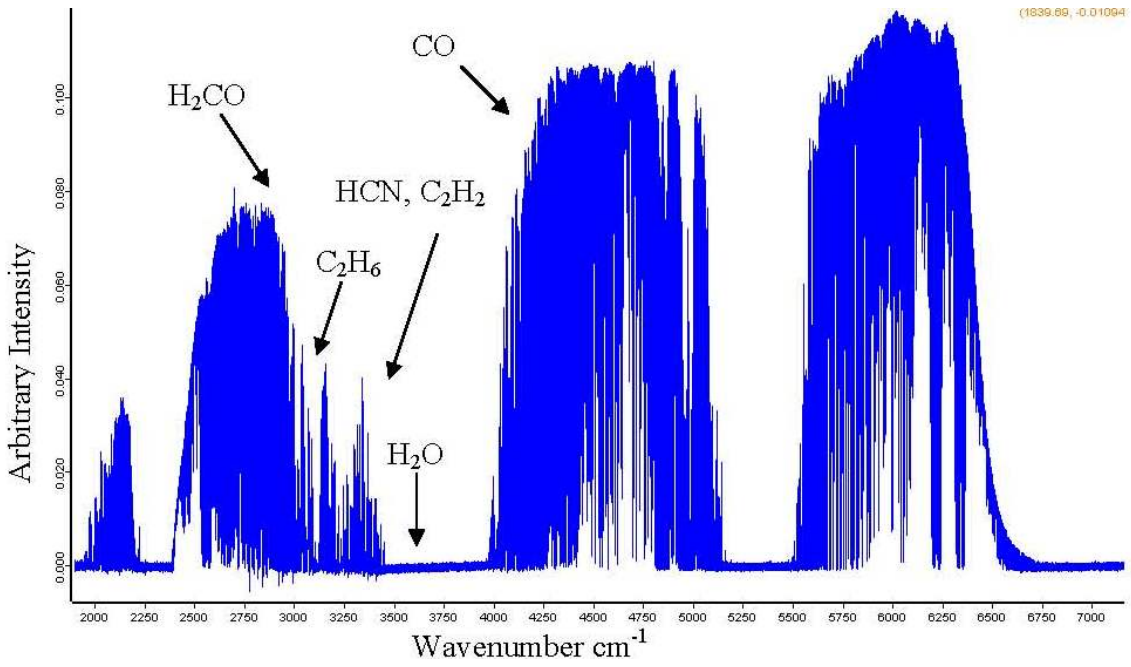

Figure 6-3: An example InSb spectra recorded from Darwin.

Analysis of Mid infrared Spectra for CO & H_2CO

The entire dataset of over eleven thousand InSb spectra was analysed for CO and H_2CO total column amounts using the optimal estimation algorithm SFIT2. For CO the overtone vibrational band at 4230cm^{-1} was used because the signal-to-noise level in the region of the fundamental band was too low. For both gases a 44 layer model atmosphere was used. The H_2CO *a priori* VMR profile was taken from a compilation based upon satellite data at 12°S from the Atmospheric Chemistry Experiment (ACE) instrument on the SCISAT-1 satellite [*personal communication Debra Wunch*]. The CO profile from this compilation has very high concentrations in the lower troposphere (e.g.

[13] The first replacement of mirrors occurred in November 2005, prior to the InSb detector being

145 ppb in the lowest 1km), which are most probably based upon Northern Hemisphere values since the ACE satellite is insensitive near the ground (see http://www.ace.uwaterloo.ca/). Again large covariances were used to encompass both clean and very smoky conditions, so that *a priori* VMRs that were biased towards the clean conditions were necessary to get stable results on the days with no smoke. Thus the tropospheric concentrations in the ACE VMR profile were reduced by approximately two-thirds for the *a priori* VMR used in the retrieval giving a clean air concentration of CO of 55 ppb in the lowest 1km.

The *a priori* covariance and the *a priori* VMR for each gas used for each layer are given in Figure 6-4. The retrievals were constrained by an exponential inter layer correlation factor of 4km[14]. Further details of the retrievals are given in Table 6-1 and example fits in Figure 6-5 and Figure 6-6.

operational.

[14] Note that the exponential interlayer correlation was used for these retrievals because the Gaussian interlayer correlation had cause some numerical instabilities in retrievals in a previous study using a layering scheme with in excess of 40 layers [personal communication N. Jones].

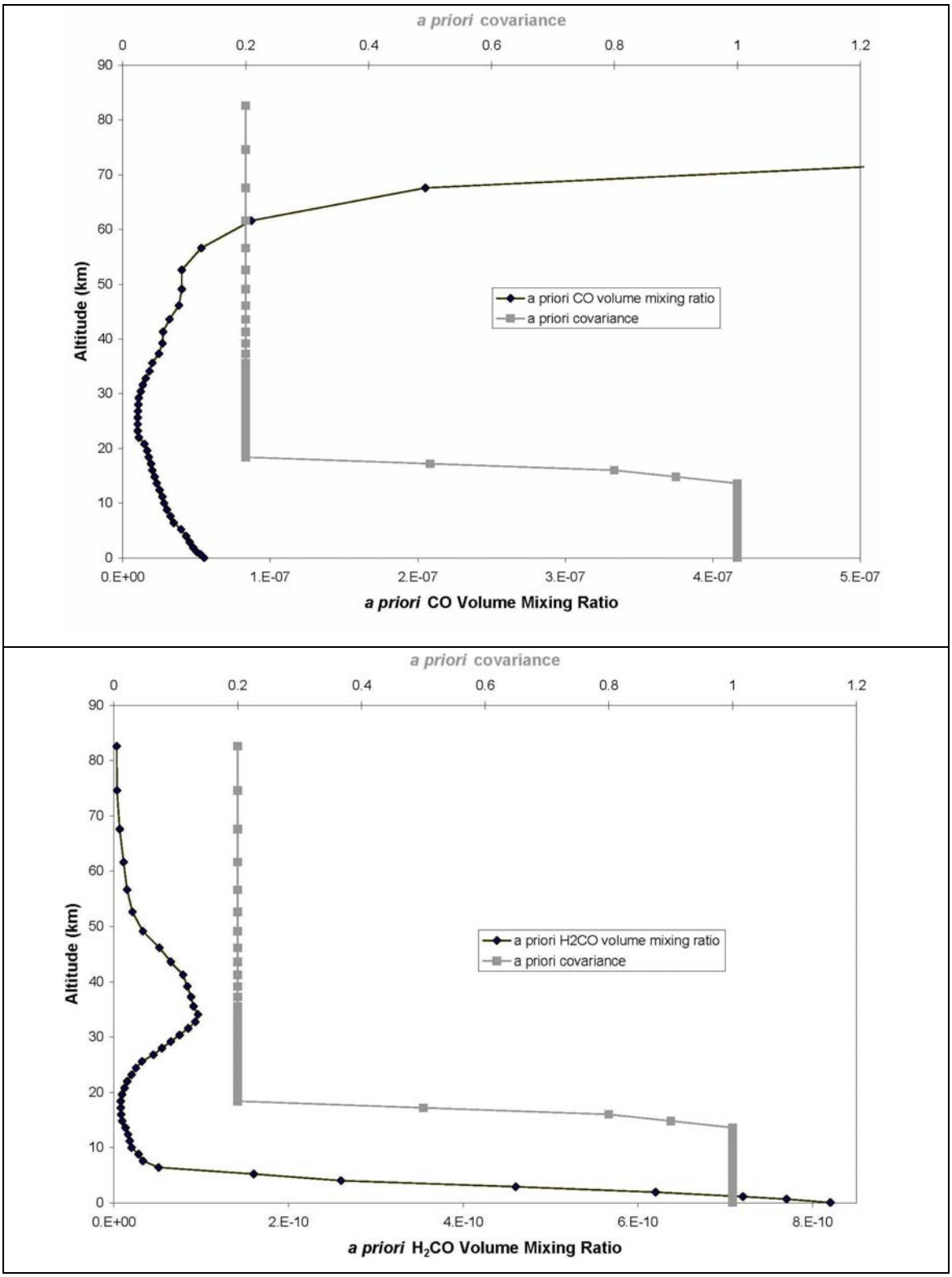

Figure 6-4: VMRs and *a priori* covariances plotted against altitude (km) for the 44 modelled layers used in the SFIT2 retrieval of CO (upper panel) and H_2CO (lower panel)

Table 6-1: Spectral intervals and interfering gases fitted for CO and H_2CO[15] retrieved using SFIT2 along with uncertainties in the derived column amounts

Trace Gas	S:N used in retrieval	Spectral Interval(s) fitted (cm^{-1})	Interfering Gases Fitted in retrieval	Smoothing Uncertainty	Signal-to-noise Uncertainty	Temperature Uncertainty	Total Uncertainty
CO	700	4226.50 - 4228.30 4231.50 - 4232.10 4274.00 - 4275.00	CH_4, HDO, H_2O CH_4, HDO, H_2O CH_4, HDO, H_2O	2.4%	1.1%	2.2%	3.4%
H_2CO	500	2777.88 – 2778.92 2780.76 – 2781.66 2869.435 – 2870.325	CH_4, O_3, HDO, N_2O O_3, CH_4, CO_2 O_3, CH_4, CO_2	3.1%	10.8%	1.6%	11.4%

[15] Note that the choice of microwindows is different from that chosen for analyzing spectra from Wollongong. This is because the information content is not identical due to lower signal-to-noise ratios and a wetter atmosphere in Darwin.

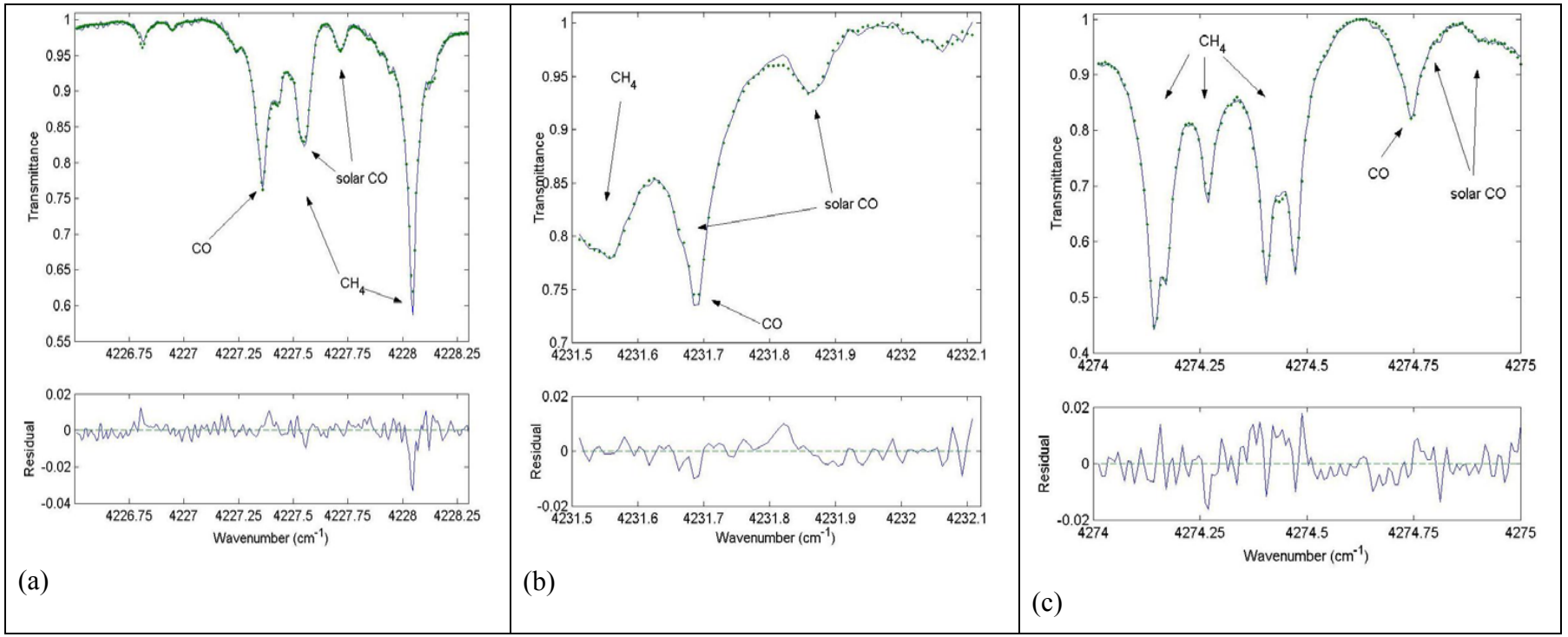

Figure 6-5: Example fits to a measured spectrum achieved in the SFIT2 retrieval of CO in all 3 microwindows used: (a) 4226.50 – 4228.30cm^{-1}, (b) 4231.50 – 4232.10cm^{-1} and (c) 4274.00 – 4275.00cm^{-1}.

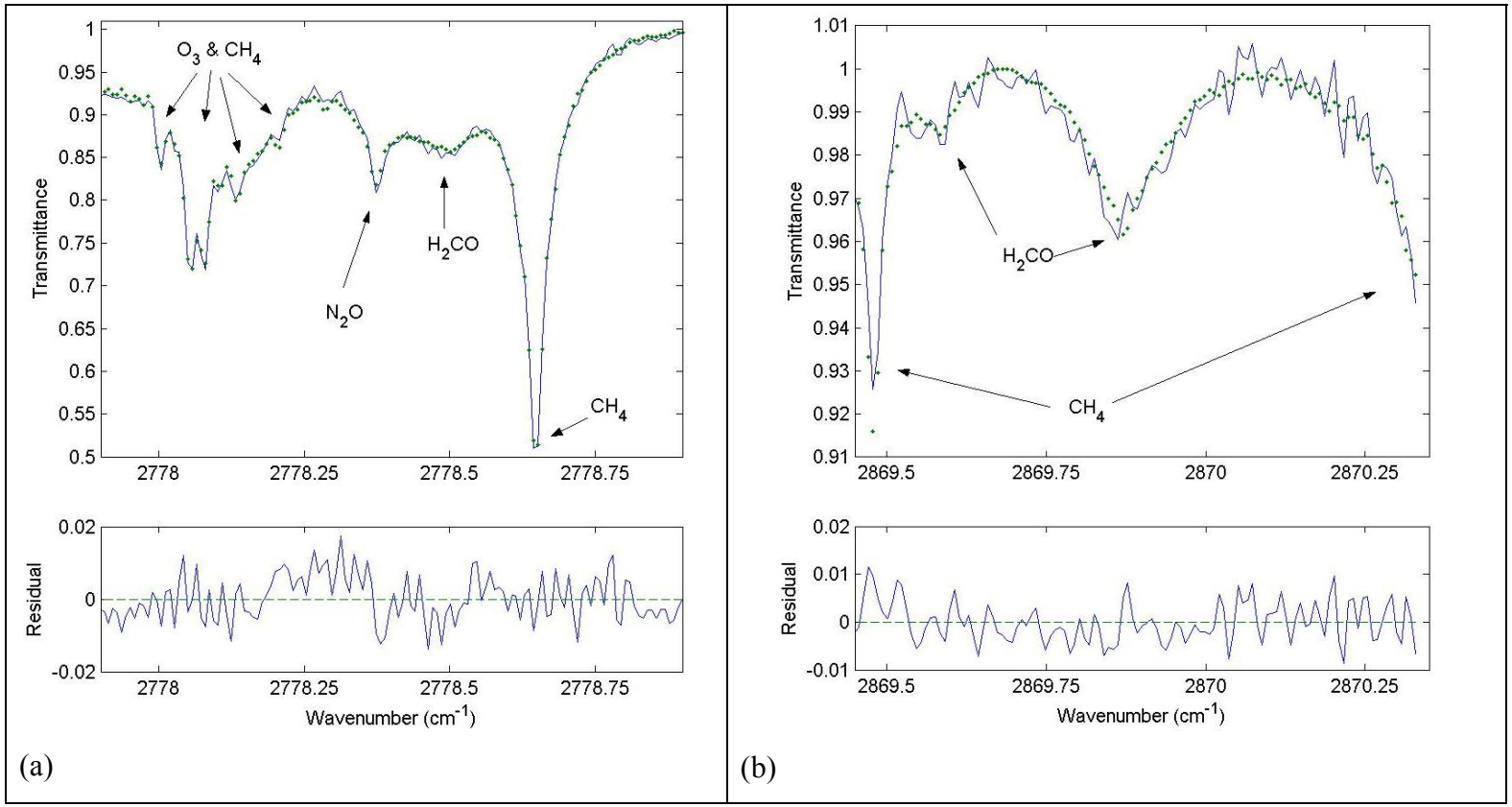

Figure 6-6: Example fits to a measured spectrum achieved in the SFIT2 retrieval of H_2CO in both microwindows used: (a) 2777.88 – 2778.92 cm^{-1} and (b) 2869.435 – 2870.325 cm^{-1}.

Analysis of Mid infrared Spectra for HCN, C_2H_2 and C_2H_6

The H_2CO absorption features are relatively weak and the signal-to-noise ratio is low, thereby reducing the precision of the measurements. For C_2H_6, C_2H_2 and HCN the situation is much worse and in many cases the absorption features were too weak to be detected above the noise level. For this reason only spectra from days when the CO was significantly enhanced were selected and the signal-to-noise was improved (~ by a factor of 3) by co-adding the spectra (usually 9 at a time) before analysis for these other gases.

Again a 44 layer model atmosphere was used and the *a priori* VMRs were taken from the compilation based upon ACE data at 12°S. This was used unaltered for HCN and was reduced by approximately two-thirds in the troposphere for C_2H_2 and C_2H_6 in keeping with the changes made to the CO profile described above. The *a priori* covariance and the *a priori* VMR for each gas used for each layer are given in Figure 6-7 . All the retrievals were constrained by an exponential inter layer correlation factor of 4km and details of interfering species fitted, microwindows and signal-to-noise values used are given alongside uncertainties in Table 6-2. Example fits are given in Figure 6-8 and Figure 6-9.

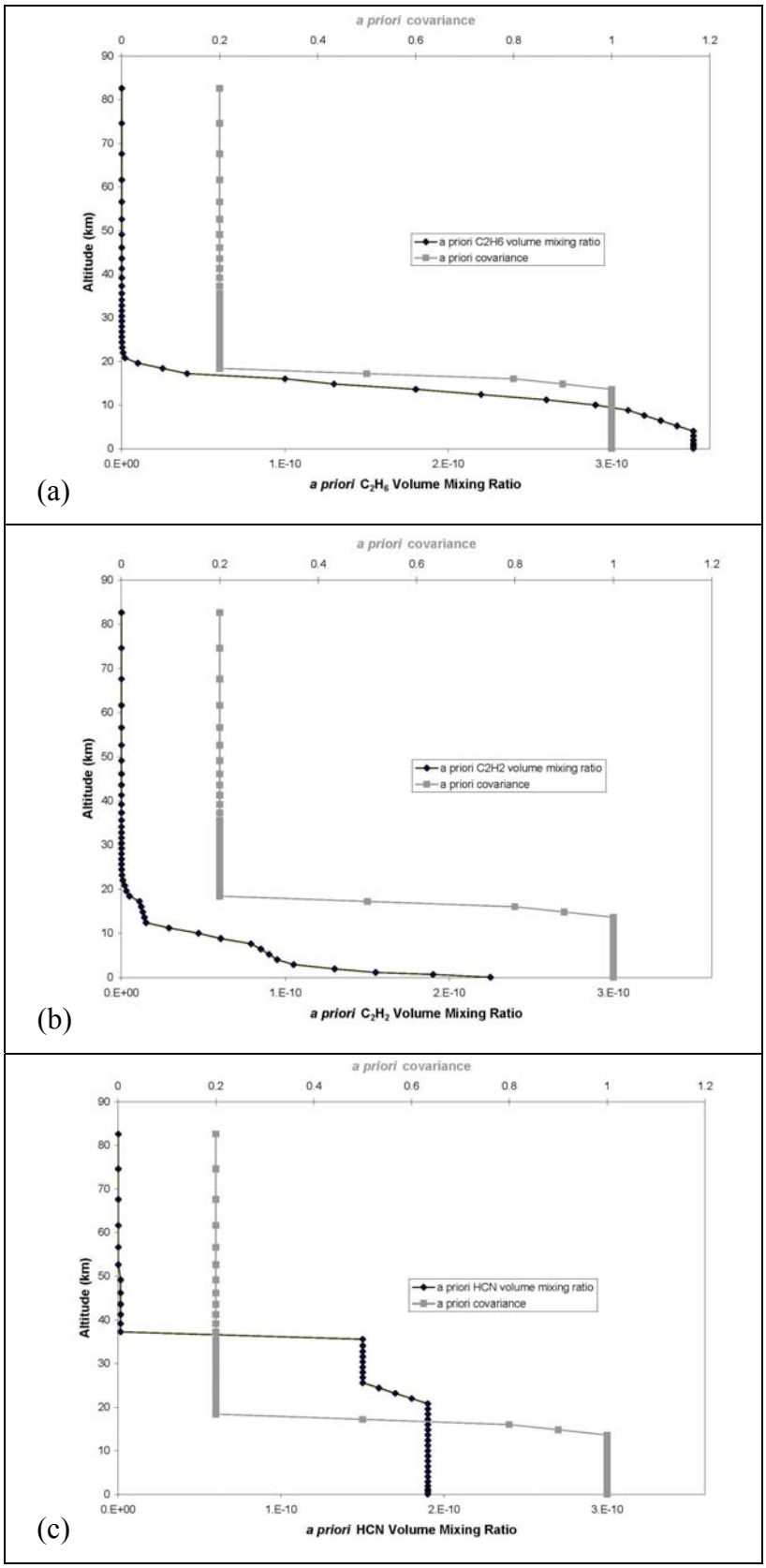

Figure 6-7: : VMRs and *a priori* covariances plotted against altitude (km) for the 44 modelled layers used in the SFIT2 retrieval of (a) C_2H_6 (b) C_2H_2 and (c) and HCN

Table 6-2: Spectral intervals and interfering gases fitted for C_2H_6, C_2H_2 and HCN retrieved using SFIT2 along with uncertainties in the derived column amounts.

Trace Gas	S:N used in retrieval	Spectral Interval(s) fitted (cm^{-1})	Interfering Gases Fitted in retrieval	Smoothing Uncertainty	Signal-to-noise Uncertainty	Temperature Uncertainty	Total Uncertainty
C_2H_6	100	2976.60 – 2977.10 2996.70 – 2997.10 3000.10- 3000.60	H_2O, CH_4, O_3 H_2O, CH_4, O_3 CH_4, O_3	17.4%	8.4%	2.3%	19.5%
C_2H_2	150	3304.70 – 3305.40	H_2O, CO_2	29.8%	13.4%	1.9%	32.8%
HCN	100	3268.00 – 3268.38 3331.40 – 3331.80	H_2O, CO_2, N_2O	20.0%	13.9%	2.1%	24.5%

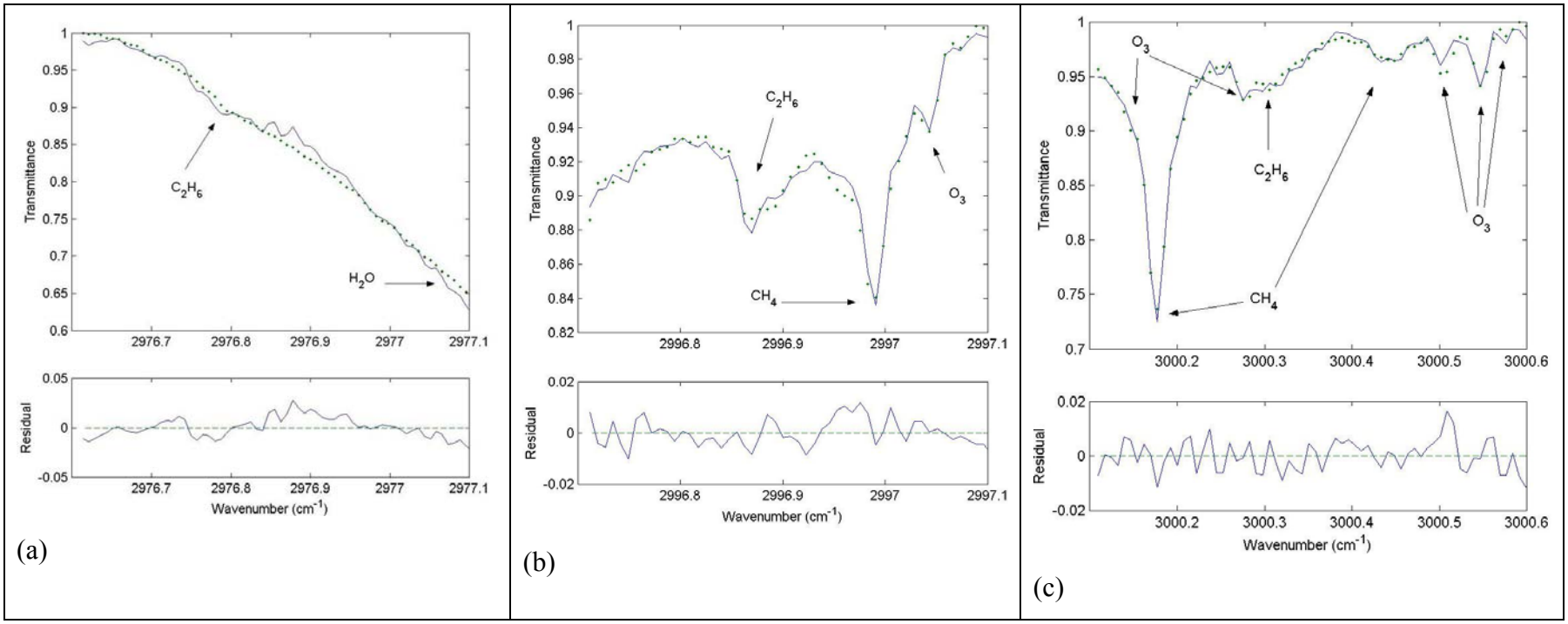

Figure 6-8: Example fits to a measured spectrum achieved in the SFIT2 retrieval of C_2H_6 in all 3 microwindows used: (a) 2976.60 – 2977.10cm^{-1} (b) 2996.70 – 2997.10cm^{-1} and (c) 3000.10 – 3000.60cm^{-1}.

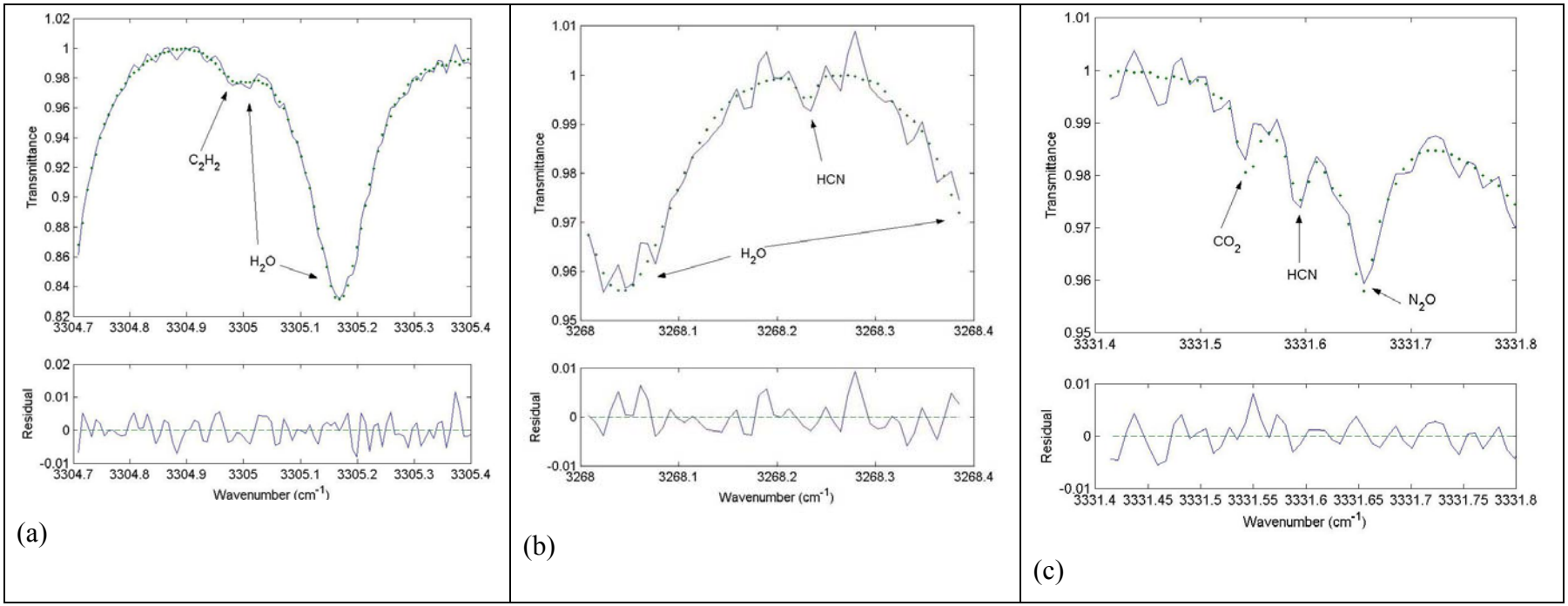

Figure 6-9: Example fits for the SFIT2 retrievals of (a) C_2H_2 from 3304.70 – 3305.40 cm-1, (b)HCN from 3268.00 – 3268.38 cm^{-1} and (c) HCN from 3331.40 – 3331.80 cm^{-1}.

6.3 Distinguishing between local and transported smoke

One of the major aims of this thesis is to provide emission ratios with respect to CO for as many gases as possible from tropical north Australian savanna fires. In practice the limited spectral region available means that emission ratios to CO may only be established for H_2CO, C_2H_2, C_2H_6 and HCN. As discussed above, at certain times of the year the measurement site at Darwin can be heavily influenced by transported smoke from Indonesia and beyond. In order to establish reliable emissions estimates for local savanna fires, the smoke plumes sampled must be from local fires and free from significant influence from significantly aged smoke or smoke transported from more distant regions. The time series of column amounts of CO derived from the near infrared spectra (see Figure 5-6) shows significant increases from as early as August, such that local fires sampled after this time may be influenced by enhanced background amounts of CO. Thus one possible approach is to limit the spectra used to derive emission ratios to those taken early in the year, thereby avoided the times when transported smoke is common.

An alternative approach is to examine back-trajectory analyses alongside MODIS true colour images and thermal anomalies to try to estimate the age of the smoke and where it originated. This was attempted but the MODIS images for the days when smoke was sampled typically contained a large number of thermal anomalies and the back-trajectories often did not clearly identify which fires were sampled. In addition many fires start in the afternoon after the time of the satellite overpasses (~UT 1:00 = 10.30 local time for Terra and ~UT 4:00 = 13.30 local time for Aqua). For these reasons it proved difficult to estimate the age of the smoke and pinpoint the location of the fires that were being sampled.

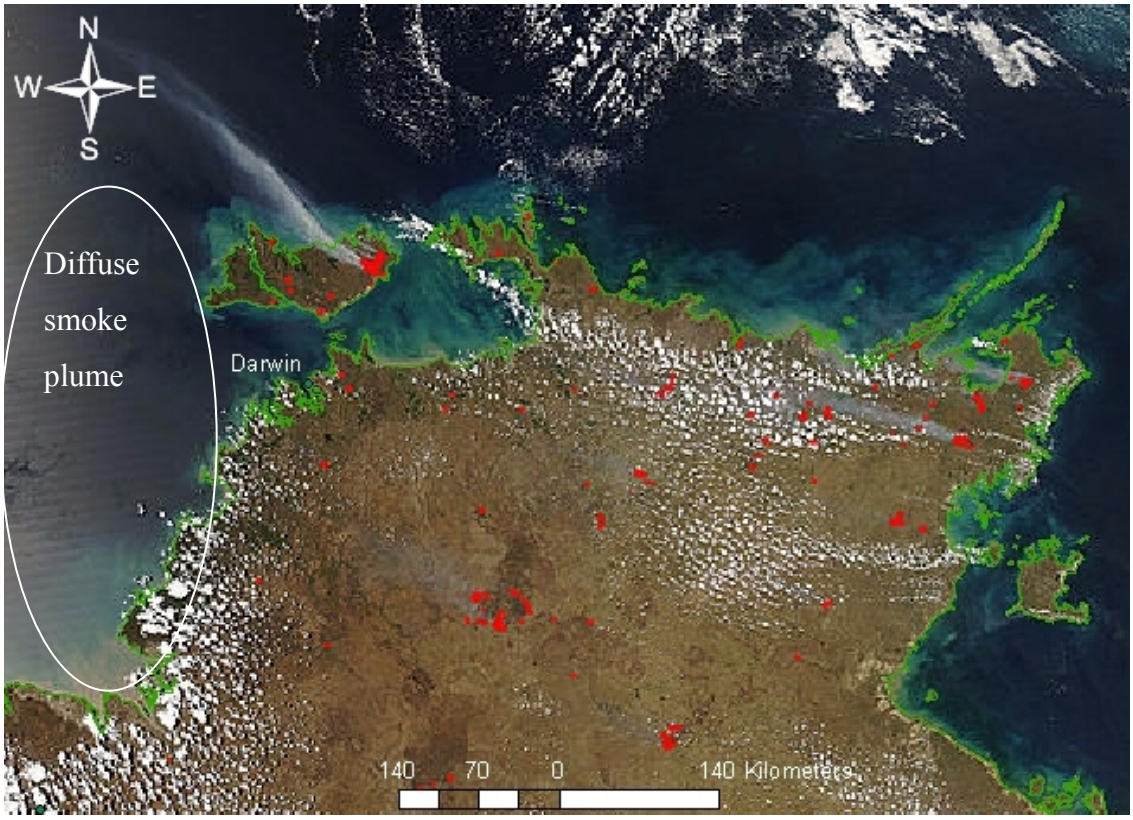

Figure 6-10: MODIS true colour image from the Aqua satellite with detected thermal anomalies shown as red spots, indicating widespread fires near Darwin on 4th October 2006. In the image cloud appears as bright white and smoke as white/grey plumes emanating from the fires.

One example that illustrates this point well is from 4th October 2006. The MODIS image from the Aqua satellite from this day (see Figure 6-10) shows wide-spread fire activity across the region, including a large fire on the island north of Darwin. There is a clear narrow plume of smoke emanating from this fire and heading to the northwest indicating south easterly winds near ground level. Also visible to the left of the image is a much larger and more diffuse plume of smoke apparently orientated from north to south. This is probably a smoke plume at some altitude above ground level that has been transported from Indonesia, but from the evidence of the MODIS image alone it could equally be diffuse smoke from Northern Australia being transported northwards. (It is clear from the direction of the smoke plumes away from the active fires in Figure 6-10 that at ground level the smoke is being blown towards the west or north-west.)

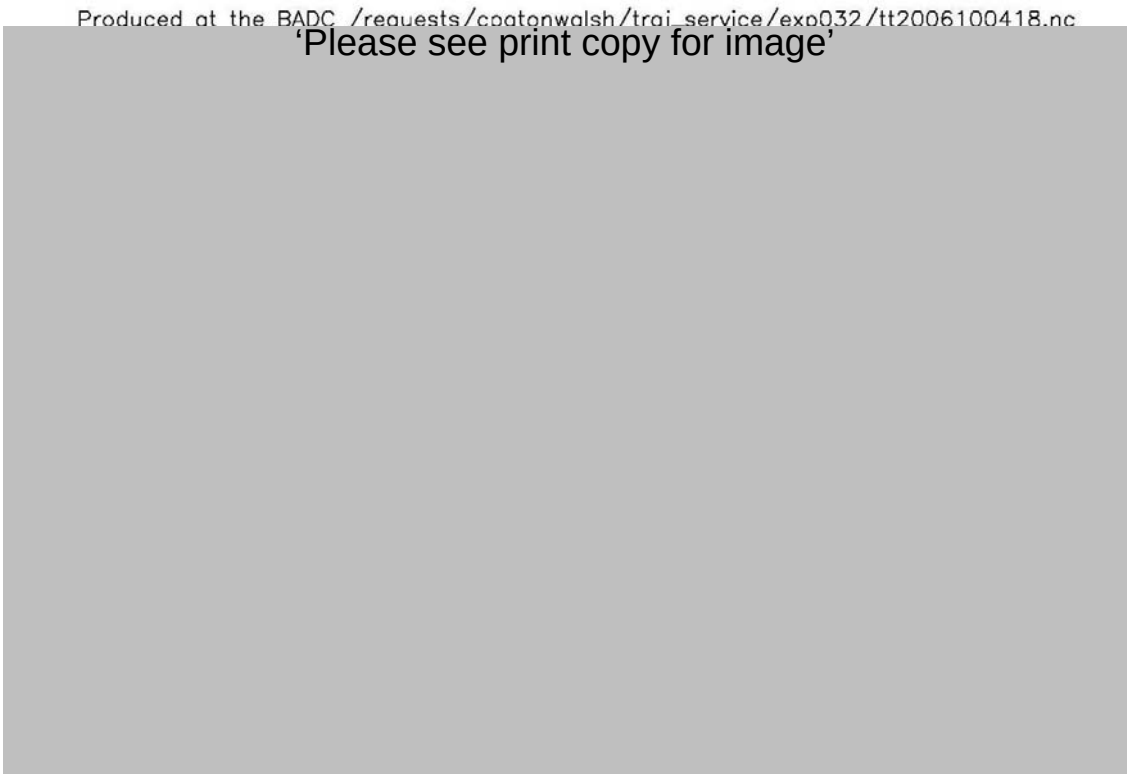

Figure 6-11: Back trajectories showing projected origin and age of parcels of air arriving over Darwin at different pressure levels: 950 hPa (pink), 750 hPa (red), 550 hPa (green) and 350 hPa (light blue). The crosses represent hour intervals back in time from 18:00 on the 4th October 2006. The back trajectories were generated by the European Centre for Medium-Range Weather Forecasts, (ECMWF) Trajectories, via the British Atmospheric Data Centre, 2006 - 2008. Available from http://badc.nerc.ac.uk/data/ecmwf-trj/ .

Further evidence might be gleaned from the back-trajectory analysis for this day (see Figure 6-11). The four traces plotted in Figure 6-11 represent air parcels at different pressures and indicate that at ground level (950 hPa) air is coming from the east, whilst at 350 hPa, which equates to approximately 8km altitude, air is coming from the west. Thus it is not possible to pinpoint which fires are being sampled and indeed it is quite possible that the smoke originates from many different fires, to the east and to the southeast as well as from the diffuse smoke plume in the west.

In some other cases it is much easier to infer the probable source of the smoke from the MODIS images. An example is the 27th June 2007 when the MODIS image from the Terra satellite (see Figure 6-12) shows two of intense fires approximately 150km southeast of Darwin. Approximately 3 hours later, when the Aqua satellite passes overhead, the progress of these particular fires is mainly obscured because of a missing swath from the instrument (see Figure 6-13). However the smoke plumes generated by these fires are clearly seen extending towards the site at Darwin.

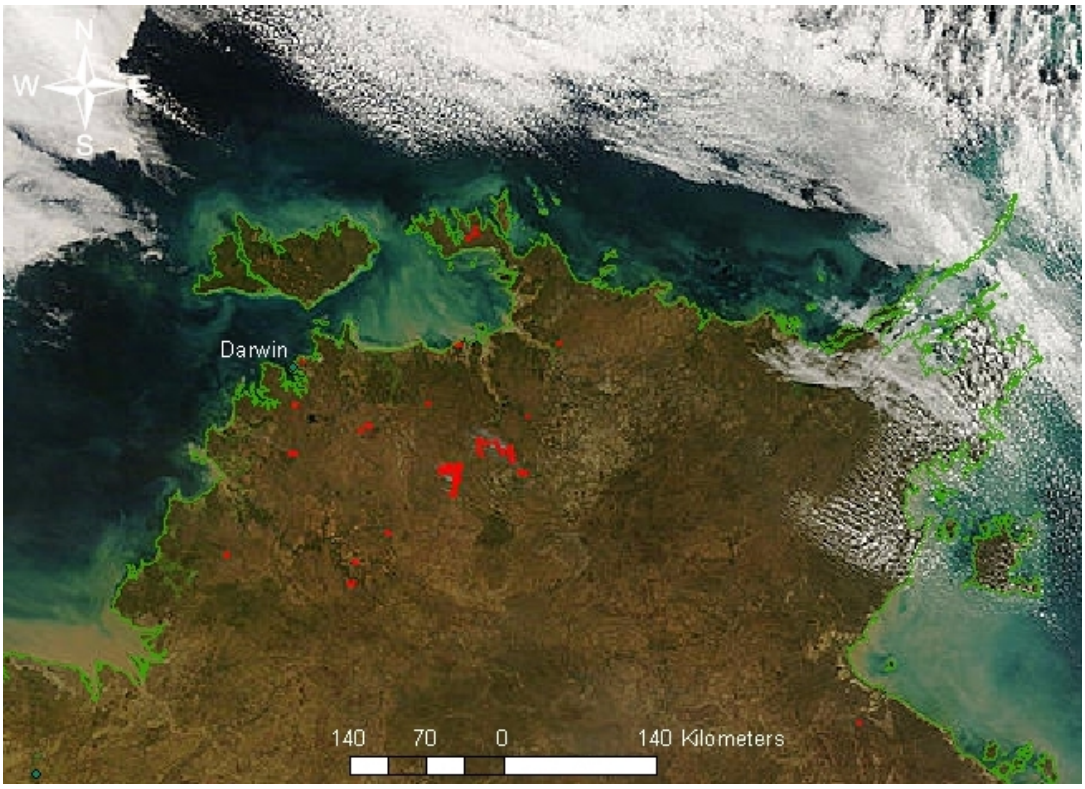

Figure 6-12: MODIS true colour image from the Terra satellite on 27th June 2007 with detected thermal anomalies shown as red spots, indicating intense fires approximately 150km southeast of Darwin. (For details of map generation please see Acknowledgements.)

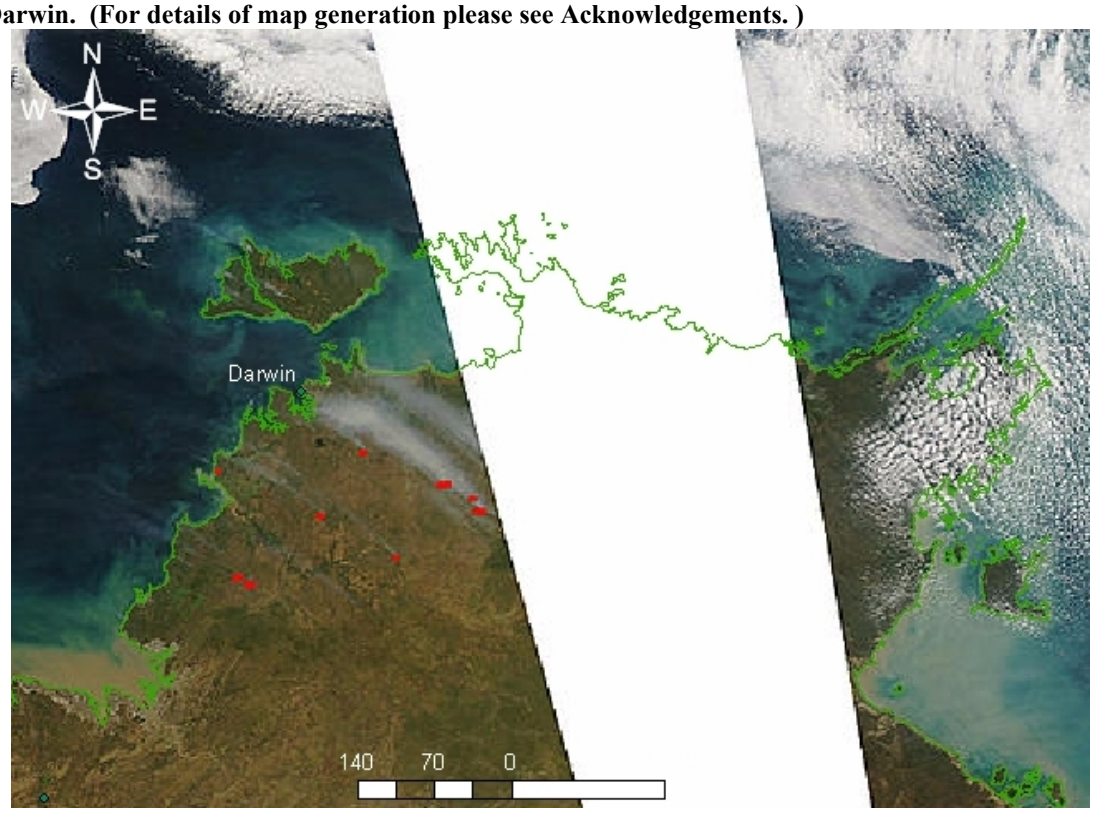

Figure 6-13: MODIS true colour image from the Aqua satellite on 27th June 2007 with detected thermal anomalies shown as red spots. One swath is missing but the smoke plumes from the fires detected by the instrument on the Terra satellite approximately 3 hours earlier are clearly seen. (For details of map generation please see Acknowledgements.)

The back-trajectory analysis for 27th June 2007 shows that only the air parcels near the ground (950 hPa) originate from the region of the fires, suggesting that all the enhancement of trace gases associated with biomass burning are located in the lowest 2km of the boundary layer (see Figure 6-14). The back trajectory analysis, (in combination with the fire locations), indicates that the smoke reaching Darwin is approximately 5 hours old.

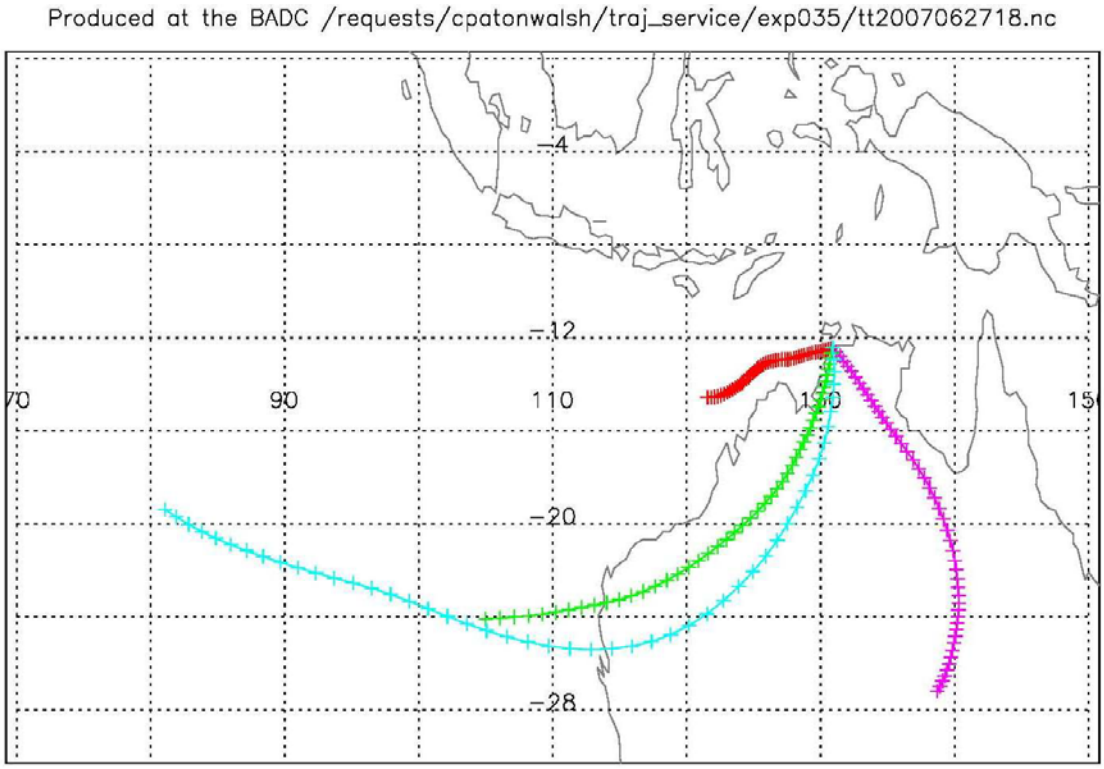

Figure 6-14: Back trajectories showing projected origin and age of parcels of air arriving over Darwin at different pressure levels: 950 hPa (pink), 750 hPa (red), 550 hPa (green) and 350 hPa (light blue). The crosses represent hour intervals back in time from 18:00 on 27th June 2007.

Another example where the location and age of the smoke can be estimated using the combination of MODIS true colour image and back trajectory analysis is shown in Figure 6-15 and Figure 6-16 for the 9th August 2007. The back trajectory analysis (see Figure 6-16) indicates that the smoke reaching Darwin is at least 12 hours old.

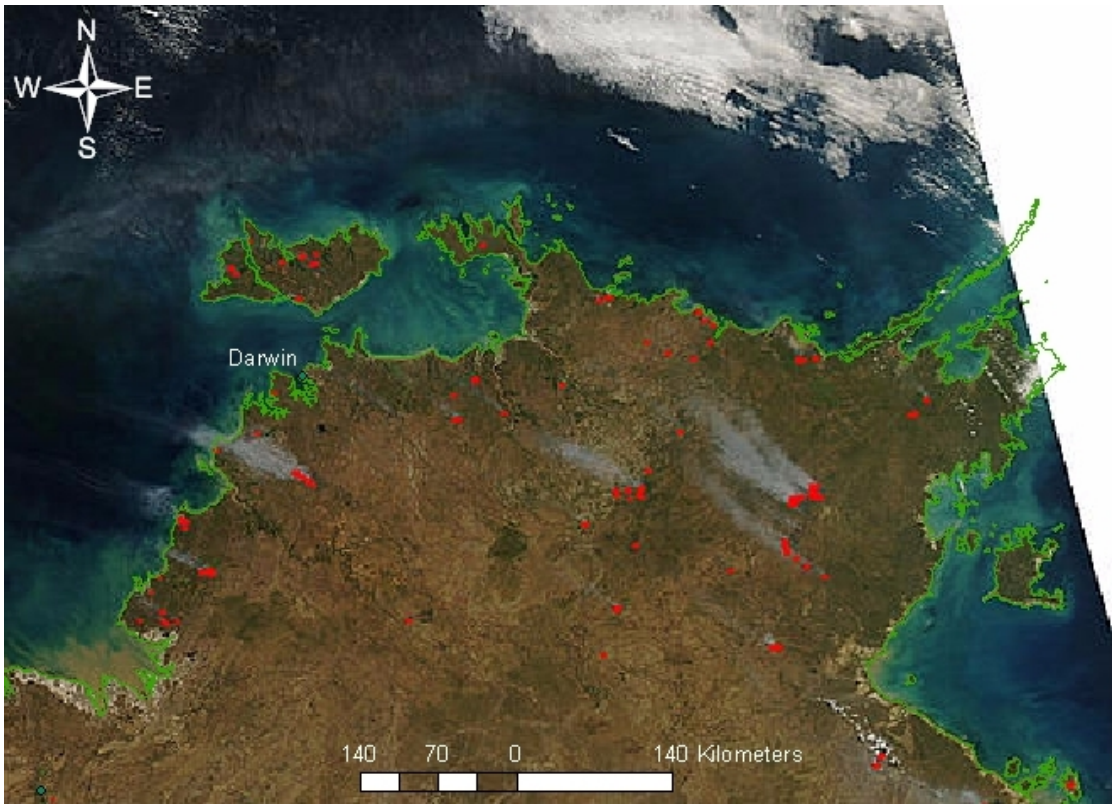

Figure 6-15: MODIS true colour image from the Aqua satellite on 9th August 2007 with detected thermal anomalies shown as red spots. Smoke plumes are visible from several fires at distances in excess of 200 km from Darwin.

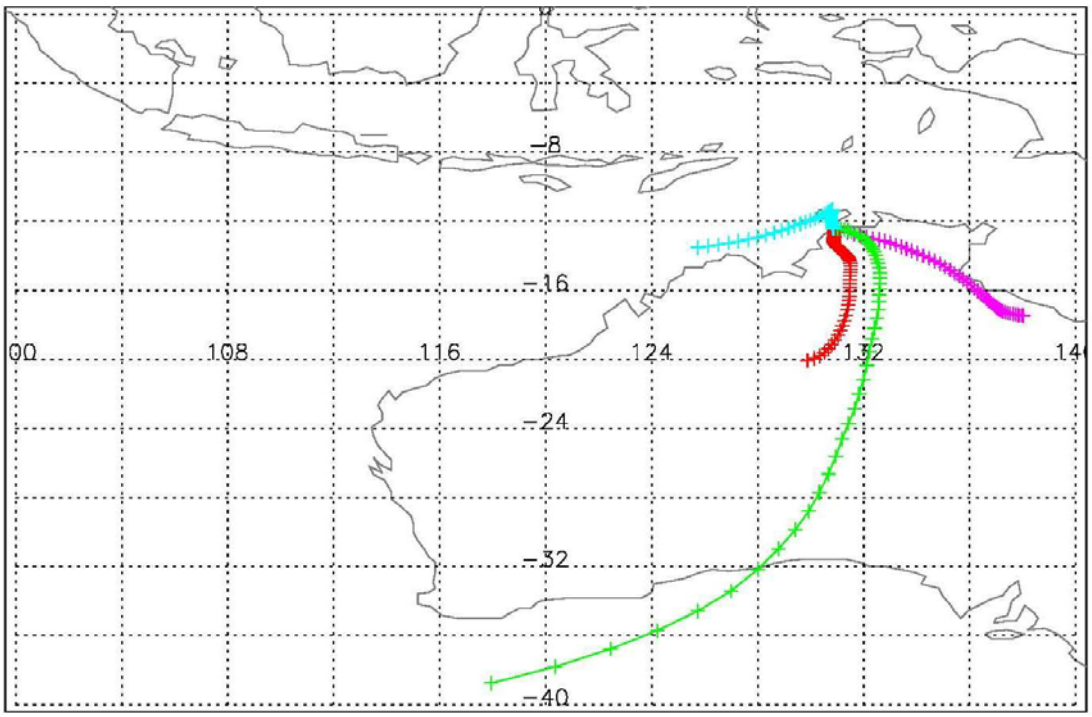

Figure 6-16: Back trajectories showing projected origin and age of parcels of air arriving over Darwin at different pressure levels: 950 hPa (pink), 750 hPa (red), 550 hPa (green) and 350 hPa (light blue). The crosses represent hour intervals back in time from 18:00 on 9th August 2007.

MODIS images also show clear evidence of transported smoke plumes on the 4th October 2006 as shown above in Figure 6-10 and on the 2nd November 2006 and 30th November 2006 shown below in Figure 6-17 and Figure 6-18 respectively.

.

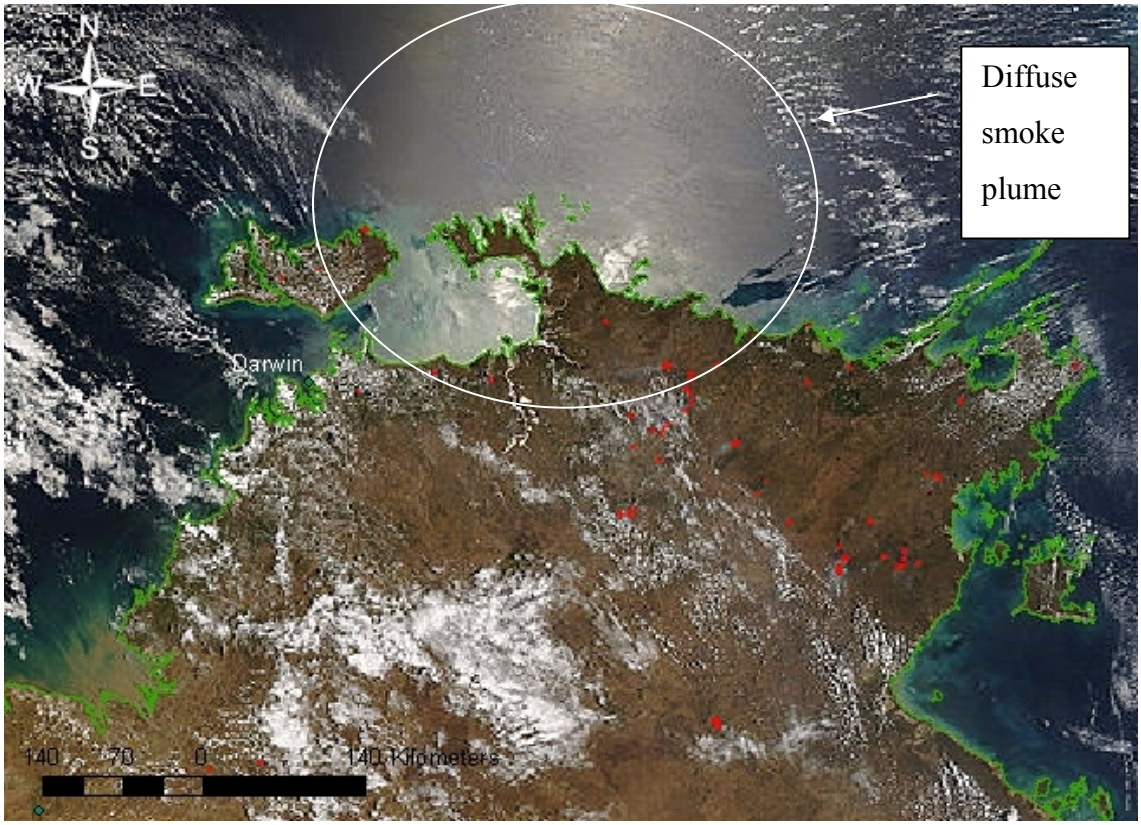

Figure 6-17: MODIS true colour image from the Terra satellite on 2nd November 2006 with detected thermal anomalies shown as red spots. Scattered fires are detected and clearly visible is a large diffuse smoke plume apparently coming from the north.

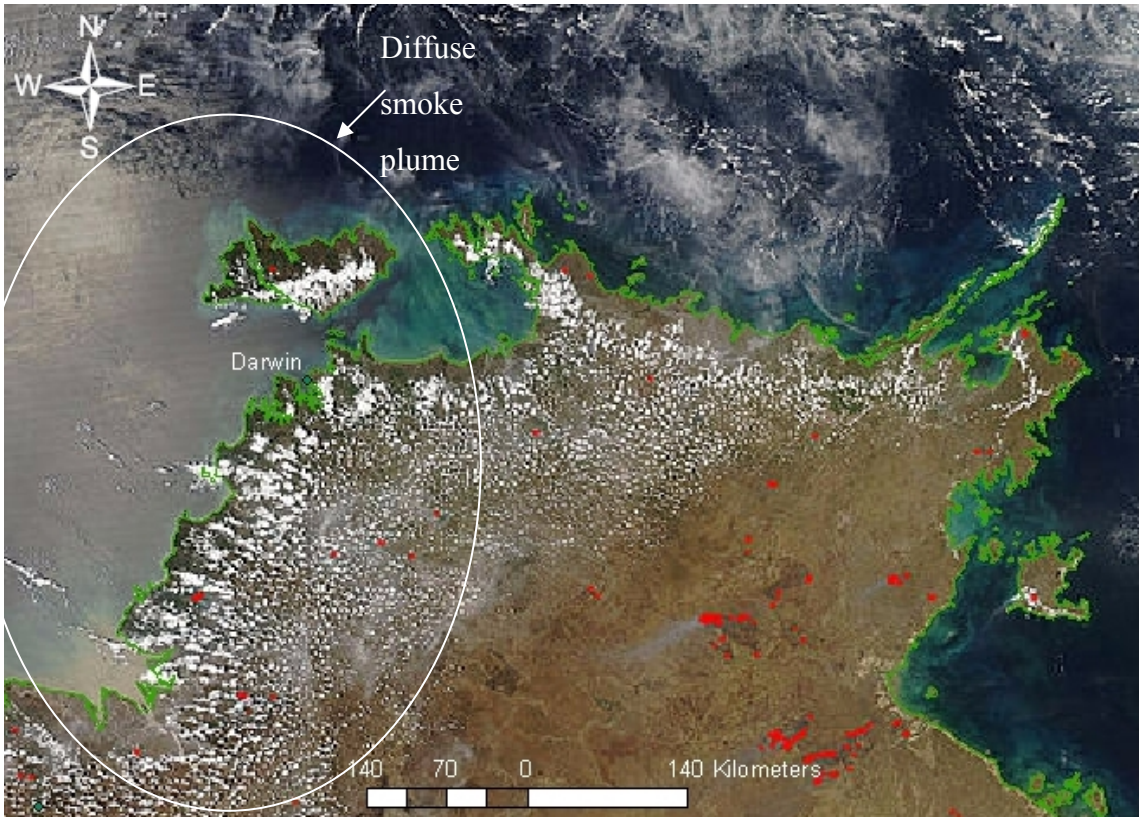

Figure 6-18: MODIS true colour image from the Aqua satellite on 30th November 2006 with detected thermal anomalies shown as red spots. Scattered fires are detected to the southeast of the region and clearly visible is a large diffuse smoke plume apparently coming from the northwest.

Also of interest is the MODIS image on the 20th September 2007 (see Figure 6-19) that shows evidence of the build up of smoke in the region that is in keeping with the increase in column amounts of CO during September that were discussed earlier and shown in the time series in Figure 5-13. Back trajectory analysis for this day suggests that the smoke is probably in the order of 24 hours old or older (see Figure 6-20).

A complete set of MODIS true colour images with thermal anomalies for all of the days on which significant smoke plumes were sampled over Darwin is given in Appendix 3, with the exception of the 20th August 2007 when, due to operational problems, no satellite images were available. Also given in Appendix 3 are the ECMWF back trajectory analyses for all smoky days.

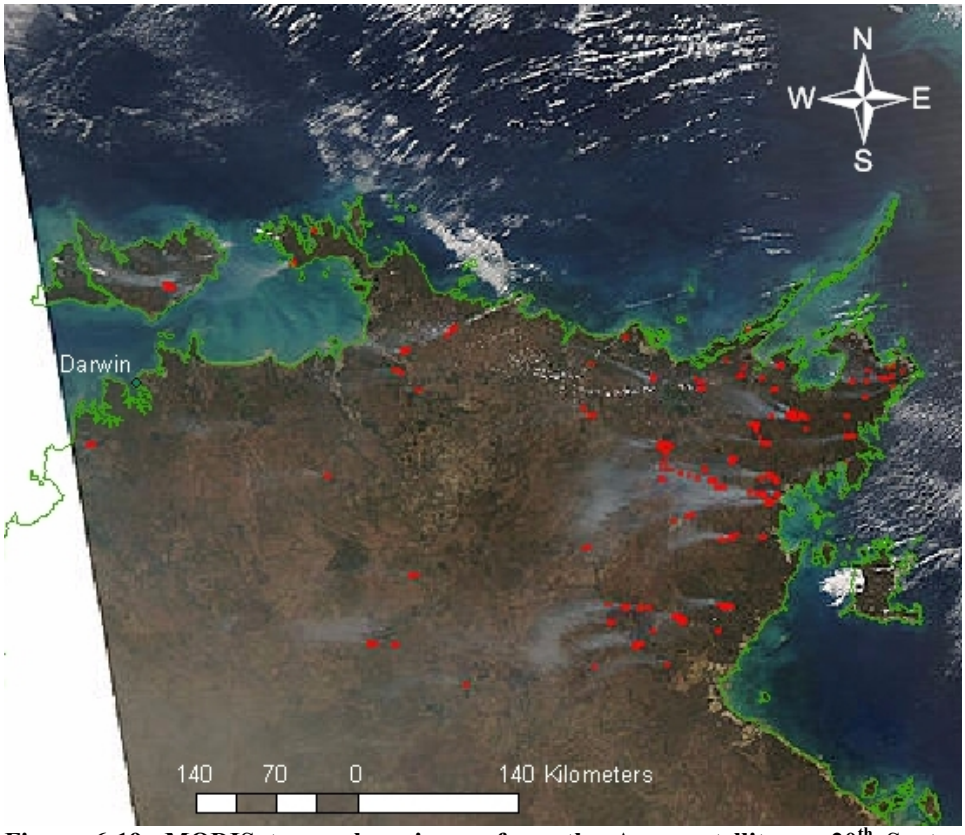

Figure 6-19: MODIS true colour image from the Aqua satellite on 20th September 2007 with detected thermal anomalies shown as red spots. Widespread fires are seen in the east and a general build-up of smoke is visible across the region.

Produced at the BADC /requests/cpatonwalsh/traj_service/exp043/tt2007092018.nc

'Please see print copy for image'

Figure 6-20: Back trajectories showing projected origin and age of parcels of air arriving over Darwin at different pressure levels: 950 hPa (pink), 750 hPa (red), 550 hPa (green) and 350 hPa (light blue). The crosses represent hour intervals back in time from 18:00 on 20th September 2007.

6.4 Correlations between derived columns of H_2CO and CO

Figure 6-21 shows the H_2CO column plotted against simultaneously measured CO column on the 20 days that smoke was sampled with the InSb detector, colour coded to distinguish data from different time periods in each year from 2006-2008.

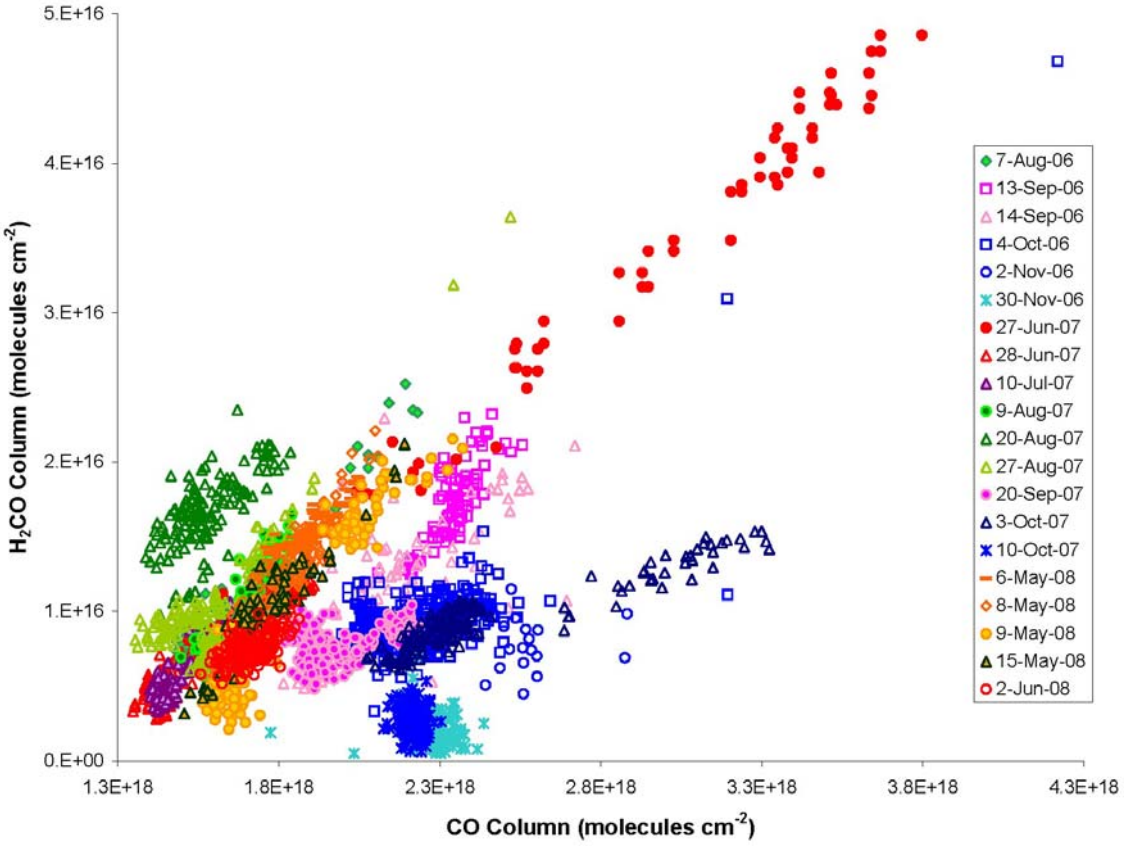

Figure 6-21 Column amounts of H_2CO plotted against column amounts of CO measured simultaneously from Darwin from 2006-2008. The results are shown for each of 20 individual days when smoke was sampled. The plot is colour coded to distinguish measurements made in different times of the year; orange/red for May/June, green for August, pink for September and blue for October/November.

The spectra recorded during May-July (orange or red points) show a very strong correlation between H_2CO and CO. Many of the spectra from August (green points) overlie data from May-July, but a significant proportion appear to have a similar value for the H_2CO to CO gradient but are shifted to the left of the plot indicating higher background H_2CO values or lower background CO amounts. In comparison most spectra from September (pink points) also show a similar H_2CO to CO gradient but are shifted to the right indicating a higher background amount of CO or depleted amounts

of H_2CO when compared to the May-July data. Again a subset of the September data does not fit the general pattern but this group of data overlies some of the May-July data. Finally spectra from October and November (blue points) are shifted furthest to the right of the plot, indicating higher background CO, and appear to have smaller H_2CO to CO gradients.

An explanation for much of the disparity between different times of the year is that later in the year CO amounts are enhanced by both the build up of smoke from local fires (see Figure 6-19) and smoke transported from biomass burning Indonesia, Africa and South America (see Figure 6-17 and Figure 6-18). H_2CO has a much short atmospheric lifetime than CO and so does not build up in the same way. The gradient of H_2CO to CO for local fires remains constant but the "background" CO increases towards the end of the year. Higher background CO amounts may also result if meteorological conditions cause air from the Northern Hemisphere to be located over Darwin. This is possible because Darwin is located close to the inter-tropical convergence zone (ITCZ) and the "chemical equator" that separates the polluted Northern Hemisphere from the more pristine Southern Hemisphere [*Hamilton et al.*, 2008].

The "background" amount of CO in the atmosphere (being the amount of CO not associated with local burning) can vary substantially from one day to the next, as polluted air is transported into or out of the region. For this reason H_2CO to CO gradients have been calculated separately for each of the 20 individual days when significant smoke plumes were sampled with the InSb detector. The H_2CO to CO data are colour-coded separately for each day in Figure 6-21 and the gradients, intercepts and the square of the correlation coefficients from the regression analyses are shown in Table 6-3.

Table 6-3: Results of regressions analyses on H_2CO and CO retrievals from each of the 20 individual days when significant smoke plumes were sampled with the InSb detector from Darwin. The gradient, intercept and value for the square of the correlation coefficient (r^2) are shown. Days with strong correlations are shown in bold, and mean values for the daily gradients and intercepts are given for spectra recorded between May and September and spectra recorded during October and November.

Date	Gradient	Intercept x 10^{16}	r^2
06-May-2008	0.012 ± 0.001	-0.48 ± 0.03	0.54
08-May-2008	**0.033 ± 0.001**	-4.6 ± 0.2	**0.86**
09-May-2008	**0.027 ± 0.001**	-3.8 ± 0.1	**0.92**
15-May-2008	**0.022 ± 0.001**	-2.6 ± 0.2	**0.91**
02-Jun-2008	0.012 ± 0.001	-1.0 ± 0.3	0.31
27-Jun-2007	**0.020 ± 0.0003**	-2.0 ± 0.1	**0.99**
28-Jun-2007	**0.019 ± 0.001**	-2.1 ± 0.1	**0.87**
10-Jul-2007	**0.032 ± 0.002**	-3.9 ± 0.3	**0.79**
07-Aug-2007	0.018 ± 0.03	-1.8 ± 0.4	0.39
09-Aug-2007	**0.033 ± 0.002**	-4.2 ± 0.3	**0.82**
20-Aug-2007	0.016 ± 0.002	-0.63 ± 0.024	0.50
27-Aug-2007	**0.024 ± 0.001**	-2.5 ± 0.1	**0.91**
13-Sep-2006	0.025 ± 0.004	-3.8 ± 0.9	0.40
14-Sep-2006	**0.016 ± 0.001**	-2.0 ± 0.2	**0.89**
20-Sep-2007*	0.003 ± 0.002	-0.35 ± 0.30	0.03
May-Sept Average*	**0.022 ± 0.007**	**-2.5 ± 1.3**	
04-Oct-2006	0.012 ± 0.001	-1.6 ± 0.2	0.51
03-Oct-2007	**0.007 ± 0.0003**	-0.62 ± 0.01	**0.85**
10-Oct-2007	-0.001 ± 0.007	0.6 ± 1.4	0.001
02-Nov-2006	0.007 ± 0.003	-1.0 ± 0.8	0.22
30-Nov-2006	-0.013 ± 0.004	3.4 ± 1.0	0.63
Oct - Nov Average	**0.002 ± 0.010**	**0.2 ± 2.0**	

* Note the data from 20th September 2007 has a value for the square of the correlation coefficient (r^2) of only 0.03 and is excluded from the May-September average values.

The H_2CO and CO retrievals from October and November are sometimes poorly correlated and there is a large scatter in the H_2CO to CO gradients derived from different days (see Table 6-3). It can be seen from Figure 6-21 that on the 30th November 2006 and the 10th October 2007 there is no appreciable enhancement in the H_2CO column amounts, although the CO columns are well above normal. This suggests that on these days only very aged smoke (probably transported from distant fires) has been sampled.

The 3rd October 2007 and to a lesser extent the 4th October 2006 show stronger correlations than the other October and November days. (Note that the 30th November 2006 has a value for the square of the correlation coefficient (r^2) of 0.63 but there are

only 7 spectra so the correlation appears spuriously high). The MODIS true colour image from the 3rd of October 2007 shows a diffuse smoke plume not apparently coming from any of the active fires shown in the thermal anomalies (see Figure 6-22) and the back-trajectory analysis indicates that parcels of air from the area of this smoke plume at 750 hPa (or approximately 2km altitude) pass over the Darwin site at 18:00 (see Figure 6-23). The diffuse smoke plume sampled on the 3rd of October 2007 may well have been significantly aged, leading to a lower H_2CO to CO gradient than the other smoke sampled.

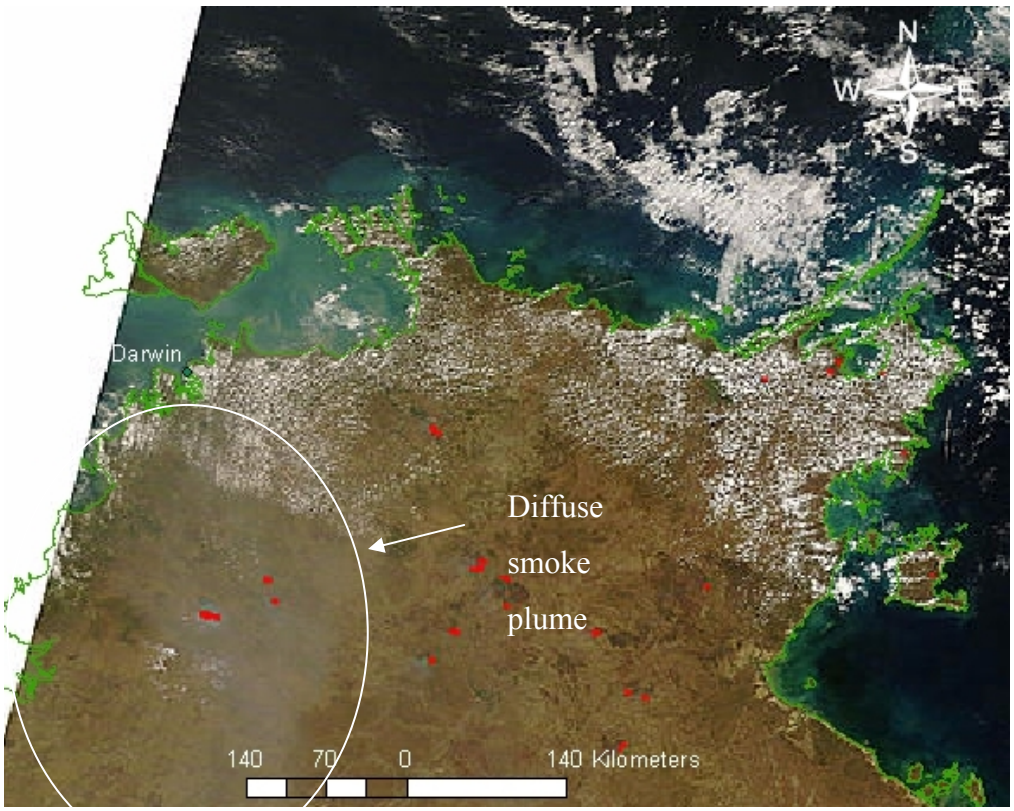

Figure 6-22: MODIS true colour image from the Aqua satellite on 3rd October 2007 with detected thermal anomalies shown as red spots.

The MODIS true colour image and back trajectory analyses for the 4th October 2007 were discussed in the previous section, and it proved impossible to pinpoint which of the many fires were being sampled (see Figure 6-10 and Figure 6-11). It was suggested that the smoke may have originated from several different fires, including a diffuse smoke plume in the west. The low H_2CO to CO gradient for the day of 0.012 ±

0.001 with a value for the square of the correlation coefficient (r^2) of 0.51 is in keeping with the idea that there may have been a mixture of fresh and aged smoke sampled on this day. The MODIS true colour image for the 2nd November 2006 and the 30th November 2006 (see Figure 6-17 and Figure 6-18) both show diffuse smoke plumes. These are most probably aged smoke because over time the smoke will become more diffuse. No clear smoke is visible in the MODIS true colour image for the 10th October 2007 (see Appendix 3).

The average and standard deviation of the H_2CO to CO gradients (for all days when spectra were recorded through smoke during October and November) are 0.002 ± 0.010 (i.e. indistinguishable from zero).

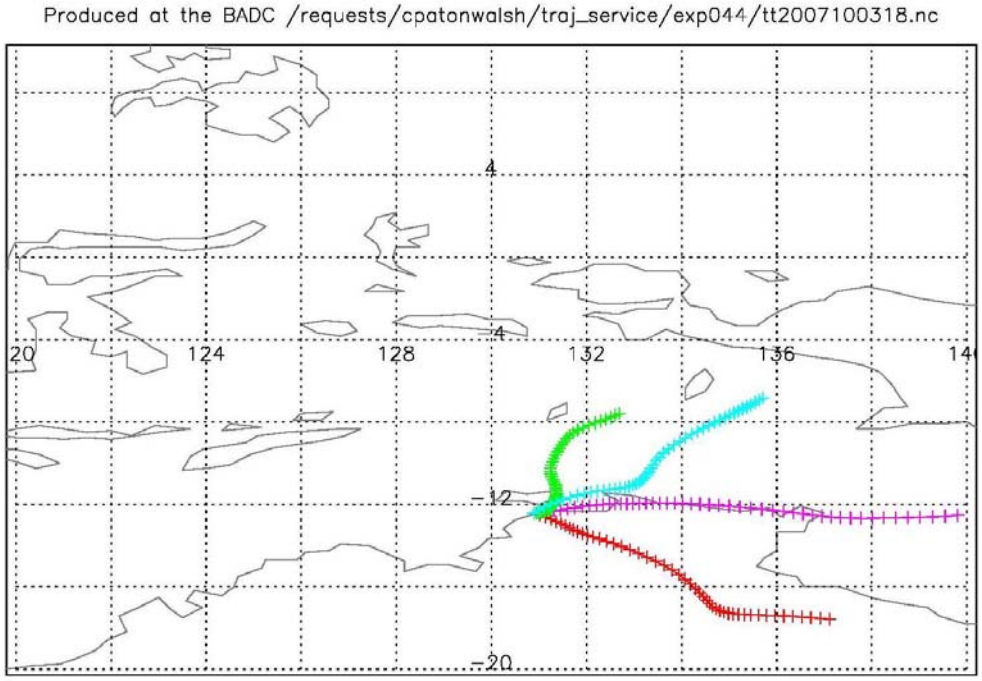

Figure 6-23: Back trajectories showing projected origin and age of parcels of air arriving over Darwin at different pressure levels: 950 hPa (pink), 750 hPa (red), 550 hPa (green) and 350 hPa (light blue). The crosses represent hour intervals back in time from 18:00 on 3rd October 2007.

In contrast to the October and November data, the H_2CO and CO retrievals from most of the days between May and September have high correlation coefficients and similar H_2CO to CO gradients, with the exception being the 20th September 2007. As noted in the previous section, the MODIS true colour image from this day shows widespread fires to the far east of Darwin and evidence of the build up of smoke in the

region (see Figure 6-19). Back trajectory analysis for the 20th September 2007 suggests that the smoke is probably in the order of 24 hours old or older (see Figure 6-20). The regressions analysis of retrievals of H_2CO and CO from the 20th September 2007 show no significant correlation ($r^2 = 0.03$) and the data from this day were excluded before an average and standard deviation H_2CO to CO gradient of 0.022 ± 0.007 was calculated for smoke sampled between May and September.

The H_2CO to CO gradients for May to September (see Table 6-3) are surprisingly consistent. H_2CO is short-lived with primary loss mechanisms being via photo-dissociation with a half-life of approximately 3 hours in daylight [*Warneck*, 2000]. The relevant reactions are:

$H_2CO + h\nu \rightarrow H + HCO$ (effective below 335 nm)
$H_2CO + h\nu \rightarrow H_2 + CO$ (effective throughout absorption region 355nm - ~ 250 nm)
$H + O_2 + M \rightarrow HO_2 + M$
where M is a suitable third body molecule [*Warneck*, 2000].

H_2CO is also lost by reaction with the OH radical via the following reaction path:

$H_2CO + OH \rightarrow H_2O + HCO$
$HCO + O_2 \rightarrow HO_2 + CO$

Thus the H_2CO to CO gradient should be very sensitive to the age of the smoke sampled because of the short atmospheric lifetime of H_2CO. Since many of the attempts to estimate the age of smoke sampled using MODIS true colour plots coupled with back-trajectories analyses were inconclusive it is possible that much of the smoke sampled was of a similar age. However there are three days for which a successful estimate was made for the age of the smoke:

1. 27th June 2007 - estimated age of smoke is 5 hours (see Figure 6-12-Figure 6-14) and the H_2CO to CO gradient is 0.020 ± 0.001
2. 9th August 2007 – estimated age of smoke is in excess of 12 hours (see Figure 6-15 and Figure 6-16) and the H_2CO to CO gradient is 0.033 ± 0.002

3. 20th September 2007 – estimated age of smoke is in excess of 24 hours (see Figure 6-19 and Figure 6-20) and the H_2CO to CO gradient is 0.003 ± 0.002

Obviously care should be taken in trying to draw conclusions from such a small set of data. However, comparing the data from the 27th June 2007 and the 9th August 2007 suggests that secondary formation of H_2CO within the smoke plume may be more significant than the combined loss of H_2CO through photo-dissociation and oxidation via reaction with OH in the first few hours after emission. As well as being a primary emission product of biomass burning, H_2CO is produced by the oxidation of methane and non-methane volatile organic compounds (NMVOCs).

The formation of H_2CO from the oxidation of CH_4 is by the following sequence

$$OH + CH_4 \rightarrow H_2O + CH_3$$
$$CH_3 + O_2 + M \rightarrow CH_3O_2 + M$$
$$CH_3O_2 + NO \rightarrow CH_3O + NO_2$$
$$CH_3O + O_2 \rightarrow H_2CO + HO_2$$

such that H_2CO is the first stable product of this reaction sequence. The formation of H_2CO by this mechanism is slow with reaction times in the order of years. Similar oxidation pathways for NMVOCs will also produce H_2CO. Many of these reactions are much faster taking minutes or hours, although the degradation mechanisms of many of the NMVOCs is poorly understood, with large uncertainties in individual yields [*Stavrakou et al.*, 2008].

Since non-methane hydrocarbons are major products of biomass burning the concentrations of these trace gases that produce H_2CO will be very significantly enhanced in fresh smoke plumes making secondary production of H_2CO an extremely significant source of H_2CO in the plumes. Stavrakou *et al*, [2008] undertook a large scale modelling exercise using the Master Chemical Mechanism v3.1 [*Saunders et al.*, 2003] to quantify the H_2CO production from vegetation fires and estimate the relative contributions of different NMVOCs to the total H_2CO production and the H_2CO production after a single day. Interestingly their model suggests that primary H_2CO emission accounts for only 14% of the total H_2CO produced over the course of the first day. The measurements described here support this finding at least qualitatively.

In the first few hours after emission, secondary formation of H_2CO from enhanced amounts NMVOCs in the smoke is more than compensating for H_2CO loss through photo-dissociation and oxidation via reaction with OH. Only when the smoke has aged sufficiently for the supply of NMVOCs to be depleted and no longer able to replenish the H_2CO, does the H_2CO to CO gradient drop significantly as seen on 20th September 2007 and much of the October and November data.

6.5 Emissions Ratios for H_2CO, HCN, C_2H_2 and C_2H_6 from Tropical North Australian Savanna Fires

The average H_2CO to CO gradient from all of the smoke sampled between May and September (excluding 20th September 2007 as explained above) is 0.022 ± 0.007. This may be used as an emission ratio of H_2CO with respect to CO for local savanna fires. As explained above, the effects of secondary formation of H_2CO in the smoke plumes may result in this emission ratio being biased to the high side compared to measurements made in fresh smoke. Using a literature value for the emission factor of CO of 65 ± 20 g kg^{-1} dry matter (DM) burned [*Andreae and Merlet*, 2001] this gives an emission factor for H_2CO of 1.5 ± 0.5 g kg^{-1} DM burned.

Emission ratios for HCN, C_2H_2 and C_2H_6 with respect to CO could not be derived in the same manner as for H_2CO. This is because there were too few data points to reliably establish a separate regression equation for each day (after the spectra were co-added in order to improve the signal-to-noise before retrieval of HCN, C_2H_2 and C_2H_6). Instead emission ratios were derived using only the data recorded between May and July so that a consistent background column amount of CO could be determined. There could be seasonal differences in these emission ratios and if this is the case these calculations will only be representative of the early dry season.

The emission ratio is the excess amount of each gas divided by the excess amount of CO, so suitable background values must first be estimated before the excess column amount of each gas coming from the smoke plumes can be determined. The

time series of CO columns derived from the NIR record at Darwin provides a good means of estimating background CO amounts. Minimum values are typically between January to April (at the end of the wet season) although controlled burning often takes place in pre-dry season times and smoke from these fires could cause some higher CO column amounts. The average values from January to April for 2006, 2007 and 2008 are $(1.2 \pm 0.1) \times 10^{18}$, $(1.3 \pm 0.1) \times 10^{18}$ and $(1.3 \pm 0.1) \times 10^{18}$ molecules cm^{-2} respectively. Data from 2006 produced the lowest of these average values, and this was taken as a best estimate of background CO, [$(1.2 \pm 0.1) \times 10^{18}$ molecules cm^{-2}], (equivalent to a ground level VMR of 80 ± 10 $nmol.mol^{-1}$ for the profile shown in Figure 5-3).

Background column amounts of the other trace gases were derived by substituting this value of CO into the simple linear regression equation derived from analyses of the data contained in the plot of each gas against CO.

The linear regression equation derived from the HCN to CO plot was:

$$HCN = 0.0017\ CO + 1.1 \times 10^{15}$$

and substituting a background CO value of $1.2 \pm 0.1 \times 10^{18}$ molecules cm^{-2} yields a background amount for HCN of $3.2 \pm 0.3 \times 10^{15}$ molecules cm^{-2}. Excess amounts of CO and HCN were calculated by deducting these background values from the derived column amounts for all spectra and the plot of excess HCN versus excess CO column is shown in Figure 6-24.

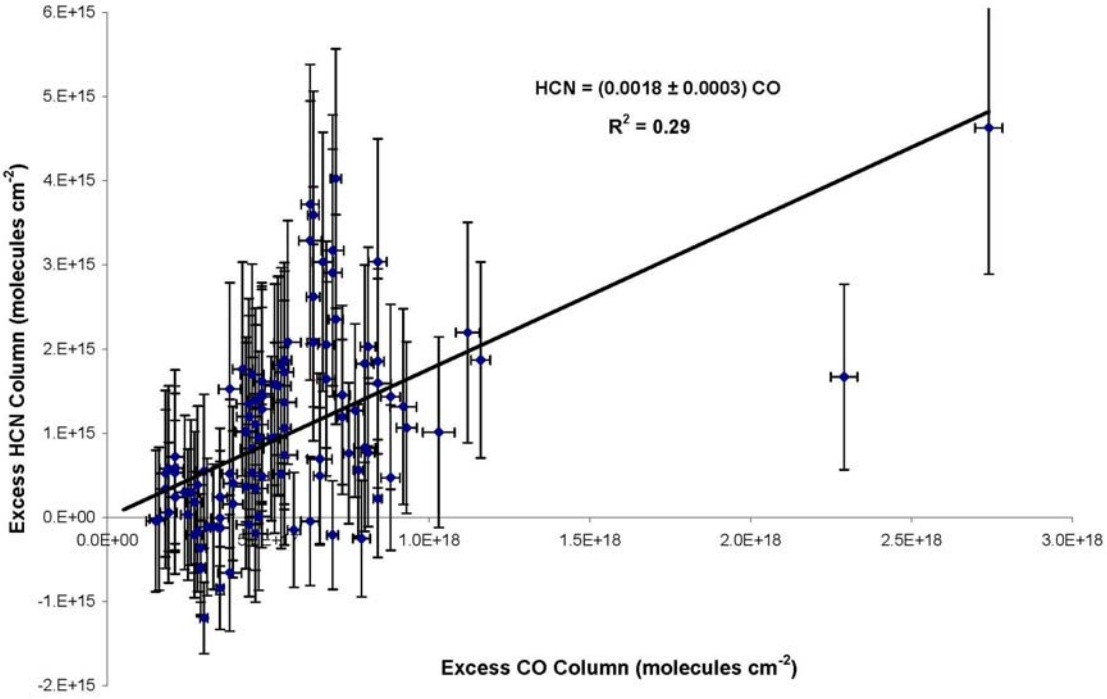

Figure 6-24. Excess HCN column plotted against excess CO column.

Generalised least squares regression analysis performed on this data taking into account uncertainties in both HCN columns and CO columns yielded an emission ratio of 0.0018 ± 0.0003. The results of the regression analysis will be heavily dependent on the two points with the highest amounts of CO, adding to the uncertainty of the emission ratio determined. Also note that the uncertainty in the regression analysis determination of the gradient assumes no correlation between points and so the actual uncertainty is likely to be larger than this. Converting to an emission factor (using 65 ± 20 g CO kg^{-1} DM burned) gives 0.11 ± 0.04 g HCN kg^{-1} DM burned.

The simple linear regression equation relating C_2H_2 and CO columns is:

$$C_2H_2 = 0.0025\ CO - 9.8 \times 10^{14}$$

yielding a background amount for C_2H_2 of 2.1 ± 0.2 $\times 10^{15}$ molecules cm^{-2}. The plot of excess C_2H_2 versus excess CO column is shown in Figure 6-25, and generalised least squares regression analysis produces an estimated emission ratio of 0.0024 ± 0.0004 and an emission factor of 0.14 ± 0.05 g C_2H_2 kg^{-1} DM burned.

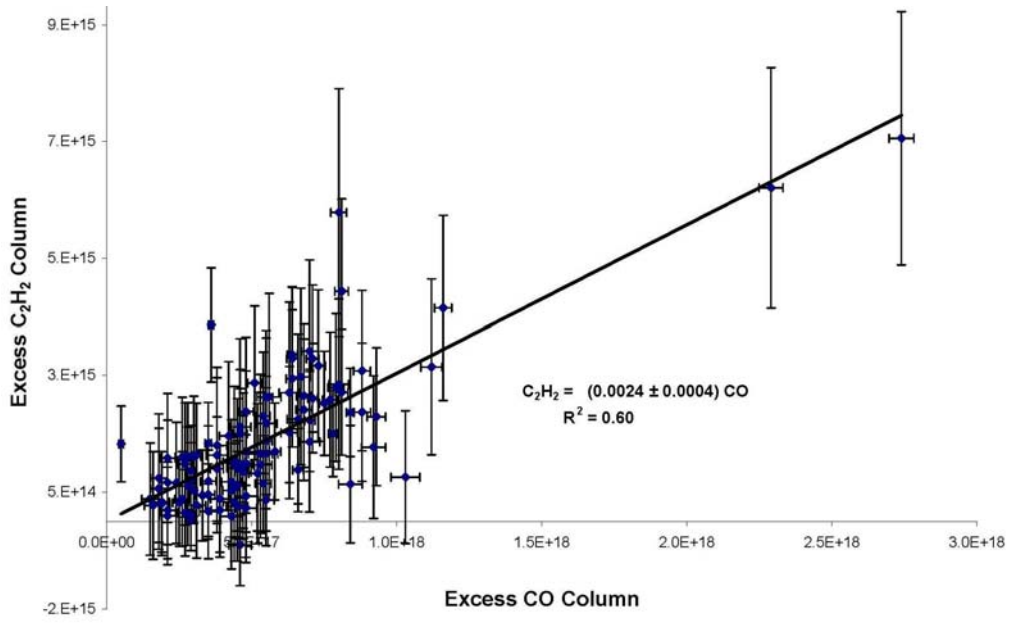

Figure 6-25. Excess C_2H_2 column plotted against excess CO column.

Finally the equation relating C_2H_6 and CO columns is:

$C_2H_6 = 0.002\ CO + 3.5\ x10^{15}$

giving a background amount for C_2H_6 of $5.9 \pm 0.5\ x10^{15}$ molecules cm^{-2}. Again note that the results of the regression analysis will be heavily dependent on the two points with the highest amounts of CO, and that the uncertainty in the gradient determined by the regression analysis will be an underestimate.

Figure 6-26 shows the excess C_2H_6 plotted against excess CO columns and yields an estimated emission ratio of 0.0018 ± 0.0003 and an emission factor of 0.13 ± 0.04 g C_2H_6 kg^{-1} DM burned.

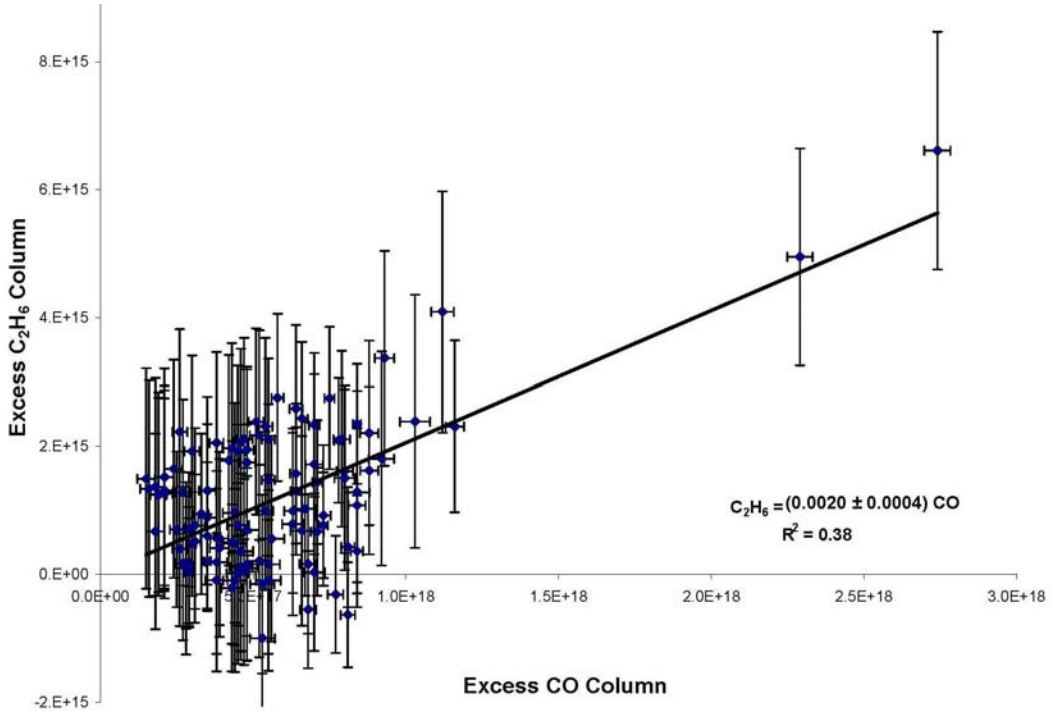

Figure 6-26. Excess C_2H_6 columns plotted against excess CO columns.

In Table 6-4 the emission ratios calculated from this work are compared to the few other existing field measurements from Australian savanna fires found in the literature [*Hurst et al.*, 1994a; *Hurst et al.*, 1994b; *Shirai et al.*, 2003b] and measurements of laboratory fires of savanna grasses using proton transfer reaction mass spectrometry [*Holzinger et al.*, 1999].

The H_2CO emission ratio calculated from this work is nearly an order of magnitude higher than the only previous field measurements from Australian savanna fires [*Hurst et al.*, 1994b]. This might be explicable by the effects of secondary formation of H_2CO by oxidation of CH_4 and NMVOCs in the smoke plume. As discussed above there is evidence that the quantity of H_2CO may reach an equilibrium value that lasts from when the smoke is just a few hours old (eg 5 hours or less) until the reservoir of NMVOCs is depleted sufficiently to no longer be able to replenish the H_2CO lost through photo-dissociation and oxidation (at least 12 hours or more). This equilibrium amount of H_2CO in the smoke plumes could be significantly higher than the amount of H_2CO directly emitted by the biomass burning and present in fresh smoke. The measurements by Hurst et al, [1994b] were made from the ground and in a light

aircraft sampling fresh smoke very near the fires and so this theory presents one possible reason for the discrepancy between the two results. Conflicting evidence comes from the laboratory measurements of Holzinger *et al* [1999] that sampled a large number of different savanna grasses when burnt. The average emission ratio found in the laboratory fires is in good agreement with that found in this study, suggesting that the measurements by Hurst *et al* [1999b] may be spuriously low.

The C_2H_2 emission ratio from this work is in good agreement with Hurst *et al*, [1994a] and Shirai *et al*, [2003] but measurements by Hurst *et al* [1999b] are more than a factor of 3 lower than all the other measurements. Given that the use of the regression analyses uncertainty in the calculated gradient is likely to produce an underestimate of the true uncertainties in the derived emission ratios (because of correlations between the uncertainties of points used in the regression), the emission ratio for C_2H_6 found in this study (0.0020 ± 0.0003) is broadly comparable to that found by Shirai *et al* [2003] of (0.0028 ± 0.0003) but significantly lower than that found by Hurst *et al* [1994a] (0.0048 ± 0.0018). Lastly the HCN measurements described here are more than a factor of 3 higher than that found by Hurst *et al* [1994a] and over 6 times higher than the value given in Hurst *et al* [1994b], but again in reasonable agreement with the laboratory studies of Holzinger *et al* [1999]. One possible explanation for the discrepancies is that many of the measurements described in the studies by Hurst *et al* [1994a] and [1994b] were based upon stored samples and gases such as H_2CO and HCN may have been subject to losses during storage.

A final comment is to point out that a large spread in values for emission ratios or emission factors obtained from different studies is not uncommon in the measurement of emissions from biomass burning [*Andreae and Merlet*, 2001]. This underlines the contribution of studies such as this in improving the reliability of estimates of the emissions of trace gases from different fire types around the world.

Table 6-4: Emission ratios with respect to CO for this work compared to other measurements in the literature.

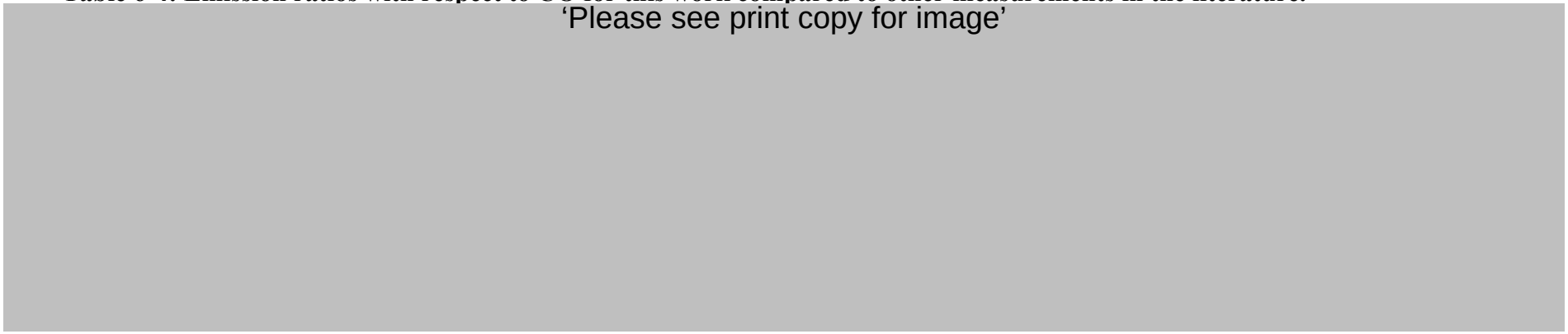

Notes: Hurst et al, 1994a and 1994b and Holzinger et al, 1999, give emission ratios as mean value calculated separately from all samples and uncertainties as 1σ standard deviation of the mean. This work and that of Shirai et al, give gradient and uncertainty of the gradient from regression analysis of trace gas versus CO plots as described in the text.

6.6 Correlations between trace gases and AOD

The mid infrared spectra from Darwin were recorded without the use of narrow band filters allowing H_2CO, HCN, C_2H_2, C_2H_6 and CO column amounts all to be derived from the same spectra. This removed the need for the use of AOD as a proxy for CO when deriving emission ratios for the tropical north Australian savanna fires. Nevertheless it is interesting to determine the correlations between AOD and the trace gases measured over Darwin in order to assess the possibility of using satellite measurements of AOD to map the emissions from savanna fires as was done for southeast Australian forest fires in Chapter 4.

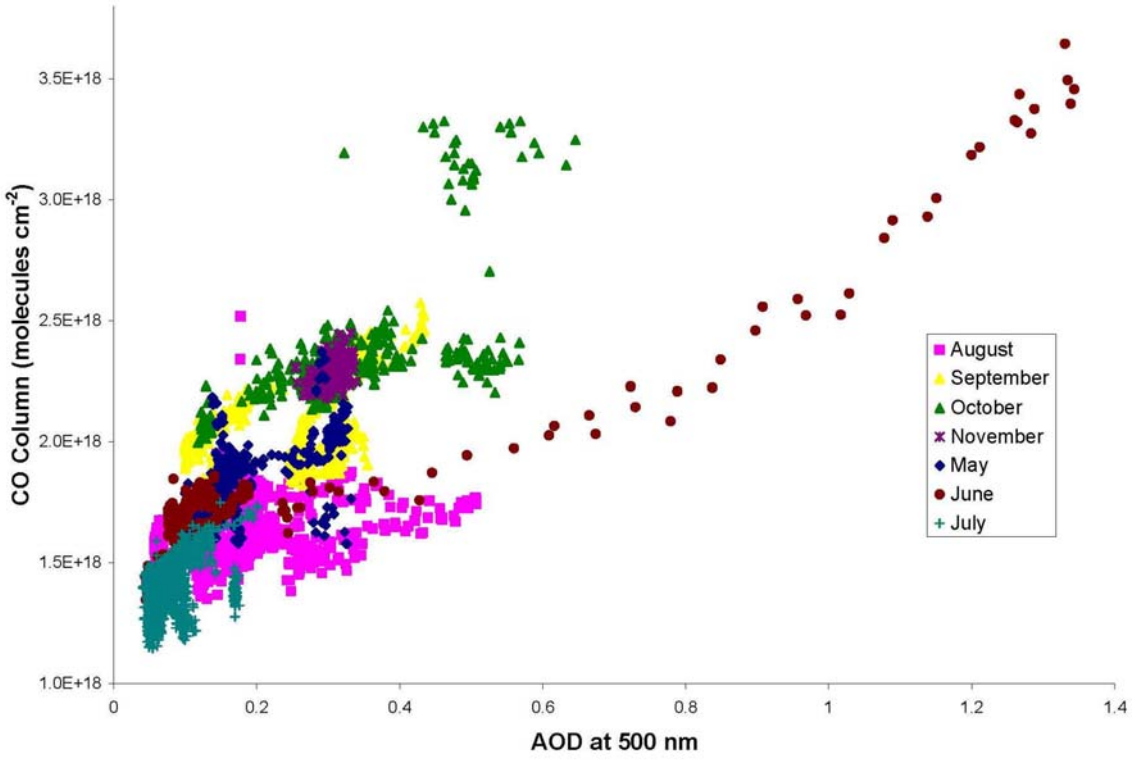

Figure 6-27: Plot of Column CO against AOD at 500 nm colour coded by month, for all InSb spectra taken during 2006-2008.

Figure 6-27 shows the total column amounts of CO derived from the spectra recorded with the InSb detector from 2006-2008. The points look quite scattered but the correlation coefficient (R^2 = 0.62) is significantly higher than that found for the NIR

spectra (R^2 =0.20) shown in Figure 5-17. This is to be expected because the InSb spectra were taken by manual intervention to the automated system in the dry season and with the aim of capturing smoke plumes from local savanna fires. Much of the variation is dependent upon the time of the year, with CO levels increasing towards the end of the year with the build-up of local and transported smoke. The aerosol component of the smoke is not as long lived in the atmosphere and so the CO to AOD ratio increases towards the end of the year.

In order to avoid the changing background levels of column CO, the data from May-July only are plotted in Figure 6-28. The correlation coefficient R^2 = 0.65 is only slightly higher than for the whole dataset together, but the CO to AOD gradient is lower as well as the background or intercept value.

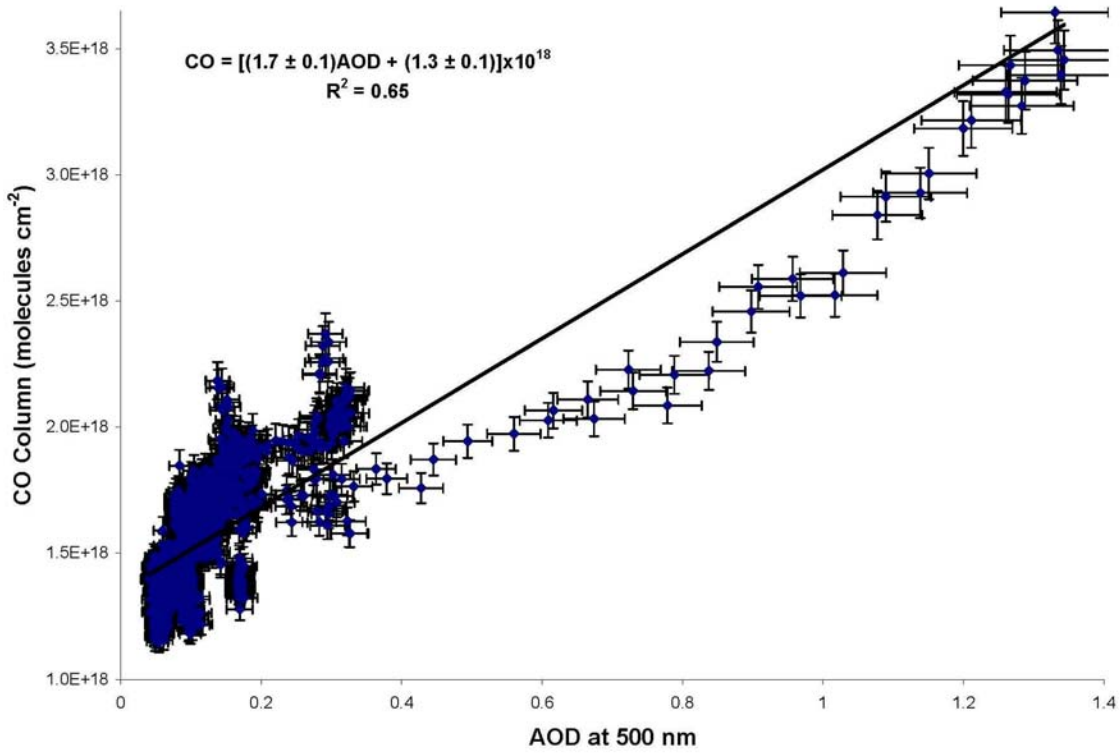

Figure 6-28: Plot of Column CO against AOD at 500 nm for subset of InSb spectra taken during May-July 2006-2008.

Compared to the result for forest fires, the early dry season background CO (1.3 ± 0.1) x10^{18} molecules cm^{-2} (as determined from the intercept of the best straight line fit to the CO to AOD data) is lower than background values around Wollongong (1.5 ± 0.1) x10^{18} molecules cm^{-2}. This is not what is expected from the latitudinal gradient

[*Connors et al.*, 1999], but both background values are supported by other measurements: ground-based NIR measurements from Darwin and MIR measurements from Wollongong and MOPITT measurements over both sites (see Chapter 5), and a local source of CO near Wollongong is implicated.

The CO relative to AOD gradient for smoke affected spectra is slightly greater at Darwin than at Wollongong, (1.7 ± 0.1 compared to 1.5 ± 0.1). The correlation coefficient is lower (R^2 = 0.65) than that found at Wollongong for forest fires (R^2=0.87), but this may be explained by the fact that at Wollongong the sunphotometer and the FTIR were sampling exactly the same column, whilst at Darwin the sun-photometer is ~100m from the FTIR spectrometer. This means that the line of sight is slightly different at Darwin and this could be significant, especially when measuring through a smoke plume that is confined to the lower boundary layer.

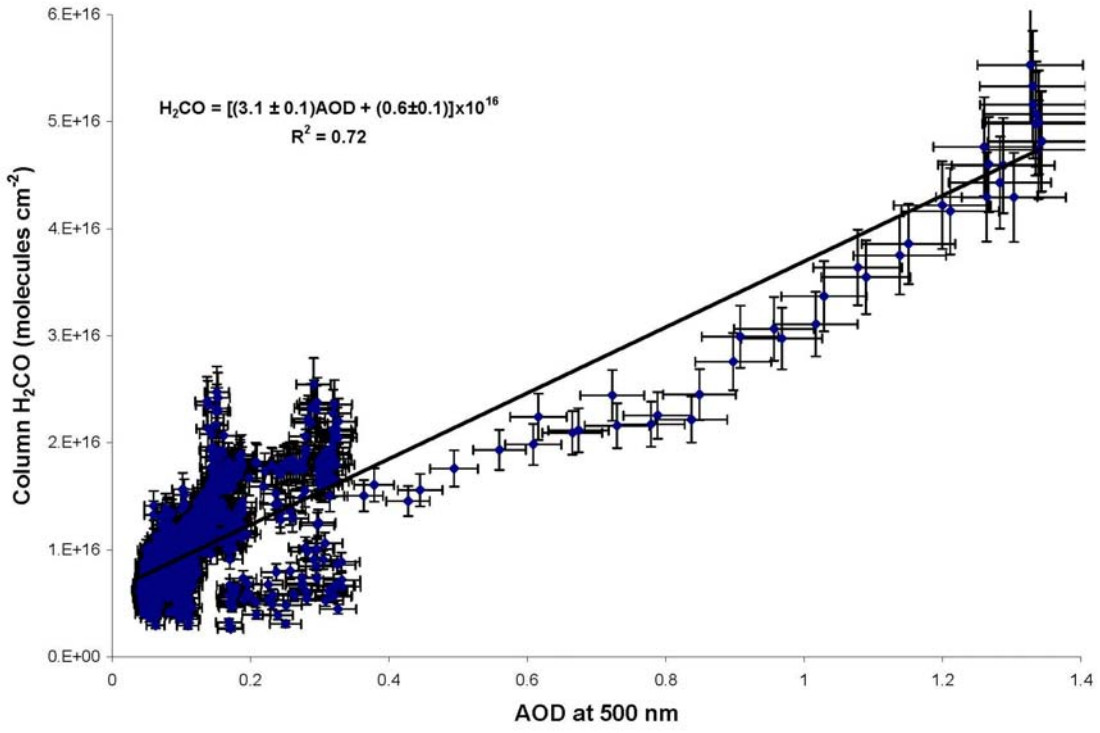

Figure 6-29: Plot of Column H_2CO against AOD at 500 nm for all InSb spectra taken during May-July 2006-2008.

The correlation coefficient between H_2CO and AOD shown in Figure 6-29 (R^2=0.72) is slightly higher than that found for CO and AOD (R^2=0.65). Exactly the

same set of spectra are analysed in both plots, so assuming that the difference is significant, then this is an indication that some effect of aged smoke exists in the dataset, despite it being limited to spectra recorded in the early dry season. Due to the longer atmospheric lifetime of CO, in aged smoke the CO remains elevated whilst aerosols and H_2CO have been lost. The influence of aged smoke may come from earlier local savanna fires or be the result of transported smoke from Indonesia or even African or South American fires.

The correlation coefficients relating the other trace gases to AOD are all less than 0.5, but this to be expected given the large uncertainties of the measurements. The spectral coverage of each individual spectrum removed the need for the use of AOD as a proxy for CO. Instead the emission ratio to CO found for HCN, C_2H_2 and C_2H_6 can be used in conjunction with the CO to AOD regression equation to estimate emissions of these trace gases from the AOD of the atmosphere.

In conclusion, the strong correlations that exist for both CO and H_2CO with AOD means that it would be possible to use satellite AOD to estimate emissions from savanna fires in the early dry season in a similar manner to that done for forest fires in Chapter 5. The complicating effects of the build-up of aged smoke and the influence of transported smoke into the region, make interpreting the measurements significantly harder than for forest fires measured from Wollongong. Extracting the local signal from smoke measured later in the year might be possible but in reality is likely to be difficult. On balance despite the improved sensitivity at the ground, the use of satellite measurements of AOD as a proxy for CO is not likely to lead to better estimates of biomass burning in the tropical north of Australia than the use of direct satellite measurements of CO such as that provided by MOPITT.

Chapter 7 : Summary and Conclusions

7.1 Overview of Main Conclusions

The objective of this thesis is to improve our knowledge of emissions to the atmosphere from biomass burning in Australia. The work described includes the analysis of ground-based solar absorption spectra taken through smoke plumes from Australian forest fires to derive vertically integrated measurements of emitted trace gases C_2H_2, C_2H_4, C_2H_6, HCOOH, CO, H_2CO, HCN, NH_3 and CH_3OH. The measured trace gas amounts have been shown to correlate well with simultaneous, co-located measurements of AOD, such that AOD can be used as a proxy for CO in deriving emission ratios to CO for the other trace gases. Converting to emission factors using an average value for the emission factor of CO from previous studies indicates that Australian forest fire emissions are broadly similar to those from other geographical regions except for comparatively low emissions of C_2H_6.

A new method of making estimates of gaseous emissions from fires has been suggested that utilises the correlations between trace gases and AOD in smoke plumes in conjunction with satellite-based measurements of AOD. This new method has potential advantages over traditional techniques because AOD is a property very closely related to a direct emission product of fires (namely aerosols). It also has possible advantages over the direct use of satellite based CO measurements in that the measurement of AOD has greater sensitivity close to the ground where much of the smoke is located. However, there are significant difficulties in applying the new method due to the fact that the view of the earth's lower atmosphere from space is often obscured by clouds or interrupted by technical problems with the measurements. This means that the estimated emissions will often be underestimated. Nevertheless the addition of another tool for making estimates of gaseous emissions from biomass burning is useful for corroborating existing techniques, especially since the sources of uncertainties inherent in the different techniques are largely independent of one another.

The new method for estimating total emissions of different trace gases has been applied to the Canberra fires of 2003, producing a value of 4.9 – 9.6 Tg CO released during the 49 days of the fires from the 8th January to the 26th of February 2003.

Ground-based Fourier transform near infrared solar remote sensing measurements from Darwin have been analysed for total column amounts of CO with the resulting time series showing a very clear annual cycle. Peak values of around 2.0 x 10^{18} molecules cm^{-2} are typical in late September and early October towards the end of the dry season compared to minimum values of about 1.1 x 10^{18} molecules cm^{-2} during January to March in the wet season. The peak in CO columns amounts is significantly larger and later in 2006 with evidence from satellite images implicating transported pollution from Indonesia where El Niño conditions caused unusually extensive fires in this year. The AOD record from Darwin corroborates this theory as the 2006 peak is not larger than the other years, which suggests that the extra CO comes from smoke aged sufficiently for much of the aerosol loading to have settled out. The CO total column time series from Darwin has been compared to measurements of CO derived for the same region from the MOPITT satellite. The agreement is within the expected uncertainties giving greater confidence to MOPITT retrievals in the tropics. The high correlation between the two datasets is indicative of the site at Darwin being influenced mainly by large-scale events that are also captured by the satellite-based instrument.

Mid infrared spectra have been recorded from the TCCON observatory at Darwin on 45 separate days since April 2006, with smoke plumes sampled on 20 of these days. Column amounts of CO, H_2CO, C_2H_2, C_2H_6 and HCN have been derived from these spectra that have yielded emission ratios to CO for the four latter gases from tropical north Australian savanna fires. These have proved to be a useful addition to the existing measurements in the literature suggesting the possibility that some earlier measurements may have suffered from sampling losses. Evidence from back-trajectory analysis indicates that the H_2CO to CO ratio remains surprisingly consistent over several hours as the smoke ages, suggesting that the loss of H_2CO through photodissociation and oxidation is largely compensated by secondary formation of H_2CO through oxidation of other non-methane hydrocarbons emitted by the fires.

Trace gas amounts from the savanna fires have also been shown to correlate reasonably well with AOD, but the complicating influence of aged smoke on the Darwin site means that it may be difficult to apply the same techniques used for estimating emissions from the Canberra fires to the savanna fires of tropical north Australia.

7.2 Outcomes for Specific Objectives of the Thesis

In Chapter 1 a number of specific objective of the thesis were listed. These are given again below in italics and the outcomes for individual objectives are discussed below.

1. *The first objective of the work described in this thesis was to analyse and interpret the existing spectroscopic measurements of smoke plumes sampled from Wollongong. The analysis was aimed at extracting information that would be useful in quantifying emissions from Australian forest fires.*

Spectra were initially analysed for total column amounts of CO, HCN, H_2CO and NH_3. The correlations between AOD and trace gases were established and a method of using satellite measurements of AOD for estimating gaseous emissions from fires was outlined. Emission ratios to CO were calculated for HCN, H_2CO and NH_3 using AOD as a proxy for CO, converted to emission factors and shown to agree well with other values in the literature for temperate forest fires. This work was published in:

Paton-Walsh, C., N.B. Jones, S.R. Wilson, A. Meier, N. Deutscher, D.W.T. Griffith, R. Mitchell and S. Campbell. (2004), Trace gas emissions from biomass burning inferred from aerosol optical depth, *Geophysical Research Letters*, *31*(5), L05116. (see Appendix 1).

New line parameters contained in the HITRAN 2000 database [*Rothman et al.*, 2003] were used to analyse the most smoke affected spectrum from the 1st January 2002

for C_2H_4. The original analysis was undertaken by colleagues at NASA Langley but later modified using the analysis procedure described in this thesis. This was the first measurement of C_2H_4 from ground-based solar remote sensing using HITRAN line parameters and the work was published in:

Rinsland, C. P., C. Paton-Walsh, N. B. Jones, D. W. T. Griffith, A. Goldman, S. W. Wood, L. Chiou and A. Meier. (2005), High spectral resolution solar absorption measurements of ethylene (C_2H_4) in a forest fire smoke plume using HITRAN parameters: Tropospheric vertical profile retrieval, *Journal of Quantitative Spectroscopy and Radiative Transfer*, *96*(2), 301.

Later the original analysis procedure was refined and the spectra reanalysed for total column amounts of CO, HCN, H_2CO and NH_3, along with additional species C_2H_2, C_2H_4), ethane (C_2H_6) and formic acid (HCOOH). Emission ratios and emission factors were calculated and a thorough uncertainty analysis was undertaken. The resulting emission factors from this work indicate that emissions from fires in southeastern Australian forests (which are predominantly varieties of eucalyptus) are broadly similar to those from other geographical regions except for comparatively low emissions of C_2H_6.

This work was published in:

Paton-Walsh, C., N. B. Jones, S. R. Wilson, V. Haverd, A. Meier, D.W.T. Griffith and C. P. Rinsland. (2005), Measurements of trace gas emissions from Australian forest fires and correlations with coincident measurements of aerosol optical depth, *Journal of Geophysical Research-Atmospheres*, *110,* D24, (see Appendix 1).

The combination of back-trajectory analysis and MODIS satellite images (showing thermal anomalies and smoke) provided evidence that the spurious data from 1st January 2002 was due to exceptionally young smoke (< 0.5 hour) being sampled. In such young smoke plumes the aerosols have not yet coalesced into a stable form, resulting in a lower AOD value than for more mature smoke.

Finally the inclusion of line parameters for CH_3OH in the HITRAN 2004 database [*Rothman et al.*, 2005] allowed column amounts of this gas to be added to the list of species retrieved from the smoke affected spectra. These measurements constituted the first ever ground-based FTIR remote sensing measurements of CH_3OH in the atmosphere and this work was published in:

Paton-Walsh, C., S. R. Wilson, N. B. Jones and D.W.T. Griffith, (2008), Measurement of methanol emissions from Australian wildfires by ground-based solar Fourier transform spectroscopy, *Geophysical Research Letters*, *35*(8), L08810. (See Appendix 1).

The above work is described in detail in Chapter 3 of this thesis.

2. *The second objective derived from the strong correlations between AOD and trace gas amounts, established whilst fulfilling the first objective. This second aim was to use these correlations along with satellite measurements of AOD to make a total emissions estimate from an individual fire episode.*

The trace gas to AOD correlations can be applied to satellite measurements of AOD to determine the total enhanced atmospheric loading of each trace gas as a result of fires in a geographical region. This technique has been applied to the Canberra fires of 2003 and atmospheric dispersion modeling (using TAPM) utilized to account for smoke plumes that are not fully dispersed at the time of the next satellite overpass being used in the calculation. The total emissions of CO from the fires (from their start on the 8th January 2003 to the time that they were extinguished by heavy rainfall in late February 2003), were estimated to be 4.9 – 9.6 Tg. This work is described in detail in Chapter 4 of this thesis and will be written up for later publication in the scientific literature.

3. *The third objective was to collect a similar dataset of spectroscopic measurements of smoke plumes from the fires in the savanna grasslands and*

woodlands in the tropical north of Australia. The resulting dataset would be analysed in a similar manner to the measurements of smoke plumes from forest fires in the southeast of the country to characterise the emissions from biomass burning throughout Australia. This work is described in Chapter 5 and Chapter 6.

A time series of total column amounts of CO from Darwin with high temporal resolution has been produced from the near infrared spectral record. The time series shows a very clear annual cycle with peak values at the end of the dry season nearly twice the magnitude of wet season minimum values (~ 1.1 x 10^{18} molecules cm^{-2}). Evidence of transportation from the severe Indonesian fires of 2006 is seen in the timing and magnitude of the peak 2006 CO columns amounts. The AOD record does not show unusually high values indicating that the enhanced CO has outlasted the aerosols indicating substantially aged pollution. The time series of CO columns from Darwin have been compared to column amounts of CO from MOPITT. This work is described in detail in Chapter 6 and included along with comparisons of MOPITT CO with CO total column time series from Wollongong and Lauder in a paper currently in preparation for publication:

Edwards, D. P., N. B. Jones, C. Paton-Walsh, G. Guerova, D. Griffith, Satellite and ground-based remote sensing of Carbon Monoxide over Australasia (*International Global Atmospheric Chemistry , plenary conference presentation, 2008* and i*n preparation for submission to Geophysical Research Letters*, 2009)

The Sentinel alert website was used along with forecasts of wind direction to predict the likelihood of smoke passing over the Darwin observatory. In total smoke plumes were successfully captured on 20 separate days from August 2006 to June 2008. These measurements are ongoing.

Column amounts of CO and H_2CO have been determined from the entire time series of InSb spectra. Attempts have been made to estimate the age of the smoke plumes sampled from Darwin using satellite images containing thermal anomalies and back-trajectory analysis. Despite difficulties in determining the age of the smoke this work

has shown strong evidence for the importance of secondary formation of H_2CO within the smoke plumes.

Column amounts of C_2H_2, C_2H_6 and HCN have also been obtained by coadding InSb spectra. Spectral signal-to-noise is still a significant contributor to the uncertainty of these retrieved columns despite the co-addition of spectra. Emission ratios with respect to CO determined from this work agree well with previous field measurements by Shirai, *et al*, [2003] and laboratory measurements by Holzinger, *et al,* [1999], but are significantly larger than field measurements by Hurst *et al,* [1994b]. The latter work involved storing samples for later analysis and it is possible that sample loss during storage accounts for these differences.

Details of the analysis and interpretation of InSb spectra from Darwin are given in Chapter 6 and a paper describing the work is currently being prepared for publication:

Paton-Walsh, C, N. M. Deutscher, D.W.T. Griffith, S.R.Wilson, N.B. Jones, B. Forgan and D.P. Edwards, Measurements of Emissions from Savanna Fires in Tropical North Australia. (*In preparation for submission to Journal of Geophysical Research*, 2009)

Both CO and H_2CO column amounts have been shown to correlate well with coincident measurements of AOD in only smoke affected spectra from Darwin. The larger uncertainties in the retrieved amounts of C_2H_2, C_2H_6 and HCN columns are probably the limiting factor in determining the relationship between AOD and these other trace gases. In principle the same techniques used to estimate total emissions of CO and other gases from the Canberra fires could be applied to a specific isolated set of fires in the tropical savanna regions of north Australia. In practice the usefulness of the technique may be limited by interference of aged smoke pollution transported from Asia and other regions of the globe.

7.3 Recommendations for future work

There are a number of improvements that could be made to the measurements and modelling described in this thesis and a few ideas for future work are listed below.

- The estimation of total emissions from the Canberra fires could be improved by repeating the modelling of the dispersion of smoke plumes using a model that is mass conserving such as the global chemical transport model MOZART [*Emmons et al.*, 2009]
- Continuing remote sensing measurements from Darwin should capture further smoke plumes for which the origin and age of the smoke may be estimated, thereby improving our understanding of the changes in H_2CO concentrations in aging smoke plumes.
- Extending measurements further into the mid-infrared by use of a MCTdetector would allow emission factors for a number of volatile organic compounds to be derived.
- Installation of some narrow band-pass optical filters could improve the signal-to-noise and reduce uncertainties in the derived emissions factors.

7.4 Concluding Comments

Biomass burning is a global phenomenon with impacts that affect global atmospheric composition and chemistry. Recent inventories that utilize satellite and landcover data in conjunction with measurements of the emission factors for gases and particulates, rank Australia as the third most significant source of carbon emissions from biomass burning [*Ito and Penner*, 2004; *Kasischke and Penner*, 2004] emitting 8% of the global total. There are only a few previously published emission factors for many important trace gases from Australian forest and savanna fires, and in many instances there are large discrepancies between different studies. The emission ratios to CO and extrapolated emission factors derived in this thesis constitute a significant addition to our knowledge of the emissions from Australian fires and have helped to clarify possible problems with previous studies. In addition a new technique for making

estimates of gaseous emissions from fires has been developed and applied to the case of the devastating Canberra fires of 2003. Despite some limitations to this method it provides a truly independent method of estimating the magnitude of trace gases released to the atmosphere for individual fire events, adding confidence to the determination of these source strengths.

References

Abrams, M. C., S. P. Davis, M. L. P. Rao, et al. (1994), High-resolution Fourier-transform spectroscopy of the Meinel system of OH, *Astrophys. J. Suppl. Ser.*, *93*(1), 351-395.

Alexander, R. C., and R. L. Mobley (1976), Monthly average sea-surface temperatures and ice-pack limits on a 1 degree global grid, *Mon. Weather Rev.*, *104*(2), 143-148.

Alexandrov, M. D., B. E. Carlson, A. A. Lacis, et al. (2005), Separation of fine and coarse aerosol modes in MFRSR data sets, *Journal Of Geophysical Research-Atmospheres*, *110*(D13), 19.

Andreae, M. O. (1990), Biomass burning - its history, use, and distribution and its impact on environmental-quality and global climate, paper presented at Chapman Conf on Global Biomass Burning : Atmospheric, Climatic, and Biospheric Implications, Williamsburg, Va, Mar 19-23.

Andreae, M. O., J. Fishman, and J. Lindesay (1996), The Southern Tropical Atlantic Region Experiment (STARE): Transport and Atmospheric Chemistry near the Equator-Atlantic (TRACE A) and Southern African Fire-Atmosphere Research Initiative (SAFARI): An introduction, *Journal Of Geophysical Research-Atmospheres*, *101*(D19), 23519-23520.

Andreae, M. O., and P. Merlet (2001), Emission of trace gases and aerosols from biomass burning, *Global Biogeochem Cy*, *15*(4), 955-966.

Barret, B., M. De Maziere, and E. Mahieu (2003), Ground-based FTIR measurements of CO from the Jungfraujoch: characterisation and comparison with in situ surface and MOPITT data, *Atmospheric Chemistry And Physics*, *3*, 2217-2223.

Bell, W., N. A. Martin, T. D. Gardiner, et al. (1994), Column Measurements of Stratospheric Trace Species over Are, Sweden in the Winter of 1991-1992, *Geophysical Research Letters*, *21*(13), 1347-1350.

Bell, W., C. PatonWalsh, T. D. Gardiner, et al. (1996), Measurements of stratospheric chlorine monoxide (ClO) from groundbased FTIR observations, *Journal of Atmospheric Chemistry*, *24*(3), 285-297.

Bell, W., C. P. Walsh, P. T. Woods, et al. (1998), Ground-based FTIR measurements with high temporal resolution, *Journal of Atmospheric Chemistry*, *30*(1), 131-140.

Beringer, J., D. Packham, and N. Tapper (1995), Biomass burning and resulting emissions in the Northern Territory, Australia, *International Journal of Wildland Fire*, *5*(4), 229-235.

Blumenstock, T., H. Fischer, A. Friedle, et al. (1997), Column amounts of $ClONO_2$, HCl, HNO_3, and HF from ground-based FTIR measurements made near Kiruna, Sweden, in late winter 1994, *Journal of Atmospheric Chemistry*, *26*(3), 311-321.

Bodhaine, B. A., N. B. Wood, E. G. Dutton, et al. (1999), On Rayleigh Optical Depth Calculations, *J Atmos Ocean Tech*, *16*(11 part 2), 1854-1861.

Brault, J. W., and O. R. White (1971), Analysis and restoration of astronomical data via fast Fourier transform, *Astron. Astrophys.*, *13*(2), 169-&.

Brault, J. W. (1996), New approach to high-precision Fourier transform spectrometer design, *Appl Optics*, *35*(16), 2891-2896.

Carvalho, J. A., N. Higuchi, T. M. Araujo, et al. (1998), Combustion completeness in a rainforest clearing experiment in Manaus, Brazil, *Journal Of Geophysical Research-Atmospheres*, *103*(D11), 13195-13199.

Carvalho, J. A., F. S. Costa, C. A. G. Veras, et al. (2001), Biomass fire consumption and carbon release rates of rainforest-clearing experiments conducted in northern Mato Grosso, Brazil, *Journal Of Geophysical Research-Atmospheres*, *106*(D16), 17877-17887.

Christian, T. J., B. Kleiss, R. J. Yokelson, et al. (2003), Comprehensive laboratory measurements of biomass-burning emissions: 1. Emissions from Indonesian, African, and other fuels, *Journal Of Geophysical Research-Atmospheres*, *108*(D23).

Chu, D. A., Y. J. Kaufman, L. A. Remer, et al. (1998), Remote sensing of smoke from MODIS airborne simulator during the SCAR-B experiment, *Journal Of Geophysical Research-Atmospheres*, *103*(D24), 31979-31987.

Chu, D. A., Y. J. Kaufman, C. Ichoku, et al. (2002), Validation of MODIS aerosol optical depth retrieval over land, *Geophysical Research Letters*, *29*(12), 8007.

Chu, D. A., Y. J. Kaufman, G. Zibordi, et al. (2003), Global monitoring of air pollution over land from the Earth Observing System-Terra Moderate Resolution Imaging Spectroradiometer (MODIS), *Journal Of Geophysical Research-Atmospheres*, *108*(D21), 18.

Connors, V. S., B. B. Gormsen, S. Nolf, et al. (1999), Spaceborne observations of the global distribution of carbon monoxide in the middle troposphere during April and October 1994, *Journal Of Geophysical Research-Atmospheres*, *104*(D17), 21455-21470.

Crutzen, P. J., L. E. Heidt, J. P. Krasnec, et al. (1979), Biomass burning as a source of atmospheric gases CO, H_2, N_2O, NO, CH_3Cl and COS, *Nature*, *282*(5736), 253-256.

Crutzen, P. J., and M. O. Andreae (1990), Biomass burning in the tropics: Impact on atmospheric chemistry and biogeochemical cycles, *Science*, *250*(4988), 1669-1678.

David, S. J., S. A. Beaton, M. H. Anderberg, et al. (1993), Determination of Total Ozone over Mauna-Loa Using Very High-Resolution Infrared Solar Spectra, *Geophysical Research Letters*, *20*(19), 2055-2058.

Davis, D. S., H. P. Larson, M. Williams, et al. (1980), Infrared Fourier spectrometer for airborne and ground-based astronomy, *Appl Optics*, *19*(24), 4138-4155.

Defries, R. S., M. C. Hansen, J. R. G. Townshend, et al. (2000), A new global 1-km dataset of percentage tree cover derived from remote sensing, *Global Change Biology*, *6*(2), 247-254.

Delmas, R. A., A. Druilhet, B. Cros, et al. (1999), Experiment for Regional Sources and Sinks of Oxidants (EXPRESSO): An overview, *Journal Of Geophysical Research-Atmospheres*, *104*(D23), 30609-30624.

Deutscher, N. M., D. W. T. Griffith, G. W. Bryant, et al. (2009), Total column CO2 measurements at Darwin, Australia - Site description and calibration against in situ aircraft profiles, *Journal of Geophysical Research*.

Dozier, J. (1980), Satellite identification of surface radiant temperature fields of subpixel resolution, N.O.A.A., Washington D.C.

Drummond, J. R., and G. S. Mand (1996), The measurements of pollution in the troposphere (MOPITT) instrument: Overall performance and calibration requirements, *J Atmos Ocean Tech*, *13*(2), 314-320.

Edwards, M., P. Hurley, and W. Physick (2004), Verification of TAPM meteorological predictions using sodar data in the Kalgoorlie region, *Australian Meteorological Magazine*, *53*(1), 29-37.

Emmons, L. K., S. Walters, P. G. Hess, et al. (2009), Description and evaluation of the Model for Ozone and Related chemical Tracers, version 4 (MOZART-4), *Geosci. Model Dev. Discuss.*, *2*(2), 1157-1213.

Farman, J. C., B. G. Gardiner, and J. D. Shanklin (1985), Large Losses of Total Ozone in Antarctica Reveal Seasonal Clox/Nox Interaction, *Nature*, *315*(6016), 207-210.

Fearnside, P. M., N. Leal, and F. M. Fernandes (1993), Rain-forest burning and the global carbon budget - biomass, combustion efficiency and charcoal formation in the Brazilian Amazon, *Journal Of Geophysical Research-Atmospheres*, *98*(D9), 16733-16743.

Fearnside, P. M., P. Graca, N. Leal, et al. (1999), Tropical forest burning in Brazilian Amazonia: measurement of biomass loading, burning efficiency and charcoal formation at Altamira, Para, *Forest Ecology and Management*, *123*(1), 65-79.

Fearnside, P. M., P. Graca, and F. J. A. Rodrigues (2001), Burning of Amazonian rainforests: burning efficiency and charcoal formation in forest cleared for cattle pasture near Manaus, Brazil, *Forest Ecology and Management*, *146*(1-3), 115-128.

Fishman, J., J. M. Hoell, R. D. Bendura, et al. (1996), NASA GTE TRACE A experiment (September October 1992): Overview, *Journal Of Geophysical Research-Atmospheres*, *101*(D19), 23865-23879.

Folkins, I., R. Chatfield, D. Baumgardner, et al. (1997), Biomass burning and deep convection in southeastern Asia: Results from ASHOE/MAESA, *Journal Of Geophysical Research-Atmospheres*, *102*(11D), 13291-13299.

Forman, M. L. (1966), Fast Fourier-transform techniques and its application to Fourier spectroscopy, *Journal of the Optical Society of America*, *56*(7), 978-&.

Fromm, M., A. Tupper, D. Rosenfeld, et al. (2006), Violent pyro-convective storm devastates Australia's capital and pollutes the stratosphere, *Geophysical Research Letters*, *33*(5).

Gonzalez, C. R., M. Schaap, G. de Leeuw, et al. (2003), Spatial variation of aerosol properties over Europe derived from satellite observations and comparison with model calculations, *Atmospheric Chemistry And Physics*, *3*, 521-533.

Goode, J. G., R. J. Yokelson, D. E. Ward, et al. (2000), Measurements of excess O_3, CO_2, CO, CH_4, C_2H_4, C_2H_2, HCN, NO, NH_3, HCOOH, CH_3COOH, HCHO, and CH_3OH in 1997 Alaskan biomass burning plumes by airborne fourier transform infrared spectroscopy (AFTIR), *Journal Of Geophysical Research-Atmospheres*, *105*(D17), 22147-22166.

Graca, P., P. M. Fearnside, and C. C. Cerri (1999), Burning of Amazonian forest in Ariquemes, Rondonia, Brazil: biomass, charcoal formation and burning efficiency, *Forest Ecology and Management*, *120*(1-3), 179-191.

Gregg, J. W., C. G. Jones, and T. E. Dawson (2003), Urbanization effects on tree growth in the vicinity of New York City, *Nature*, *424*(6945), 183-187.

Gregoire, J. M., K. Tansey, and J. M. N. Silva (2003), The GBA2000 initiative: developing a global burnt area database from SPOT-VEGETATION imagery, *Int. J. Remote Sens.*, *24*(6), 1369-1376.

Griffith, D. W. T. (1996), Synthetic calibration and quantitative analysis of gas phase infrared spectra, *Applied Spectroscopy*, *50*(1), 59-70.

Griffith, D. W. T., N. B. Jones, and W. A. Matthews (1998a), Interhemispheric ratio and annual cycle of carbonyl sulfide (OCS) total column from ground-based solar FTIR spectra, *Journal of Geophysical Research-Atmospheres*, *103*(D7), 8447-8454.

Griffith, D. W. T., N. B. Jones, and W. A. Matthews (1998b), Interhemispheric ratio and Annual Cycle of Carbonyl Sulphide (OCS) Total Column from Ground-Based FTIR Spectra, *J. Geophys.Res.*, *103*(D7), 8447-8454.

Griffiths, P. R., and J. A. de_Haseth (1986), *Fourier Transform Infrared Spectrometry*, Wiley, New York.

Hamilton, J. F., G. Allen, N. M. Watson, et al. (2008), Observations of an atmospheric chemical equator and its implications for the tropical warm pool region, *Journal Of Geophysical Research-Atmospheres*, *113*(D20), 12.

Hansen, M. C., R. S. DeFries, J. R. G. Townshend, et al. (2002), Towards an operational MODIS continuous field of percent tree cover algorithm: examples using AVHRR and MODIS data, *Remote Sens. Environ.*, *83*(1-2), 303-319.

Hase, F., T. Blumenstock, and C. Paton-Walsh (1999), Analysis of the instrumental line shape of high-resolution Fourier transform IR spectrometers with gas cell measurements and new retrieval software, *Appl Optics*, *38*(15), 3417-3422.

Hase, F., J. W. Hannigan, M. T. Coffey, et al. (2004), Intercomparison of retrieval codes used for the analysis of high-resolution, ground-based FTIR measurements, *Journal Of Quantitative Spectroscopy & Radiative Transfer*, *87*(1), 25-52.

Hase, F., P. Demoulin, A. J. Sauval, et al. (2006), An empirical line-by-line model for the infrared solar transmittance spectrum from 700 to 5000 cm(-1), *Journal Of Quantitative Spectroscopy & Radiative Transfer*, *102*(3), 450-463.

Hoelzemann, J. J., M. G. Schultz, G. P. Brasseur, et al. (2004), Global Wildland Fire Emission Model (GWEM): Evaluating the use of global area burnt satellite data, *J. Geophys. Res.*, *109*(D14S04).

Holzinger, R., C. Warneke, A. Hansel, et al. (1999), Biomass burning as a source of formaldehyde, acetaldehyde, methanol, acetone, acetonitrile, and hydrogen cyanide, *Geophysical Research Letters*, *26*(8), 1161-1164.

Hu, Y. T., and M. T. Odman (2008), A comparison of mass conservation methods for air quality models, *Atmospheric Environment*, *42*(35), 8322-8330.

Hurley, P. (2000), Verification of TAPM meteorological predictions in the Melbourne region for a winter and summer month, *Australian Meteorological Magazine*, *49*(2), 97-107.

Hurley, P., P. Manins, S. Lee, et al. (2003), Year-long, high-resolution, urban airshed modelling: verification of TAPM predictions of smog and particles in Melbourne, Australia, *Atmospheric Environment*, *37*(14), 1899-1910.

Hurley, P. J., A. Blockley, and K. Rayner (2001), Verification of a prognostic meteorological and air pollution model for year-long predictions in the Kwinana industrial region of Western Australia, *Atmospheric Environment*, *35*(10), 1871-1880.

Hurley, P. J., W. L. Physick, and A. K. Luhar (2005), TAPM: a practical approach to prognostic meteorological and air pollution modelling, *Environmental Modelling & Software*, *20*(6), 737-752.

Hurst, D. F., D. W. T. Griffith, J. N. Carras, et al. (1994a), Measurements of trace gases emitted by Australian savanna fires during the 1990 dry season, *Journal of Atmospheric Chemistry*, *18*(1), 33-56.

Hurst, D. F., D. W. T. Griffith, and G. D. Cook (1994b), Trace gas emissions from biomass burning in tropical Australian savannas, *Journal of Geophysical Research*, *99*(D8), 16,441 - 416,456.

Ito, A., and J. E. Penner (2004), Global estimates of biomass burning emissions based on satellite imagery for the year 2000, *Journal Of Geophysical Research-Atmospheres*, *109*(D14), 18.

Jacob, D. J. (2007), Lectures on Inverse Modeling, edited.

Jones, N. B., M. Koike, W. A. MAtthews, et al. (1994), Southern Hemisphere Seasonal Cycle in total column Nitric Acid, *Geophys. Res. Lett.*, *21*(7), 593-596.

Kasischke, E. S., and J. E. Penner (2004), Improving global estimates of atmospheric emissions from biomass burning, *Journal Of Geophysical Research-Atmospheres*, *109*(D14), 9.

Kaufman, Y. J., R. S. Fraser, and R. A. Ferrare (1990), Satellite Measurements of Large-Scale Air Pollution: Methods, *Journal of Geophysical Research*, *95*(D7), 9895-9909.

Kaufman, Y. J. (1993), Aerosol Optical-Thickness and Atmospheric Path Radiance, *Journal Of Geophysical Research-Atmospheres*, *98*(D2), 2677-2692.

Kaufman, Y. J., D. Tanre, H. R. Gordon, et al. (1997), Passive remote sensing of tropospheric aerosol and atmospheric correction for the aerosol effect, *Journal Of Geophysical Research-Atmospheres*, *102*(D14), 16815-16830.

Kaufman, Y. J., P. V. Hobbs, V. Kirchhoff, et al. (1998a), Smoke, Clouds, and Radiation - Brazil (SCAR-B) experiment, *Journal Of Geophysical Research-Atmospheres*, *103*(D24), 31783-31808.

Kaufman, Y. J., C. O. Justice, L. P. Flynn, et al. (1998b), Potential global fire monitoring from EOS-MODIS, *Journal Of Geophysical Research-Atmospheres*, *103*(D24), 32215-32238.

Kaufman, Y. J., J. M. Haywood, P. V. Hobbs, et al. (2003), Remote sensing of vertical distributions of smoke aerosol off the coast of Africa, *Geophysical Research Letters*, *30*(16), 1831.

King, M. D., Y. J. Kaufman, D. Tanré, et al. (1999), Remote sensing of tropospheric aerosols from space: past, present and future., *Bulletin of the American Meteorological Society*, *80*, 2229-2259.

Kleidman, R. G., N. T. O'Neill, L. A. Remer, et al. (2005), Comparison of moderate resolution Imaging spectroradiometer (MODIS) and aerosol robotic network (AERONET) remote-sensing retrievals of aerosol fine mode fraction over ocean, *Journal Of Geophysical Research-Atmospheres*, *110*(D22).

Koike, M., N. B. Jones, P. I. Palmer, et al. (2006), Seasonal variation of carbon monoxide in northern Japan: Fourier transform IR measurements and source-labeled model calculations, *Journal Of Geophysical Research-Atmospheres*, *111*(D15).

Kondo, Y., N. Takegawa, Y. Miyazaki, et al. (2003), Effects of biomass burning and lightning on atmospheric chemistry over Australia and South-east Asia, *International Journal of Wildland Fire*, *12*(3-4), 271-281.

Lentile, L. B., Z. A. Holden, A. M. S. Smith, et al. (2006), Remote sensing techniques to assess active fire characteristics and post-fire effects, *International Journal of Wildland Fire*, *15*(3), 319-345.

Levine, J. S. (1991), Global Biomass Burning: Atmospheric, Climactic and Biospheric Implications- Introduction, in *Global Biomass Burning: Atmospheric, Climactic and Biospheric Implications*, edited by J. S. Levine, MIT Press, Cambridge, Mass.

Levy, R. C., L. A. Remer, S. Mattoo, et al. (2007), Second-generation operational algorithm: Retrieval of aerosol properties over land from inversion of Moderate Resolution Imaging Spectroradiometer spectral reflectance, *Journal Of Geophysical Research-Atmospheres*, *112*(D13).

Li, Q. B., D. J. Jacob, I. Bey, et al. (2000), Atmospheric hydrogen cyanide (HCN): Biomass burning source, ocean sink?, *Geophysical Research Letters*, *27*(3), 357-360.

Lindesay, J. A., M. O. Andreae, J. G. Goldammer, et al. (1996), International Geosphere-Biosphere Programme International Global Atmospheric Chemistry SAFARI-92 field experiment: Background and overview, *Journal Of Geophysical Research-Atmospheres*, *101*(D19), 23521-23530.

Liu, X., R. D. Blatherwick, F. J. Murcray, et al. (1992), Measurements and Model-Calculations of Hcl Column Amounts and Related Parameters over Mcmurdo During the Austral Spring in 1989, *Journal Of Geophysical Research-Atmospheres*, *97*(D18), 20795-20804.

Lobert, J. M., D. H. Scharffe, W. M. Hao, et al. (1990), Importance of biomass burning in the atmospheric budgets of nitrogen-containing gases, *Nature*, *346*(6284), 552-554.

Luhar, A. K., and P. J. Hurley (2003), Evaluation of TAPM, a prognostic meteorological and air pollution model, using urban and rural point-source data, *Atmospheric Environment*, *37*(20), 2795-2810.

Luhar, A. K., and P. J. Hurley (2004), Application of a prognostic model TAPM to sea-breeze flows, surface concentrations, and fumigating plumes, *Environmental Modelling & Software*, *19*(6), 591-601.

Mahieu, E., C. P. Rinsland, R. Zander, et al. (1995), Vertical Column Abundances of HCN Deduced from Ground-Based Infrared Solar Spectra - Long-Term Trend and Variability, *Journal of Atmospheric Chemistry*, *20*(3), 299-310.

Mahieu, E., R. Zander, L. Delbouille, et al. (1997), Observed trends in total vertical column abundances of atmospheric gases from IR solar spectra recorded at the Jungfraujoch, *Journal of Atmospheric Chemistry*, *28*(1-3), 227-243.

Matthews, E. (1997), Global litter production, pools, and turnover times: Estimates from measurement data and regression models, *Journal Of Geophysical Research-Atmospheres*, *102*(D15), 18771-18800.

Mauzerall, D. L., J. A. Logan, D. J. Jacob, et al. (1998), Photochemistry in biomass burning plumes and implications for tropospheric ozone over the tropical South Atlantic, *Journal Of Geophysical Research-Atmospheres*, *103*(D7), 8401-8423.

Meier, A., A. Goldman, P. Manning, et al. (2003), Improvements to Air Mass Calculations for Ground-Based Infrared Measurements, *J. Quant. Spectrosc. Radiat. Transfer*, *doi:10.1016/S0022-4073(02)00018-3*.

Meier, A., G. Toon, C. Rinsland, et al. (2004), Spectroscopic Atlas of Atmospheric Microwindows in the Middle Infra-red, Institutet for Rymdfysik, Kiruna, Sweden.

Migeotte, M. V. (1948), Spectroscopic evidence of methane in the earth's atmosphere, *Phys Rev*, *73*, 519-520.

Migeotte, M. V. (1949), The fundamental band of carbon monoxide at 4.7 microns in the solar spectrum, *Phys Rev*, *75*, 1108-1109.

Mitchell, R. M., D. M. O'Brien, and S. K. Campbell (2006), Characteristics and radiative impact of the aerosol generated by the Canberra firestorm of January 2003, *Journal Of Geophysical Research-Atmospheres*, *111*(D2), 15.

Myneni, R. B., R. R. Nemani, and S. W. Running (1997), Estimation of global leaf area index and absorbed par using radiative transfer models, *Ieee Transactions on Geoscience and Remote Sensing*, *35*(6), 1380-1393.

Nagahama, Y., and K. Suzuki (2007), The influence of forest fires on CO, HCN, C_2H_6, and C_2H_2 over northern Japan measured by infrared solar spectroscopy, *Atmospheric Environment*, *41*(40), 9570-9579.

Notholt, J. (1994), The Moon as a Light-Source for Ftir Measurements of Stratospheric Trace Gases During the Polar Night - Application for Hno3 in the Arctic, *Journal Of Geophysical Research-Atmospheres*, *99*(D2), 3607-3614.

Notholt, J., G. C. Toon, R. Lehmann, et al. (1997), Comparison of Arctic and Antarctic trace gas column abundances from ground-based Fourier transform infrared spectrometry, *Journal Of Geophysical Research-Atmospheres*, *102*(11D), 12863-12869.

Notholt, J., G. Toon, N. Jones, et al. (2006), Spectral line finding program for atmospheric remote sensing using full radiation transfer, *Journal Of Quantitative Spectroscopy & Radiative Transfer*, *97*(1), 112-125.

Pan, L. W., J. C. Gille, D. P. Edwards, et al. (1998), Retrieval of tropospheric carbon monoxide for the MOPITT experiment, *Journal Of Geophysical Research-Atmospheres*, *103*(D24), 32277-32290.

Paton-Walsh, C., N. Jones, S. Wilson, et al. (2004), Trace gas emissions from biomass burning inferred from aerosol optical depth, *Geophysical Research Letters*, *31*(5), -.

Paton-Walsh, C., N. B. Jones, S. R. Wilson, et al. (2005), Measurements of trace gas emissions from Australian forest fires and correlations with coincident measurements of aerosol optical depth, *Journal Of Geophysical Research-Atmospheres*, *110*(D24).

Paton-Walsh, C., S. R. Wilson, N. B. Jones, et al. (2008), Measurement of methanol emissions from Australian wildfires by ground-based solar Fourier transform spectroscopy, *Geophysical Research Letters*, *35*(8).

Petersen, A. K., T. Warneke, M. G. Lawrence, et al. (2008), First ground-based FTIR observations of the seasonal variation of carbon monoxide in the tropics, *Geophysical Research Letters*, *35*(3).

Phillips, F. A. (2001), Determination of atmospheric ozone by solar infrared, ultraviolet and visible spectroscopy, University of Wollongong, Wollongong.

Pougatchev, N. S., B. J. Connor, and C. P. Rinsland (1995), Infrared measurements of the ozone vertical-distribution above Kitt Peak, *Journal Of Geophysical Research-Atmospheres*, *100*(D8), 16689-16697.

Pougatchev, N. S., N. B. Jones, B. J. Connor, et al. (1998), Ground-based infrared solar spectroscopic measurements of carbon monoxide during 1994 Measurement of Air Pollution From Space flights, *Journal Of Geophysical Research-Atmospheres*, *103*(D15), 19317-19325.

Radke, L. F., D. A. Hegg, J. H. Lyons, et al. (1988), Airborne measurements on smokes from biomass burning, in *Aerosols and Climate*, edited by P. V. H. a. M. P. McCormick, pp. 411-422, A. Deepak, Hampton, Va.

Rasool, S. I., and S. Schneide (1971), Atmospheric Carbon Dioxide and Aerosols - Effects of Large Increases on Global Climate, *Science*, *173*(3992), 138-&.

Remer, L. A., D. Tanré, Y. J. Kaufman, et al. (2002), Validation of MODIS aerosol retrieval over ocean, *Geophysical Research Letters*, *29*(12), 8008.

Rinsland, C. P., M. A. H. Smith, P. L. Rinsland, et al. (1982), Ground-based infrared spectroscopic measurements of atmospheric hydrogen-cyanide, *Journal Of Geophysical Research-Oceans and Atmospheres*, *87*(NC13), 1119-1125.

Rinsland, C. P., R. E. Boughner, J. C. Larsen, et al. (1984), Diurnal-variations of atmospheric nitric-oxide - ground-based infrared spectroscopic measurements and their interpretation with time-dependent photochemical model-calculations, *Journal Of Geophysical Research-Atmospheres*, *89*(ND6), 9613-9622.

Rinsland, C. P., R. Zander, L. R. Brown, et al. (1986), Detection of Carbonyl Fluoride in the Stratosphere, *Geophysical Research Letters*, *13*(8), 769-772.

Rinsland, C. P., N. B. Jones, B. J. Connor, et al. (1998), Northern and Southern Hemisphere Ground-Based Infrared Spectroscopic Measurements of Tropospheric Carbon Monoxide and Ethane, *Journal of Geophysical Research*, *103*, 28,197-128,218.

Rinsland, C. P., A. Goldman, F. J. Murcray, et al. (1999), Infrared solar spectroscopic measurements of free tropospheric CO, C_2H_6, and HCN above Mauna Loa, Hawaii: Seasonal variations and evidence for enhanced emissions from the Southeast Asian tropical fires of 1997-1998, *Journal Of Geophysical Research-Atmospheres*, *104*(D15), 18667-18680.

Rinsland, C. P., E. Mahieu, R. Zander, et al. (2000), Free tropospheric CO, $C2_{H6}$, and HCN above central Europe: Recent measurements from the Jungfraujoch station including the detection of elevated columns during 1998, *Journal Of Geophysical Research-Atmospheres*, *105*(D19), 24235-24249.

Rinsland, C. P., A. Meier, D. W. T. Griffith, et al. (2001), Ground-based measurements of tropospheric CO, C_2H_6, and HCN from Australia at 34 degrees S latitude during 1997-1998, *Journal Of Geophysical Research-Atmospheres*, *106*(D18), 20913-20924.

Rinsland, C. P., A. Goldman, E. Mahieu, et al. (2002), Ground-based infrared spectroscopic measurements of carbonyl sulfide: Free tropospheric trends from a 24-year time series of solar absorption measurements, *Journal Of Geophysical Research-Atmospheres*, *107*(D22), -.

Rinsland, C. P., C. Paton-Walsh, N. B. Jones, et al. (2005), High spectral resolution solar absorption measurements of ethylene (C_2H_4) in a forest fire smoke plume using HITRAN parameters: Tropospheric vertical profile retrieval, *Journal Of Quantitative Spectroscopy and Radiative Transfer*, *96*(2), 301.

Rinsland, C. P., M. Luo, M. W. Shephard, et al. (2008), Tropospheric emission spectrometer (TES) and atmospheric chemistry experiment (ACE) measurements
of tropospheric chemistry in tropical southeast Asia during a moderate El Nin˜o in 2006, *Journal Of Quantitative Spectroscopy & Radiative Transfer*.

Rodgers, C. D. (1990), Characterization and error analysis of profiles retrieved from remote sounding measurements, *Journal of Geophysical Research*, *95*, 5587-5595.

Rodgers, C. D. (2000), *Inverse Methods for Atmospheric Sounding: Theory and Practice*, World Scientific Publishing Co. Pte. Ltd, New Jersey.

Rodgers, C. D., and B. J. Connor (2003), Intercomparison of remote sounding instruments, *Journal Of Geophysical Research-Atmospheres*, *108*(D3), 14.

Rothman, L. S., C. P. Rinsland, A. Goldman, et al. (1998), The HITRAN molecular spectroscopic database and HAWKS (HITRAN Atmospheric Workstation): 1996 edition, *Journal Of Quantitative Spectroscopy & Radiative Transfer*, *60*(5), 665-710.

Rothman, L. S., A. Barbe, D. C. Benner, et al. (2003), The HITRAN molecular spectroscopic database: edition of 2000 including updates through 2001, *Journal Of Quantitative Spectroscopy & Radiative Transfer*, *82*(1-4), 5-44.

Rothman, L. S., D. Jacquemart, A. Barbe, et al. (2005), The HITRAN 2004 molecular spectroscopic database, *Journal Of Quantitative Spectroscopy & Radiative Transfer*, *96*(2), 139-204.

Russell-Smith, J., A. C. Edwards, and G. D. Cook (2003), Reliability of biomass burning estimates from savanna fires: Biomass burning in northern Australia during the 1999 Biomass Burning and Lightning Experiment B field campaign, *Journal Of Geophysical Research-Atmospheres*, *108*(D3), 12.

Saunders, S. M., M. E. Jenkin, R. G. Derwent, et al. (2003), Protocol for the development of the Master Chemical Mechanism, MCM v3 (Part A): tropospheric degradation of

non-aromatic volatile organic compounds, *Atmospheric Chemistry And Physics*, *3*, 161-180.

Sawa, Y., H. Matsueda, Y. Tsutsumi, et al. (1999), Tropospheric carbon monoxide and hydrogen measurements over Kalimantan in Indonesia and northern Australia during October, 1997, *Geophysical Research Letters*, *26*(10), 1389-1392.

Schmid, B., J. Redemann, P. B. Russell, et al. (2003), Coordinated airborne, spaceborne, and ground-based measurements of massive thick aerosol layers during the dry season in southern Africa,, *Journal Of Geophysical Research-Atmospheres*, *108*(D13).

Schultz, M. G. (2002), On the use of ATSR fire count data to estimate the seasonal and interannual variability of vegetation fire emissions, *Atmospheric Chemistry and Physics*, *2*, 387-395.

Schultz, M. G., A. Heil, J. J. Hoelzemann, et al. (2008), Global wildland fire emissions from 1960 to 2000, *Global Biogeochem Cy*, *22*(2), 17.

Seiler, W., and P. J. Crutzen (1980), Estimates of Gross and Net Fluxes of Carbon Between the Biosphere and the Atmsophere from Biomass Burning

Clim. Change, *2*(3), 207-247.

Senten, C., M. De Maziere, B. Dils, et al. (2008), Technical note: New ground-based FTIR measurements at Ile de La Reunion: observations, error analysis, and comparisons with independent data, *Atmospheric Chemistry And Physics*, *8*(13), 3483-3508.

Shirai, T., D. R. Blake, S. Meinardi, et al. (2003a), Emission estimates of selected volatile organic compounds from tropical savanna burning in northern Australia, *Journal of Geophysical Research-Atmospheres*, *108*(D3).

Shirai, T., D. R. Blake, S. Meinardi, et al. (2003b), Emission estimates of selected volatile organic compounds from tropical savanna burning in northern Australia, *Journal Of Geophysical Research-Atmospheres*, *108*(D3), -.

Solomon, S., D. Qin, M. Manning, et al. (2007), Technical Summary, in *Climate Change 2007: The Physical Science Basis. Contribution of Working Group 1 to the Fourth Assessment Report of the Intergovernmental Panel on Climate Change*, edited by S. Solomon, et al., Cambridge University Press, Cambridge, UK.

Soufflet, V., C. Devaux, and D. Tanre (1992), Modified Langley Plot Method for Measuring the Spectral Aerosol Optical-Thickness and Its Daily Variations, *Appl Optics*, *31*(12), 2154-2162.

Stavrakou, T., J. F. MÃ¼ller, I. De Smedt, et al. (2008), Evaluating the performance of pyrogenic and biogenic emission inventories against one decade of space-based formaldehyde columns, *Atmos. Chem. Phys. Discuss.*, *8*(5), 16981-17036.

Sumner, P., M. C. Abrams, and J. W. Brault (2001), Fourier transform spectrometry edited, Amsterdam : San Diego : Academic Press, c2001.

Tanre, D., Y. J. Kaufman, M. Herman, et al. (1997), Remote sensing of aerosol properties over oceans using the MODIS/EOS spectral radiances, *Journal Of Geophysical Research-Atmospheres*, *102*(D14), 16971-16988.

Tomasi, C., F. Prodi, M. Sentimenti, et al. (1983), Multiwavelength Sun-Photometers for Accurate Measurements of Atmospheric Extinction in the Visible and near-Ir Spectral Range, *Appl Optics*, *22*(4), 622-630.

Toon, G. C., J. F. Blavier, B. Sen, et al. (1999), Ground-based observations of Arctic O_3 loss during spring and summer 1997, *Journal Of Geophysical Research-Atmospheres*, *104*(D21), 26497-26510.

Toon, O. B., and M. A. Tolbert (1995), Spectroscopic Evidence against Nitric-Acid Trihydrate in Polar Stratospheric Clouds, *Nature*, *375*(6528), 218-221.

Trentmann, J., M. O. Andreae, and H. F. Graf (2003), Chemical processes in a young biomass-burning plume, *Journal Of Geophysical Research-Atmospheres*, *108*(D22), -.

van der Werf, G. R., J. T. Randerson, G. J. Collatz, et al. (2003), Carbon emissions from fires in tropical and subtropical ecosystems, *Global Change Biology*, *9*(4), 547-562.

Velazco, V., J. Notholt, T. Warneke, et al. (2005), Latitude and altitude variability of carbon monoxide in the Atlantic detected from ship-borne Fourier transform spectrometry, model, and satellite data, *Journal Of Geophysical Research-Atmospheres*, *110*(D9).

Volz, F. E. (1974), Economical Multispectral Sun Photometer for Measurements of Aerosol Extinction from 0.44 Mum to 1.6 Mum and Precipitable Water, *Appl Optics*, *13*(8), 1732-1733.

Ward, D. E., and R. M. Hardy (1984), Advances in the characterisation and control of emissions from prescribed fires,, paper presented at 77th Annual Meeting, Air Pollution Control Assoc, San Franciso, California.

Warneck, P. (2000), *Chemistry of the natural atmosphere* 2nd ed ed., Academic Press, San Diego, Calif. ; London

Washenfelder, R. A., G. C. Toon, J. F. Blavier, et al. (2006a), Carbon dioxide column abundances at the Wisconsin Tall Tower site, *Journal Of Geophysical Research-Atmospheres*, *111*(D22), 11.

Washenfelder, R. A., G. C. Toon, J. F. Blavier, et al. (2006b), Carbon dioxide column abundances at the Wisconsin Tall Tower site, *J Geophys Res-Atmos*, *111*(D22).

Webb, R., C. J. Davis, and S. Lellyett (2004), Meteorological aspects of the ACT bushfires of January 2003, paper presented at Bushfire 2004 Conference, Dept. for Environment and Heritage, , Adelaide, Australia.

Wilson, S. R., and B. W. Forgan (2002), Aerosol optical depth at Cape Grim, Tasmania, 1986 -1999, *Journal of Geophysical Research*, *107*(D8).

Yokelson, R. J., D. W. T. Griffith, and D. E. Ward (1996), Open-path Fourier transform infrared studies of large-scale laboratory biomass fires, *Journal of Geophysical Research*, *101*(D15), 21,067-021,080.

Yokelson, R. J., R. A. Susott, D. E. Ward, et al. (1997), Emissions from smouldering combustion of biomass measured by open-path Fourier transform infrared spectroscopy, *Journal of Geophysical Research*, *102*(D15), 18,865-818,877.

Yoshinori, M., and T. Kanno (1997), Emissions of trace gases (CO_2, CO, CH_4, and N_2O) resulting from rice straw burning, *Soil Science and Plant Nutrition*, *43*(4), 849-854.

Zander, R., C. P. Rinsland, C. B. Farmer, et al. (1986), Observation of Several Chlorine Nitrate (Clono2) Bands in Stratospheric Infrared-Spectra, *Geophysical Research Letters*, *13*(8), 757-760.

Zander, R., P. Demoulin, and E. Mahieu (1994), Monitoring of the Atmospheric Burdens of CH_4, N_2O, CO, $CHClF_2$ and CF_2Cl_2 above Central-Europe During the Last Decade, *Environmental Monitoring and Assessment*, *31*(1-2), 203-209.

Zhao, T. X. P., I. Laszlo, O. Dubovik, et al. (2003), A study of the effect of non-spherical dust particles on the AVHRR aerosol optical thickness retrievals, *Geophysical Research Letters*, *30*(6), -.

Zhao, Y., Y. Kondo, F. J. Murcray, et al. (2000), Seasonal variations of HCN over northern Japan measured by ground-based infrared solar spectroscopy, *Geophysical Research Letters*, *27*(14), 2085-2088.

Zhao, Y., K. Strong, Y. Kondo, et al. (2002), Spectroscopic measurements of tropospheric CO, C_2H_6, C_2H_2,and HCN in northern Japan, *Journal Of Geophysical Research-Atmospheres*, *107*(D18), -.

List of Appendices:

Appendix 1: Papers already published as a result of the work described in this thesis.

Appendix 2: MODIS images of enhanced AOD from the Canberra fires that were chosen for use in making a total emissions estimate from these fires along with the TAPM model predictions for this time from the day's model run and the predicted remaining emissions taken from the previous day's model run.

Appendix 3: MODIS true colour images with thermal anomalies and ECMWF back trajectory analyses for all of the days on which significant smoke plumes were sampled over Darwin.

Appendix 4: Additional material supplied as suggested by examiners.